

**A study of the stratigraphy, lithofacies
and geochemistry of Taal Caldera
Volcano, Philippines, and its
implications for the understanding of
flooded caldera volcanoes**

Thesis submitted for the degree of Doctor of
Philosophy at the University of Leicester

By

Yannick Withoos

School of Geography, Geology and the Environment
University of Leicester

January 2022



UNIVERSITY OF
LEICESTER

Abstract

Explosive eruptions from flooded caldera volcanoes are some of the most violent on Earth. Taal Caldera Volcano, Philippines, is one of the most dangerous because it is poorly understood and in the middle of a densely populated area. A new stratigraphic framework for Taal's prehistoric eruptions increases the number of major ($>5 \text{ km}^3$ DRE) explosive eruptions from 4 to 7, records 3 new minor eruption-units, and newly identifies the Sampaga Formation as the oldest pyroclastic eruption-unit. This study significantly increases the estimated eruption volume for the youngest major eruption-unit, the Buco Formation, from 3 km^3 to 28 km^3 DRE, and for the largest eruption-unit, the Pasong Formation, from 31 km^3 to 90 km^3 DRE. Ash aggregates, fluidal juvenile bomb-rich and poorly-lithified ignimbrites, the presence of fine ash-rich cross-bedded facies, and active and passive ash grain textures are more common in younger eruption-units, especially the Buco Formation, compared to older eruption-units like the Alitagtag Formation. This study therefore hypothesises that water had more access to erupting magma during recent major eruptions, although no major eruption is thought to have been triggered by the explosive interaction of water with magma. All major eruption-units show evidence of plagioclase, pyroxene and magnetite fractionation, although magma evolution for the youngest three eruption-units was dominated by mixing processes. Over time, major eruption-units have been becoming more mafic (from 63 wt.% SiO_2 for the Alitagtag Formation to 58 wt.% SiO_2 for the Buco Formation); almost all major eruption-units can be chemically distinguished from each other using a combination of Y, Fe_2O_3 and Cu.

Major eruptions are punctuated by smaller, but more frequent explosive eruptions, similar to Taal's historical eruptions, which continue today and upon which hazard maps are based. However, this study has shown that Taal's prehistoric eruptions were significantly larger and more frequent than previously thought and that major eruptions have occurred in the past, and therefore could in the future, following a phase of smaller-scale eruptions, similar to Taal's current eruptive phase.

Acknowledgements

This thesis would not have been finished without the help and support of the wonderful people that have been by my side over these past years. Firstly, this thesis would not have existed without the endless efforts and kindness of Catherine Lit. Thank you for showing me the Philippines and giving up your own time to join me on fieldwork. Without your expertise and work in the field, the data collected for this thesis would have been nowhere near as thorough as it is. I would also like to thank the extended Lit family, especially Jose Mari Lit who also joined me in the field, for welcoming me into their home and the hospitality they showed me while I was there.

Thank you to my supervisors: Dr. Mike Branney, Dr. Tiffany Barry and Dr. Andrew Miles, for providing feedback on and discussing the research. Thank you to Gregor Hahn and Alastair Hodgetts for lots of discussions, proofreading, and general moral support over the years. To Dr. Catherine Russell, Dr. Ben Clarke, and Dr. Tom Knott, thank you for showing an interest in my research and helping me further my thesis through discussion and detailed comments on my writing. Further thanks to all my field assistants and friends who flew all the way to the Philippines: Gregor Hahn, Alastair Hodgetts, Ed McGowan, George Stonadge, Elly Tennant, and Andrew Mitchell. I wouldn't have made it through those long months of fieldwork without you all! An additional thank you to Isabel Ashman and Emma Ownsworth for taking the time to proofread two of my chapters for me. I would also like to thank Dr. Mahar Lagmay and Dr. Sandra Catane and their students for coming from Manila to join me in the field and offer their expertise and advice, which were invaluable. Thank you to Dr. Ed Listanco, Dr. Ronnie Torres and Dr. Sandra Catane for allowing me access to their unpublished works and data on Taal Caldera. A further thank you to Ma. Antonia V. Bornas, Dr. Renato U. Solidum Jr. and their colleagues at PHIVOLCS for allowing me to conduct fieldwork, sharing with me some field localities and photographs, discussing their thoughts on Taal's eruptions, and granting me access to the PHIVOLCS library.

The analytical work would not have been achieved without Lin Marvin, Dr. Annika Burns, Dr. Tom Knott, and the rest of the technical team at the University of Leicester. A special thanks to Lin for putting up with my endless questions about XRF prep! A big thank you as well to Rasse Shrestha and Lucy Blain who did an excellent job preparing a multitude of my samples for XRF analysis. I'm also grateful to have had Charlotte Langley and Lyndsay McCarthy as administrators during my thesis, thank you for always having all the answers.

When I started my PhD I was put into an office with people I now have the privilege of calling some of my best friends. Neil, Laura, Steve, Tom and Lewis, we've been through a lot of ups and downs together and I thank you for always lifting me back up whenever I was down. This thesis would not have been finished without you all.

To my family, you have been the best support network I could have asked for, even coming out to the Philippines when I was struggling to keep going. It's been tough not being able to see each other often these past two years, but knowing you're always a call away has pushed me through it.

Finally, to Andrew, there aren't enough words to express how grateful I am for all your love and support over these past few years. Thank you for putting up with my endless stress and for believing in me when I didn't. I could not have done this without you.

Table of Contents

Abstract	i
1. Introduction	1
1.1 Project motivation	1
1.2 Thesis structure, aims, and objectives	2
1.3 Philippine volcanism	4
1.3.1 Study area	6
1.3.2 Field strategies in tropical environments	7
1.4 Pyroclastic density currents	13
1.5 Hydrovolcanism	18
1.5.1 Eruptive processes	19
1.5.2 Transportation processes	22
1.5.3 Identifying hydrovolcanism in prehistoric deposits	23
2. The pyroclastic succession of Taal Caldera Volcano: prehistoric caldera-forming eruptions	30
2.1 Introduction	30
2.1.1 Geological setting	31
2.1.2 Previous stratigraphic workspace	31
2.1.3 The pre-Taal regional landscape	35
2.1.4 Aims and objectives	36
2.2 Methods	36
2.2.1 Fieldwork and sampling	36
2.2.2 Estimating eruption volumes	37
2.3 The Taal Group	40
2.3.1 The Sampaga Tuff Formation	43
2.3.2 The Batangas Tuff Formation	44
2.3.3 The Alitagtag Banded Pumice Ignimbrite Formation	46
2.3.4 The Calumpang Tuff Formation	47
2.3.5 The Tadalac Cave Ignimbrite Formation	48
2.3.6 The Indang Banded Fluidal Juvenile Bomb Ignimbrite Formation	50
2.3.7 The Pasong Fluidal Juvenile Bomb-Rich Ignimbrite Formation	53
2.3.8 The Buroi Ignimbrite Formation	57

2.3.9 The Balagbag Ignimbrite Formation	60
2.3.10 The Tagaytay Pumice and Ash Fall and Tuff Units.....	61
2.3.11 The Buco Ignimbrite and Tuff Formation	64
2.3.12 The Alaminos Tuff Units	68
2.4 The Antonio Carpio Tuff Units.....	69
2.5 Discussion.....	70
2.5.1 Comparison with previous stratigraphy.....	70
2.5.2 Eruption volumes.....	71
2.5.3 Eruption frequency	75
2.6 Conclusions	79

3. Eruption styles of a flooded caldera volcano: eruptive and emplacement processes deduced from the pyroclastic lithofacies of prehistoric eruptions at Taal Caldera Volcano, Philippines 82

3.1 Introduction	82
3.1.1 Aims and objectives.....	87
3.2 Methods	88
3.2.1 Field data.....	88
3.2.2 Lab work methods	90
3.3 Lithofacies at Taal Caldera Volcano	90
3.3.1 Ash aggregates and vesiculated tuff.....	101
3.3.2 Fluidal juvenile bomb-bearing ignimbrites	106
3.3.3 Bedforms	108
3.3.4 Clast textures.....	113
3.4 Vertical lithofacies associations at Taal Caldera Volcano	115
3.5 Markov Chain Analysis	122
3.5.1 Methods.....	122
3.5.2 Results	125
3.5.3 Interpretations.....	129
3.5.4 Effectiveness of Markov Chain Analysis.....	130
3.6 Eruption and depositional styles at Taal Caldera Volcano	131
3.6.1 Depositional styles interpreted from vertical facies associations	131
3.6.2 Eruption styles at Taal Caldera Volcano.....	134
3.6.3 Magma – water interaction at Taal Caldera Volcano	141
3.6.4 Temporal changes in eruption style.....	143
3.7 Explosive eruptions at flooded calderas.....	146

3.7.1 Are flooded caldera deposits finer grained than non-flooded caldera deposits?	146
3.7.2 Do fluidal juvenile bombs indicate magma – water interaction?	148
3.7.3 Implications of magma – water interaction on ignimbrite induration	150
3.7.4 Do flooded caldera pyroclastic deposits have indicative lithofacies associations.....	151
3.8 Conclusions	153
4. The geochemical and petrographic characterisation and evolution of prehistoric eruptions from Taal Caldera Volcano	158
4.1 Introduction	158
4.1.1 Taal Caldera eruptive history and geochemistry.....	160
4.1.2 Regional geochemistry	161
4.1.3 Aims and objectives.....	163
4.2 Methods	164
4.2.1 Field sampling and XRF analysis	164
4.2.2 Data quality.....	165
4.2.3 Geochemical variation within datasets	172
4.2.4 JMP statistical analysis.....	173
4.3 The Taal Group in a regional context.....	176
4.4 Characterising the Taal Group.....	181
4.4.1 Petrographic characterisation	181
4.4.2 Geochemical characterisation	186
4.5 Differentiating named formations within the Taal Group	200
4.5.1 Major element geochemistry.....	200
4.5.2 Trace element geochemistry	201
4.5.3 Distinguishing formations.....	208
4.5.4 The temporal geochemical evolution of Taal Caldera Volcano.....	212
4.5.4 Geochemistry of large, caldera-forming eruptions	215
4.6 Conclusions	218
5. Summary, implications and further work.....	220
5.1 Summary of main conclusions	220
5.2 Hazard implications.....	226
5.3 Further work.....	229
Appendices.....	231

Appendix A: locality table	231
Appendix B: sample table	238
Appendix C: Markov Chain Analysis data	243
Appendix D: Geochemistry data	257
Appendix E: Precision and accuracy calculations	276
Appendix F: JMP Tukey Kramer and canonical structure data	280
References	285

List of Figures

<u>Figure number</u>	<u>Description</u>	<u>Page</u>
Figure 1.1	Location map of the Philippines.	5
Figure 1.2	Location map of Taal Caldera Volcano and the study area.	6
Figure 1.3	Photo of a developing andisol on a Taal tephra deposit.	8
Figure 1.4	Photo of a palaeosol and water logged Taal tephra deposits.	9
Figure 1.5	Photo of a palaeosol intruded by modern roots.	10
Figure 1.6 A-B	Photos of two different localities taken at three separate time intervals.	11
Figure 1.7 A-D	Photos of reworked deposits.	13
Figure 1.8	Diagram of different zones of a pyroclastic density current.	14
Figure 1.9	Diagram of the flow-boundary zone compared to the pyroclastic density current and aggrading ignimbrite.	16
Figure 1.10	Diagram of four end-member flow-boundary zones with several photos showing features of the deposits associated with the different flow-boundary zones.	18
Figure 1.11	Chart of the different types of hydrovolcanism.	19
Figure 1.12	Diagram showing the progression of magma-fuel coolant interactions.	20
Figure 1.13	Graph of different eruption styles based on fragmentation and dispersal index.	21
Figure 1.14 A-B	Photos of accretionary lapilli in Taal Caldera Volcano deposits.	25
Figure 1.15 A-B	Diagrams of the formations of accretionary lapilli according to (A) Brown et al. (2010, 2012) and (B) Van Eaton and Wilson (2013).	26
Figure 1.16	Photo of a fluidal juvenile bomb in a massive lapilli-tuff from Taal Caldera Volcano.	28
Figure 2.1	Location maps of the Philippines and Taal Caldera Volcano.	30
Figure 2.2	Logs of the Taal stratigraphy based on this study together with a log of the previous stratigraphy based on Listanco (1994) and Martinez and Williams (1999).	33
Figure 2.3 A-C	Location map of southeast Luzon with photos of a lava (A) and welded ignimbrite (B) along Tagaytay Ridge and soft sediment deformation (C) along the eastern edge of Lake Taal.	34
Figure 2.4 A-F	Photos of Taal tephra deposits overlying country rock and a map showing the locations of the photos.	42
Figure 2.5	Photo of a clastic dyke in the Sampaga Formation.	43
Figure 2.6	Diagram of the Sampaga and several other formations being cut out by the Buco Formation and an Antonio Carpio Unit.	44
Figure 2.7 A-F	Logs of type localities for the Sampaga, Batangas, Alitagtag and Calumpang formations (D), photos of key features (A, B, E), locality map (C), and a map of the Alitagtag ignimbrite distribution (F).	45
Figure 2.8 A-F	Log of the type locality for the Tadalac Cave Formation (A), photos of key features (C-E), locality map (B), and a Harker plot (F).	49
Figure 2.9 A-H	Logs of multiple localities of the Indang Formation (D), photos of key features (E-H), locality maps (A,B), and a map of the Indang ignimbrite distribution (C).	52
Figure 2.10 A-G	Logs of multiple localities of the Pasong Formation (D), photos of key features (B,E,F,G), locality map (A), and a map of the Pasong ignimbrite distribution (C).	55
Figure 2.11	Harker plot highlighting the high TiO ₂ composition of the BuroI and Balagbag formations.	57
Figure 2.12 A-H	Logs of type localities for the BuroI and Balagbag formations (C, H), photos of key features (D,E,F,G), and locality maps (A,B).	59
Figure 2.13	Logs of the BuroI and Balagbag formations tentatively linked to an unclassified log from previous fieldwork from Punongbayan et al. (1995).	60

Figure 2.14 A-D	Logs of multiple localities of the Tagaytay Units (D), photos of key beds (C,B,E), and locality maps (A).	63
Figure 2.15 A-G	Logs of multiple localities of the Buco Formation (D), photos of key features (A,E,F,G), locality map (B), and a map of the Buco ignimbrite distribution (C).	65
Figure 2.16	Logs of the Taal stratigraphy with distinguishing features of each formation and unit.	81
Figure 3.1	The generalised vertical section of the Taal Group.	86
Figure 3.2	Lithification scale used during fieldwork with key features of each lithification category.	89
Figure 3.3	The impacts of changing deposition rate, shear rate and concentration on flow-boundary zones. Different lithofacies have been placed in an approximate location on the diagram.	100
Figure 3.4 A-B	Photos a matrix rim attached to a fluidal juvenile bomb in a scoria agglomerate in the Pasong Formation (A) and a massive tuff with accretionary lapilli in the Indang Formation (B).	103
Figure 3.5 A-D	Photos of ash aggregates scanned on a flatbed scanner (A-D).	104
Figure 3.6 A-D	Photos of ash pellet tuffs and vesiculated tuffs (A-D).	105
Figure 3.7 A-E	Photos of fluidal juvenile bombs in ignimbrites and scoria agglomerates (A-E).	106
Figure 3.8	Photo of lithic clasts included in a fluidal juvenile bomb from the Buco Formation.	108
Figure 3.9 (A-E)	Photos, sketches and a locality map of dune-bedforms within the Buco Formation (A-E).	110
Figure 3.10	Sketches of Types A, B and C structures based on Douillet (2021).	111
Figure 3.11 A-B	Buco dune-bedforms wavelength and wave height compared to other pyroclastic deposits with dune-bedforms (A) and a locality map (B).	112
Figure 3.12 A-F	Photos of ash grains from various lithofacies and formations taken on a Desktop Scanning Electron Microscope (A-F).	115
Figure 3.13	Graph of facies under- and overlying palaeosols split by accretionary lapilli presence.	122
Figure 3.14	Facies relationship diagram derived from Markov Chain Analysis.	128
Figure 3.15	Log of the Pasong Formation exposure at L3.39.	132
Figure 3.16	Map of Taal with faults in the area, including those associated with the topographic outline of the caldera.	135
Figure 3.17	Photo of a lithic breccia overlying a massive lapilli-tuff with accretionary lapilli in the Tadalac Cave Formation.	136
Figure 3.18 A-C	A compilation of logs of common eruption sequences of Taal Caldera Volcano (A-C).	137
Figure 3.19	Photo of a massive lapilli-tuff overlying a palaeosol, with a massive tuff with accretionary lapilli and massive lapilli-tuff underlying it	138
Figure 3.20 A-C	A compilation of logs of common eruption sequences of Taal Caldera Volcano (A-C).	156
Figure 4.1	Logs of the Taal stratigraphy based on this study together with a log of the previous stratigraphy based on Listanco (1994) and Martinez and Williams (1999).	159
Figure 4.2	Graph adapted from Listanco (1994) identifying two potential geochemical trend lines within a Taal geochemical dataset.	160
Figure 4.3	Location map of Taal Caldera Volcano and other volcanoes near southwest Luzon and different segments of the Luzon Arc.	162
Figure 4.4	Graphs showing an immobile, potentially mobile and mobile element as identified by the loss on ignition reliability test.	167
Figure 4.5	Graph of the isocon analysis for the Buco Formation.	170
Figure 4.6	Regional map of Taal Caldera Volcano with regional volcanoes and the Macolod Corridor.	176

Figure 4.7 A-B	Harker plots of K ₂ O (A) and Zr (B) with named formations from the Taal Group and fields for different regional volcanoes.	178
Figure 4.8	Multi-element plots comparing Taal's most primitive and evolved prehistoric juvenile samples, a sample from the 2020 eruption of Taal's Volcano Island, Laguna de Bay Caldera, San Cristobal Volcano, and the 3 other sections of the Luzon Arc.	179
Figure 4.9	Alkaline series grouping for Taal samples with Luzon arc segment fields, including the Macolod Corridor.	180
Figure 4.10	Log of the Alitagtag Formation and data points split by stratigraphic height for three elements.	187
Figure 4.11	ANOVA diamond plot showing results of SiO ₂ for different juvenile types found in the Alitagtag Formation.	189
Figure 4.12	Log of the Tadalac Cave Formation and data points split by stratigraphic height for four elements.	190
Figure 4.13	ANOVA diamond plot showing results of SiO ₂ and Zn for different juvenile types found in the Tadalac Cave Formation.	191
Figure 4.14	Log of the Indang Formation and data points split by stratigraphic height for four elements.	192
Figure 4.15	ANOVA diamond plot showing results of TiO ₂ for different stratigraphic height groups.	193
Figure 4.16	Log of the Pasong Formation and data points split by stratigraphic height for three elements.	194
Figure 4.17	ANOVA diamond plot showing results of Nd for different stratigraphic height groups.	195
Figure 4.18	Log of the Buroi Formation and data points split by stratigraphic height for three elements.	197
Figure 4.19	Log of the Balagbag Formation and data points split by stratigraphic height for three elements.	197
Figure 4.20	Log of the Bucu Formation and data points split by stratigraphic height for three elements.	198
Figure 4.21 A-B	ANOVA diamond plots for TiO ₂ and Y for different stratigraphic height groups using a complete dataset (A) and a dataset with several outlying samples removed (B).	199
Figure 4.22	Harker plots for all immobile and potentially mobile major oxides.	200
Figure 4.23	Harker plots for all immobile and potentially mobile trace elements.	203
Figure 4.24	Biplots of key elements against the incompatible element Rb with simple fractional crystallisation curves and mixing lines.	207
Figure 4.25	Linear discriminant analysis plots showing the two canonicals that show the maximum separation between formations for datasets of immobile elements, immobile and potentially mobile elements, and all elements.	210
Figure 4.26 A-B	The Fe ₂ O ₃ vs. Y bivariate plot (A) and the Sc vs. Y bivariate plot (B).	211
Figure 4.27	Temporal changes within the Taal Group for key elements alongside the generalised vertical section for the Taal Group.	213
Figure 4.28	The K ₂ O Harker plot for all named formations from the Taal Group compared with several VEI 7 eruptions from the past 10,000 years and multiple other caldera-forming eruptions.	217
Figure 5.1	Logs of the Taal stratigraphy with distinguishing features of each formation and unit.	221
Figure 5.2 A-C	A compilation of logs of common eruption sequences of Taal Caldera Volcano (A-C).	223
Figure 5.3	Map displaying the current hazard map for 'base surges' and buffer zone from the published PHIVOLCS hazard map and the deposit extent for the Pasong eruption.	227

Chapter 1

Introduction

1.1 Project motivation

Flooded caldera volcanoes produce some of the most violent eruptions on Earth, yet remain one of the least understood. Caldera-forming eruptions can include so-called 'super-eruptions' (e.g. Chesner, 2012; Knott et al., 2020), which devastate regions (<20,000 km²) surrounding the volcano, and impact the global climate (Self and Blake, 2008). The aim of this study is to better understand the behaviour of flooded caldera volcanoes through the reconstruction of the prehistoric eruptions of Taal Caldera Volcano - one of the world's sixteen 'Decade Volcanoes' (Torres et al., 1995) - and a likely candidate for future VEI ≤7 eruptions (Newhall et al., 2018). There are 2.4 million people living within a 30 km radius of the volcano (GVP, 2021B), a number that only keeps growing as urban sprawl continues in the region. Despite the enormous impact a large eruption would have on the region, limited work has been done on the prehistorical record of Taal Caldera Volcano's large, ignimbrite-forming eruptions (Geronimo, 1988; Listanco, 1994; Punongbayan et al., 1995; Martinez and Williams, 1999).

This study is only the second to put together a generalised vertical section (GVS) of all the prehistoric eruptions of Taal Caldera Volcano, the first being that of Listanco (1994). There are an additional 5 eruption-units recognised in this GVS, equalling 10 in total. At least 4 of these, possibly 7, were major, caldera-forming eruptions. The major eruptions show an increased impact of magma – water interaction over time, a trend first identified in this study, which implies that any future eruptions from Taal Caldera Volcano are likely to be highly explosive. Extensive fieldwork has highlighted an abundance of flow deposits upon which major cities surrounding Lake Taal such as Batangas and Lipa City, are built. These flow deposits do not just belong to the major eruptions, suggesting that even relatively minor eruptions from Taal Caldera Volcano may impact an area beyond anything covered by pyroclastic density currents produced by any historical eruptions, on which hazard maps are

currently based. This study thus provides large steps towards better understanding the past and therefore future behaviour of Taal Caldera Volcano as a case study of a flooded caldera volcano.

1.2 Thesis structure, aims, and objectives

Chapter 1 outlines the aims and objectives of the thesis and the motivation behind the study. It introduces volcanism in the Philippines, the study area and the challenges of working in tropical environments. Essential research concerning the dynamics of pyroclastic density currents and their deposits is reviewed, as well as hydrovolcanic processes.

Chapter 2 concerns the stratigraphy of the prehistoric eruptions of Taal Caldera Volcano. It was key to put this chapter first because the other chapters require the establishment of the updated stratigraphy. The aims and objectives of this chapter are as follows:

- To determine the minimum number of prehistoric eruptions, their size, styles and whether or not they involved caldera collapse. This was achieved by characterising each eruption by identifying palaeosols in the field and key features of eruption-units to correlate different deposits. Chemical analysis and petrography also assisted in eruption-unit characterisation.
- To estimate an eruption frequency for major and minor prehistoric eruptions. This was achieved by combining various published dates and field exposures of named eruption-units.

Chapter 3 identifies, describes and interprets the lithofacies within the Taal deposits mainly through the use of field logs. The aims and objectives of this chapter are as follows:

- To analyse the preferred eruption and depositional styles from Taal Caldera Volcano, even if certain deposits were not able to be placed within the stratigraphy. This was achieved through describing and interpreting lithofacies and their associations where original data was

based on fieldwork. Additional field observations and lab work concerning fluidal juvenile bombs, ash aggregates, dune bedforms, and ash grain textures complimented the lithofacies analysis and provided more details regarding Taal's eruption and depositional styles.

- To establish any temporal trends in eruption and depositional behaviour, including extents of magma – water interaction. This was achieved by using only lithofacies data from named eruptions units put into stratigraphic order based on the generalised vertical section.
- To determine any preferred lithofacies (associations) or deposit characteristics (e.g. fluidal juvenile bombs, ignimbrite induration) for flooded caldera volcanoes. This was achieved by comparing data from Taal Caldera Volcano and other flooded caldera volcanoes to similar data from non-flooded caldera volcanoes. This established any similarities between the two types of caldera volcanoes and highlighted any differences, especially concerning the eruption and depositional styles of flooded caldera volcanoes.

Chapter 4 focuses on the chemistry of prehistoric eruptions from Taal Caldera Volcano. The aims and objectives of this chapter are as follows:

- To test the reliability and quality of different elements prior to using any for eruption-unit fingerprinting. This was achieved through analysing error bars based on XRF standards (for quality), loss on ignition data (for reliability), and isocon analysis (for reliability).
- To fingerprint each eruption-unit as best as possible, which was achieved using XRF and petrographic data. Statistical differences within eruption-units were statistically evaluated using linear discriminant analysis (LDA).
- To determine whether eruption-units could be statistically distinguished from each other based solely on chemical characteristics. This was achieved using LDA, where all possible elements were combined to maximise the differences in the data.
- To evaluate whether eruption-units can be chemically distinguished from each other using excel plots and which elements should be used on these plots. This was achieved by noting which elements distinguished the most eruption-units from each other on LDA, and which elements had

the most weighting for each canon in LDA (see chapter 4 for details). From this, elements were narrowed down on a trial-and-error basis on excel plots.

- To identify any temporal chemical trends at Taal. This was achieved by plotting elements for all the eruption-units in chronological order and visibly noting any trends.
- To determine whether deposits from Taal Caldera Volcano can be chemically distinguished from other volcanoes in the region (i.e. Macolod Corridor). This was achieved by plotting published data from deposits from these other volcanoes on various chemical plots together with data from Taal Caldera Volcano. Fields were drawn around each volcano and any overlap noted.
- To identify any chemical trends amongst caldera-forming eruptions. Data from Taal Caldera Volcano was plotted on various elemental plots together with published data from well-studied caldera-forming eruptions.

Chapter 5 summarises key findings of the thesis, discusses implications and explores avenues for essential further studies.

1.3 Philippine volcanism

The Philippines is a composite terrane whose tectonics are controlled by multiple, opposing subduction zones on the east and west sides of the archipelago (Barrier et al., 1991; Aurelio, 2000; Yumul Jr et al., 2003). The Sunda plate subducts eastward along the Manila, Negros, Sulu and Cotabato trenches, while the Philippine Sea Plate subducts westward along the Philippine and East Luzon trenches (Fig. 1.1). The Manila Trench is of interest in this study because this is the subduction zone (partly) responsible for volcanism at Taal Caldera Volcano. Early models suggest subduction along the Manila Trench began in the Oligocene (Barrier et al., 1991), however, new evidence suggests this only began in the late Miocene (Yumul Jr et al., 2003). Subduction was initiated along the Manila Trench when a piece of mainland Asia, known as the Palawan-Mindoro microcontinental block (Fig. 1.1), rifted away and collided

with the Philippines (Yumul Jr et al., 2003). As this collision occurred, Luzon rotated several degrees counter-clockwise, causing the existing shear zone between it and the South China Sea to turn into a subduction zone (Yumul Jr et al., 2003). This same collision is thought to be responsible for the initiation of subduction of the Philippine Sea Plate (Barrier et al., 1991) and the steepening of the subduction angle of the South China Sea plate (Ku et al., 2009; Fan et al., 2017). This steepening has caused the Wadati-Benioff zone to move from its position below the northeast of the Macolod Corridor to the southwest, which is where Taal Caldera Volcano is located (Förster et al., 1990). Some argue, however, that the dip of the South China Sea plate is now so steep that the Wadati-Benioff zone no longer underlies the Macolod Corridor at all (Förster et al., 1990).

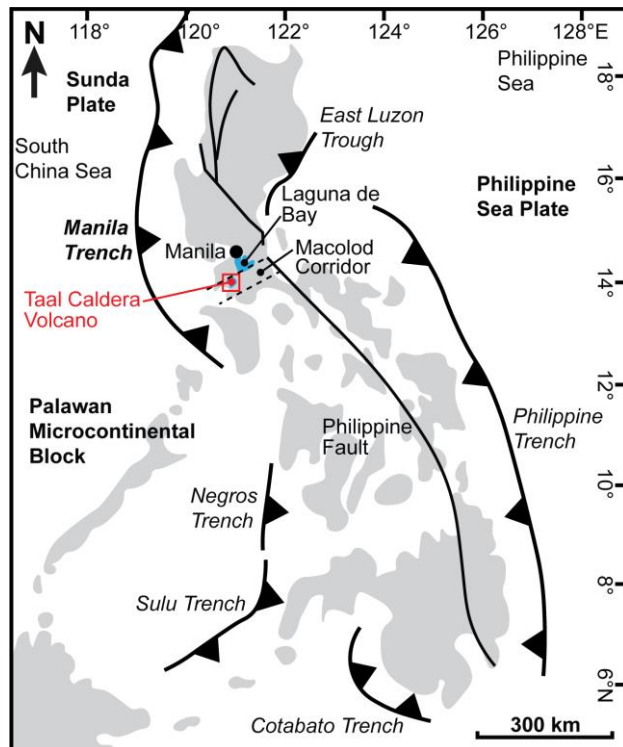


Fig. 1.1: A map of the Philippine archipelago showing subduction zones, the Philippine Fault, Macolod Corridor and the locations of Taal Caldera Volcano and Laguna de Bay. Based on Paguican et al. (2021).

The movement of the Wadati-Benioff zone has shifted the focus of large-scale volcanic activity in the Macolod Corridor from Laguna de Bay, another caldera volcano, in the northeast of the Corridor towards Taal Caldera Volcano in the southwest (Fig. 1.1; Wolfe and Self, 1983; Bautista et al., 2001; Ku et al., 2009). The Macolod Corridor itself is an extensional zone, formed due to the rotation of southwest Luzon as a result of the opposing movements along the Manila Trench and the Philippine Fault (Fig. 1.1; Galgana et al., 2007; Calibo et al., 2010). The Philippine Fault Zone and associated smaller faults accommodate any excess stress resulting from the various plate collisions occurring around the Philippines that is not yet accommodated by the subduction zones (Armada

et al., 2012; Hsu et al., 2016). All this tectonic activity has produced at least 300 volcanoes in the Philippines (PHIVOLCS, 2018) of which 24 are currently active (Delos Reyes et al., 2018) and 26 are potentially active (PHIVOLCS, 2018).

1.3.1 Study area

Previous fieldwork was used as a starting guide for this study's field seasons (Geronimo, 1988; Listanco, 1994; Punongbayan et al., 1995; Martinez and Williams, 1999). However, most of these studies do not provide GPS references and any exposures that were located were covered in cement, overgrown,

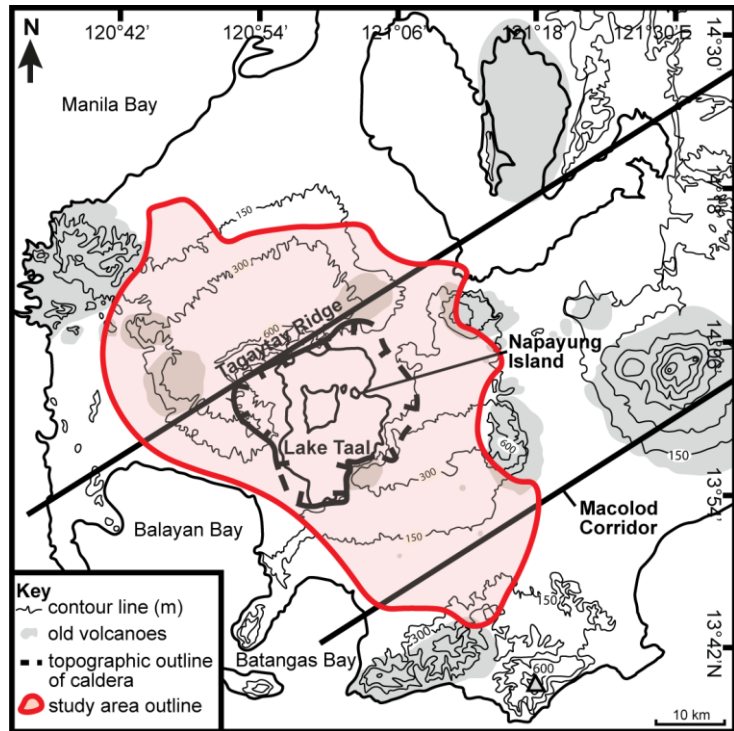


Fig. 1.2: The study area highlighted in red together with key features in the area. The topographic outline of Taal Caldera Volcano is based on Punongbayan et al. (1995).

or too weathered to identify. Therefore, without much guidance, the study area initially focused on the shore areas of Lake Taal and Tagaytay Ridge. This was then extended to Napayung Island and up to 30 km away from the lakeshore (Fig. 1.2). It was essential to conduct three separate field seasons instead of one long one because new exposures are continuously, but often temporarily, revealed in the Philippines. Consequently, key exposures that were found in 2020, were not exposed back in 2018. The best exposures could be found along road cuts, in new building developments, in quarries, or in river valleys.

1.3.2 Field strategies in tropical environments

Volcanoes located in tropical environments tend to have poor exposure and may be situated near highly populated, rapidly expanding urban areas (e.g. Santa María Volcano, Guatemala; Ilopango Caldera, El Salvador; Mount Merapi, Indonesia). Taal Caldera Volcano provides such an environment to work in, therefore I will briefly discuss the challenges and factors taken into consideration when conducting fieldwork here.

The identification of palaeosols was essential during this study. Palaeosols are formed through pedogenesis, which is usually a topdown process (Lowe and Tonkin, 2010), meaning that it starts from the top of the deposit. In active volcanic regions, however, these topdown processes interact with additions of tephra to the top of the developing soils. As a result of this aggradation, the soilification can develop upwards, and thus has been termed 'upbuilding pedogenesis' (Lowe and Tonkin, 2010). Where the accumulation of tephra is slow, weathering advances through the new tephra to reach the older forming soil beneath (Lowe and Tonkin, 2010). If, however, a thicker layer of new tephra is deposited rapidly, the older material is buried too deeply to be affected by subsequent soil formation processes (Lowe and Tonkin, 2010). The buried soil is referred to as a palaeosol. Erosion by water, wind or pyroclastic density currents, may remove one or several soils. Consequently, the palaeosols preserved in the record may not represent the complete soil that was exposed at the surface when new tephra deposited (Lowe, 2016).

An andisol is a soil formed on volcanic ash (Fig. 1.3). Their development depends on substrate type, climate and time (Ugolini and Dahlgren, 2002). In humid, tropical environments like the Philippines, andisols tend to form quickly (Navarrete et al. 2008), taking about <100 – 300 years (Uehara, 2005; Delmelle et al., 2015). Their defining properties are the presence of allophane, imogolite, ferrihydrite, humus and volcanic glass (Dahlgren et al., 2004; Parfitt, 2009; Soil Survey Staff, 2014). These properties often allow andisols to retain large quantities of water (Shoji et al., 1993; McDaniel et al., 2012; Delmelle et al., 2015). A moist andisol can feel greasy (Fig. 1.4) and smears when touched

(Navarrete et al., 2008; McDaniel et al., 2012). These features demonstrate their thixotropic nature (Neall, 2006; Dahlgren et al., 2008), meaning that if a shear force is applied it suddenly loses strength and may behave like a fluid. Once the force is removed, the andisol recovers (part of) its original strength (McDaniel et al., 2012). If an andisol surface dries up, however, it becomes denser and more cohesive, but can retain less water and is less likely to behave like a fluid (McDaniel et al., 2012). Further changes may occur in the andisol simply due to time progression.



Fig. 1.3: A profile of a thick tephra deposit from Taal along Tagaytay Ridge undergoing pedogenesis, forming a thick andisol.

Andisol characteristics may be sustained over time if there are occasional, moderate additions of tephra (Ugolini and Dahlgren, 2002). However, during long repose periods, volcanic glass devitrifies and the soil transforms into other soil types as weathering progresses (Ugolini and Dahlgren, 2002; Delmelle et al., 2015). These soils may have a redder colour if they contain sufficient iron to oxidise, as is often the case with the relatively mafic tephra at Taal Caldera Volcano. It is likely that red soils thus represent a longer repose period with longer subaerial exposure prior to burial.

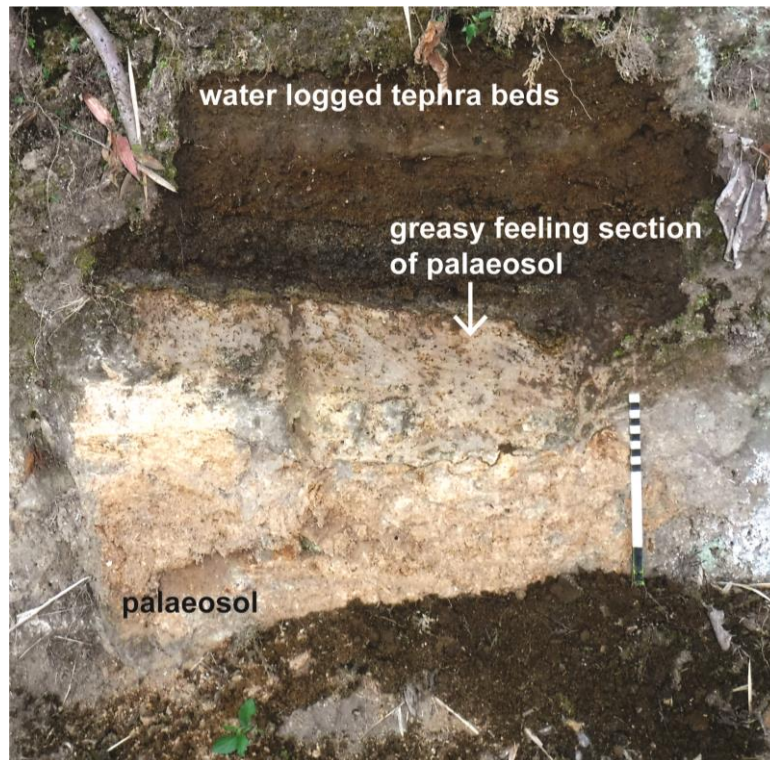


Fig. 1.4: Dark brown tephra beds along Tagaytay Ridge are water logged, likely because the water table is currently level with these rocks. Parts of the rocks had water seeping out of it.

Root traces, nodules, concretions, and mottles can help identify palaeosols and provide further information about the environment they developed in. Mottles are areas within a soil that have a different colour to the main soil matrix. Red-yellow mottles suggest a period of oxidation and concentration of iron and manganese, whereas grey-green mottles indicate the reduction and removal of iron and manganese. Mottling, therefore, indicates that pedogenesis occurred in alternating wet (reduction) and dry periods (oxidation; Vepraskas, 1992; Tabor et al., 2017). Mottles, however, can also form due to diagenesis. Therefore care needs to be exerted when relating palaeosol features to their original soil forming environments.

When palaeosols are exposed to the surface again in the Philippines and other tropical environments, modern roots take advantage and settle in them (Fig. 1.5). Therefore, it can be unclear if root traces in palaeosols are modern or remnants of pre-eruptive vegetation. The location of the modern water table can

also cause palaeosols or primary tephra to appear damp and wet when they originally were not (Fig. 1.4). This can also happen to buried primary tephra because high capillary tension in the fine-grained tephra can prevent water from moving into other beds below, therefore preferentially weathering the tephra bed (Mancarella and Simeone, 2012). The water can be sourced from rain, but also the original volcanic deposit (Brown and Andrews, 2015). These diagenetic processes make palaeosol identification in tropical environments difficult.

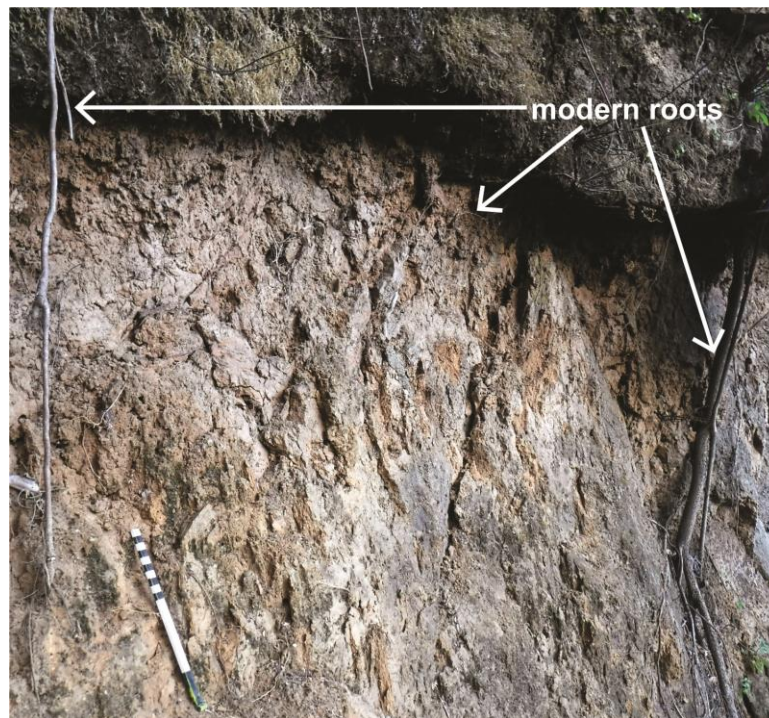


Fig. 1.5: A palaeosol on Tagaytay Ridge near Lake Taal shows modern roots intruding into it.

In addition to the difficulties of soil formation, weathered deposits in general provide a challenge. In weathered deposits clasts can be completely altered or missing, making it almost impossible to correlate these deposits to their less weathered counterparts. It was therefore paramount to find as many recently exposed deposits in the field as possible. Fresh exposures found during the 2018 field season, however, were sometimes already intensely weathered when they were revisited in 2019 and 2020 (Fig. 1.6). Recently exposed deposits may also appear different depending on the time of year, with particular reference to the rainy and dry seasons. A preliminary, short study conducted during fieldwork for this thesis showed significant differences, with exposures looking

more weathered and sometimes impossible to characterise during the rainy season (Fig. 1.6).



Fig. 1.6: (A) An exposure along Tagaytay Ridge freshly exposed in March 2018, showing a dark weathered surface in February 2019 and covered in thick vegetation during the rainy season in October 2019. (B) An exposure along the southern shore of Lake Taal freshly exposed in February 2019, covered in vegetation and a weathered surface during the rainy season in October 2019, and in the dry season in February 2020.

Deposit reworking is also common in tropical environments (e.g. Selles et al., 2015). It may be challenging, however, to distinguish between primary and reworked deposits (e.g. Sohn and Sohn, 2019), especially with regards to lahar deposits. The best way to distinguish between lahar and pyroclastic density

current (PDC) deposits is through palaeomagnetism or the presence of charcoal. However, these methods are only effective if the lahar was relatively cold (Vallance and Iverson, 2015). If a deposit is welded or indurated then this is a relatively good indicator that the deposit is primary. Where deposits are non-welded, those belonging to lahars tend to be less friable, have vesicles within their matrix, and contain more lithic clasts (Vallance and Iverson, 2015). Lahars may be split into debris flows and hyperconcentrated flows, the former being coarser grained, massive, and very poorly sorted. The latter is weakly stratified (much less so than alluvial/fluvial deposits) and can contain silty layers formed during deposit compaction and dewatering (Vallance and Iverson, 2015). Both debris flow and hyperconcentrated flow deposits can have lighter clasts preferentially appearing at the top, which is attributed to pumice rafts forming during transport (Vallance and Iverson, 2015). These rafts can also form in PDCs (Branney and Kokelaar, 2002), however, and therefore this is not a characteristic distinctive to reworked deposits. Debris avalanches are easier to distinguish from primary material because of their characteristic brecciated texture, often described as jigsaw-fit textures (van Wyke de Vries and Davies, 2015). They are poorly sorted and boundaries between different source units may be fluidal. Clastic dykes are also common, frequently associated with faults (van Wyke de Vries and Davies, 2015). Landslides, although possibly similar in appearance to primary PDC deposits, usually have a significantly more limited spatial distribution (Vallance and Iverson, 2015).

Fluvial deposits are relatively abundant around Taal Caldera Volcano with many modern and ancient rivers incising the ignimbrite plains and caldera collapse scarp. These deposits are easily distinguished from ignimbrites by their relatively rounded lithic clasts, better sorting and pervasive cross-bedding (see Miall, 1996 and Aslan, 2013 for a review). Due to the presence of Lake Taal possible lacustrine deposits also need to be taken into consideration. Any lake level drops may expose lacustrine deposits. These are most likely to be relatively near-shore deposits and therefore include coarser material like boulders and gravel, possibly sourced from the steep caldera walls, instead of only silt and clay which would be expected in deeper sections of the lake (Reeves, 1968). Although several examples of reworked deposits were

identified during this study (Fig. 1.7), they are only mentioned when important to any primary volcanic deposits and are not discussed in any more detail.

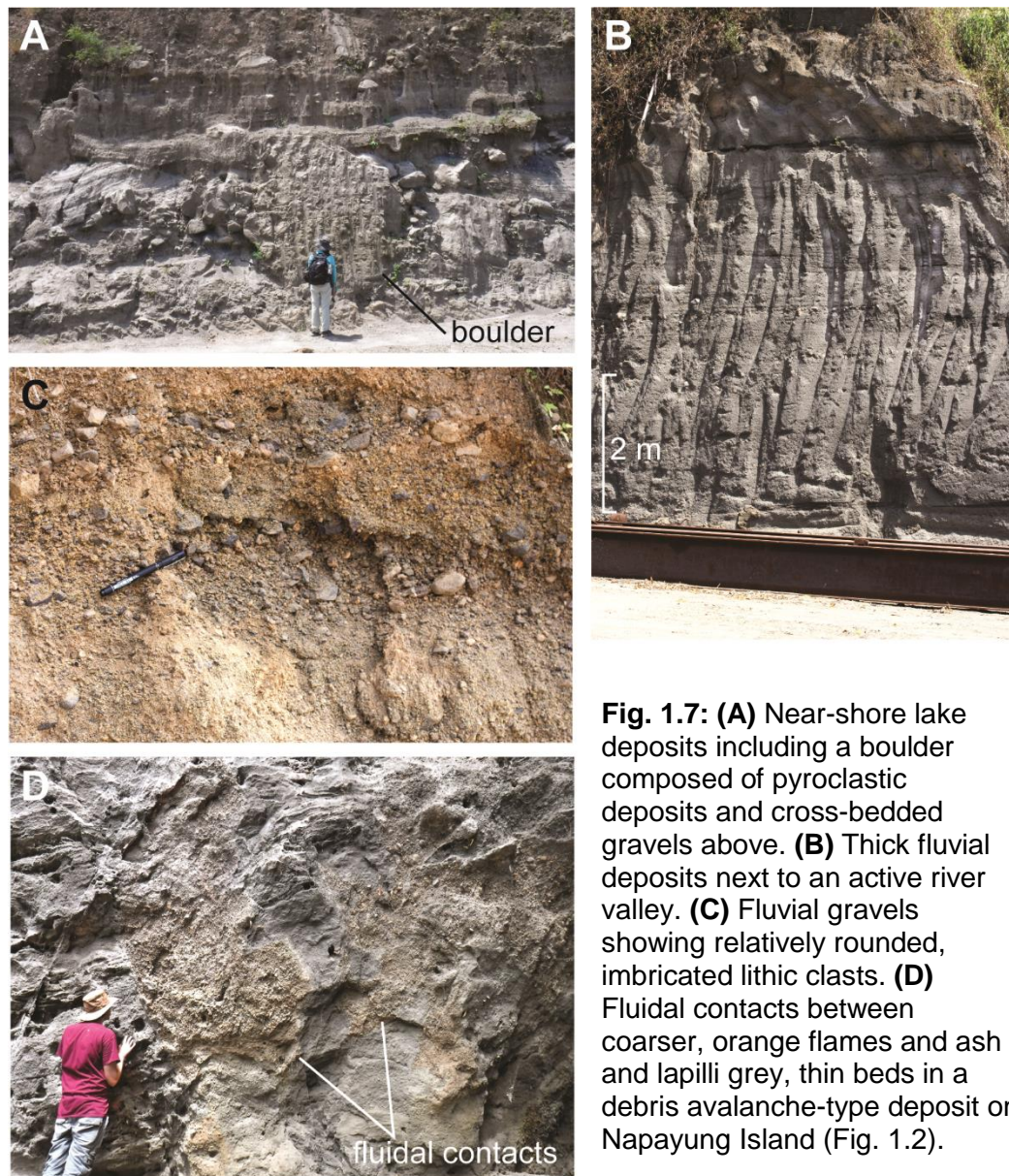


Fig. 1.7: (A) Near-shore lake deposits including a boulder composed of pyroclastic deposits and cross-bedded gravels above. (B) Thick fluvial deposits next to an active river valley. (C) Fluvial gravels showing relatively rounded, imbricated lithic clasts. (D) Fluidal contacts between coarser, orange flames and ash and lapilli grey, thin beds in a debris avalanche-type deposit on Napayung Island (Fig. 1.2).

1.4 Pyroclastic density currents

The following sections describe depositional and eruption styles pertinent to the deposits found around Taal Caldera Volcano. Pyroclastic fountaining, lateral blasts and lava dome collapses can produce pyroclastic density currents (PDCs). PDCs are gravity-driven dispersions of hot gas, volcanic juvenile particles and lithic clasts, and are denser than the surrounding air they flow through (Branney and Kokelaar, 2002). This section of the PDC is referred to as

an underflow, while material transported above this section is called a co-ignimbrite plume because it is less dense than the surrounding air and thus able to loft (Fig. 1.8; Dobran et al., 1993; Sparks et al., 1997). It should be noted that the underflow can also have a relatively low particle concentration (section 1.5.2). Eventually, the entirety of the PDC will loft because it has deposited enough material and/or entrained enough air. This happens at the PDC's runout distance. In travelling its runout distance, a PDC's path will frequently be topographically controlled, preferentially channelling into topographic depressions. Where they are not able to channel (e.g. plains) they spread out laterally and form thalwegs where the flow velocity, competence and/or clast concentration will be higher than in laterally adjacent sections of the flow. These thalwegs tend to increase a PDC's runout distance, although any topographic obstacles can abruptly stop the current (Branney and Kokelaar, 2002). When a PDC hits a topographic obstacle, deposition, especially of dense material, is encouraged. This can cause (part of) the current to loft, be reflected, or flow-stripped. The latter means that the less dense parts of the current are able to overpass the topographic obstacles, while the denser sections are stopped or diverted (Baines, 1995; Woods et al., 1998).

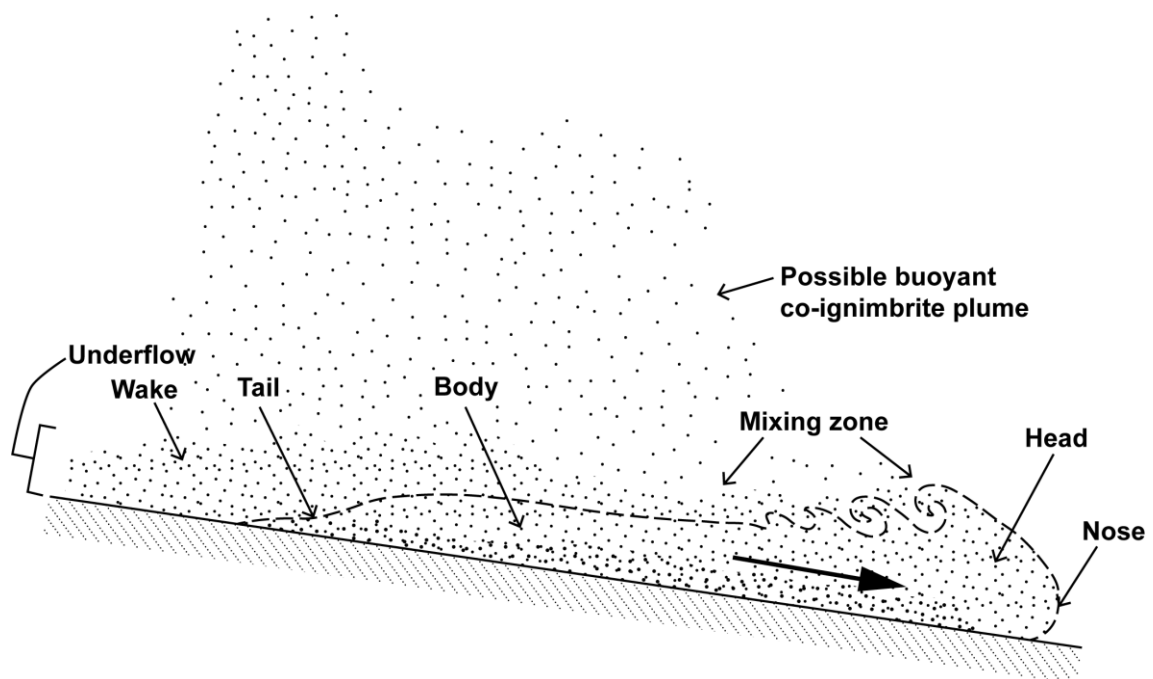


Fig. 1.8: The different zones of a pyroclastic density current, highlighting different areas of the underflow as well as the possible co-ignimbrite plume that may form above, based on Branney and Kokelaar (2002).

The flow dynamics of a PDC are complex and affected by many variables. Importantly, PDCs are temporally and spatially inhomogeneous. A density current is referred to as steady if parameters (velocity, mass flux, composition, or competence) remain the same at any one fixed location. If these parameters increase or decrease at this location, the flow is unsteady, while it may be called quasi-steady if parameters undergo only minor fluctuations about a constant value (Branney and Kokelaar, 2002). The uniformity of a PDC meanwhile relates to the spatial variability of parameters, such that a current is non-uniform if parameters change with distance. An accumulative current would see a spatial increase in a parameter, e.g. higher velocities as slope steepens, while a depletive current undergoes a spatial decrease in a parameter, e.g. lower velocities as the gradient of a slope lessens (Branney and Kokelaar, 2002).

Any information regarding the flow dynamics of PDCs, however, can only be deduced from their deposits because there is currently no method to directly observe their internal processes. Their deposits only record conditions at the lower flow boundary, which is part of the flow-boundary zone (Fig. 1.9). Conditions here do not necessarily reflect conditions higher up in the current, which tends to be less particle-concentrated. The flow-boundary zone also includes the lowermost part of the PDC and the upper section of the aggrading deposit (Fig. 1.9; Branney and Kokelaar, 2002). Noting that the deposit aggrades is key, because it was initially hypothesised that PDCs deposited en-masse (Sparks et al., 1973; Sparks, 1976). The progressive aggradation model (Branney and Kokelaar, 1992, 1994, 1997; Kokelaar and Branney, 1996), however, has become favoured and is used in this study. PDC deposits are usually referred to as ignimbrites, mostly associated with granular fluid-based PDCs in which clasts are concentrated highly enough in the lower flow boundary so that they are supported by the momentum transferred during their collision and/or fluid escape. On the other end of the spectrum are fully dilute PDCs, where the momentum transferred during particle collisions does not control particle support in any section of the current (Branney and Kokelaar, 2002).

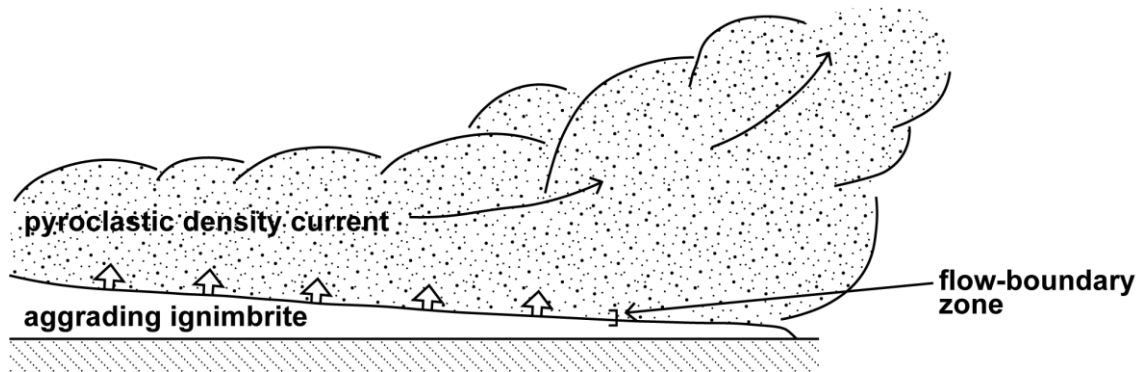


Fig. 1.9: Identification of the flow-boundary zone compared to the pyroclastic density current and aggrading ignimbrite (i.e. the aggrading deposit), based on Branney and Kokelaar (2002).

Ignimbrites do not only provide details regarding the type of current that deposited them, but also the internal conditions at their flow-boundary zone. These conditions are ever-changing, therefore, to make it easier to describe, four end-member flow-boundary zones were created (Fig. 1.10; Branney and Kokelaar, 2002), as follows:

- (1) **Direct fallout-dominated flow-boundary zone:** the current is too dilute in the lower flow zone so that clast interactions and fluid escape are not important. The flow velocity is also too low to allow traction, although slightly higher velocities can orientate depositing clasts, forming weak directional grain fabrics. This flow-boundary zone may also develop at higher velocities if settling clasts immediately stick to the aggrading deposit or when deposition occurs quickly enough to bury deposited material almost instantaneously.
- (2) **Traction-dominated flow-boundary zone:** the current is dilute enough so that clast interactions are not important, unlike fluid turbulence which is the main mechanism of transportation. A sharp change in velocity and rheology at the flow-boundary zone produces high shear rates, which cause clasts to lift back up and roll, saltate or slide prior to deposition. Grain fabrics in the deposit are relatively strong and bedforms (e.g. dune structures) may be produced due to the local non-uniform nature of the

current, which also allows effective segregation of clasts at the flow-boundary zone.

- (3) **Granular flow-dominated flow-boundary zone:** clast interactions are dominant due to high clast abundances and shear rates. Grain fabrics in the deposit are relatively strong, but different clasts do not segregate at the flow-boundary zone because during steady deposition clasts interlock as a pack rather than individually.
- (4) **Fluid escape-dominated flow-boundary zone:** high clast concentrations and low shear rates typify this flow-boundary zone. Shear is prevented by the friction between the concentrated, compacted deposited clasts, which together have a high viscosity and create density gradients. These latter effects prevent any turbulence in the lower flow zone from affecting the deposited material. The continued deposition of clasts expels fluid (dusty gas) upwards, which produces the main clast support mechanism.

Material being transported by the PDC can become variably segregated at the flow-boundary zone, as well as higher up in the flow and in the deposit. This segregation is responsible for the character of the deposit, which is defined by particular lithofacies. Each lithofacies is distinctive and defined by certain characteristics such as grain size, stratification or componentry. In this study, the nomenclature employed in Branney and Kokelaar (2002) will be followed and used to characterise the lithofacies identified in deposits from Taal Caldera Volcano.

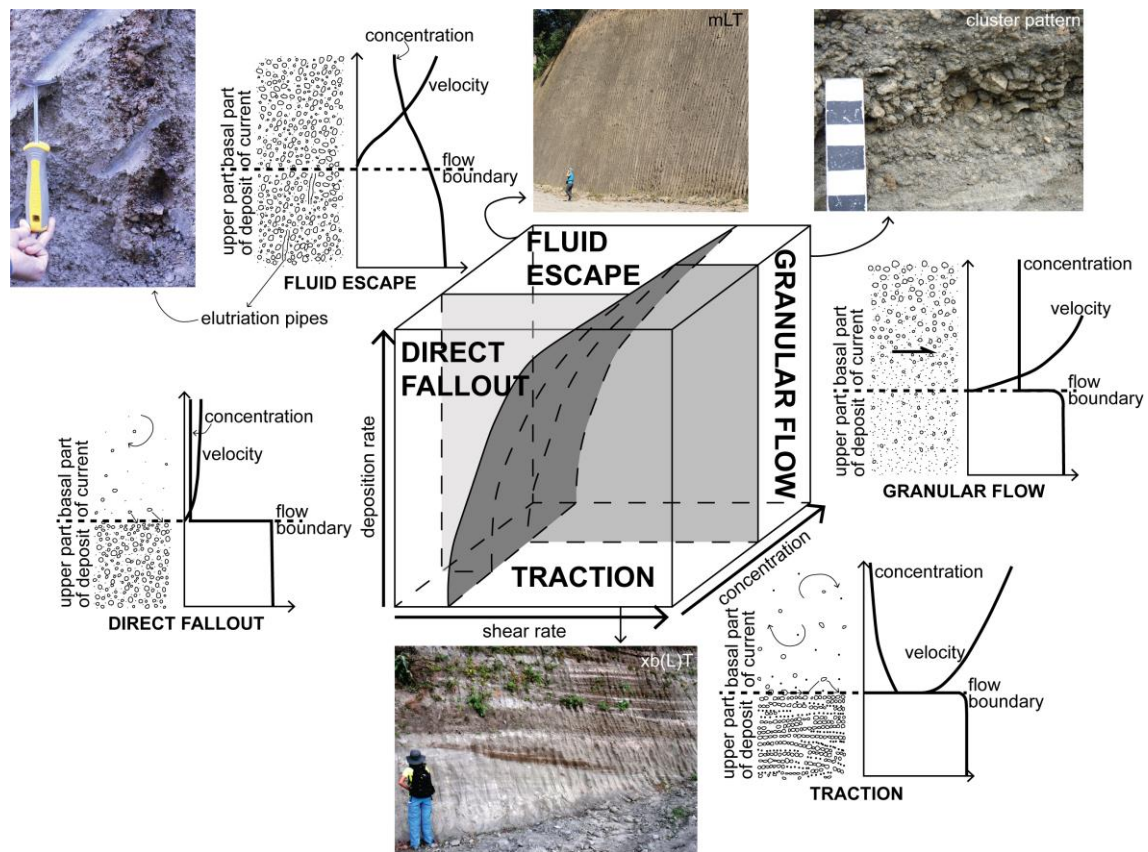


Fig. 1.10: The four different types of flow-boundary zones shown as schematics with graphs identifying how the clast concentration and current velocity changes across the flow-boundary zone. The box graph demonstrates how variations in deposition rate, shear rate and clast concentration can change the type of flow-boundary zone. Examples of features of different flow-boundary zones found in Taal deposits are presented, including elutriation pipes, massive lapilli-tuff (mLT), clast cluster patterns, and cross-bedded (lapilli-) tuff (xb(L)T). These flow-boundary zones are end-members, thus deposits may show characteristics of multiple end-members. Figure based on Branney and Kokelaar (2002).

1.5 Hydrovolcanism

Hydrovolcanism (or hydromagmatism) and phreatomagmatism are commonly used as synonyms. However, recently phreatomagmatism has been mainly referred to as those eruptions where magma-fuel coolant interaction (MFCI) is the main fragmentation mechanism (Németh and Kósik, 2020). Hydrovolcanism is used as the blanket term, referring to all types of magma water interaction in a geological context (Fig. 1.11). Under this classification, phreatomagmatism is a type of hydrovolcanism that is most likely to occur when groundwater is involved (Fig. 1.11). These types of eruptions also include Taalian eruptions (i.e. eruptions involving the interaction of magma with an aquifer; Kokelaar,

1986) and although Taalian is not frequently used in the literature (Németh and Kósik, 2020), it will be used in this study, no less because this study focuses on Taal Caldera Volcano, the volcano that gave this eruption style its name (Kokelaar, 1986). These eruption styles are part of the direct explosive hydrovolcanism group, which also includes Surtseyan, deep subaqueous, Phreatoplinian and Vulcanian eruption styles (Fig. 1.11; Németh and Kósik, 2020). It may be challenging to differentiate between these types of direct explosive hydrovolcanism in pyroclastic deposits, therefore, unless a specific eruption style is hypothesised, the general term hydrovolcanism will be used to imply magma water interaction occurred, but that the source driving fragmentation is unclear.

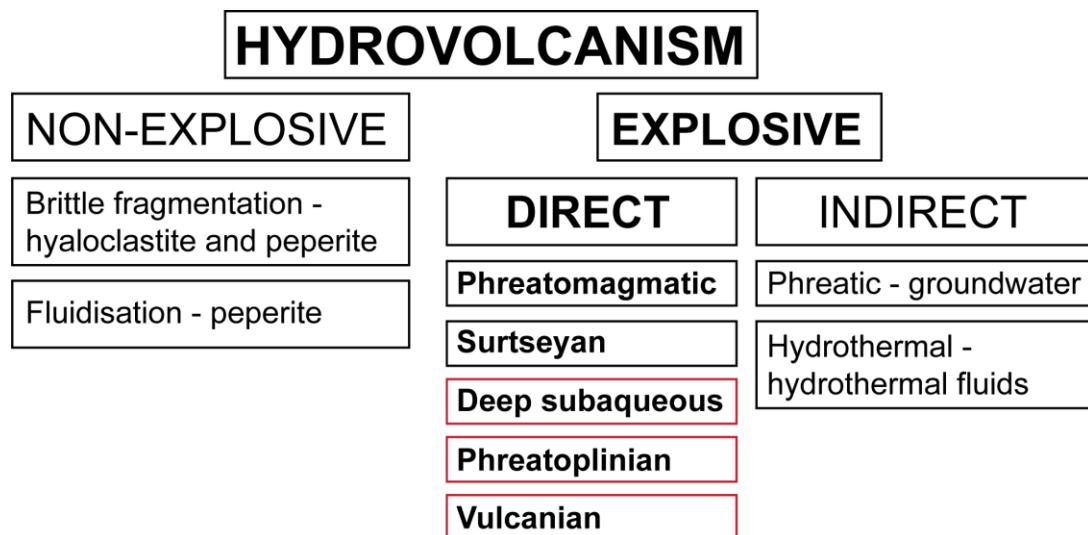


Fig. 1.11: Different nomenclature relating to hydrovolcanism. The key terms used in this study are highlighted in bold. Figure based on Németh and Kósik (2020).

1.5.1 Eruptive processes

A fuel coolant interaction involves the fast conversion of thermal to mechanical energy (Witte et al., 1970). This thermal energy is provided by magma in magma-fuel coolant interactions (MFCI). Initially a small volume of water interacts with the hot magma and vaporises. This vaporisation energy causes magma fragmentation, increasing the surface area of the magma (Corradini, 1982) and allowing a larger volume of water to interact with it (Fig. 1.12). A positive feedback is consequently initiated, allowing the phreatomagmatic eruption to continue as increasing amounts of magma fragment (Sheridan and

Wohletz, 1983A). This process, however, is not realistic for highly viscous melts because they cannot mix water and melt effectively enough to induce

MFCI (Austin-Erickson et al., 2008). Phreatoplinian eruptions usually involve more viscous melts

because it is difficult for volatiles to escape from these melts, so they are more likely to produce explosive, Plinian-style eruptions (Francis and Oppenheimer, 2003). It is

therefore unlikely that Phreatoplinian eruptions are dominated by the same MFCI fragmentation processes as smaller-scale phreatomagmatic eruptions (Palladino et al., 2015). More viscous melts are thought to be able to interact with water due to brittle fracturing of the melt as it is quenched and deformed at the melt-water interface (Austin-Erickson et al., 2008).

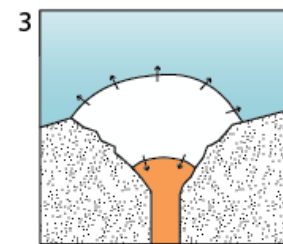
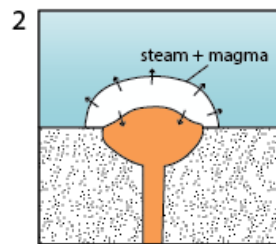
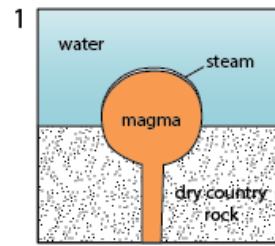


Fig. 1.12: The interaction of a rising magma body with water in a MFCI style. A thin layer of steam forms first before expanding into a magma-steam mixture as the water comes into contact with a larger surface area of the magma as the interaction continues. Based on Sheridan and Wohletz, 1983A.

A question arising is then whether this magma-water interaction is able to trigger an eruption or whether magma started vesiculating and the eruption was already initiated prior to the magma-water interaction. Studied ash grains from known phreatomagmatic events do exhibit a significant number of vesicles, which suggests that gas exsolution and associated purely magmatic fragmentation mechanisms must have been at play before any magma-water interaction occurred (Self and Sparks, 1978; Barberi et al., 1988; Cioni et al., 1992; Houghton et al., 2003). If water interacted with magma immediately, vesicles are unlikely to be found because they would have never formed. The addition of water simply stalls any further vesiculation, quickly quenching the magma and allowing for very efficient fragmentation (Mastrolorenzo et al., 2001,

De Rita et al., 2002; Brown and Andrews, 2015). This gives hydrovolcanic eruptions higher fragmentation indexes compared to their magmatic counterparts (Fig. 1.13).

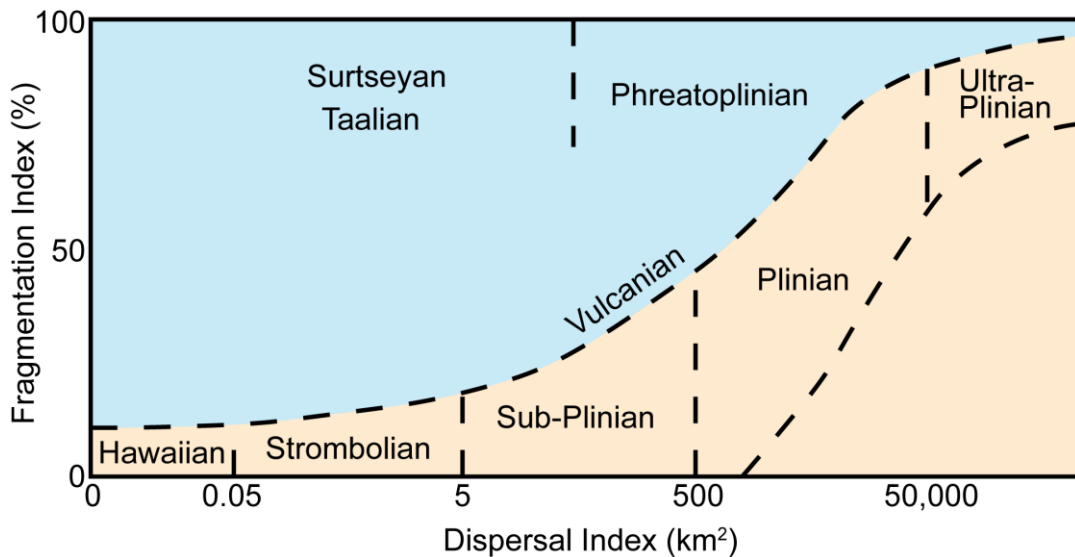


Fig. 1.13: Different eruption styles based on fragmentation and dispersal index. The orange region represents magmatic eruption styles, while the blue region represents hydrovolcanic eruption styles. Vulcanian straddles the two regions. Figure based on Self and Sparks (1978).

Several different magma:water ratios have been quoted as the optimal ratio for efficient fragmentation. They range from 0.4 (Colgate and Sigurgeirsson, 1973) to 0.1 – 0.3 (Sheridan and Wohletz, 1983A) all the way down to 0.03 – 0.04 (Wohletz and McQueen, 1984). This large discrepancy suggests that hydrovolcanic fragmentation mechanisms likely do not just depend on the magma:water ratio, but also on factors such as conduit geometry and style of magma-water interaction (i.e. is the magma static or moving during interaction; White and Valentine, 2016). Furthermore, there currently appears to be a school of thought that takes the lack of evidence of any phreatomagmatic fragmentation as proof that no such eruption occurred (White and Valentine, 2016). However, we must be cautious when jumping to such conclusions as our knowledge of magma-water interaction indicators is still in its infancy and each potential indicator needs to be analysed carefully and balanced with other evidence in order to hypothesise the style of eruption. A key point to consider in this process is that only those regions of the magma that came into direct contact with water will provide evidence of hydrovolcanism (White and

Valentine, 2016). Experimental work has shown that the percentage of magma in direct contact with the water may be as low as 33% (Zimanowski et al., 1997). This is perhaps not surprising, especially for eruptions with high discharge rates, where it would be difficult for water to intrude to significant depths (Houghton et al., 2003) and have enough time to interact with abundant magma.

1.5.2 Transportation processes

Surtseyan eruptions produce one of the most well-known transportation mechanisms associated with hydrovolcanism, namely cock's tail plumes, also called tephra jets. These jets transport pyroclasts and steam along ballistic projectile-like trajectories away from the vent (e.g. Cole et al., 2001). When these jets are large enough, they can form pyroclastic density currents (PDCs) as they descend (Houghton et al., 2015). These PDCs, as well as those associated with other hydrovolcanic eruptions, are typically fully dilute and turbulent. They are often referred to as base or pyroclastic surges in older published literature (e.g. Moore, 1966; Waters and Fisher, 1971; Crowe and Fisher, 1973), but will be referred to as fully dilute PDCs in this thesis. For relatively small-scale hydrovolcanic eruptions these density currents tend to have a runout distance of <10 km because they quickly lose energy as they travel. Many of these dilute currents can be produced, however, because these eruptions are characterised by multiple, rapid, successive explosions (Brown and Andrews, 2015). As many as several thousand explosions may occur during one eruptive phase (Giordano et al., 2002). Breaks in between individual flow events may be preserved in the volcanic record by co-PDC fall deposits (Brown and Branney, 2004; Dávila-Harris et al., 2013; Brown and Andrews, 2015).

PDCs tend to be the preferred method of transport for hydrovolcanic eruptions, including Phreatoplinian eruptions. This is related to the often unstable nature of the eruption column (Van Eaton et al., 2012 ascent dynamics; Houghton et al., 2015). If a significant amount of cold water is added to erupting magma, not all the water is likely to vaporise, and the rising mixture of magma and water will

not become buoyant and form an eruption column. If the added water is less than 15% of the total erupted mass, however, a Plinian-style eruption column is likely to form (Koyaguchi and Woods, 1996). This column does not necessarily form above the eruption source because, unlike during a magmatic eruption, wet plumes may obtain maximum vertical velocities some distance away from the vent since their formation is (partly) driven by moist convection (Houghton et al., 2015). Plumes produced by eruptions with relatively low eruption rates ($<10^8$ kg/s) are less likely to be significantly affected by the amount of interacting water, while for those with eruption rates $>10^8$ kg/s plume height decreases as water mass increases. In these eruptions increasing amounts of water are being carried to the top of the eruption column, therefore significant portions of thermal energy are being used to convert this water to steam instead of on heating the surrounding air to allow buoyancy (Koyaguchi and Woods, 1996). Any hydrovolcanic eruption plume tends to be more ash-rich than its magmatic counterpart and spreads out radially from the source. Their radial distribution is explained by the dominance of moist convection in wet plumes, which allows a significant amount of erupted material to enter the troposphere where it can no longer rise and thus spreads radially instead (Houghton et al., 2015).

1.5.3 Identifying hydrovolcanism in prehistoric deposits

Ever since hydrovolcanism was first recorded in the early 1800s (Németh and Kósik, 2020) volcanologists have been trying to identify evidence for these kinds of eruptions in pyroclastic deposits. Several avenues of investigation have been explored:

(1) Vesicularity

The vesicularity of juvenile material provides insight into the fragmentation mechanisms and eruption styles that produced that deposit (Cashman and Scheu, 2015; White and Valentine, 2016). It was initially thought that hydrovolcanic deposits lacked vesicularity (Heiken, 1972), because magma-water interaction either halted vesiculation at an early stage (e.g. De Rita et al., 2002) or magma was fragmented to such an extent that no vesicles remained intact (Rausch et al., 2015). Although some hydrovolcanic deposits are poorly

vesicular, such as those from the 1.8 ka eruption of Taupo, New Zealand (Houghton et al., 2003) and the AD 472 eruption of Somma Volcano, Italy (Rolandi et al., 2004), many deposits exhibit a wide range of vesicularities (Houghton and Wilson, 1989). The reasoning behind this being that water may not interact with all the melt at the same depth, therefore some melt will have had a longer time to vesiculate (White and Valentine, 2016). Consequently, those sections of melt that interact with water at a shallower level will form more vesicles and thus exhibit higher levels of vesicularity compared to melt that interacted with water at greater depth (White and Valentine, 2016). However, other studies have found that magmatic deposits show a similar range of vesicularities as hydrovolcanic deposits (Rausch et al., 2015; Stovall et al., 2012; Gurioli et al., 2014).

(2) Granulometry

Due to the high levels of fragmentation typically observed during hydrovolcanic eruptions, their deposits are commonly finer grained than their magmatic counterparts (Walker and Croasdale, 1971; Büttner et al., 1999; White and Valentine, 2016). This is based on field evidence from several hydrovolcanic eruption sites such as the Whorneyside Tuff Formation, UK (Branney, 1991), the Oruanui eruption, New Zealand (Wilson, 2001), and Colli Albani, Italy (Trolese et al., 2017). Specifically, proximal deposits are usually finer grained than similarly proximal magmatic deposits (Self and Sparks, 1978; Wilson, 2001) and hydrovolcanic fall deposits show minimal change in medial grain size with distance from source (Sheridan and Wohletz, 1983A). Reasons for this remain unclear but may be related to ash aggregation, a process intensified by any moisture present during particle transport (Self and Sparks, 1978).

(3) Ash aggregation

Ash aggregation may occur via two processes: the sticking together of particles (agglomeration) and/or the layer-by-layer sticking of smaller particles to a larger core (accretion; Brown et al., 2010). When this ash is not stuck together firmly particle clusters form (Brown et al., 2012) that easily disintegrate upon deposition (Walker, 1981; Sisson, 1982). More lithified ash aggregates may be grouped into types of accretionary lapilli (Fig. 1.14), pellets and coated clasts

(Brown et al., 2010; Brown et al., 2012; Van Eaton and Wilson, 2013).

Examples of these ash aggregates have been found in multiple locations where hydrovolcanic eruptions are hypothesised to have occurred including the Whorneyside Tuff Formation, UK (Branney, 1991), Vesuvius, Italy (Cioni et al., 1992), and Taupo, New Zealand (Wilson, 2001). However, evidence of ash aggregation has also been found in deposits where water is not thought to have been present at the source. The multitude of pyroclastic deposits on Tenerife are an example of this (Brown et al., 2010). In this case, and in other examples, the source of water for ash aggregation came from the sea, where water was evaporated as hot density currents surpassed the coastline (e.g. Dufek et al., 2007). Other potential water sources include atmospheric moisture (e.g. Darteville et al., 2002), the exsolution of magmatic volatiles via condensation in the atmosphere (Brown et al., 2010), or rainfall (e.g. Talbot et al., 1994). Alternatively, ash aggregates may form due to electrostatic attraction (e.g. Sorem, 1982; James et al., 2002) or due to the presence of ice in the atmosphere (e.g. Veitch and Woods, 2001; Textor et al., 2006).

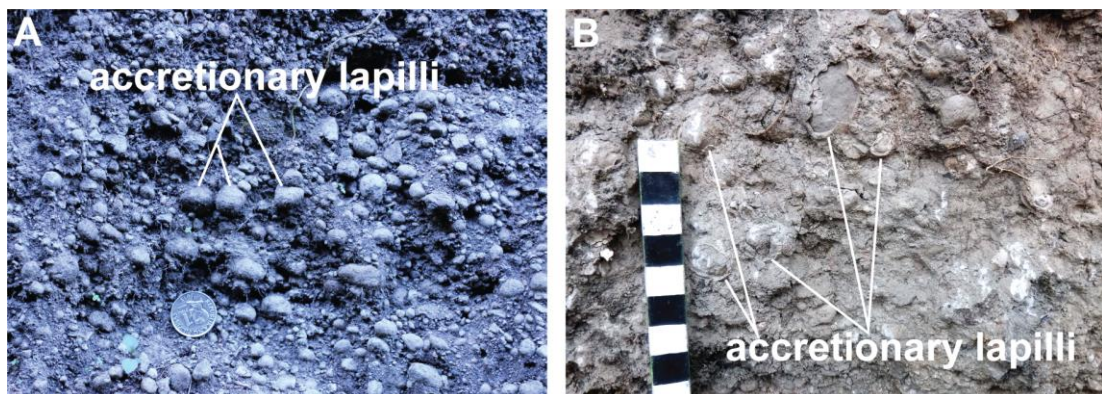


Fig. 1.14: (A) accretionary lapilli within a massive lapilli-tuff found to the east of Taal Caldera Volcano. (B) Accretionary lapilli within a massive tuff found along Tagaytay Ridge (Fig. 1.2). Note the multiple rims of fine grained ash exposed due to the weathering away of outer fractured rims.

The ash aggregate formation process is also somewhat disputed. Although there is consensus that pyroclastic density currents are involved in their formation, discussion arises as to whether fine layers of ash are accreted within the density current (Fig. 1.15; Brown et al., 2010; Brown et al., 2012) or in the region between the density current and an eruption cloud (either vent-derived or co-ignimbrite) above (Fig. 1.15; Van Eaton and Wilson, 2013). For this study, the presence of voluminous pyroclastic density currents is most essential,

however, and therefore a detailed discussion regarding exact methods of the formation of these ash aggregates is beyond the scope of this thesis.

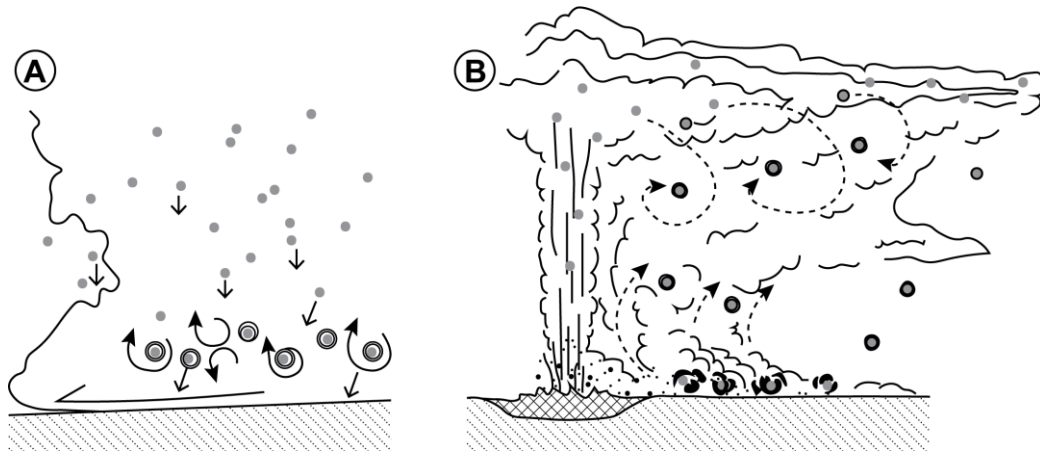


Fig. 1.15: (A) Ash pellets drop down in a pyroclastic density current from the co-ignimbrite plume above where they accrete ash rims prior to deposition (Brown et al., 2010, 2012). (B) Ash pellets drop from a primary and/or co-ignimbrite plume into the region between the plume and pyroclastic density current where they accrete ash rims. This model highlights that accretionary lapilli are likely to disintegrate in the density current (Van Eaton and Wilson, 2013).

(4) Temperature

Magmatic pyroclastic density currents (PDCs) are generally assumed to travel at higher temperatures than their hydrovolcanic counterparts. Ranges of temperatures for hydrovolcanic PDCs have been estimated at 150 – 250 °C (Wilson, 2001) and 200 – 400 °C (Trolese et al., 2017). Even when specific temperature studies of ignimbrites are not carried out, evidence of emplacement at low temperatures includes a lack of welding as seen at Quilotoa volcano, Ecuador (Hall and Mothes, 2008) and in the Oruanui eruption deposits, New Zealand (Wilson, 2001). Contrastingly, a lack of charcoal at Colli Albani has been interpreted as evidence for high temperatures with which the PDC completely incinerated any vegetation (Trolese et al., 2017). An alternative interpretation of this, however, is that PDCs were too cold to burn any vegetation and remnants of vegetation preserved in the ignimbrite have rotted away (e.g. McClelland et al., 2004).

(5) Chemistry

Glass formed during hydrovolcanic eruptions is more likely to alter than glass formed during magmatic eruptions (Wohletz, 1983; Cioni et al., 1992). Variations in elements such as potassium, sodium, silica, alumina and iron can

be used to distinguish altered from fresh glass (Sheridan and Wohletz, 1983A) and could thus be used as an additional indicator of magma-water interaction. The presence of water may also encourage the growth of secondary minerals on or within hydrovolcanic deposits (Cioni et al., 1992). In all these cases, however, it is important to note that a humid environment may also provide moist conditions supporting alteration of deposits.

(6) Ash shapes and textures

When ash shapes were first described, hydrovolcanic shards were referred to as blocky (Heiken, 1972; Self and Sparks, 1978). Later a more sophisticated scheme identified 5 main hydrovolcanic shard shapes; 2 for grains $>100\ \mu\text{m}$: (1) irregular and vesicular with smooth surfaces and (2) equant and blocky, and 3 for grains $<100\ \mu\text{m}$: (3) platy, (4) convoluted and mossy, (5) drop- or sphere-like (Wohletz, 1983). Platy shards were found to be especially common for hydrovolcanic eruptions involving silicic magmas (Self and Sparks, 1978). The different shard shapes and sizes are hypothesised to be a product of different fragmentation mechanisms (Rausch et al., 2015). The grains of $>100\ \mu\text{m}$ are thought to form due to thermal shock waves, while the smaller grains are more likely formed due to the collapse of vapour films (Wohletz, 1983). With recent developments of more quantitative ash shape analysis (e.g. Liu et al., 2015), we may also be able to identify evidence of the faster abrasion experienced by quenched pumice (Patel et al., 2013) and quantitatively distinguish shard types (Liu et al., 2015). The quantitative work on ash shapes is beyond the scope of this study, and thus only initial data from a qualitative analysis of ash grains is presented. This includes textural evidence of magma-water interaction in shards, such as quenching cracks (Heiken, 1972; Büttner, 1999), development of normal jointing on surfaces (e.g. Allen and McPhie, 2000), and pitting (Heiken and Wohletz, 1985).

(7) Further field evidence

The cohesion provided by the water in wet PDCs (Sheridan and Wohletz, 1983A; Cioni et al., 1992) allows their deposits to be plastered onto cliffs or other objects (Heiken, 1971). Furthermore, for large-scale hydrovolcanic eruptions, PDCs are much larger and thus emplace sheet-like ignimbrites as seen in the Whorneyside Tuff Formation, UK (Branney, 1991). Due to the often soft nature of these deposits, they can form gulleys (Walker, 1981; Branney, 1991) or show evidence of other types of soft sediment deformation like

slumping (Sheridan and Wohletz, 1983A; Branney, 1991; Cioni et al., 1992; Büttner, 1999). Volcanic bombs with quenched surface textures, known as cauliflower bombs (Lorenz, 1974), as well as fluidal juvenile scoria bombs (Fig. 1.16; Branney and Kokelaar, 2002) could provide further evidence of magma-water interaction.



Fig. 1.16: An example of a fluidal juvenile scoria bomb found in a massive lapilli-tuff to the west of Taal Caldera Volcano.

A lack of any of these magma – water indicators does not necessarily mean that no water was involved during the eruption. Our current knowledge of these indicators is not yet sufficient to ever completely rule out the presence of water (White and Valentine, 2016), but by using several indicators together, we can be more confident in our conclusions. For example, fine grain size alone cannot be used as an indicator of water involvement at the source because high levels of fragmentation can also occur during a Plinian eruption to produce a fine grained deposit (e.g. Self and Sparks, 1978). However, when a fine grained deposit is found in conjunction with evidence of plastering, a lack of welding, ash aggregates, and grains exhibiting quenching cracks, it is likely that the eruption was hydrovolcanic to some extent. Once this has been established, vesicularity measurements could be used to provide more information about where in the system water interacted with the magma; i.e. if the interaction occurred higher in the conduit, more bubbles will have had a chance to form,

thus preserved vesicularity is likely to be higher than if the magma-water interaction occurred deeper in the conduit (White and Valentine, 2016).

Chapter 2

The pyroclastic succession of Taal Caldera Volcano: prehistoric caldera-forming eruptions

2.1 Introduction

Taal Caldera Volcano in southwest Luzon, Philippines (Fig. 2.1), is one of the world's best known examples of a flooded caldera volcano, which produce some of the most violent volcanic eruptions on Earth. It threatens almost 25 million people living within 100 km of it (GVP, 2021B), but its caldera-forming eruptions remain poorly understood. The dense vegetation and extensive urbanisation make fieldwork challenging, which, together with the more immediate hazards posed by the smaller eruptions from Volcano Island (Fig. 2.1), means little work has been done on Taal Caldera Volcano's much larger prehistorical eruptions.

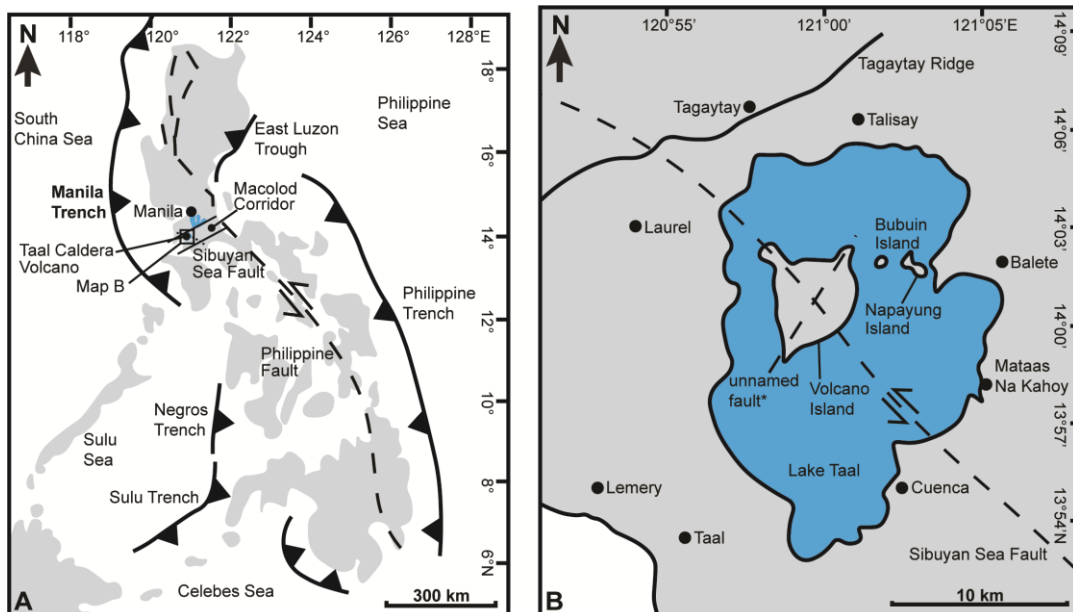


Fig. 2.1: Map A showing the Philippines with trenches (solid lines) on either side of the islands. The capital city Manila, the Macolod Corridor, the Sibuyan Sea Fault (dashed), the Philippine Fault (dashed) and Taal Caldera Volcano are also highlighted (based on Paguican et al., 2021). Map B shows a close-up of Taal Caldera Volcano with several surrounding towns and cities, highlighting Tagaytay Ridge and the islands within Lake Taal (based on Punongbayan et al., 1995). *no movement direction is recorded for the unnamed fault (dashed).

2.1.1 Geological setting

Taal Volcano is a lake-filled caldera volcano (26 x 25 km in size; Fig. 2.1). It lies within the Macolod Corridor (Fig. 2.1), a pull-apart rift zone associated with NW-SE shearing between the Philippine fault and the southern part of the Manila trench (Förster et al., 1990; Galgana et al., 2007). The Macolod Corridor divides the Mindoro and Bataan sections of the Manila Trench, where the South China Sea plate subducts underneath the Philippine Sea plate (Defant et al., 1989; Defant et al., 1991; Delmelle et al., 1998). Taal Caldera Volcano is the youngest and only active volcanic centre in southwest Luzon. Its deposits therefore cover most of the older pyroclastics and any prevolcanic basement. Taal Caldera Volcano's northern and southern rims may be fault controlled and the southern rim likely represents a fault scarp along which part of the caldera collapsed (Zlotnicki et al., 2017A). Several volcanic islands lie in Lake Taal: Bubuin Island, Napayung Island and Volcano Island (Fig. 2.1; Yokoyama et al., 1975). A set of conjugate faults is thought to cross Volcano Island and may exert a control on the location of past and future eruptive centres (Lim, 1983; Listanco, 1994). Taal Caldera Volcano has experienced devastating caldera-forming eruptions as well as smaller-scale explosive events.

2.1.2 Previous stratigraphic workspace

Taal is thought to have experienced at least four caldera-forming ignimbrite eruptions, and three groups of non-caldera-forming eruptions, only the youngest of which is named (Listanco, 1994; Fig. 2.2). The caldera-forming eruptions and deposits are given the same names and are, from youngest to oldest: (1) the 'Scoria Pyroclastic Flow' (SPF; Martinez and Williams, 1999), and 'Scoria Agglutinate' (SAG); (2) the 'Sambong ignimbrite' (SAM); (3) the 'Caloocan pumice flow', (CAL); (4) the 'Alitagtag pumice flow', (ALI; Listanco, 1994; Delos Reyes et al., 2018). A potentially older unit was observed beneath the 'Alitagtag pumice flow' at its type locality along the southern shore of Lake Taal, but this has not been named or described (Punongbayan et al., 1995). The 'Alitagtag pumice flow' in full overlies volcanic and sedimentary deposits from the older

volcanoes such as Mt. Macolod and Mt. Sungay, and it overlies Tertiary limestones, wackes and local intrusive and volcanic deposits near the Batangas Mountains (Listanco, 1994; Fig. 2.3). Several other unnamed eruption-units along the southern shore of Lake Taal are briefly described: two of these are tentatively linked to the 'Alitagtag pumice flow' and the 'Sambong ignimbrite' (Punongbayan et al., 1995).

The start of Taal Caldera Volcano activity is estimated to be as much as 0.14 Ma, which is based on the date of 'proto-Taal' lavas on Napayung Island (Fig. 2.1). Previous studies place these lavas either above (Miklius et al., 1991) or below (Oles, 1991; Listanco, 1994) a prominent, but unnamed ignimbrite on Napayung Island. However, a possible earlier start is indicated by another unnamed tuff unit on the south shore of Lake Taal that was dated as 670 ± 200 Ka (Ar-Ar method; Punongbayan et al., 1995) and another as 300 – 800 Ka (Ar-Ar method; Torres and Self, unpub. data). A 27, 190 \pm 940 year old ^{14}C date was reported from the 'Diliman Tuff Formation' (Newhall, unpub. data in Listanco, 1994), which may overlie deposits from Laguna de Bay Caldera (Fig. 2.3). If all deposits from Laguna de Bay are older than those from Taal Caldera Volcano, this would imply that volcanic activity at Taal Caldera Volcano started after 27 190 \pm 940 years ago (Newhall, unpub. data in Listanco, 1994). The 'Diliman Tuff Formation', however, is chemically distinct from both Laguna de Bay and Taal Caldera Volcano deposits, and its source is not known (Arpa et al., 2008). Therefore this start date, which relies on several stratigraphic suppositions, is not very reliable. The 'Scoria Pyroclastic Formation' in full is the only other dated deposit in the stratigraphy, with ^{14}C dates ranging from 5380 \pm 70 years (Newhall, unpub. data in Listanco, 1994) to 6830 \pm 80 years (Martinez and Williams, 1999). Taal Caldera Volcano is currently active; all historical eruptions have been significantly smaller than the prehistorical caldera-forming ones and centred on Volcano Island (Figs. 2.1, 2.3). This includes its most recent eruptions in 2020, 2021 and 2022.

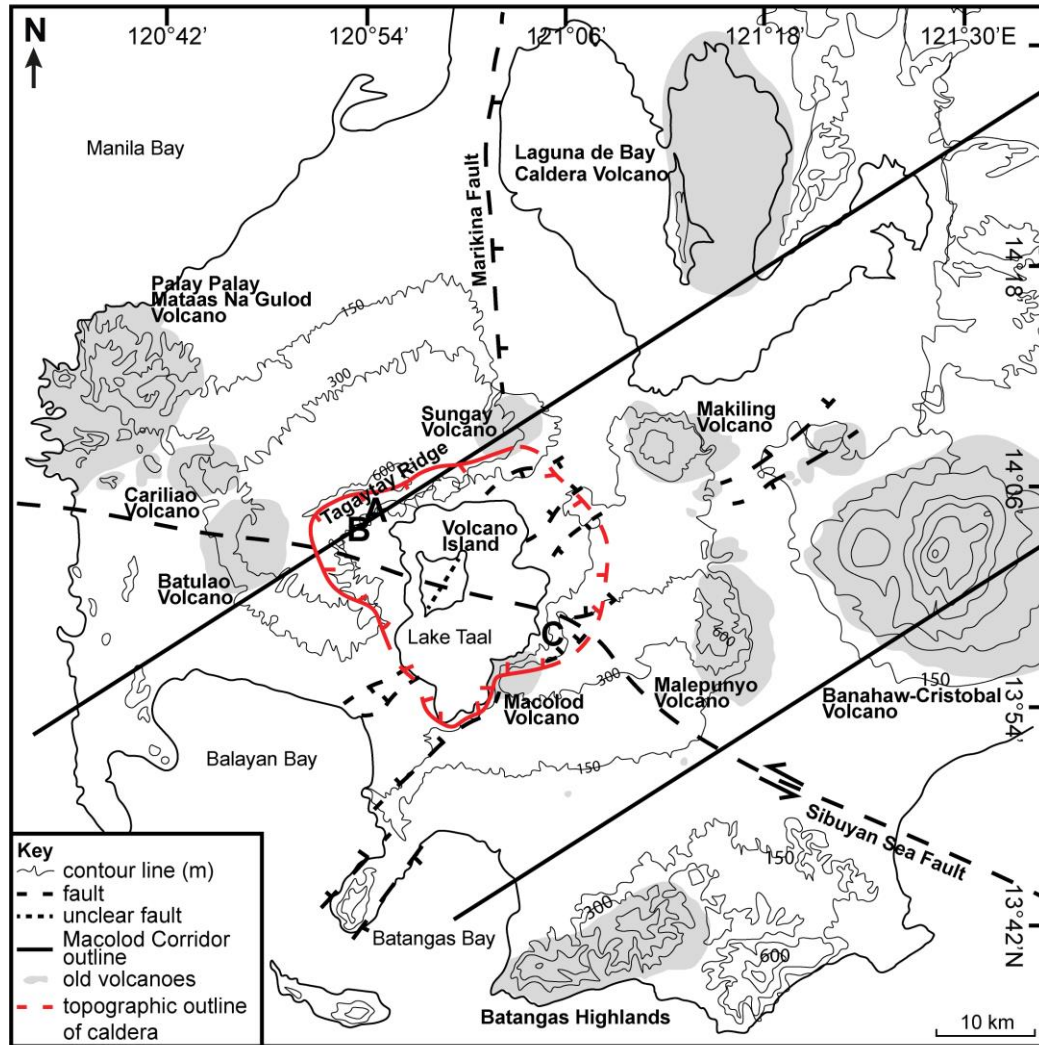


Fig. 2.3: Lake Taal, Volcano Island and the topographic outline of Taal Caldera Volcano (Punongbayan et al., 1995). Older volcanoes are highlighted, the Banahaw-Cristobal Volcano is the only known active volcano besides Taal. Localities and photos of lava at 425 m asl **(A)** and welded ignimbrite at 460 m asl **(B)** along Tagaytay Ridge, and ignimbrites showing soft sediment deformation at 80 m asl along the eastern edge of Lake Taal **(C)**.

2.1.3 The pre-Taal regional landscape

The landscape prior to Taal's caldera-forming eruptions is thought to have been reasonably similar to the present-day landscape. The stratovolcanoes and scoria cones that surround Lake Taal (Fig. 2.3) are all thought to be older than Taal Caldera Volcano (Listanco, 1994). Land between these old volcanoes has been flat and low in elevation since the Pleistocene, prior to which the Batangas Highlands were separated from the rest of Luzon by a shallow sea (Gervasio, 1968). Lake Taal is only 3 m asl and was connected to the China Sea as recently as the 1700s (Wolfe and Self, 1983; Ramos, 1986) and considering Taal Caldera Volcano lies in a zone of extension, there is limited evidence of any large topographic barriers being present during Taal's prehistoric eruptions that are not evident in the modern topography. The level of Lake Taal has fluctuated significantly, even during Taal's historic past, with several old towns currently on the lake floor (Hargrove, 1991). These water level fluctuations seem to have been more pronounced in prehistoric times, with evidence of pyroclastic deposition on older wet ignimbrite in the form of flame structures currently at 100 m elevation (Fig. 2.3).

Tagaytay Ridge may be part of an uplifted fault block (Punongbayan et al., 1995), but it is not known when it reached its current elevation. However, (part of) the ridge probably predates Taal Caldera Volcano because one of the oldest identified eruption-units, the Alitagtag Formation, is exposed at 300 m asl along Tagaytay Ridge. Therefore, for all eruptions younger than the Alitagtag eruption, Tagaytay Ridge was >300 m asl. This is further supported by lavas near the top of the ridge (380 – 425 m asl) associated with Mt. Sungay (Listanco, 1994) and another old unnamed volcano (Fig. 2.3; N. Irapta, 2018, pers. comm.). In addition, this study reports an intensely welded, lava-like ignimbrite at 460 m asl along Tagaytay Ridge (Fig. 2.3), buried by the Tagaytay Units and an unknown dacitic Taal ignimbrite. No intensely welded ignimbrite has been reported from Taal, but several are known from Laguna de Bay (Arpa et al., 2008). Therefore, this welded ignimbrite along Tagaytay Ridge could be from the older Laguna de Bay Caldera. It is appreciated that the entirety of Tagaytay Ridge could have

uplifted recently, but lacking any clear cut evidence in favour of this, this study will assume that Tagaytay Ridge existed with a minimum elevation of 300 m asl at the time of Taal's prehistoric eruptions.

2.1.1 Aims and objectives

This chapter aims to describe and interpret the pyroclastic succession of Taal Caldera Volcano, focusing on eruption-units that record large, caldera-forming explosive events. Fieldwork data from around Lake Taal, and supporting geochemical analyses, are used to correlate deposits, and intervening palaeosols are recorded to help establish the number of eruption-units. Proximal exposures at the caldera wall and near the caldera rim, particularly Tagaytay Ridge, present the best continuous exposures. More distal surrounding areas were explored up to 30 km from the lakeshore, to determine the geographic area covered by each eruption-unit, to help estimate their eruption volumes.

2.2 Methods

2.2.1 Fieldwork and sampling

Thirteen weeks of fieldwork, during three separate visits in 2017 – 2020 were undertaken (Appendix A). Potential field sites were identified using previous work (Listanco, 1994; Punongbayan et al., 1995; Martinez and Williams, 1999; M.A.V. Bornas, pers. comm. 2019). Most of these, however, were visited over 30 years ago and have no published GPS data. This, in combination with the constantly changing and densely vegetated and urbanised region, meant that few of these old sites could be re-accessed. Prior to each field visit, exposures were reconnoitred using Google Earth. The most up-to-date satellite images were used because there are several recent new road cuts and quarries, whereas other previously exposed areas become rapidly vegetated and

inaccessible. In the field, further exposures were found by driving along roads, especially where they cut topography, and by talking to the local population.

The lakeshore was the initial focus of the study in the hope of finding a number of the thickest exposures and proximal eruption-units. From there, the field area was extended 30 km to the north, and 5 – 10 km to the east, south and west. Fewer exposures were found in the east because older volcanoes there have not been described so their deposits could not be confidently distinguished from Taal deposits. To the south exposure is limited, with flat and urbanised coastal plains. To the west, dense vegetation gives way to flat farmland with few exposures. Exposures are likely at greater distances to the east, south and west, but require further exploration.

Over 230 localities were visited, photographed, described, sketched and logged, and juvenile samples taken (Appendix A). Eruption-units were defined in the field, mostly using palaeosols. Surface layers and crusts at most exposures were scraped off and defoliated. Where possible, samples of juvenile clasts, of lithic clasts and the bulk material were collected for microscopy, componentry, granulometry, and chemical analysis.

Two weeks before the planned third, final field visit in January 2020, Taal Volcano erupted. During subsequent fieldwork the alert level was at 3 and planned investigation of lakeshore gullies could not be undertaken since these were within the evacuated danger zone.

2.2.2 Estimating eruption volumes

Field exposures and unit thicknesses were plotted on Google Earth. Minimum thicknesses were given where basal contacts were not visible or the deposit was overlain by reworked material. In these areas, a reasonable conservative thickness estimate was made based on surrounding exposures and palaeotopography (i.e. valley-ponded vs. ignimbrite veneer). The geographic distribution of the inferred pyroclastic density currents (PDCs) was based on

this field information, together with previous work (Listanco, 1994; Martinez and Williams, 1999). Limited exposure and field time constraints meant that the area delineated by visited exposures will considerably underrepresent the true geographic areas inundated by PDCs (Cioni et al., 2020). Therefore, areas of inundation were extrapolated based on palaeotopography (e.g. likely topographic barriers to the PDCs) and by considering the thickness of the most distal exposure (5 m thick deposit was taken to indicate that the PDC travelled further from this site than for a 0.5 m deposit in the same place). For formations older than Pasong, no modern day valleys will be infilled without geological evidence of ignimbrite thickening due to the uncertainties in the palaeo-landscape. An area of PDC inundation was determined using expert judgment, as has been used successfully in similar studies (e.g. Neri et al., 2014, 2015; Cioni et al., 2020). The line encompassing the area of inundation is the 0 m ignimbrite isopach. Different levels of certainty are indicated on this isopach based on where the biggest discrepancies arose using expert judgment. The largest discrepancies tended to be where PDCs entered water or travelled across extensive plains, whereas small discrepancies existed where PDCs hit topographic obstacles. Runout distances across water are relatively conservatively estimated, in comparison to distances estimated at other caldera-forming eruptions such as Krakatau, Campi Flegrei and the Kos Plateau Tuff, where flows travelled 35 – 80 km across water (Fisher et al., 1993; Carey et al., 1996; Allen and Cas, 2001).

The drawn area was used to calculate 5 different eruption volumes. A minimum volume assuming a uniform thickness equal to the minimum exposed thickness, a maximum volume assuming a uniform thickness equal to the maximum exposed thickness, and an average volume assuming a uniform thickness equal to the average of all exposed thicknesses. This average volume was also calculated assuming an estimated maximum thickness for the Lake Taal area. Measured deposit thicknesses were used to draw ignimbrite isopachs. The areas enclosed by individual isopachs were then multiplied by their respective deposit thicknesses to obtain a volume. Volumes are added together for all regions to provide an estimate of total ignimbrite volume for each Formation. All

volumes are converted to a dense rock equivalent (DRE) value (Table 2.1; note that this conversion will ignore the lithic content of the ignimbrites, but this is unlikely to have a significant impact on the final volumes):

$$\text{dense rock equivalent of } O (O_{DRE}) = O \times \frac{\text{deposit density}}{\text{magma density}} \quad (1)$$

Formation	Deposit Density (kg m ⁻³) ¹	Magma Density (kg m ⁻³) ²
Alitagtag	1500	2400
Indang	1750	2500
Pasong	1600	2550
Buco	1500	2500

Table 2.1: deposit and magma densities for the formations for which volume and magnitude calculations were done. ¹Deposit densities based on values from Folkes et al., 2011. ²Magma densities based on Croswell et al., 2012.

Although the isopach method (Crandell, 1989) has been shown to provide overestimates of deposit volumes (Cioni et al., 2020), this is not seen as a problem for this study because volume calculations are considered an underestimate. Conservative estimates of deposit thicknesses were selected where lower contacts were not exposed, in addition to the uncertain travel distance of PDCs across the water, both likely providing an underestimate of the total ignimbrite volume. Limited fall deposits are identified in the study area. However, it is unlikely that eruptions that produced the ignimbrite volumes calculated here did not have a significant fall component, be that an eruption column and/or co-ignimbrite clouds. For caldera-forming eruptions (ignimbrite volumes (DRE) >5 km³; Hughes and Mahood, 2011), fall deposit volumes have been shown to be approximately equal to volumes of ignimbrite outflow sheets (Mason et al., 2004). A separate eruption volume based on this assumption will be calculated. Lastly, another assumption is that for caldera-forming deposits, the intracaldera volume approximately equals the ignimbrite volume (Mason et al., 2004). Although there are uncertainties about the size of the calderas and density of the caldera fill produced in Taal's prehistoric eruptions, separate calculations are undertaken following this assumption to provide a maximum

eruption volume. These assumptions do not hold true in all volcanic provinces (e.g. Salisbury et al., 2011), but it is currently the best method to estimate eruption volumes for Taal's prehistoric eruptions. Despite the uncertainties, estimates of eruption volumes will be useful to inform future modelling and hazard planning. The three volumes will be used to calculate three different eruption masses and magnitudes:

$$\text{Erupted mass } (m) = V_{DRE} (\text{in } m^3) \times \text{magma density} \quad (2)$$

$$\text{Magnitude } (M) = \log_{10}(m) - 7.0 \quad (3)$$

The VEI of eruptions will also be estimated based only on eruption volume (non-DRE) because the eruption duration and column heights for eruptions are unknown (Newhall and Self, 1982). No volume calculations were attempted for formations with fewer than 3 exposures; rather, deposits were matched with the most similar, better exposed formation, and a similar eruption volume was assumed.

2.3 The Taal Group

The Taal Group (new name) refers to the prehistoric pyroclastic succession of Taal Caldera Volcano and includes 10 named formations and three informal 'units' (Fig. 2.2). For simplicity, where possible, each formation comprises a single eruption-unit, which is bounded from the enclosing formations by a palaeosol or reworked deposits. Informal 'units' comprise a package of several, relatively thin deposits with numerous palaeosols. The individual beds within a 'unit' are not sufficiently distinctive to correlate widely, but in some cases it has been possible to correlate a sequence of beds within a 'unit'.

The Taal Group has a maximum thickness of ≤ 180 m and is exposed around Lake Taal, Tagaytay Ridge and the surrounding ignimbrite plains to the coastline (Fig. 2.2). Best exposures are along river valleys, (new) road-cuts and quarries. The Taal Group is overlain by historical deposits from Volcano Island and is underlain by older scoria cones and Miocene – Palaeocene aged sedimentary and igneous intrusive rocks (Fig. 2.4; Wolfe et al., 1978; Listanco,

1994). Several ignimbrites extend below lake level and the contacts with the pre-Taal Volcano basement are rarely exposed. Where they are exposed, ignimbrites of the Taal Group unconformably overlie a Mt. Sungay lava, the Lipa and Saimsim scoria cones, the Upper Miocene Dingle Limestone and the Lower Miocene Tolos Batholith (Fig. 2.4; Wolfe et al., 1978). Nowhere does the same eruption-unit from the Taal Group lie on top of country rock. Part of the Taal Group may be sedimentary (e.g. laharcic; fluvial), but in the absence of clear field or textural evidence, deposits were taken to be pyroclastic.

The formations and units within the Taal Group are described below in stratigraphic order. The order was determined using field evidence from exposures available at the time of study incorporating previous work where possible (Listanco, 1994; Martinez and Williams, 1999; S. Self, pers. comm., 2020). Not all units previously included in the Taal stratigraphy could be confidently linked to deposits found during the present study (Fig. 2.3). The stratigraphy (Fig. 2.3) would benefit from further updating as new exposures are created and discovered.

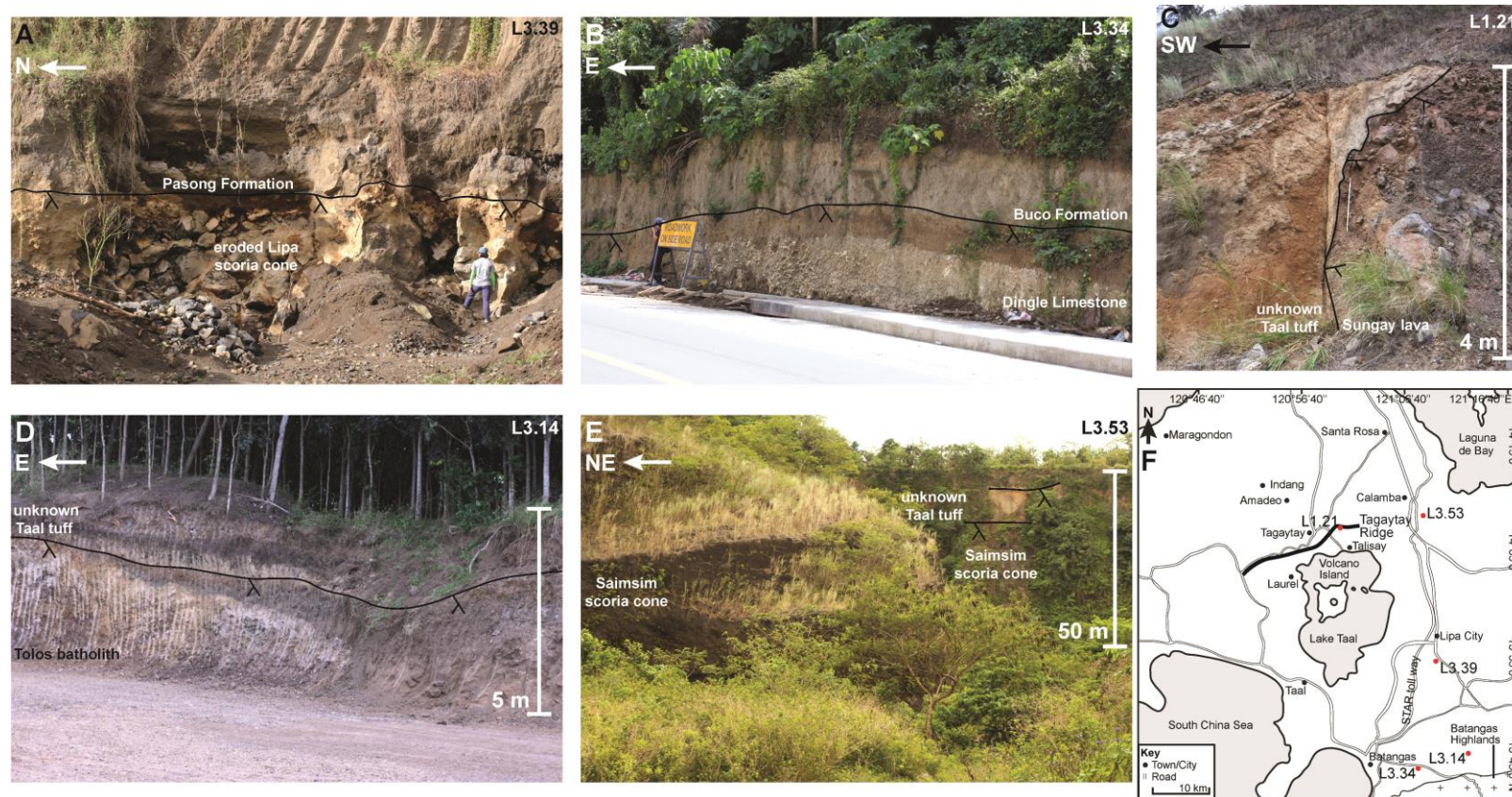


Fig. 2.4: Localities where the Taal Group pyroclastic units directly overlie older country rock (inset map, F, gives site locations). **(A)** The Pasong Formation overlies a red soil on top of an eroded scoria cone near Lipa City [$13^{\circ} 54.631'N$ $121^{\circ}10.745'E$]. **(B)** The Buco Formation overlies a red/orange soil developed on the Upper Miocene Dingle Limestone near the Batangas Highlands, a significant unconformity [$13^{\circ} 45.130'N$ $121^{\circ}08.263'E$]. **(C)** Weathered Taal Group tuff (unnamed) deposited against a near vertical dark red soil on lava from Mt. Sungay Volcano [$14^{\circ} 07.575' N$ $121^{\circ} 00.890' E$]. **(D)** An unknown Taal Group tuff overlies the Lower Miocene Tolos Batholith near the Batangas Highlands [$13^{\circ} 45.348'N$ $121^{\circ}12.599'E$]. **(E)** An unknown Taal Group tuff overlies a scoria cone near Saimsim [$14^{\circ} 09.700'N$ $121^{\circ}08.979'E$].

2.3.1 The Sampaga Tuff Formation

The Sampaga Tuff Formation (new name) is the lowest known eruption-unit in the Taal Group, although no age determination is currently available. It is a poorly lithified, dark grey – white tuff, 2.4 m thick, with rare coarse ash-sized black pumices and broken accretionary lapilli in a fine ash matrix of unknown composition. A low-angle cross-bedded basal part, 1.2 m thick, with aligned lithic clasts is overlain by a white accretionary lapilli-tuff, 1.2 m thick. The Sampaga Formation and underlying palaeosol (belonging to an unknown deposit) are locally cut by a clastic dyke (Fig. 2.5). The top of the southern extent of the Sampaga Formation is erosional with a thin upper palaeosol overlain by several younger deposits thought to include the Buco Formation (Fig. 2.6). The upper tuff contains layers of subhorizontal white concretions that give the appearance of bedding, and it passes up into an orange palaeosol that also contains white calcrete-like concretions (Fig. 2.7), with evidence of plants in thin section. Above this palaeosol lies the Batangas Formation. The Sampaga Formation type locality is along a new southern bound road-cut off of Antonio Carpio Rd near the Sampaga Barangay Hall (L3.35, Fig. 2.7) and it records an explosive eruption that produced at least one dilute, possibly hydrovolcanic, pyroclastic density current.



Fig. 2.5: A clastic dyke cutting the Sampaga Formation and the underlying palaeosol at L3.35 [13° 45.226'N 121°06.037'E].

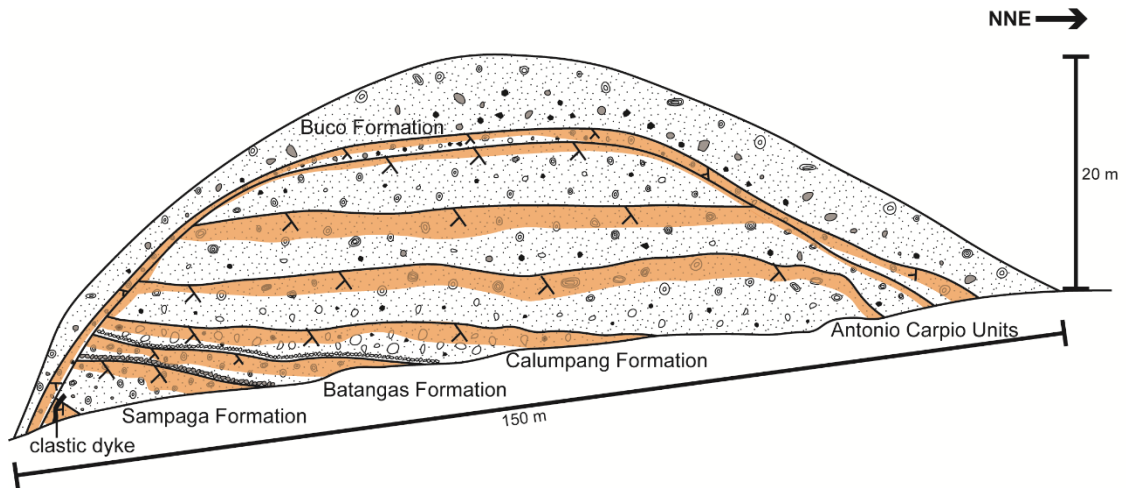
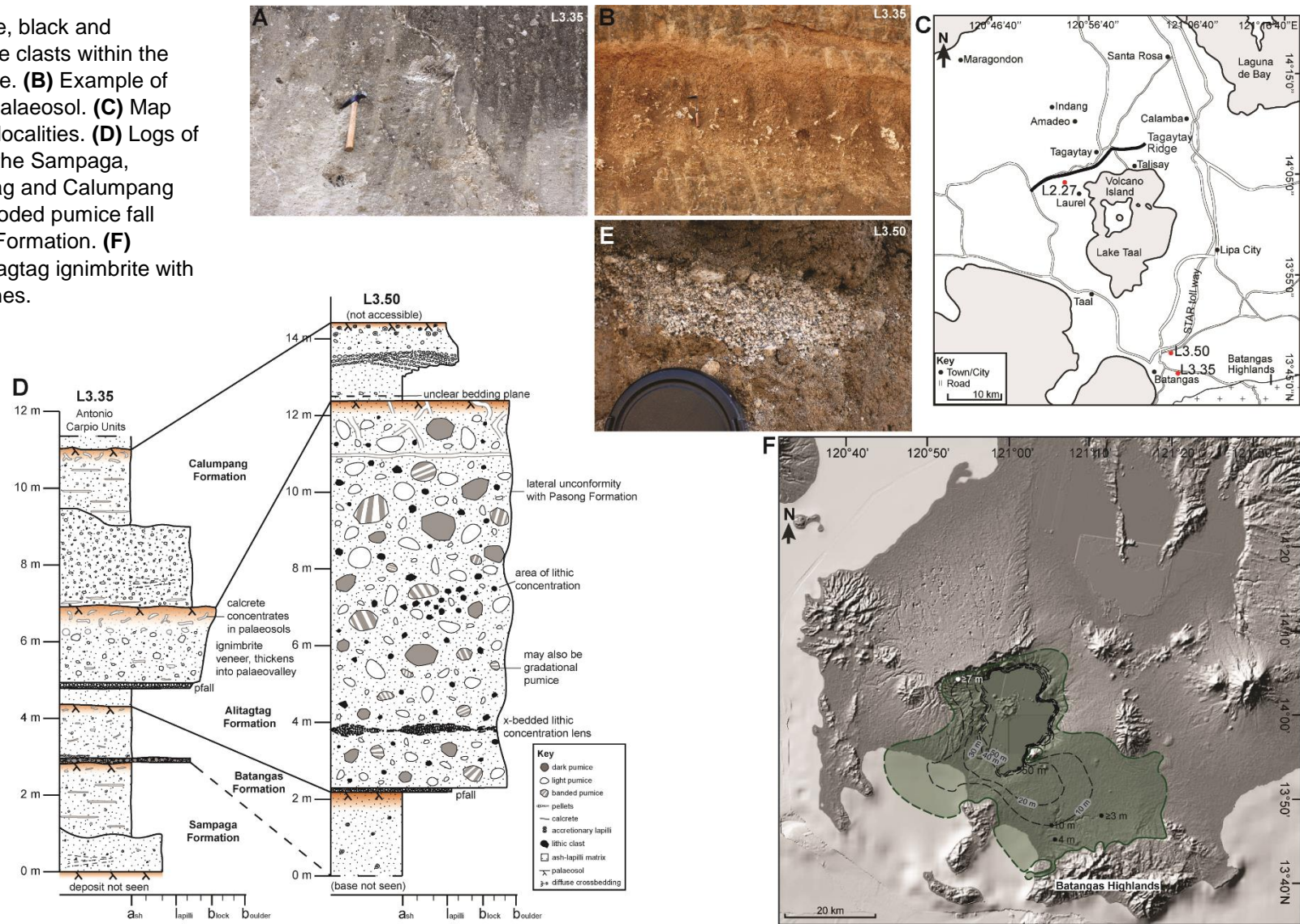


Fig. 2.6: The Buco Formation and an unknown Antonio Carpio Unit locally cut out the Sampaga Formation, and multiple other older formations, towards the SSW at L3.35 [13° 45.226'N 121°06.037'E].

2.3.2 The Batangas Tuff Formation

The Batangas Tuff Formation (new name) is of unknown composition and comprises a bed of non-lithified, clast-supported, black, subrounded, pumice lapilli overlain by a thin pellet layer and massive accretionary lapilli-tuff. At its type locality (L3.35, same as Sampaga Formation; Fig. 2.7) it is 1.2 m thick, but elsewhere it exceeds 2.2 m thick (L3.50, base not seen; Fig. 2.7). The formation has an upper calcrete-bearing orange palaeosol and is conformably overlain by the Alitagtag Formation (Fig. 2.7). There is no radiometric date for the Batangas Formation, but it provides evidence of an explosive eruption with at least two pyroclastic density currents. The first current was pumice-rich with a co-ignimbrite plume that deposited fine ash in the form of pellets; this layer thus represents a flow-unit boundary (as commonly reported elsewhere, Brown et al., 2010). Following this, a more dilute pyroclastic density current passed before the eruption ceased to allow soil formation.

Fig. 2.7: (A) White, black and gradational pumice clasts within the Alitagtag ignimbrite. (B) Example of calcrete within a palaeosol. (C) Map detailing relevant localities. (D) Logs of type localities for the Sampaga, Batangas, Alitagtag and Calumpang formations. (E) Eroded pumice fall deposit Alitagtag Formation. (F) Distribution of Alitagtag ignimbrite with deposit contour lines.



2.3.3 The Alitagtag Banded Pumice Ignimbrite Formation

The Alitagtag Banded Pumice Ignimbrite Formation (new name, previously 'Alitagtag Pumice Flow'; Listanco, 1994) is a non-lithified largely dacitic ignimbrite, 10 m thick, with characteristic highly vesicular, banded or black – white gradational pumice clasts, and a thin, lithic-rich, dacitic pumice fall deposit at its base. The rare black dacitic pumice only occurs as bombs with fluidal shapes, which are slightly less vesicular than the white and banded pumice. Both pumice types may have rare andesitic compositions. The Alitagtag Formation is defined at a type locality (L3.50; Fig. 2.7) NE of Batangas City, 1.4 km south of the Southern Tagalog Arterial Road toll way. The new road-cut is near the Calumpang River, across which a bridge was constructed in February 2020. Here, the Alitagtag Formation overlies the upper palaeosol of the Batangas Formation and is separated from the overlying Calumpang Formation (Fig. 2.7) by a calcrete-bearing, orange, 0.5 m thick palaeosol. Both contacts are conformable and sub-horizontal. To the NW, a thin orange palaeosol runs along an erosive contact between the Alitagtag and overlying Pasong Formation, which locally cuts out the Alitagtag Formation. The formation is recognised at two other localities, including as a veneer deposit (L3.35) in which no black pumice is present (Fig. 2.7). A useful exposure was found North of Lake Taal, where the Alitagtag Formation has previously only been tentatively identified (Punongbayan et al., 1995). There is no radiometric date for the Alitagtag Formation, but it represents a large, ignimbrite-forming eruption with a pumice fallout phase followed by at least one pyroclastic density current, which first eroded part or all of the fall deposit.

Alitagtag Distribution

The Alitagtag inundation area is based on five exposures: three from this field study and two from past work (Listanco, 1994). Four of these are found to the South of Lake Taal, while only one is found to the North (Fig. 2.7). No exposures were identified north of Tagaytay Ridge, therefore there is currently no evidence to suggest that the Alitagtag pyroclastic density current overtopped Tagaytay Ridge. The pyroclastic density current travelled to the south, infilling

valleys where possible, but generally travelling unopposed across relatively flat land, spreading out in a fan-like manner. No deposits are found on top of or on the other side of southern topographic barriers like the Batangas Highlands. Therefore, flows likely did not overtop these, but instead were funnelled into the surrounding bays and perhaps further out to sea. It is possible that flows travelled further across flat land to the East, but fieldwork was not conducted in this region. The drawn inundation area is seen as a minimum estimate because the Alitagtag Formation is one of the older Taal deposits. Therefore, it is entirely possible that flows did travel elsewhere but their deposits are buried by younger flow deposits, eroded away, or have not yet been identified as belonging to the Alitagtag Formation.

2.3.4 The Calumpang Tuff Formation

The Calumpang Tuff Formation (new name) is up to 4 m thick and consists of a lower pale grey, partly diffusely cross-bedded, pumice-rich lapilli-tuff and an upper white – beige, massive, accretionary lapilli-rich tuff, both of unknown composition. At its type locality (L3.35, Fig. 2.7) it is separated from the older Alitagtag Formation and from a younger Antonio Carpio unit by thick, orange, calcrete-bearing palaeosols. Pumice clasts in the soft and poorly lithified lower lapilli-tuff may align along the cross-bedding and, where weathered, this bed is moist and clay-like. Sub-horizontal white concretions (<10 cm) are common at the base of the lower bed and throughout the entire upper accretionary lapilli-rich tuff (Fig. 2.7). This upper accretionary lapilli-rich tuff is well lithified, likely helped by the hard calcrete, and has a sharp but erosive contact with the lower lapilli-tuff. The Calumpang Formation is only recognised at one other locality (L3.50, Fig. 2.7), where the bottom half of the deposit is heavily weathered. There is no radiometric date for the Calumpang Formation, but it represents the passing of at least one pyroclastic density current, which became more dilute over time.

2.3.5 The Tadalac Cave Ignimbrite Formation

The Tadalac Cave Ignimbrite Formation (new name) is a light grey, lithified, massive and diffusely cross-bedded ignimbrite with andesitic black – white and mingled pumice lapilli/blocks. It is underlain by a lithic breccia and finer grained ignimbrite with whole and broken, hardened accretionary lapilli. The massive portions of the ignimbrite have abundant elutriation pipes halfway up the exposure, in which only lithic clasts concentrate. Subordinate black pumice lapilli/blocks are larger than white pumice lapilli and some have irregular, but not fluidal, shapes. The Tadalac Cave Formation has an andesitic composition with rare glassy black, likely accidental, dacitic clasts. All pumice in the Tadalac Cave Formation has a noticeably lower TiO_2 content (0.67 – 0.76 wt. %) than andesites from other Taal Group formations (0.78 – 1.05 wt. %, 3 outliers below 0.78 wt. %; Fig. 2.8).

The Tadalac Cave Formation is identified at two localities along the south shore of Lake Taal, which represents part of Taal's caldera wall (Punongbayan et al., 1995). Its type locality (L2.9, Fig. 2.8) is Tadalac cave, 2 km NNW of the Parish Church and public market in Alitagtag, and in 2019 was only accessible by boat from Lake Taal. The formation has a maximum exposed thickness of 21.7 m, but its base and top contacts are not exposed. Its low elevation, passing into the lake (Fig. 2.8), and the intense vegetation cover where not eroded suggests it is one of Taal's prehistoric eruption-units, other examples of which have been found in the cliffs on the south coast of the lake (Listanco, 1994). A lack of exposure on the ignimbrite plains suggests the formation is covered by material from younger eruptions, including the Indang and Pasong eruptions. However, it is not clear from field relations whether it is younger than the 'Caloocan Formation' identified in previous work (Listanco, 1994) and no absolute age is determined. The Tadalac Cave Formation provides evidence of an ignimbrite-producing, likely caldera-forming eruption because it contains a proximal lithic breccia and has a volume estimation of 17 km^3 , sufficient for caldera formation (see Section 2.5.2; Hughes and Mahood, 2011).

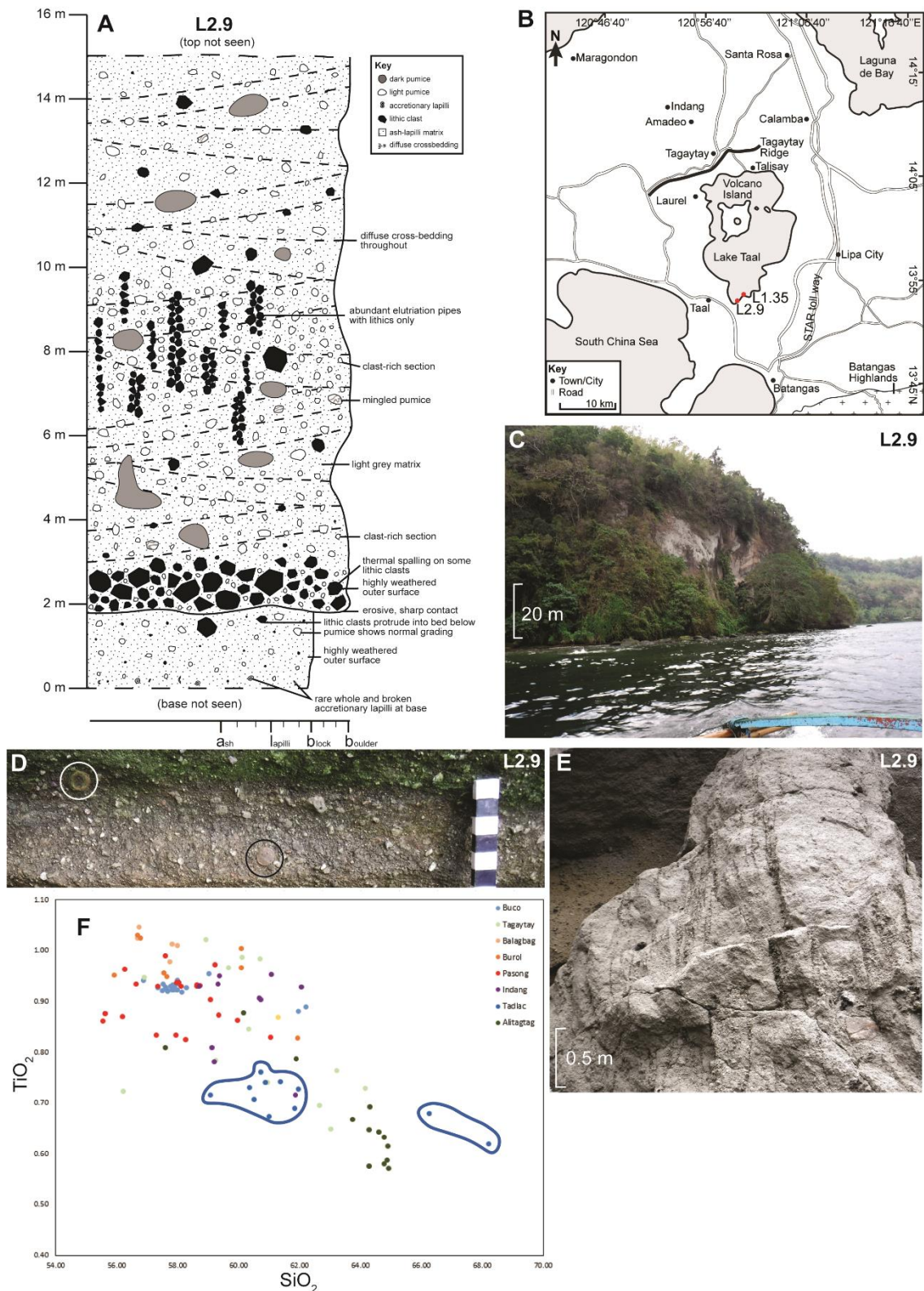


Fig. 2.8: The Tadlac Cave Formation. **(A)** Log of the type locality (see inset map **B** for this location and other locality). **(C)** Tadlac Cave, the type locality, as seen from Lake Taal. **(D)** Accretionary lapilli in the lowest exposed bed of the formation. **(E)** Elutriation pipes in the massive portion of the main ignimbrite of the formation. **(F)** The TiO_2 and SiO_2 values for selected juvenile and whole rock samples from the Tadlac Cave Formation. Their TiO_2 content is noticeably lower for their respective SiO_2 contents (see Chapter 4 for a comprehensive overview of the geochemistry).

Early in the eruption a pyroclastic density current deposited the lower finer grained ignimbrite with accretionary lapilli. This was followed by a sudden increase in discharge rate and possible caldera collapse, depositing the lithic breccia. After this the discharge rate remained high, rapidly depositing the thick upper hot ignimbrite, which lost fines in abundance. The record of the eruption cessation is missing and an upper palaeosol is not preserved/exposed.

2.3.6 The Indang Banded Fluidal Juvenile Bomb Ignimbrite Formation

The Indang Banded Fluidal Juvenile Bomb Ignimbrite Formation (new name, previously 'SPF3'; Martinez and Williams, 1999) is a sintered, ≤ 15 m thick, massive ignimbrite with occasionally banded and light grey to black gradational andesitic juvenile material overlain by a clast-poor, white tuff at its type locality. Light grey andesitic juvenile clasts are smaller than andesitic black juvenile bombs with fluidal/elongate shapes, breadcrust textures and lithic (volcanic, plutonic and sedimentary) inclusions. All the juvenile particles have a coat of fine ash, the ash coating on the black fluidal rags is commonly fused. The type locality (L1.25, Fig. 2.9) is a river valley, near the town of Indang, about 25 km NW of the centre of present-day Lake Taal. There, juvenile clasts are imbricated to dip 38° NNE (away from Lake Taal, Fig. 2.9). The formation is best exposed in the NW, where several exposures display elutriation pipes, and along Tagaytay Ridge (Fig. 2.9). At the type locality, the top of the Indang Formation has a 0.4 m thick orange, crumbly, palaeosol conformably overlain by the Pasong Formation. The base of the Indang Formation is only seen on Tagaytay Ridge (Fig. 2.9), where it is represented by a grey pumice lapilli-tuff (exposed for only 10 cm before several meters of vegetative cover). This lapilli-tuff is overlain by a 1.1 m thick non-lithified, diffusely cross-bedded lithic breccia with subordinate glassy to poorly vesicular, fluidal-shaped, black scoria up to 15 cm, and a 0.4 m thick, white, well-lithified accretionary lapilli-rich (80-90%) tuff. Palaeosols separate the formation from an older unknown ignimbrite and the younger Pasong Formation (Fig. 2.9). The Indang Formation was previously grouped together with the now-called Pasong Formation in the 'Scoria Pyroclastic Flow' (Martinez and Williams, 1999). However, a palaeosol

separates them. In this work, the two formations are named according to their type locality, not just their componentry. The age of the Indang Formation is not known, but it is taken to be older than the non-calibrated 6680 ± 310 yr BP ^{14}C age, which is the oldest date reported for the Pasong Formation (Martinez and Williams, 1999).

Indang Distribution

Deposits of the Indang Formation are found only north of Lake Taal (Fig. 2.9). To the south, the formation is missing from exposed sections, and the Pasong Formation directly overlies unidentified ignimbrites or an older eroded scoria cone. These unidentified ignimbrites could belong to the Indang Formation, but field and geochemical data currently available do not justify such correlation. Therefore, it is proposed that the Indang pyroclastic currents were directed north, easily overtopping Tagaytay Ridge and depositing the majority of ignimbrites on the gentle slope north towards Manila and Manila Bay (Fig. 2.9). It is likely that the currents were partly confined to valleys, as thicknesses change from ≥ 15 m to 6 m over short distances (e.g. between L2.7 and L2.6 in Fig. 2.9). The ignimbrite remains ≥ 7 m thick close to the sea (Fig. 2.9) and it is likely that the pyroclastic density current travelled significant distances beyond the coast. The ignimbrite is not exposed near Laguna de Bay and within metro-Manila, but the gently sloping land here will have provided little resistance for the pyroclastic density current to run out in this direction until it had deposited enough material to loft, and it seems reasonable to think it would have reached modern metro-Manila (Fig. 2.9).

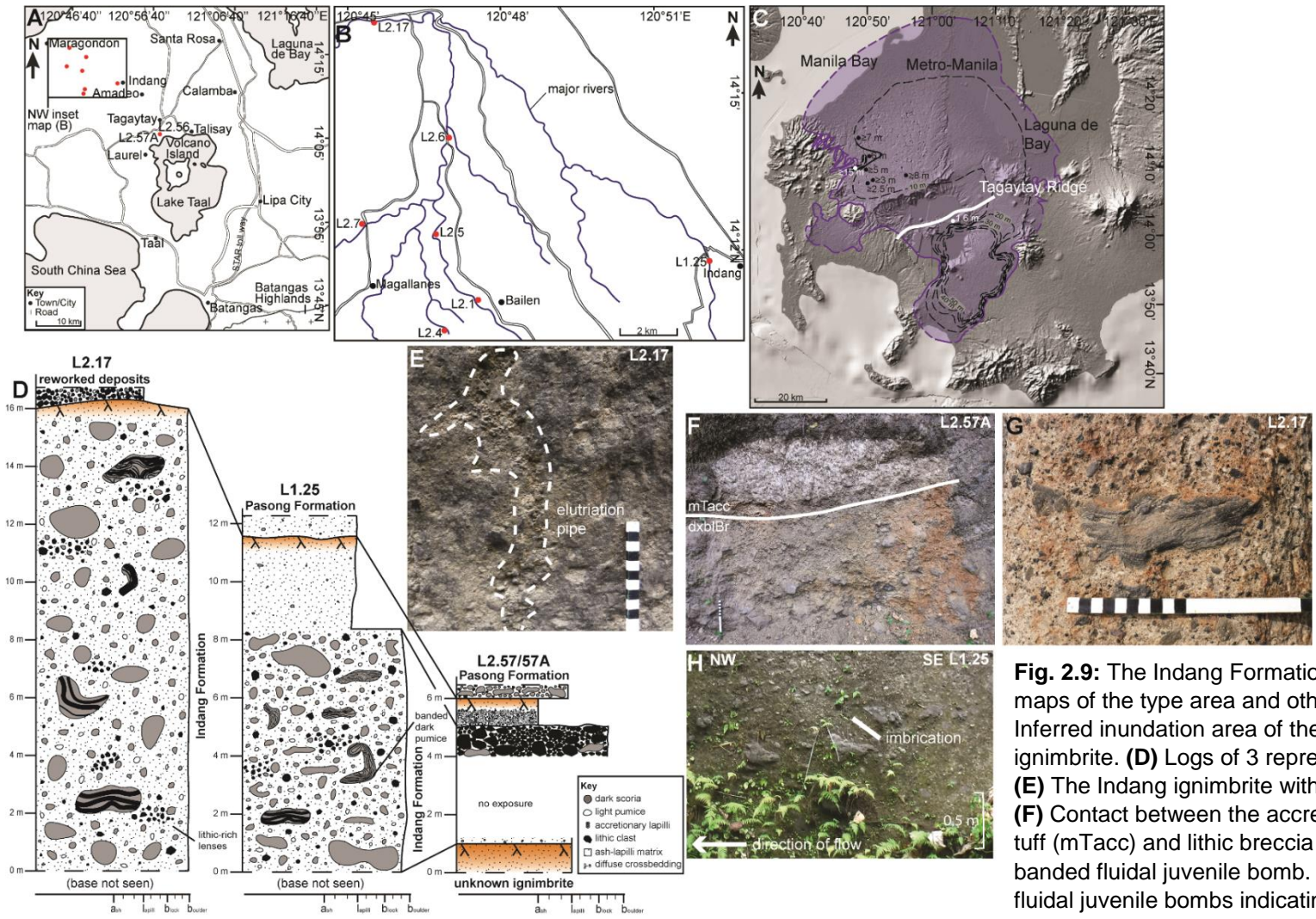


Fig. 2.9: The Indang Formation **(A, B)** Location maps of the type area and other exposures. **(C)** Inferred inundation area of the Indang ignimbrite. **(D)** Logs of 3 representative sites. **(E)** The Indang ignimbrite with elutriation pipe. **(F)** Contact between the accretionary lapilli-rich tuff (mTacc) and lithic breccia (dxblBr). **(G)** A banded fluidal juvenile bomb. **(H)** Imbricated fluidal juvenile bombs indicating a flow direction away from Lake Taal.

2.3.7 The Pasong Fluidal Juvenile Bomb-Rich Ignimbrite Formation

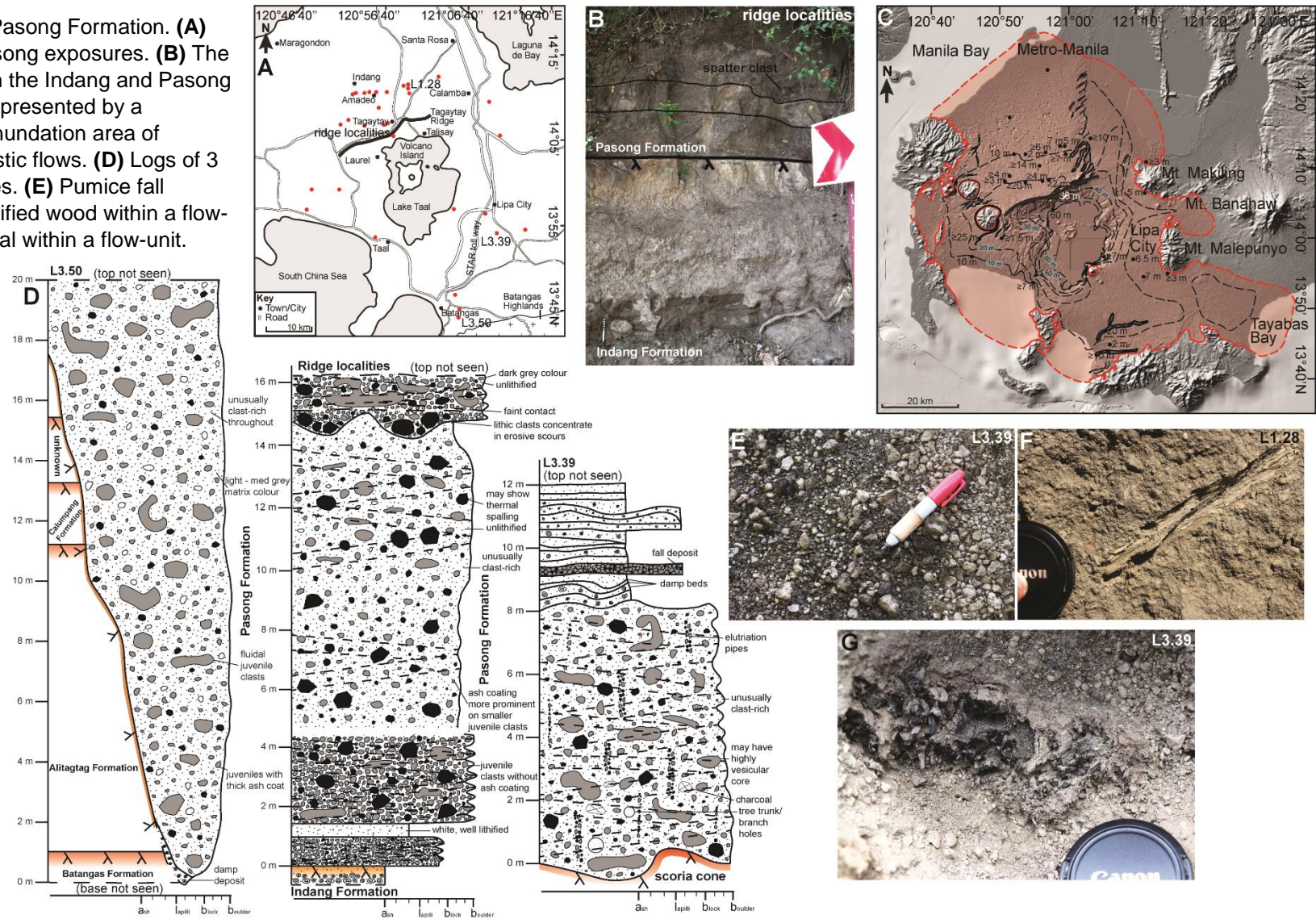
The Pasong Fluidal Juvenile Bomb-Rich Ignimbrite Formation (new name; previously 'SPF1' and 'SPF2' of the 'Scoria Pyroclastic Flow'; Martinez and Williams, 1999) is the best exposed of the Taal Group. It is light to dark grey, poorly to well lithified and contains light grey to black, basaltic and basaltic andesite pumice and scoria lapilli with larger black fluidal juvenile bombs. Some flow-units contain characteristic light orange older ignimbrite clasts, which are only ever seen elsewhere in the younger Buco Formation. In other formations, similar accidental lithic clasts have a darker orange colour. The Pasong Formation consists of at least 4 – 5 fall deposits (3 pellet fall layers and 1-2 pumice fall layers) and 5 ignimbrite flow-units. The flow-units are separated by thin clast-supported pellet layers or pumice fall layers and comprise massive and diffuse cross-bedded lapilli-tuffs, some with rare accretionary lapilli, tuffs with abundant accretionary lapilli, and breccias with abundant fluidal juvenile bombs.

The type locality of the Pasong Formation is 20 km southeast of the centre of Lake Taal, in an abandoned quarry 3.7 km SSE of Lipa (L3.39 [13° 54.631'N 121°10.745'E], Fig. 2.10). There, the formation overlies a subhorizontal palaeosol above an older scoria cone (Fig. 2.4) and it grades into a modern soil at the top. A diffuse cross-bedded ignimbrite at the base of the formation passes up into several thin crosscutting beds with at least one pumice fall deposit (Fig. 2.10).

The Pasong Formation is exposed radially around Lake Taal, and its maximum thickness is 45 m, on Tagaytay Ridge, where it is separated from the older Indang Formation by a crumbly light orange palaeosol, 40 cm thick, and has an upper crumbly bright orange palaeosol, ~4 m thick, overlain by the younger Tagaytay Units (Fig. 2.10). Elsewhere, the Pasong Formation oversteps the older Batangas, Alitagtag and Calumpang formations (e.g. L3.50 [13° 47.067'N 121°05.509'E]), overlies the Antonio Carpio Units, and is overlain by the

younger Buco Formation (e.g. L3.35 [13° 45.226'N 121°06.037'E]). The Pasong Formation is the only deposit in which both charcoal, and newly in this study, petrified wood, are identified. Both types of wood are not found in the same bed and occur as individual fragments or inside cylindrical moulds, which likely used to be filled with charcoal and/or petrified wood that has since been weathered out. At some localities only these remnant holes remain. The charcoal is found within lithic breccias in the northern sector (Fig. 2.10) and within diffusely cross-bedded lapilli-tuff in the eastern sector (Fig. 2.10). The charcoal may be intruded by modern rootlets and <1 cm clasts may stick to it. Charcoal has been previously ¹⁴C dated providing ages between 6680 ± 310 yr BP and 5380 ± 70 yr BP (non-calibrated ages; Listanco, 1994; Martinez and Williams, 1999). The Pasong Formation represents the passing of at least 5 pyroclastic density currents at some localities, but more often evidence for one or two pyroclastic density currents is found. These pyroclastic density currents were quasi-steady and concentrated, some becoming more dilute over time to deposit matrix and accretionary lapilli-rich tuffs. Pyroclastic density currents produced co-ignimbrite clouds to deposit pellet layers. In between flow activity, buoyant eruption columns also produced rare pumice fall deposits. There are no palaeosols between any of these deposits, suggesting that the eruption was relatively continuous but unstable, producing eruption columns that seem to have (partially) collapsed frequently. Flows travelled radially outwards from their source, somewhere within Lake Taal, crossing abundant flat land to likely reach the surrounding sea (Fig. 2.10).

Fig. 2.10: The Pasong Formation. (A) Localities of Pasong exposures. **(B)** The contact between the Indang and Pasong formations as represented by a palaeosol. **(C)** Inundation area of Pasong pyroclastic flows. **(D)** Logs of 3 different localities. **(E)** Pumice fall deposit. **(F)** Silicified wood within a flow-unit. **(G)** Charcoal within a flow-unit.



Pasong Distribution

The Pasong Formation is exposed in all sectors around Lake Taal, suggesting pyroclastic density currents spread out radially from a source within the lake. Flows overtopped Tagaytay Ridge to reach the northern ignimbrite plains where they flowed both in and out of valleys, leaving thick valley-filling deposits of ≥ 20 m and veneer-like deposits of ~ 2 m. Although no exposures near the coast or metro-Manila were identified in this study, previous work has done so (Listanco, 1994; Martinez and Williams, 1999), suggesting flows likely reached Manila Bay and present-day metro-Manila. Flows easily spread east, inundating old scoria cones near Lipa City, but not overtopping more significant topographic barriers like Mt. Makiling and Mt. Malepunyo because no deposits have been found on the eastern side of these barriers. Deposits to the East of Lake Taal are still 7 m thick, therefore it seems reasonable to assume that flows continued southeast, eventually flowing into Tayabas Bay (Fig. 2.10). Flows are unlikely to have travelled even further east up the slopes of Mt. Banahaw.

To the South of Lake Taal, flows infilled valleys where present, but more dilute versions of the current inundated the entire region. Deposits are still ≥ 7 m very close to the modern shore line, therefore flows must have entered the bays here and likely flowed a significant distance across water. No evidence is seen that flows overtopped topographic barriers along the south shore. Flows also filled and overtopped valleys to the west. Land in between the western shoreline and the old stratovolcanoes consists of very flat farmland and therefore exposures are few and far between. However, since deposits near this flat land are still at least 10 m thick, it is likely flows crossed this stretch of land, reaching the sea where topographic barriers were not in the way.

2.3.8 The Burol Ignimbrite Formation

The Burol Ignimbrite Formation (new name) is a light to dark grey, lithified to indurated, diffusely cross-bedded, ignimbrite consisting of four separate beds, which are overlain by a lens of framework-supported pumice lapilli and cobbles with subordinate lithic clasts and an accretionary lapilli-rich tuff. Contacts between the ignimbrite beds are sharp, but undulating. Juvenile material is black – dark grey (basaltic) andesite pumice, which may be banded in certain beds. Pumice can be identified by its relatively high TiO_2 values (avg. 0.97 wt.%, excluding outlier; Fig. 2.11) compared to most other formations in the Taal Group.

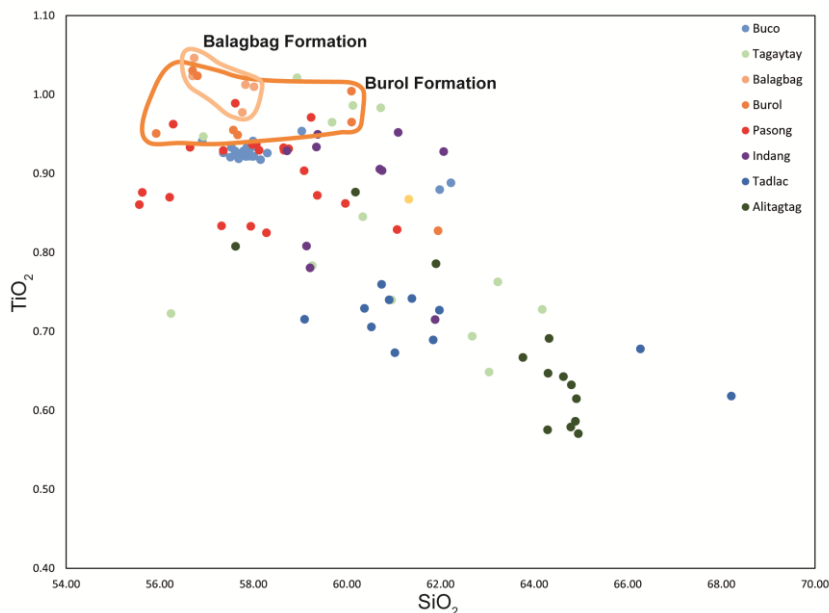


Fig. 2.11: All samples taken from the Burol and Balagbag formations have relatively high TiO_2 values compared to all other formations, except for one Burol sample outlier of 0.83 wt. % TiO_2 (see Chapter 4 for a comprehensive overview of the geochemistry).

Its type locality is by a newly constructed southern circumferential road along the SW shore of Lake Taal (L2.73 [13° 53.559'N 120°58.816'E], L2.85 [13° 52.686'N 120°59.338'E]; Fig. 2.12). Here, it is separated from the younger Balagbag Formation by a 1 m thick orange palaeosol or is overlain by reworked materials, which are interpreted as lake deposits. The lake deposits imply that the lake level used to be higher. Deposits frequently contain sulphur near the reworked material, which may represent fossil fumaroles, formed due to

circulation of fumarolic gases through the deposit (Brown and Andrews, 2015; Rodríguez and van Bergen, 2017). The Burol Formation's lower contact is not exposed, therefore only a minimum thickness of ~25 m can be established. It has not yet been identified elsewhere, but may be similar to deposits described elsewhere along the southern shore of Lake Taal (Fig. 2.13; Punongbayan et al., 1995). The deposits represent the passing of at least one unsteady, concentrated pyroclastic density current, which underwent several phases of waxing and waning causing its behaviour to vary between erosive and depositional at the Burol Formation type locality. This unsteadiness is reflected by the cross-stratification and pumice lens, while waxing and waning is represented by the sharp, undulating contacts between ignimbrite beds (Branney and Kokelaar, 2002). The pyroclastic density current eventually became more dilute and waned until it came to a stop, depositing only fine ash to form the accretionary lapilli-tuff at the top of the Burol Formation.

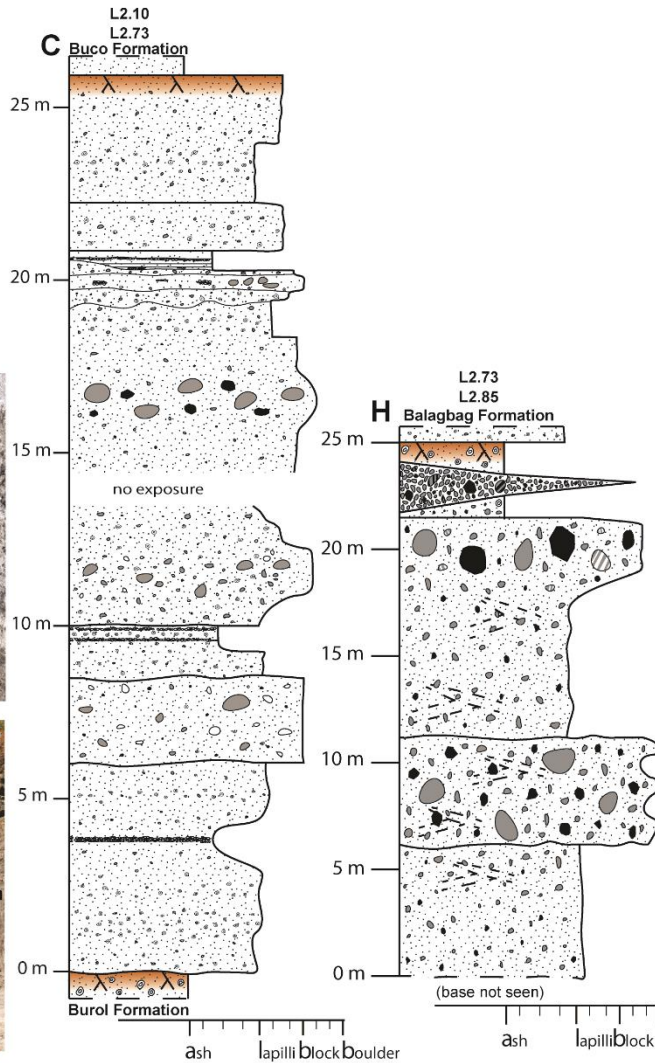
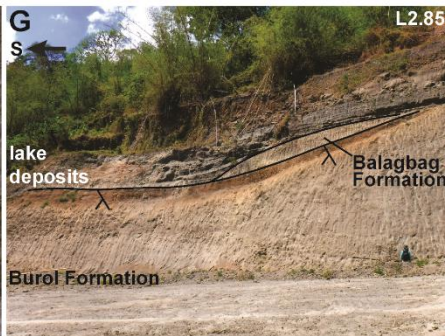
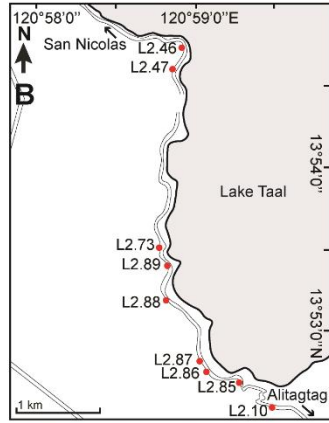
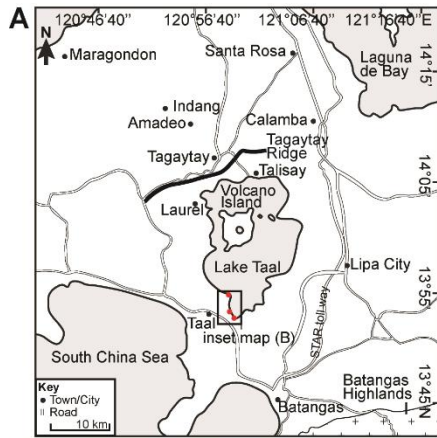


Fig. 2.12: The Burol and Balagbag formations. **(A, B)** Localities of exposures. **(C)** Combined log for the Burol Formation from 2 exposures. **(D)** Palaeosol between the Balagbag and Burol formations. **(E)** Pellet bed within the Balagbag Formation. **(F)** Palaeosol between the Balagbag and Buco formations. **(G)** Palaeosol between the Burol Formation and reworked deposits above. **(H)** Combined log for the Balagbag Formation based on 2 exposures.

2.3.9 The Balagbag Ignimbrite Formation

The type locality for the Balagbag Ignimbrite Formation (new name) is also along the newly constructed southern circumferential road along the SW shore of Lake Taal, connecting San Nicolas to Alitagtag (L2.13 [13° 52.549'N 120°59.577'E], L2.73 [13° 53.559'N 120°58.816'E]; Fig. 2.12). This is a newly identified

formation, although similar deposits have been described along the southern shore of Lake Taal (Fig. 2.13; Punongbayan et al., 1995). The deposits are andesitic, with characteristically high TiO₂ values (avg. 1.01 wt. %; Fig. 2.11). They consist of 3 sets of thin tuff beds and 3 thicker lapilli-tuffs. There is a section of no exposure in the middle of the formation, therefore only a minimum thickness (25 m) could be estimated.

The Balagbag Formation is conformably separated by one, ~1 m thick orange palaeosol from the older Burol Formation, and by one ~1 m thick (L2.10), or several thinner orange palaeosols (L2.73) from the younger Buco Formation. Where there are multiple palaeosols, it implies short breaks in between relatively small-scale volcanic activity between the Balagbag and Buco formations. Material from this activity may not have deposited at L2.10, or thinner palaeosols were eroded away, leaving only one palaeosol. All lapilli-tuffs are massive, well lithified – indurated, light grey – beige, with black – light grey poorly – moderately vesicular dense pumice (rare banded types in one ignimbrite), accidental and accessory lithic clasts (lavas, old ignimbrites, rare hydrothermally altered clasts) and accretionary lapilli throughout two beds. The

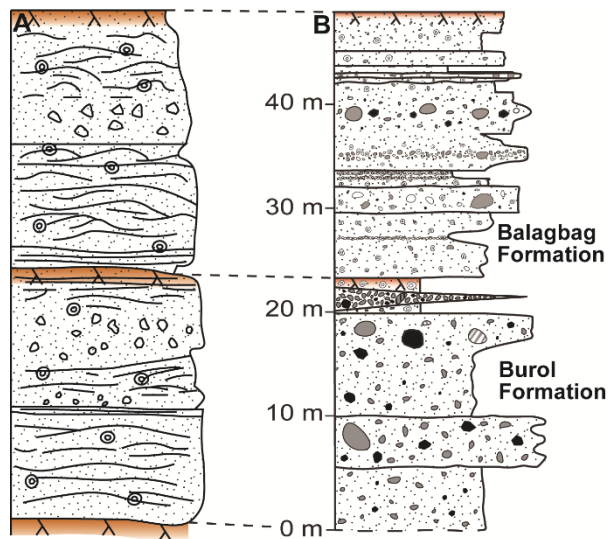


Fig. 2.13: A section of a log from a locality along the southern shore of Lake Taal based on previous fieldwork (Punongbayan et al., 1995). No scale or key are available for this log. It is tentatively linked to the Burol and Balagbag formations identified in this study.

sets of tuff beds are always matrix-rich and consist of a maximum of 13 different beds, either with erosive and sharp or gradational contacts. They vary between indurated, white, well-sorted, often pellet-rich beds and poorly lithified, poorly-sorted, light to dark grey tuffs with abundant accretionary lapilli and/or subordinate pumice and lithic clasts. Pumice in tuffs is black – dark grey, never light grey. The white tuffs are amalgamated pellet layers, which are flow-unit boundaries, therefore the Balagbag Formation represents the passing of at least 13, mostly dilute, pyroclastic density currents and associated co-ignimbrite fall deposits.

2.3.10 The Tagaytay Pumice and Ash Fall and Tuff Units

The Tagaytay Pumice and Ash Fall and Tuff Units (new name, previously the 'Airfall and Base Surge Sequence'; Listanco, 1994) are a large number of thin beds (max thickness of individual bed: 1.5 m; max exposed thickness of all beds: ≥ 25 m) found along the upper section of Tagaytay Ridge and in a faulted section along the western shore of Lake Taal, occasionally seen with spatially changing, variably developed palaeosols between them. Exposures frequently have a weathered outer surface, which makes them look like one bed unless this outer surface is scraped off. The Tagaytay Units are thought to be $\leq 5380 \pm 70$ yr BP (non-calibrated ages; Listanco, 1994; Martinez and Williams, 1999) and likely represent a phase of more frequent, smaller-scale eruptions. Alternatively, some of these beds could represent fall deposits associated with the larger, major eruptions. However, current field evidence needs to reject this hypothesis because no deposits from the Tagaytay Units can be confidently correlated with fall deposits associated with ignimbrites.

The majority of beds consist of either matrix-supported, dark grey, lithic-rich, coarse ash deposits or clast-supported black/dark grey or light grey/white pumice deposits, with rare accretionary lapilli-bearing tuffs. Most pumice deposits represent fall deposits, but one black pumice deposit and accretionary lapilli-bearing tuffs show (diffuse) cross-bedding and therefore represent flow deposits. The abundance of clast-supported pumice beds makes these units

unique and easily recognisable compared to other deposits from the Taal Group, which mainly consist of (lapilli) tuffs. Contacts between individual beds are generally regular, with some exceptions. Certain exposures have slumped or slipped possibly due to shaking from volcanic eruptions or related earthquakes. This deformation can make beds look intermingled. The beds are either subhorizontal or dip 5 - 10° NE or NW. Although it is difficult to trace individual beds, two different bed sets can be identified in several places along Tagaytay Ridge (Fig. 2.14). The Tagaytay Units are separated from the older Pasong Formation by a ~4 m thick bright – light orange palaeosol and are overlain by the younger Buco Formation. A palaeosol was found between the Buco Formation and the Tagaytay Units during fieldwork conducted in the 1990s (S. Self, pers. comm., 2020), but this contact was no longer exposed during fieldwork conducted for this study in 2019. The eruptions associated with the Tagaytay Units formed buoyant, (sub-) Plinian eruption columns. Occasionally, this plume must have collapsed to form pyroclastic density currents, which deposited the matrix-supported beds.

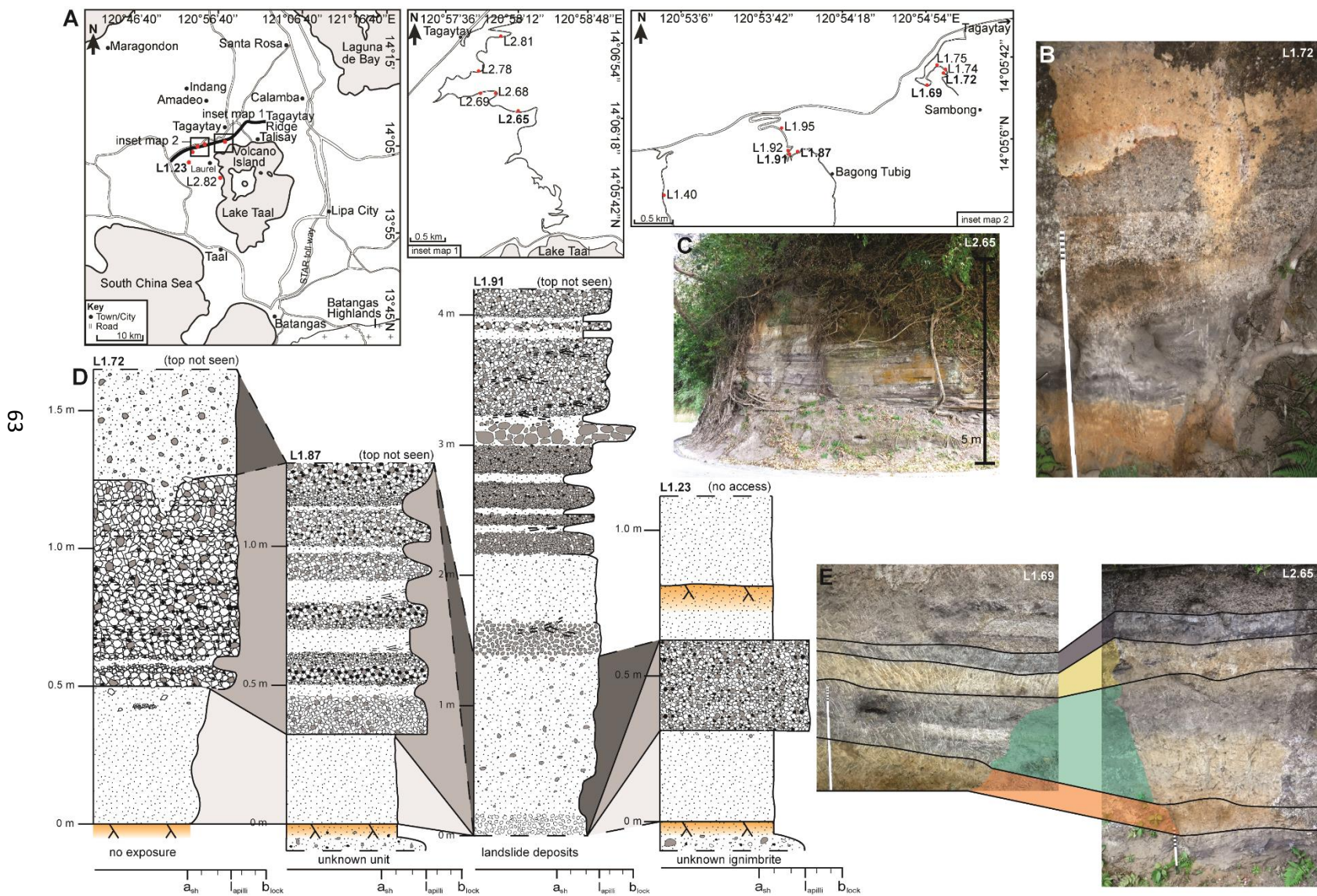


Fig. 2.14: The Tagaytay Units **(A)** Map with two inset maps with relevant localities. **(B)** Photo of L1.72 log with orange palaeosol at base and erosive, weathered orange pyroclastic flow deposit. **(C)** Well bedded ash and pumice beds. **(D)** Logs from various locations, with connected sections highlighted. This is one bed set that can be identified along Tagaytay Ridge. **(E)** Connections between individual beds within the second identifiable bed set along Tagaytay Ridge.

2.3.11 The Buco Ignimbrite and Tuff Formation

The Buco Ignimbrite and Tuff Formation (new name, previously the 'Buco Base Surge'; Geronimo, 1988) is a relatively well exposed, light grey, ≤ 15 m thick, poorly lithified to unlithified set of (lapilli) tuff beds with a basal and upper ignimbrite, containing andesitic black – dark and light grey scoria and pumice, various lithic clasts and commonly randomly dispersed accretionary lapilli. Its type locality (L3.22, Fig. 2.15) is at the western base of Mt. Makiling, 21 km northeast from the current centre of Lake Taal and 4 km northeast of Tanauan City. Here, it conformably overlies the Pasong Formation, from which it is separated by reworked material and a palaeosol. Above, it is separated from the Alaminos Units by a palaeosol (Fig. 2.15). The Alaminos Units can only be traced on the eastern side of Lake Taal, elsewhere only modern soil is seen above the Buco Formation.

The basal bed is an ignimbrite, diffusely cross-bedded with accretionary lapilli and abundant bird holes. The bird holes are common throughout the Buco Formation due to its soft, poorly lithified nature. This ignimbrite may look similar to the Pasong ignimbrite, but tends to be lighter grey, less lithified, and always contains accretionary lapilli on the ignimbrite plains. Characteristically, the Buco ignimbrite is dominated by black and dark grey, rarely light grey, scoria, whereas the Pasong ignimbrite may contain smaller light grey pumice. Additionally, the Buco ignimbrite may include mm-sized glassy juvenile material, while in the Pasong ignimbrite glassy textures may be seen within larger juvenile material only. Another key difference between them is the distribution of juvenile grain sizes. Except for deposits on the shore of Lake Taal, the Buco ignimbrite has a much tighter grain size distribution than the Pasong Formation, with clasts ranging from ~ 0.5 cm to 15 cm, while clasts in Pasong deposits range from 1 mm to 0.5 m. The lithic assemblage of the Buco Formation includes hydrothermally altered, green and red coloured, soft lithic clasts, which are rarely seen in any other formations.

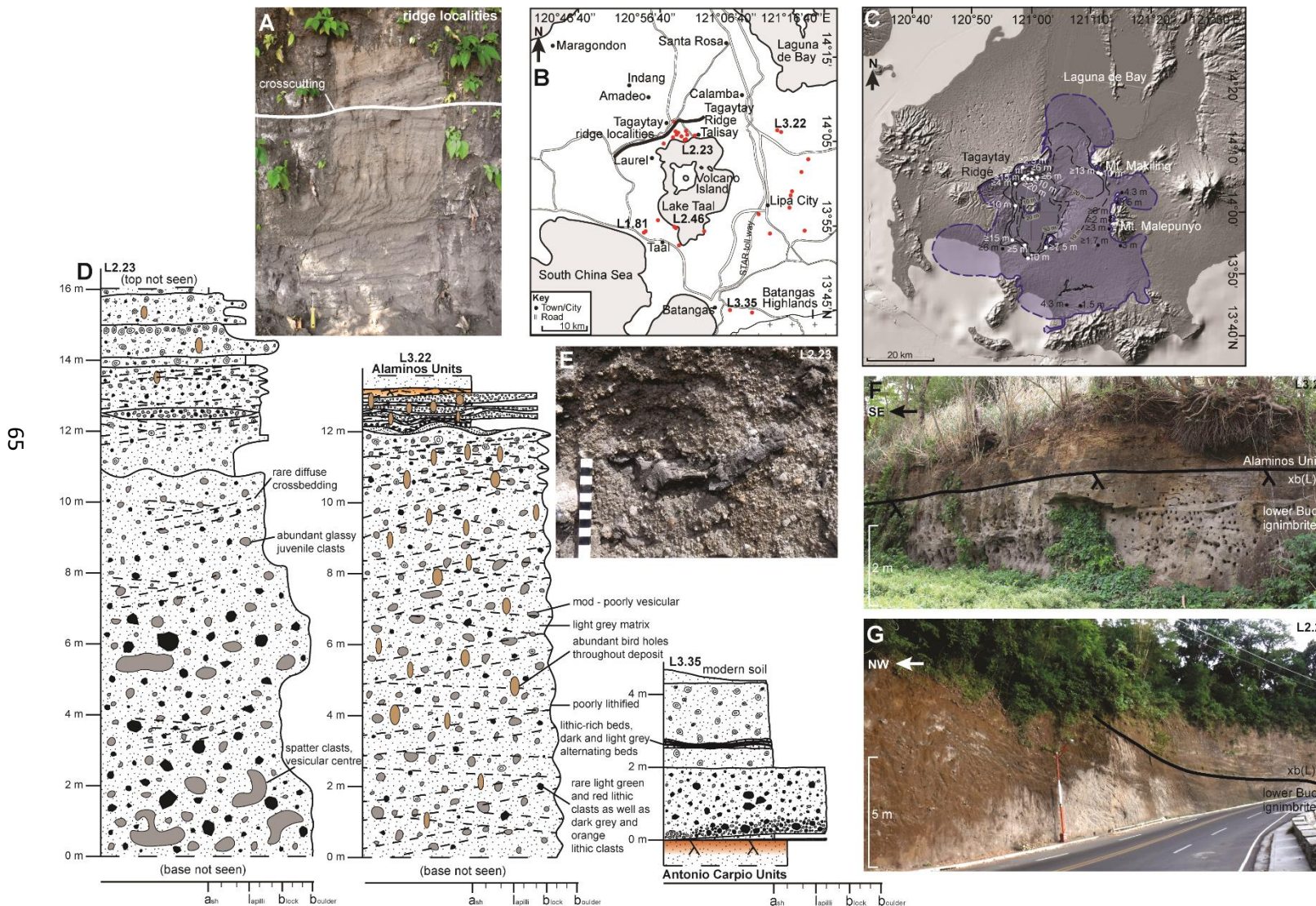


Fig. 2.15: (A) Photo of crosscutting tuff bed sets above the Buco ignimbrite (contact not seen here); scraper for scale. (B) Map with relevant Buco Formation exposures. (C) Hypothesised flow extent of Buco pyroclastic flows. (D) Logs from 3 selected Buco exposures. (E) Glassy-looking fluidal juvenile bomb in the Buco ignimbrite. (F) Contact between the Alaminos Units and the Buco Formation, including erosive contact between the Buco ignimbrite and overlying cross-bedded (lapilli) tuff beds. (G) Erosive contact between the Buco ignimbrite and cross-bedded (lapilli) tuff beds above.

Along the northern shore of Lake Taal (L2.23) the 10 m thick Buco ignimbrite contains m-sized elongate/fluidal shaped black, poorly vesicular scoria and is unconformably overlain by crosscutting sets of thinner beds (cm size), consisting of ash and accretionary lapilli or pumice-rich soft, poorly lithified beds, or harder, well lithified, lithic-rich beds. Contacts between these beds undulate and are frequently erosive, causing beds to change thickness laterally (Fig. 2.15). These sets of thinner beds are seen at various localities around Lake Taal, with or without upper or basal ignimbrites, and often form dune structures. Since they are so thin and usually have erosive contacts, it is impossible to trace an individual bed or even bed sets across large distances. Therefore, individual beds may be exposed elsewhere around Lake Taal, but have not yet been positively identified as the Buco Formation. The lower Buco ignimbrite and associated thinner beds are plastered up Tagaytay Ridge until ~300 m MSL, an observation that was also postulated in previous work (Listanco, 1994; Punongbayan et al., 1995).

The Buco ignimbrite reappears in the eastern section of Tagaytay Ridge around 455 m MSL with a thickness of at least ~30 m. Here, it overlies the Tagaytay Units, with a poorly exposed palaeosol between the two deposits (S. Self, pers. comm., 2020). At this elevation, a poly lithic breccia with black to light grey scoria and rare fluidal juvenile bombs underlies the lower Buco ignimbrite. The maximum juvenile clast size within the ignimbrite decreases to only 5 cm, compared to 1 m at lakeshore level and 15 cm at the base of Mt. Makiling. There appears to be a soil above the Buco ignimbrite at the top of the ridge, suggesting that there was no deposition of the thinner bed sets seen above the Buco ignimbrite elsewhere. Rather, a clast-supported pumice bed, multiple tuffs, a lithic breccia and fine ash-rich lapilli-tuffs overlie this palaeosol. These beds are poorly lithified and often contain accretionary lapilli, thus showing similar characteristics to the thinner dune structured bed sets. It is possible that this short break in volcanic activity suggested by the palaeosol is not recorded elsewhere because the palaeosol was eroded away, which seems likely since there is usually an erosive contact between the Buco ignimbrite and the thin bed sets.

To the South of Lake Taal, the Buco Formation has been identified both on top of the Pasong and Balagbag formations, as well as the Antonio Carpio Units (Fig. 2.15). It frequently shows its characteristic crosscutting dune structures. Deposits along the new southern circumferential road are identifiable by their relatively high juvenile crystallinity (<15%), microcryst abundance and clinopyroxene dominance over orthopyroxene. The SiO₂ range is pushed up to ~62 wt. % in the southern sector, meaning that the Buco Formation spans the entire andesite range (avg. ~58 wt. %). Here, it also includes a pumice fall deposit, and along the lakeshore near San Nicolas, there is a younger massive lapilli-tuff in erosive contact with reworked beds and the older, thinner bed sets. This upper ignimbrite grades up into modern soil and is lithic-rich compared to the older, basal ignimbrite that is seen more widely. This younger deposit is only found at two southern localities (L2.46, L1.81), and its lithic-rich nature and association with reworked beds below means that its own origin as a potential debris flow or similar secondary flow, instead of a vent-derived pyroclastic density current, cannot be ruled out.

Further SE the Buco Formation is associated with the youngest Antonio Carpio unit (unit 1), which, at its type locality along a new road cut going South off Gov. Antonio Carpio Road (L3.35), crosscuts all older Antonio Carpio Units and the Pasong, Sampaga, Batangas, Alitagtag and Calumpang formations. It is found at various other localities along Gov. Antonio Carpio Road, where it can be seen to directly overlie the Miocene-aged Dingle Limestone that outcrops in this region (Fig. 2.4; Wolfe et al., 1978). It consists of two grey tuffs with remnants of coalesced pellets (one parallel laminated), interbedded with accretionary lapilli-rich tuffs. This is followed by a 2 m-thick ignimbrite with black pumice and larger lithic clasts; this ignimbrite may correlate with the younger ignimbrite seen along the southern circumferential road. Below this are a tuff and clast-supported, subrounded pumice bed, both of which laterally thin out.

The Buco eruption began with a concentrated pyroclastic density current, depositing the lower Buco ignimbrite. This was followed by a series of high velocity, dilute pyroclastic density currents, which came in quick succession as shown by the lack of palaeosols between the dune bed sets. This activity was

followed by quiescence during which deposits were reworked before another potential eruption produced a lithic-rich pyroclastic density current flowing towards the south, depositing the younger upper Buco ignimbrite. The deposits above the upper ignimbrite record the passing of two dilute pyroclastic density currents, each followed by co-ignimbrite ash and pellet falls.

Buco Distribution

The Buco Formation is largely exposed along the shore of Lake Taal and further south and east (Fig. 2.15). Despite deposits of ≥ 20 m thick along the northern lakeshore, there is no evidence that the Buco pyroclastic density currents overtopped Tagaytay Ridge. The Formation is found near the top of the 600 m high ridge, which explains why flows were able to travel south, easily overtopping the ~ 200 m cliff along parts of the southern lake shoreline. Flows inundated the flat land to the south, likely infilling valleys and travelling into the southern bays, failing to surmount the southern topographic barriers. To the east, flows travelled unopposed until they reached Mt. Makiling and Mt. Malepunyo, where thick deposits indicate that flows dumped remaining material before lofting. Land towards the northeast of Lake Taal slopes down towards Laguna de Bay, therefore it seems likely that Buco pyroclastic density currents flowed further in this direction than their exposure suggests. The Buco Formation contains many cm-sized, erosive (lapilli) tuff beds, most of which look incredibly similar, so the correlation of individual beds was largely impossible in the field. Consequently, it is conceivable that on some occasions more dilute pyroclastic density currents were able to overtop Tagaytay Ridge and deposit material to the north, but these deposits have not yet been connected to the Buco Formation.

2.3.12 The Alaminos Tuff Units

The Alaminos Tuff Units consist of several beds of light grey tuff, with rare black pumice lapilli or (coalesced) pellets at their base and/or subparallel or cross-bedding near their top. These beds are usually well lithified, although pellet-

dominated beds can be softer. Beds vary in thickness from 3 – 15 cm. Thicker beds are more likely to contain pumice, while thinner beds are dominated by clast-supported pellets and/or fine ash. They have inconsistent palaeosols between them, which can contain remnants of black pumice. These units overlie the Buco Formation and are mostly exposed in the eastern and rarely in the southern sectors. They are most accessible along a new road cut going SE off the Maharlika Highway by the town of Alaminos, ~9 km SSE of Mt. Makiling (type locality L3.20 [14° 03.406'N 121°14.565'E]) where they have a maximum combined thickness (1.6 m). Their stratigraphic position makes the Alaminos Units some of the youngest deposits at Taal, representing several episodes of dilute pyroclastic density currents followed by co-ignimbrite ash falls that were directed South and East, likely due to the flat topography in these regions. Its inability to overtop Tagaytay Ridge and higher topography to the West suggests these eruptions were not as large as the caldera-forming ones.

2.4 The Antonio Carpio Tuff Units

The Antonio Carpio Tuff Units are deposits exposed along a new road-cut off of Gov. Antonio Carpio Road near Sampaga Barangay Hall, ~30 km SE of the centre of Lake Taal. The Sampaga, Batangas, Alitagtag and Calumpang formations are identified here, as well as the younger Buco Formation and Alaminos Units, but all of the deposits in between cannot be correlated with any other deposits found around Lake Taal. Therefore, they have not yet been included in the Taal Group, but it is hypothesised that these deposits do originate from Taal Volcano. There are at least 9 units in between the Calumpang and Buco formations (Fig. 2.3), one of which is tentatively identified as the Pasong Formation (unit 3). All units have orange palaeosols (one compound) between them, ranging from 5 cm to 1.5 m thick. Together, these units are 22 m thick, with individual units ranging from 0.5 m to 3.8 m thick, and split up into a maximum of 12 different beds. The top unit, together with the Buco Formation, crosscuts all the older units.

All Antonio Carpio Units contain accretionary lapilli, either at the top of poorly sorted ignimbrites or randomly distributed throughout matrix-rich tuffs. Pellet layers exist, but are rare. Contacts between beds are often sharp and erosive. Lithic clasts are always subordinate and smaller than juvenile material. Juvenile material is pumiceous and ranges from black – light grey in colour. It is never white. Tops of deposits may be partly indurated due to the presence of groundwater and root calcretes (Klappa, 1980; Srivastava et al., 2019), which are also abundant in several of the palaeosols (Fig. 2.7). The Antonio Carpio Units provide evidence of multiple episodes of volcanic activity, with periods of quiescence in between, allowing for palaeosol development. These episodes of volcanic activity involved explosive eruptions that produced both concentrated, but mainly dilute pyroclastic density currents as well as ash falls. It should be noted that these deposits may be ignimbrite veneers (e.g. Brown and Branney, 2004), and thus could have been produced by a concentrated pyroclastic density current and represent much larger eruptions than implied by these deposits.

2.5 Discussion

2.5.1 Comparison with previous stratigraphy

This study identifies 10 different formations and 3 units, comprising of 7 major eruption-units and many more minor eruption-units (Table 2.2). A major eruption is here defined as one exceeding $>5 \text{ km}^3$ direct rock equivalent (DRE) of material, at least partly as PDCs. This volume is the minimum suggested for caldera collapse (Hughes and Mahood, 2011) and equals that of the 1991 Mt. Pinatubo eruption, which was one of the most powerful eruptions of the 20th century (Self and Blake, 2008). Only 4 formations identified in this study are linked to the previously published stratigraphy (Listanco, 1994). It was difficult to correlate the old 'Caloocan Pumice Flow', 'Sambong Ignimbrite' and 'Unknown B and A' to any deposits from this study (Fig. 2.3) because almost no localities mentioned in previous work (Listanco, 1994; Punongbayan et al., 1995) could be located. Stratigraphically, the Tadalac Cave and Calumpang formations are in

the same place as the above mentioned units and thus may correlate. This study has no field or lab evidence to support this, however. The Batangas and Sampaga formations are newly identified as the oldest deposits from Taal Caldera, while the old 'Scoria and Pyroclastic Flow' is split into the new Pasong and Indang formations. The 'Scoria Agglutinate' is now grouped in with the Pasong Formation. The Antonio Carpio Units fall somewhere between the Calumpang and Pasong Formation. The Buroi and Balagbag formations are placed in between the Pasong and Buco formations, suggesting they are younger than 5380 ± 70 years (non-calibrated; Listanco, 1994). This placement is somewhat tentative, however, because their type section is associated with erosion and reworked lake deposits, and no direct contact with any older formation is seen. The old 'Airfall and Base Surge Sequence', which included the 'Buco Base Surge' is now split into the Tagaytay Units, the Buco Formation, and the Alaminos Units.

2.5.2 Eruption volumes

The volume of the outflow sheet (ignimbrites) was calculated using five different methods (Section 2.2.2). Out of these the isopach method is preferred because it attempts to take into account the dynamic behaviour of PDCs with topography and the thinning of their deposits away from source. No Indang deposits are found along the lakeshore to provide a thickness estimate for deposits inside Lake Taal. However, since the Indang Formation is thicker than the Pasong Formation in a similar area, a thickness of at least 50 m for the Indang Formation along the lakeshore (compared to 60 m for Pasong) seems reasonable. The total eruptive volume includes a fall component volume if any fall deposit is seen in the field. However, an additional intracaldera fill volume is not included due to the uncertainty with regards to the sizes of formed calderas.

According to the volume estimations, the Pasong eruption was the largest followed by the Indang, Alitagtag and Buco eruptions (Table 2.2). Eruption size thus does not appear to be temporally correlated. All volumes are $>5 \text{ km}^3$ DRE, suggesting that all these eruptions were capable of forming calderas (Hughes

and Mahood, 2011). Other formations did not have sufficient exposure to calculate useful eruption volumes, but estimates were made based on the most similar well exposed formation.

No chemistry data is available for the Sampaga, Batangas and Calumpang formations, but they are exposed near the Alitagtag Formation, and are thinner with smaller juvenile and lithic clasts. Therefore, for volume calculations, a similar chemistry and a similar distribution area to the Alitagtag Formation was assumed, but an average thickness of the individual formation was used for the whole distribution area. This gives eruptions volumes of 2 km³ DRE for the Sampaga and Calumpang formations and 1 km³ DRE for the Batangas Formation (Table 2.2). Therefore, these 3 eruptions are classified as minor. Individual eruption-units within the Antonio Carpio Units are of similar thicknesses to these 3 formations and thus without further field evidence are here assumed to have similar eruption volumes.

The Tadalac Cave Formation appears most similar to the Alitagtag Formation in terms of componentry, lithification and bedding, although it is only exposed along the lakeshore where its top and base are never seen. Here, it is thicker than the Alitagtag Formation is anywhere, but no fall deposit (vent-derived or co-ignimbrite) is identified. Consequently, an eruption volume of 17 km³ DRE is estimated, which equates to the Alitagtag ignimbrite-only volume (Table 2.2).

The Burol and Balagbag formations consist of abundant, erosive beds, in similar style to the lakeshore deposits of the Buco Formation. Although the Burol and Balagbag formations are thicker along the lakeshore than the Buco Formation, the uncertainty of their distribution area means the Balagbag Formation is assigned a volume only equal to that of the Buco Formation (28 km³ DRE), while the Burol Formation is assigned a volume equal to the ignimbrite outflow sheet of the Buco Formation only (14 km³ DRE) because no fall deposits (vent-derived or co-ignimbrite) are identified in the Burol Formation (Table 2.2).

The Alaminos Units, being much thinner than any other prehistoric Taal deposits, likely have volumes closer to those of historical Taal eruptions (e.g.

1911 VEI 4 eruption deposited a bulk volume of 0.08 km³; Delos Reyes et al., 2018; Table 2.2). The Tagaytay Units may represent eruptions similar to or slightly larger than historical eruptions. The biggest historical eruption, a VEI 5 in 1754, deposited 20 cm of ash fall (Delos Reyes et al., 2018) in the same place that the Tagaytay Units show a 50 cm pumice lapilli fall deposit. This suggests that the largest eruption within the Tagaytay Units was bigger than the largest historical eruption, although there are numerous other factors that can account for a difference in fall deposit thickness, including wind direction and strength.

Formation	Eruption volume (km ³)	Eruption volume DRE (km ³)	Magnitude	VEI	Eruption classification	Dated units
Alaminos Units		0.08		4	minor	
Buco	46	28	6.8	6	major	submitted for Ar-Ar
Tagaytay Units					minor	
Balagbag	46	28	6.8	6	major*	
Burol	23	14	6.5	6	major*	
Pasong	144	90	7.4	7	major	~6 ka ^{1,2}
Indang	72	50	7.1	6	major	submitted for Ar-Ar
Tadlac Cave	27	17	6.6	6	major*	
Calumpang	3	2	5.8	5	minor	
Alitagtag	55	34	6.9	6	major	submitted for Ar-Ar
Batangas	1	1	5.3	5	minor	
Sampaga	4	2	5.7	5	minor	

Table 2.2: Named formations and units of the Taal Group with their eruption volumes where estimated, magnitude, VEI, eruption classification and any dates available. ¹Listanco, 1994; ²Martinez and Williams, 1999. *more uncertainty is associated with the classification of these eruption-units as major because their field exposures are more spatially limited compared to the other major eruption-units. Ar-Ar dating has been delayed due to the covid-19 pandemic. When dates are known eruption frequency calculations may need to be revised.

Previous estimates of Taal's prehistoric eruption volumes are lower than those calculated in this study. For comparative eruption-units, Listanco's (1994) Alitagtag unit has a 15 km³ bulk volume (~9 km³ DRE), compared to 34 km³ DRE in this study. Although the method of volume calculation is not stated by Listanco (1994), some discrepancy can be explained if Listanco only calculated ignimbrite volumes and did not include fall deposit volumes. Listanco's (1994) Caloocan and Sambong units were not identified in the field, but are in the same stratigraphic position as the Tadalac Cave and Indang formations. Comparing bulk volumes of these deposits, Caloocan (15 – 30 km³ bulk; Listanco, 1994) is similar to the Tadalac Cave Formation (27 km³ bulk), while the Sambong unit (50 km³ bulk; Listanco, 1994) has a smaller volume than the Indang Formation (72 km³ bulk).

It is stressed that the Tadalac Cave and Indang formations are not confirmed to be the same as the Sambong and Caloocan units. Previous volume estimates for the Pasong Formation, part of the Scoria Pyroclastic Flow (Martinez and Williams, 1999), are given as 50 km³ bulk (Listanco, 1994; Martinez and Williams, 1999; Delos Reyes et al., 2018), which equates to 31 km³ DRE, calculated using density values from this study (Section 2.2.2). This volume only takes into account the outflow sheet (Martinez and Williams, 1999), but even compared to the outflow sheet volume calculated in this study (45 km³ DRE) it is an underestimate. Similarly, the eruption volume calculated for the 'Buco Base Surge', now known as the Buco Formation, only came to 5 km³ bulk (Geronimo, 1988), while this study estimates it as 46 km³ bulk. This discrepancy is most significant because it suggests a major, caldera-forming eruption occurred less than ~5 ka (Listanco, 1994).

Comparing Taal's eruption volumes to better studied calderas, the Buco eruption may compare to the 41 ka eruption of Irosin caldera, which produced a 121 km² caldera (Kobayashi et al., 2014). The Alitagtag eruption, being of similar volume to the 1425 formation of Kuwae caldera in Vanuatu, may have formed a 72 km² caldera (Robin et al., 1994). The Indang eruption has an eruptive volume equivalent to that of the 6845 BP Mt. Mazama eruption, which formed a 80 km² caldera. The Pasong eruption produced 15 km³ DRE more

material than the eruption that formed Kikai caldera 7.3 ka. Therefore, the Pasong caldera may have been larger than 340 km² (Maeno and Taniguchi, 2007).

Caldera sizes tend to depend on the geometry of the magma chamber, however, and do not necessarily indicate eruption volumes (Roche et al., 2000). Nevertheless, none of these estimated caldera sizes equate to the current size of Lake Taal (650 km²) and it is unlikely that the exact same area collapsed during each event. This supports published hypotheses that the current caldera lake is not the result of one caldera-forming eruption (Listanco, 1994; Delos Reyes et al., 2018). Although the calculated volumes for Taal's prehistoric eruptions here are not at suggested lower boundaries for 'super-eruptions' (>450 km³ DRE; Self, 2006), these boundaries are arbitrary (Miller and Wark, 2008), and with calculated eruption volumes likely being underestimates, Taal should be considered as a possible site for future super-eruptions. The potential scale of volume underestimation is highlighted by the 200 m thick ignimbrites accumulated during the 1991 Pinatubo eruption (Rymer et al., 2005), which erupted only 5 km³ DRE of material (Newhall et al., 1998). Therefore, maximum thicknesses for Taal deposits (60 m) are likely gross underestimates of actual deposit thicknesses.

2.5.3 Eruption frequency

There is limited age data available for Taal's prehistoric deposits, therefore most estimates for the age of Taal Caldera are based on dates of deposits from other volcanoes or of unknown origin. The most commonly published estimate for the age of Taal Caldera is 140 ka (Oles, 1991; Delos Reyes et al., 2018). This date is based on a lava of unknown origin on Napayung Island. Previous studies disagree on the location of this lava, however, with it either being placed above (Miklius et al., 1991) or below (Listanco, 1994) a prominent ignimbrite. Although the lava was not identified on fieldwork for this study, boulders were found both on the island's shoreline and at the highest reachable point on foot. The ignimbrite rises out of the water and is exposed along the shore, and thus if

the lava were beneath it, this should not appear, even as boulders, on the island, especially at relatively high elevations. Therefore this study agrees with the finding that the Napayung Island lava appears above the island's ignimbrite (currently not able to be correlated within the stratigraphy). Consequently, we cannot use the 140 ka age as a base to calculate potential eruption frequencies.

An alternate age of ~30 ka has been suggested for Taal Caldera, however, this is a Carbon-14 date from the Cubao pumice flow-unit, which belongs to the Diliman Tuff Formation (Listanco, 1994; Arpa et al., 2008). There is currently no clear source volcano for the Diliman Tuff Formation because the chemistry does not match either published Taal or Laguna de Bay chemistry (Arpa et al., 2008). Therefore, 30 ka also does not seem appropriate to use despite suggestions by previous studies that it could represent the maximum age of Taal Caldera (Listanco, 1994).

This study identified the Pasong Formation overlying lavas from the Anilao Hill scoria cone. This scoria cone has a lava at its base, possibly the one being overlain by the Pasong Formation, which has been dated to 870 ka (Oles, 1991). This is the same date as the maximum Ar-Ar age (670 ± 200 ka) for an unnamed ignimbrite from the southern shore of Lake Taal (Punongbayan et al., 1995). Therefore, it is possible that Taal experienced some of its first large, ignimbrite-forming eruptions while the Anilao scoria cone was still active. The unnamed ignimbrite is underlain by unclassified tuffs and the Alitagtag Formation. Therefore the unnamed ignimbrite is the next major deposit above the Alitagtag Formation. The unnamed ignimbrite has been suggested to correlate to the previously named 'Sambong Ignimbrite' (Punongbayan et al., 1995) from Listanco's (1994) stratigraphy, but according to this study's stratigraphy the next major deposit above the Alitagtag Formation is the Tadalac Cave Formation. Therefore, using the 670 ± 200 ka age as an estimate for the Tadalac Cave Formation's age when calculating eruption frequencies seems to be the most stratigraphically robust option available. The only age estimate available for the Alitagtag Formation is the age of basal Mt. Macolod Volcano lavas (2.03 Ma; Oles, 1991), because they are overlain by the Alitagtag Formation (Listanco, 1994). As the only dated formation, the Pasong Formation

provides the upper constraint when calculating eruption frequencies. No previous study has attempted to calculate an eruption frequency for Taal's prehistoric eruptions.

Major eruptions

This study identifies 7 major eruptions (Table 2.2). Assuming an average age for the Tadalac Cave Formation (670 ka; Punongbayan et al., 1995) and Pasong Formation (6.8 ka; Listanco, 1994), with only the Indang Formation erupting in between them, gives an eruption frequency of 330 k years. Including the Alitagtag Formation (estimated age of 2.03 Ma; Oles, 1991) in this calculation gives an eruption frequency of 670 k years (including the Tadalac Cave Formation). The Buco, Burol and Balagbag eruptions are younger than ~6 ka (i.e. the age of the Pasong Formation), suggesting a major eruption occurred every 2000 years from Taal Caldera Volcano. Global averages suggest eruptions $100 > 10 \text{ km}^3$ DRE, into which the conservative estimates of Taal's eruption volumes fall, occur once every 100 years (Newhall and Self, 1982; Miller and Wark, 2008). Meanwhile, estimates for eruption frequencies of VEI 7 eruptions are 1 to 2 per 1000 years (Newhall et al., 2018). Therefore a major eruption (i.e. $> 5 \text{ km}^3$ DRE), possibly, but not necessarily a VEI 7 sized eruption, occurring from Taal Caldera Volcano every 2000 years seems reasonable.

The 2000 year recurrence time for major eruptions from Taal Caldera Volcano in the last 6000 years is wildly different from the 330 k year recurrence interval estimated for eruptions older than 6000 years. It is possible that more major eruption-units older than 6000 years exist, but are covered by younger pyroclastic deposits or have been reworked. At Mt. Pinatubo, for example, it only took one decade to rework 60% of deposits (Newhall et al., 2018). However, assuming eruptions occur at regular intervals is an oversimplification and several volcanoes show clusters of major eruptions, followed by periods of quiescence, or less frequent eruptions (e.g. the Yellowstone Hotspot; Knott et al., 2020). It is thus also possible that the frequency of major eruptions from Taal Caldera Volcano is increasing, which makes calculating a more accurate eruption frequency essential.

Minor eruptions

Minor eruptions are defined here as any eruptions with volumes $<5 \text{ km}^3$ DRE (Table 2.2). These include all of Taal's historical eruptions (e.g. Delos Reyes et al., 2018). Minor eruptions inherently occur more frequently, with those ejecting $>10^{-5} \text{ km}^3$ DRE of material occurring daily on a global scale (Newhall and Self, 1982; Miller and Wark, 2008). The first recorded eruption at Taal was in 1572 AD, after which 33 events, 9 of which are uncertain, of VEI 1 – 5 have occurred (Delos Reyes et al., 2018), including the recent eruptions in 2020, 2021 and 2022. All these eruptions were centred on Volcano Island, which can be categorised as a post-caldera edifice. A similar edifice exists within the Santorini Caldera, Greece, in the form of Nea Kameni (Vespa et al., 2006), while at Aso Caldera, Japan, multiple edifices are exposed, although only Nakadake is currently active (Miyabuchi, 2009). At both these calderas, periods of minor, but more frequent eruptions follow episodes of caldera-collapse (Vespa et al., 2006; Miyabuchi, 2009); a pattern that is also seen at calderas like Campi Flegrei, Italy (e.g. Di Vito et al., 1999), Crater Lake, USA (Druitt and Bacon, 1986), and Toba, Indonesia (Chesner, 2012). At Santorini these periods of more minor activity lasted 17000 – 45000 years and were followed by quiescence before a caldera-forming eruption (Vespa et al., 2006). A similar trend seems likely at Taal, with the Tagaytay Units representing intercaldera activity between the Pasong and Buco eruptions, while the Alaminos Units and historical deposits provide evidence of a post-Buco intercaldera phase.

Without dates for most prehistoric Taal eruptions, it is difficult to estimate how long periods of intercaldera activity lasted. Historically, individual eruptions occur once every 13 years or every 18 years on average if the 9 uncertain eruptions are excluded. Even on a relatively short historic timescale, however, there are periods of intense activity, followed by periods of quiescence that coincide with a shift in the eruptive locus from the main crater on Volcano Island to peripheral vents or vice versa. The 2020 eruption was the first one in 43 years and occurred at the main crater, while previously the peripheral Mt. Tabaro was the source of the eruptions during the last eruptive period (1965 –

1977). This suggests Taal may have entered another period of heightened activity, supported by the fact that fumarolic activity and phreatic and phreatomagmatic eruptions are occurring in the Volcano Island main crater at present (PHIVOLCS, 2022). Periods of quiescence at Taal last between 62 and 18 years, while time between individual eruptions within active periods can be as short as 1 year (Delos Reyes et al., 2018). Such patterns of activity and quiescence may have also governed the timing of the Tagaytay eruptions and any older intercaldera activity. At least 41 palaeosols are recognised within the Tagaytay Units; if we assume that the Buco eruption roughly represents the present-day, then on average a relatively minor eruption occurred every 146 years in between the Pasong and Buco eruptions. This is much less frequent than historical activity, but 146 years is likely an underestimate since the Tagaytay Units have limited exposure and eruptions with smaller plumes (~ <3 km) may not have deposited significant material to the north since the prevailing wind at this altitude is from the east (Ku et al., 2009; OCHA, 2020). This was highlighted by the 2020 eruption, where the majority of material fell southwest of Lake Taal.

Although no field evidence of a sequence of minor eruptions like the Tagaytay Units in between caldera-forming eruptions older than the Pasong eruption was found, previous field studies have postulated their existence (Listanco, 1994). Therefore, it seems typical for Taal to experience minor eruptions in between its catastrophic, caldera-forming eruptions. At calderas similar to Taal (e.g. Santorini, Campi Flegrei), such intercaldera activity is thought to signal magma chamber growth (Townsend et al., 2019). Consequently, despite its minor eruptions, Taal may currently be growing its magma storage region, possibly building up to its next major, caldera-forming eruption.

2.6 Conclusions

- At least 7 major eruption-units, 3 minor eruption-units, and 2 sets of minor, but more frequent eruptions are identified. Further eruption deposits are identified as the Antonio Carpio Units, but these cannot be

stratigraphically placed at this time (Fig. 2.16). The 10 named formations is an increase on the 5 previously named units (Geronimo, 1988; Listanco, 1994; Martinez and Williams, 1999). Importantly, a new oldest formation is identified in the Sampaga Formation. The most recent major eruption is the Buco Formation, which occurred less than ~5380 years ago.

- Eruption volumes are upgraded from previous estimates, most notably the Pasong Formation increasing from 31 km³ (DRE) to 90 km³ (DRE) and the Buco Formation increasing from 3 km³ (DRE) to 28 km³ (DRE).
- All major eruptions likely formed a caldera, potentially ranging in size from 72 km² to 340 km². None of these equate to the total area of Lake Taal (650 km²), supporting the hypothesis that Lake Taal is a nested caldera.
- Recurrence times for major eruptions are estimated at 330 k years and 670 k years, while in the past 6000 years 2 definite major eruptions have taken place. This could imply that major eruptions are starting to occur more frequently. More age data is desperately needed to gain a more accurate understanding of the frequency of Taal's major eruptions.
- Historical minor eruptions occur every 18 years on average, but every 146 years for the Tagaytay Units, although the latter is likely an underestimate.
- Taal seems to experience a multitude of minor eruptions in between its major eruptions. Current activity at Taal points to a phase of minor eruptions, suggesting Taal may be building up its magma storage region to produce another major, perhaps caldera-forming eruption.

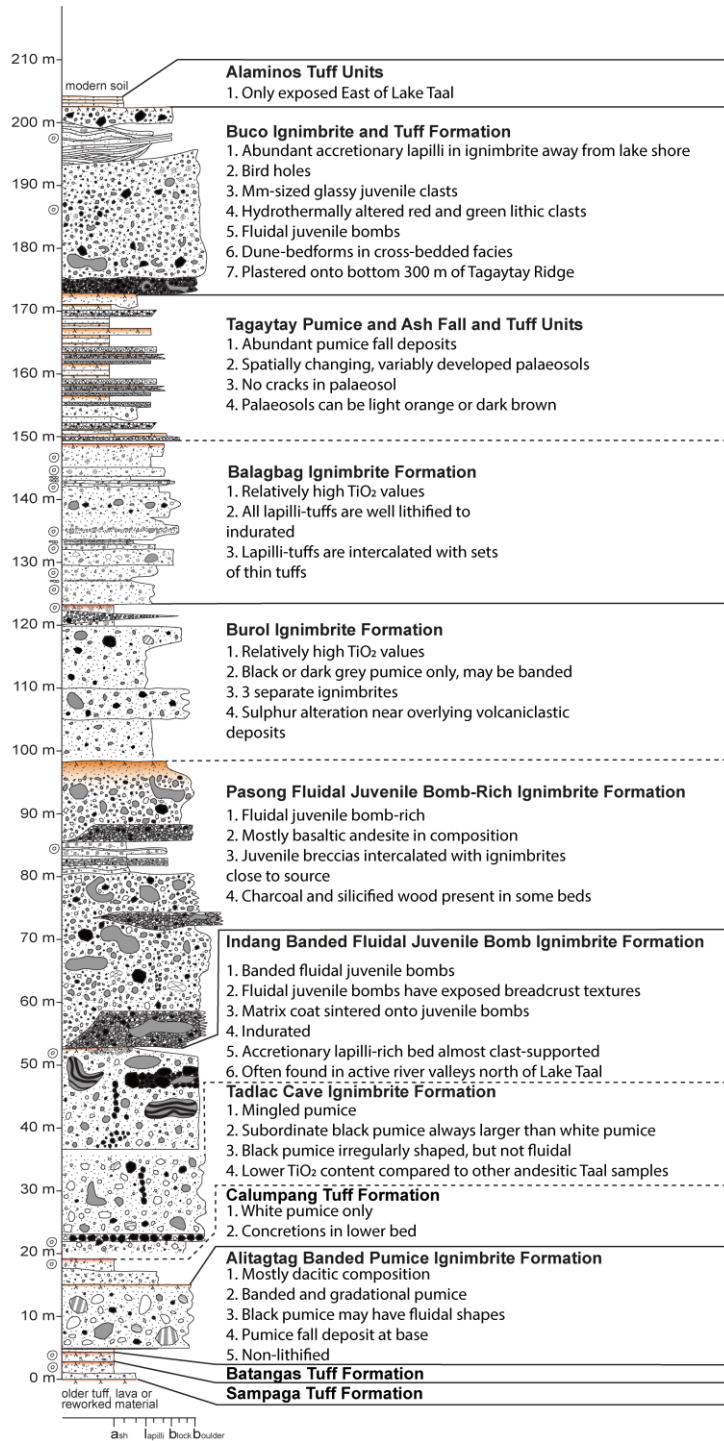
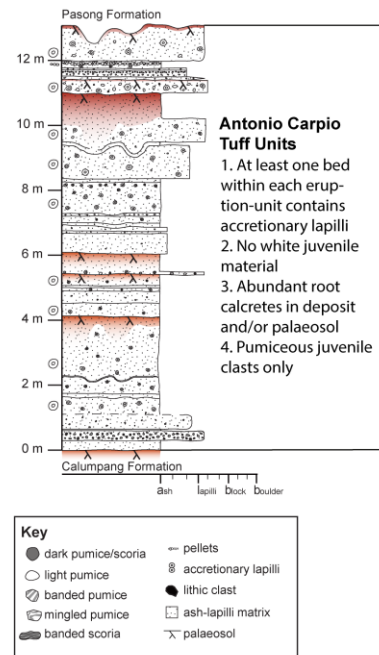


Fig. 2.16: GVS of the Taal Group, including the Antonio Carpio Units, with the key identifiable features of named formations and units where possible.



Chapter 3

Eruption styles of a flooded caldera volcano: eruptive and emplacement processes deduced from the pyroclastic lithofacies of prehistoric eruptions at Taal Caldera Volcano, Philippines

3.1 Introduction

Flooded caldera volcanoes produce some of the most violent volcanic eruptions on Earth (e.g. the Oruanui eruption, New Zealand; Wilson, 2001); the Minoan eruption of the flooded caldera Santorini (Bond and Sparks, 1976), for example, wiped out the Minoan settlement on Santorini, arguably reducing the strength of the entire Minoan civilisation (Karátson et al., 2020). Pyroclastic density currents of the Taupo and Oruanui eruptions from the flooded Taupo Caldera, New Zealand, devastated surrounding landscapes and changed the courses of rivers and the regional vegetation (Barker et al., 2020). Poorly lithified, fine-grained tephra common at flooded caldera volcanoes is easily remobilised, producing a lahar hazard that may persist decades (Manville et al., 2005). Despite the significant hazard posed by flooded caldera volcanoes, they remain poorly understood (Németh and Kósik, 2020). It is still unclear what the exact role of water is in the fragmentation process, whether water drives and controls fragmentation, or whether it simply alters the eruption style (Németh and Kósik, 2020). In addition, the eruption styles associated with flooded caldera volcanoes are poorly defined and whether these volcanoes exhibit any ‘typical behaviour’ remains unknown.

To better understand the processes and hazards at flooded caldera volcanoes, studies have attempted to identify and understand the differences and similarities between the deposits from various flooded caldera volcanoes. A key early study was that of Self and Sparks (1978), who coined the term Phreatoplinian (the phreatomagmatic equivalent of Plinian (dispersal index

>500 km²) and Sub-Plinian (those with a dispersal index >50 km² and <500 km²) eruptions; Self and Sparks, 1978) while describing the deposits from the Oruanui eruption from the Taupo Volcanic Complex (members 1 – 5) and the 1875 eruption of Askja (layer C). The fall deposits from these eruptions were finer grained and more poorly sorted than magmatic (e.g. Askja layer D in Self and Sparks, 1978) fall deposits, and negatively skewed (i.e. the grain size distribution has a long tail on the left hand side with the majority of the data concentrated on the right hand side of a bell curve plot) while magmatic fall deposits are positively skewed (i.e. the grain size distribution has a long tail on the right hand side with the majority of the data concentrated on the left hand side of a bell curve plot) if at all. The Phreatoplinian fall deposits were also highly stratified and showed coarse tail grading and a downwind decrease in sorting, but not in median diameter (Self and Sparks, 1978).

This initial research was developed and expanded upon with studies aiming to identify a record of magma – water interaction in volcanic deposits. Success was achieved using field-based work in which flow deposits produced by Phreatoplinian eruptions were found to usually be relatively thin (Sparks et al., 1981; Cole and Scarpati, 1993; Lloyd et al., 1996), and to contain abundant bedforms, including dune-bedforms (Lloyd et al., 1996; Pérez et al., 2020) and cross-bedding (Druitt et al., 1989; Nairn et al., 1995; Lloyd et al., 1996; Houghton et al., 2003; Pérez et al., 2020). Phreatoplinian ignimbrites can be wet enough to plaster onto near-vertical surfaces (e.g. Geronimo, 1988) and are usually non-welded or even non-lithified (e.g. Nairn et al., 1995; Lloyd et al., 1996; Wilson, 2001), hence, making them prone to erosion (Manville and Wilson, 2004) and alteration processes (Brown and Andrews, 2015) such as zeolitisation (Giordano et al., 2002; Scarpati et al., 2020).

To further characterise Phreatoplinian ignimbrites their componentry (clast types) was investigated. The componentry of Phreatoplinian ignimbrites is commonly limited in lapilli- and especially boulder- and bomb-sized clasts (e.g. the Oruanui ignimbrite; Wilson, 2001). However, proximal ignimbrite from flooded caldera volcanoes can include fluidal-shaped bombs (e.g. folded or twisted spatter rags), but the significance and origin of these remains to be

clearly established (Druitt et al., 1989; Mellors and Sparks, 1991; Valentine et al., 2000; Branney and Kokelaar, 2002; Palladino and Simeï, 2005; Kokelaar et al., 2007). These fluidal bombs commonly contain lithic fragments (Allen, 2005), and may have glassy rims with contraction cracks possibly suggesting rapid quenching of hot juvenile material against relatively cold water or steam (Mellors and Sparks, 1991; Monzier et al., 1994; Wilson, 2001; Németh and Kósik, 2020).

More recently, microscopic studies into pumice density and vesicularity were conducted for Phreatoplinian eruptions such as the 1875 Askja eruption (Carey et al., 2009). The hydrovolcanic phase of the Askja eruption had similar vesicle number densities, vesicle volume distributions and clast vesicularity ranges compared to its two magmatic phases, suggesting that water did not impact either deep or shallow conduit processes (Carey et al., 2009). However, Askja's Phreatoplinian fall phase did display the most complex vesicle textures of the entire eruption. This complexity was explained by vent widening and therefore complex vesicle textures are not related to magma – water interaction in this context (Carey et al., 2009). Pumice density and vesicularity are therefore not independent indicators of magma – water interaction. Microscopic features that have been identified as evidence of magma – water interaction are quenching cracks (Heiken, 1972; Büttner, 1999) and moss-like patterns (Austin-Erickson et al., 2008) found on ash grains, although most of this work has focused on smaller-scale hydrovolcanic eruptions, not Phreatoplinian eruptions.

Taal Caldera Volcano is used as a case study because it is one of the best known, but least studied, examples of a flooded caldera volcano. Its record of caldera-forming eruptions (Fig. 3.1), proximity to densely populated, large cities (2.4 million within a 30 km radius; GVP, 2021B), and its tropical location (i.e. larger global climate impact; Robock, 2000) make it a hazardous volcano on a regional scale. This study is the fourth to investigate Taal's prehistoric eruptions (previous work is by Geronimo, 1988; Listanco, 1994; and Martinez and Williams, 1999), but the first to use a field-based lithofacies approach. Typically pyroclastic deposits are interpreted by analysing internal variations within single eruption-units (e.g. Sparks et al., 1981; Wilson, 2001; Brown and Branney,

2013; Scarpati et al., 2020). However, due to time constraints and vegetation cover at Taal Caldera Volcano this was not possible for individual eruption-units. Therefore interpretations about emplacement and eruption processes have been generated on a more general level for Taal Caldera Volcano by attempting to analyse the overall pattern of lithofacies in vertical sequences of deposits and apply quantitative and statistical analysis to identify and interpret any patterns within the deposits. This approach can make use of isolated exposures of successions whose detailed stratigraphic relations are unresolved. Although this method is not a common approach in physical volcanology and has limitations, its use is warranted in this study because Taal Caldera Volcano is hazardous and currently active.

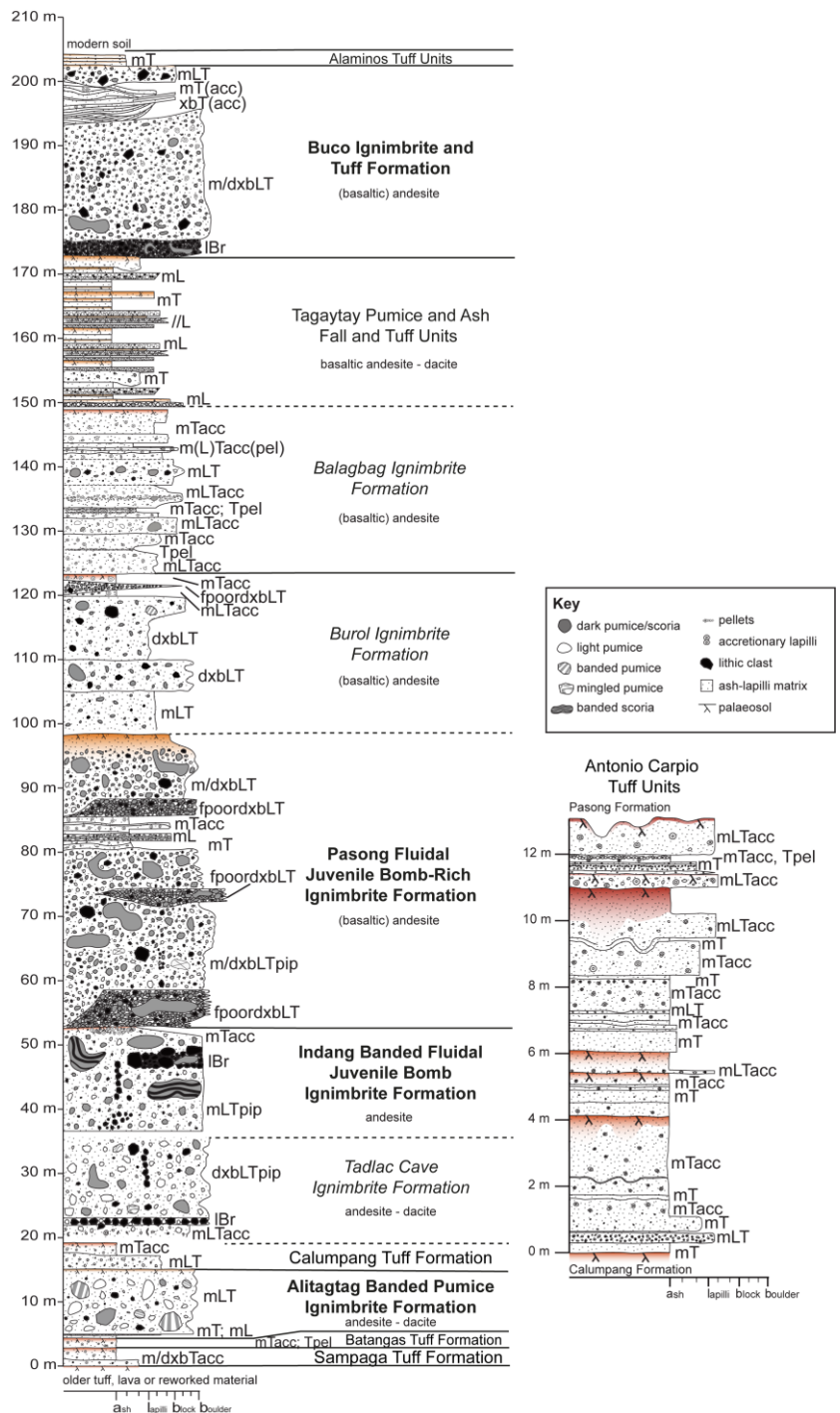


Fig. 3.1: Taal's prehistoric stratigraphy. Formation names in bold record major eruptions, those in italics record possible major eruptions. The Antonio Carpio Tuff Units are tentatively placed somewhere between the Calumpang and Pasong Formation.

3.1.1 Aims and objectives

This chapter aims to do the following:

- Characterise the lithofacies identified in Taal Caldera Volcano deposits using field data.
- Interpret the lithofacies to determine the eruption and depositional styles associated with each facies.
- Describe and interpret ash aggregates, fluidal juvenile bombs and bedforms, and clast textures associated with certain lithofacies.
- Determine vertical lithofacies associations by identifying the most common (sets of) facies transitions and interpret eruption and depositional styles associated with individual associations.
- Statistically investigate vertical lithofacies associations using two methods of Markov Chain Analysis and interpret eruption and depositional styles based on the facies relationship diagram.
- Comment on the use of the different methods of Markov Chain Analysis in a volcanological context.
- Identify common eruption sequences and patterns that will provide insight into what future eruptions from Taal Caldera Volcano might look like.
- Evaluate the evidence for magma – water interaction in prehistoric eruptions from Taal Caldera Volcano.
- Investigate any trends in eruption styles at Taal Caldera Volcano over time by linking lithofacies (associations) with named formations in the generalised vertical section (GVS) where possible (Fig. 3.1).
- Place findings from Taal Caldera Volcano in a broader context to evaluate any common lithofacies associations between Taal and hydrovolcanoes, as well as any trends between flooded and non-flooded caldera-forming eruptions.

3.2 Methods

3.2.1 Field data

Detailed field observations were recorded for individual pyroclastic strata at 239 localities (Appendix A) as much as 40 km from the centre of Lake Taal (Fig. 1.2). Observations included the percentage of matrix, deposit sorting, the abundances of different clast types (i.e. pumice, scoria, spatter, lithic), the colour of juvenile clasts, the abundances of different types of lithic clasts (e.g. porphyritic lava, hydrothermally altered clast), whether the deposit was matrix- or clast-supported, any grading patterns found within the deposit, the presence of clast concentration zones (e.g. elutriation pipes, pumice lenses), clast imbrication or alignment, the thickness of individual strata, the type of contact with upper and lower strata (erosive, sharp, or gradational), the lithification of the deposit, and the field sorting of the deposit. The deposits of Taal Caldera are non-welded, therefore a lithification scale was designed to enable more useful distinction of non-welded deposits than simply 'non-welded' and 'indurated'. This included unlithified, poorly, moderately and well lithified, and indurated (Fig. 3.2).

Indurated	Well lithified	Moderately lithified	Poorly lithified	Unlithified
				
not possible to scrape with hand scraper	only thin surface layer removed with hand scraper	only intended material removed by hand scraper (i.e. no extra material will fall out of exposure due to poor lithification)	only intended material removed by hand scraper (i.e. no extra material will fall out of exposure due to poor lithification)	hand scraper removes more than intended material (i.e. non-scraped material falls out due to poor lithification)
may have orange/purple colour	no colour alteration	no colour alteration	no colour alteration	may have red/orange colour
clasts removed with hammer	clasts removed with hammer	clasts removed with hand scraper	clasts removed by hand	clasts removed by hand
preferentially less eroded	preferentially less eroded	average amount of erosion	preferentially more eroded	preferentially more eroded
frequently lapilli-tuffs	frequently tuffs	frequently lapilli-tuffs	frequently lapilli-tuffs, lapillistone or lithic breccias	frequently lapillistone or lithic breccias
frequently make up river bed of active river valleys	often aggregated pellet layers			may have loose material deposited at base of exposure

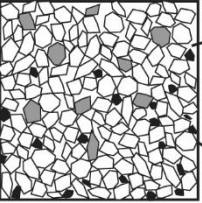
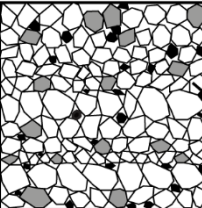
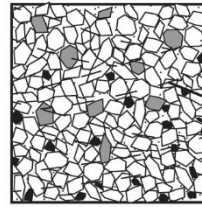
Fig. 3.2: The lithification scale used for this study with key identifying features for each class.

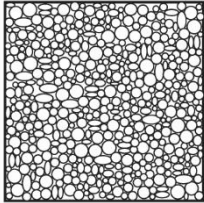
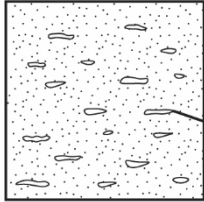
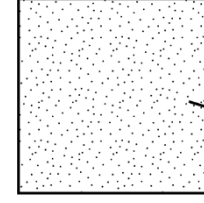
3.2.2 Lab work methods

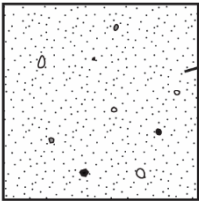
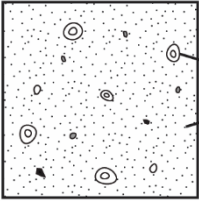
Seventeen ash samples of various grain sizes (<2 mm), covering the widest possible range of lithofacies and named formations, were qualitatively described and photographed using the desktop SEM at the University of Leicester (Appendix B). Ash aggregates from various facies were also thin sectioned and observed under the optical microscope (Appendix B).

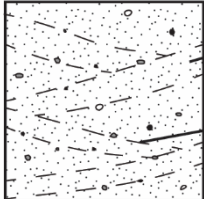
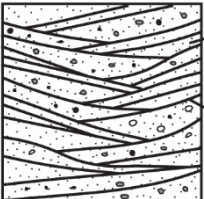
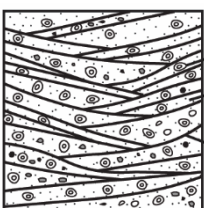
3.3 Lithofacies at Taal Caldera Volcano

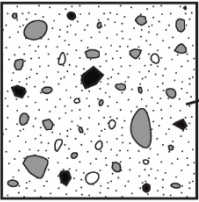
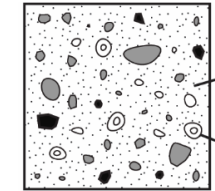
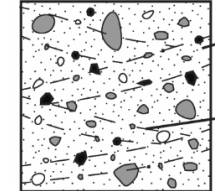
Lithofacies identified at Taal Caldera Volcano are characterised before their vertical and lateral associations are documented. There is a wide range of lithofacies associated with the prehistorical deposits from Taal Caldera Volcano (Table 3.1), suggesting Taal had a variety of eruption styles and depositional processes. Following the summary of lithofacies provides in Table 3.1, ash aggregates, fluidal juvenile bomb-bearing ignimbrites, bedforms and clast textures from selected lithofacies and named formations will be described in more detail to provide further information about Taal's eruption styles and depositional processes.

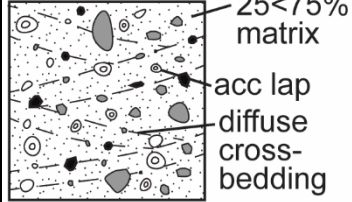
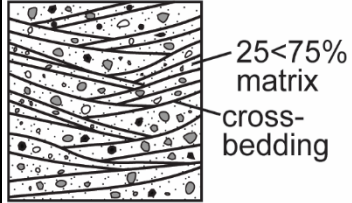
Lithofacies	Description	Possible Interpretations	Cartoon Representation
Massive lapillistone (mL)	<p>Lithology: usually juvenile-rich; clast-supported, well sorted angular pumice lapilli with fine lithic lapilli in pneumatic equivalence; lithic assemblage: fresh/weathered glassy, aphanitic lavas and/or tuffs.</p> <p>Structure: massive (m); normal (n) and reverse (r) grading; 0.0015 – 1 m thick.</p> <p>Lithification: unlithified – indurated</p> <p>Stratigraphic occurrence: Alitagtag Formation, Bucu Formation, Tagaytay Units and unnamed.</p>	<p>(Sub)Plinian pumice fallout beds. Normal and reverse grading indicates waning and waxing conditions¹ and/or changing wind direction and/or strength.</p>	 <p><25% matrix</p> <p>angular pumice</p>
Parallel-bedded lapillistone (//L)	<p>Lithology: juvenile-rich; clast-supported, well sorted angular pumice lapilli with fine lithic lapilli in pneumatic equivalence; lithic assemblage: fresh/weathered glassy, aphanitic lavas and/or tuffs.</p> <p>Structure: parallel-bedded (//); normal (n) and reverse (r) grading; 0.03 – 0.75 m thick.</p> <p>Lithification: unlithified.</p> <p>Stratigraphic occurrence: Tagaytay Units and unnamed.</p>	<p>(Sub)Plinian pumice fallout beds. Normal and reverse grading indicates waning and waxing conditions¹ and/or changing wind direction and/or strength.</p>	 <p><25% matrix</p> <p>parallel-bedding</p> <p>angular pumice</p>
Diffuse cross-bedded lapillistone (dxbL)	<p>Lithology: juvenile-rich; clast-supported, well sorted angular pumice lapilli with fine lithic lapilli in pneumatic equivalence; lithic assemblage: fresh/weathered glassy, aphanitic lavas and/or tuffs.</p> <p>Structure: low- to high-angle diffuse cross-bedded (dxb) throughout; 0.01 – 0.8 m thick.</p> <p>Lithification: unlithified – poorly lithified.</p> <p>Stratigraphic occurrence: Tagaytay Units.</p>	<p>(Sub)Plinian fallout beds, affected by passing dilute pyroclastic density currents or wind gusts to produce diffuse cross-bedding¹.</p>	 <p><25% matrix</p> <p>diffuse cross-bedding</p> <p>angular pumice</p>

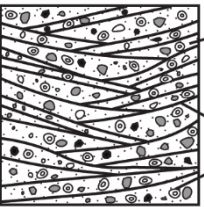
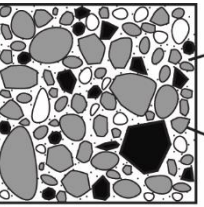
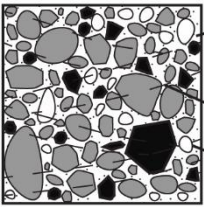
Ash pellet tuff (Tpel)	<p>Lithology: rare fine pumice lapilli and ash-sized lithic clasts; well-sorted rounded pellets and/or anhedral ash aggregates or disaggregated pellets; rare whole accretionary lapilli (acc lap); various amounts of matrix depending on percentage of coalesced pellets.</p> <p>Structure: clast-supported; may occur as lenses in other facies; 0.005 – 0.2 m thick.</p> <p>Lithification: poorly – well lithified.</p> <p>Stratigraphic occurrence: Alaminos Units, Antonio Carpio Units, Balagbag Formation, Batangas Formation, Bucu Formation, Pasong Formation, Tagaytay Units and unnamed.</p>	Possible fallout from a primary eruption cloud or a co-ignimbrite plume once the PDC has passed ² . Remnant accretionary lapilli formed in final, weak PDC turbulence while pellets already falling. Where pellets occur as lenses, esp. in mLT, they could represent ash clumps that formed from ash sticking together on trees prior to falling into the aggrading deposit. Well lithified deposits represent a moisture-rich depositional environment ^{1,8} .	 <p>ash pellet</p>
Vesiculated tuff (Tves)	<p>Lithology: rare coarse ash-sized, pumice matrix-supported in well sorted vitric tuff.</p> <p>Structure: elongated – rounded vesicles within fine ash matrix; 0.01 – 0.15 m thick.</p> <p>Lithification: well lithified.</p> <p>Stratigraphic occurrence: Antonio Carpio Units, Balagbag Formation and unnamed.</p>	Produced during moist fallout from a co-ignimbrite plume or primary eruption cloud ⁸ ; may represent coalesced pellets.	 <p>vesicle</p>
Parallel-bedded tuff (IT)	<p>Lithology: well sorted vitric tuff; may be infiltrated by lapilli-sized pumices from vertically associated lapillistone.</p> <p>Structure: parallel-bedded (//); normal (n) and reverse (r) grading; 0.08 – 0.2 m thick.</p> <p>Lithification: poor.</p> <p>Stratigraphic occurrence: Bucu Formation and Tagaytay Units.</p>	Without any good lateral exposure revealing whether deposits mantle topography or not, it is difficult to determine whether //Ts are ash fall deposits, either from primary eruption fallout or co-ignimbrite plumes, or dilute PDC deposits. Normal and reverse grading indicates waning and waxing conditions ¹ .	 <p>parallel-bedding</p>

<p>Massive tuff (mT)</p>	<p>Lithology: minor fine pumice and/or scoria lapilli and mostly subordinate similar sized lithic clasts matrix-supported in poorly sorted vitric tuff; lithic assemblage: fresh/weathered glassy, aphanitic lavas and/or tuffs.</p> <p>Structure: massive (m); rare normal (n) and reverse (r) grading; rare lithic and pumice lenses (lens) and clast concentration zones; frequent lateral thickness variations; 0 – 1 m thick.</p> <p>Lithification: unlithified – well lithified.</p> <p>Stratigraphic occurrence: Alaminos Units, Alitagtag Formation, Antonio Carpio Units, Balagbag Formation, Buco Formation, Pasong Formation, Tagaytay Units and unnamed.</p>	<p>Deposited from a dilute PDC with a direct fallout-dominated flow-boundary zone. Steady and uniform deposition, with rare periods of unsteadiness and non-uniformity during deposition of clast-rich lenses, representing clast segregation¹. Normal and reverse grading indicates waning and waxing conditions¹. Without good lateral exposure, it is difficult to rule out mT representing an ash fall deposit or a veneer deposit².</p>	 <p>>75% matrix</p> <ul style="list-style-type: none">  scoria and dark pumice  light pumice  lithic clast  accretionary lapilli  matrix
<p>Massive tuff with accretionary lapilli (mTacc)</p>	<p>Lithology: minor fine pumice and/or scoria lapilli, mostly subordinate similar sized lithic clasts and whole and fragmented accretionary lapilli (acc) matrix-supported in poorly sorted vitric tuff; accretionary lapilli can be the only clast type; lithic assemblage: fresh/weathered glassy, aphanitic lavas and/or tuffs.</p> <p>Structure: massive (m); rare normal (n) grading; frequent lateral thickness variations; 0.01 – 7 m thick.</p> <p>Lithification: unlithified – well lithified.</p> <p>Stratigraphic occurrence: Antonio Carpio Units, Balagbag Formation, Batangas Formation, Buco Formation, Burolo Formation, Calumpang Formation, Indang Formation, Pasong Formation, Tadolac Cave Formation and unnamed.</p>	<p>Deposited from a dilute PDC with a direct fallout-dominated flow-boundary zone¹. Normal grading indicates waning conditions¹. Moisture levels high enough so that ash cores formed in upper part of current or co-ignimbrite plume that fall into current accrete layers of fine ash before depositing^{2,3}. Accretionary lapilli fragments indicate they were hard enough to fracture in a brittle way. Without good lateral exposure, it is difficult to rule out mTacc representing a veneer deposit². One almost clast-supported mTacc bed in the Indang Formation (Chapter 2) is hypothesised to have formed in a hybrid plinian-co-ignimbrite cloud system⁵.</p>	 <p>acc lap</p> <p>>75% matrix</p>

Diffuse cross-bedded tuff (dxbT)	<p>Lithology: minor fine – medium pumice lapilli, and similarly-sized lithic clasts matrix-supported in poorly sorted vitric tuff; lithic assemblage: fresh/weathered glassy, aphanitic lavas and/or tuffs.</p> <p>Structure: diffuse cross-bedded (dxb) throughout; rare lithic alignment; 0.005 – 0.5 m thick.</p> <p>Lithification: unlithified – lithified.</p> <p>Stratigraphic occurrence: Antonio Carpio Units, Buco Formation, Calumpang Formation, Pasong Formation, Sampaga Formation, Tagaytay Units and unnamed.</p>	Deposition from a dilute PDC with a direct fallout- to traction-dominant environment ¹ . Small-scale unsteadiness produces diffuse bedding ² . Clast alignments support temporary granular shear components or granular-flow dominant boundary zone ¹ .	 <p>>75% matrix diffuse cross-bedding</p>
Cross-bedded tuff (xbT)	<p>Lithology: minor fine – medium pumice lapilli and/or similar sized lithic clasts matrix-supported in a poorly sorted vitric tuff; lithic assemblage: fresh/weathered glassy, aphanitic lavas and/or tuffs.</p> <p>Structure: low- to high-angle cross-bedded (xb); rare normal (n) and reverse (r) grading; bedforms common; highly laterally discontinuous; 0.002 – 0.5 m thick.</p> <p>Lithification: unlithified – well lithified.</p> <p>Stratigraphic occurrence: Antonio Carpio Units, Balagbag Formation, Buco Formation, Pasong Formation, Tagaytay Units and unnamed.</p>	Deposition from a granular fluid-based PDC with a traction-dominated flow-boundary zone, but current is more dilute compared to xbLT. Grain fabrics show increased shear and/or lower aggradation rates. Discontinuous beds imply a non-uniform current and normal and reverse grading indicates waning and waxing conditions ¹ .	 <p>>75% matrix cross-bedding</p>
Cross-bedded tuff with accretionary lapilli (xbTacc)	<p>Lithology: minor fine – medium pumice lapilli, mostly subordinate similar sized lithic clasts and whole and fragmented accretionary lapilli (acc) matrix-supported in a poorly sorted vitric tuff; lithic assemblage: fresh/weathered glassy, aphanitic lavas and/or tuffs; accretionary lapilli may be the only clast type.</p> <p>Structure: low- to high-angle cross-bedded (xb); bedforms common; highly laterally discontinuous; 0.01 – 1 m thick.</p> <p>Lithification: unlithified – well lithified.</p> <p>Stratigraphic occurrence: Buco Formation, Pasong Formation and unnamed.</p>	Deposition from a dilute PDC with a traction-dominated flow-boundary zone. Discontinuous beds imply a non-uniform current ¹ . Moisture levels high enough so that ash cores formed in upper part of current or co-ignimbrite plume that fall into current accrete layers of fine ash before depositing ^{2,3} . Accretionary lapilli fragments indicate they were hard enough to fracture in a brittle way.	 <p>acc lap >75% matrix cross-bedding</p>

Massive lapilli-tuff (mLT)	<p>Lithology: variable proportions of pumice and/or (dense, fluidal) scoria lapilli, blocks and bombs, and similar sized lithic clasts matrix-supported in poorly sorted vitric tuff; lithic assemblage: fresh/weathered glassy, aphanitic or porphyritic lavas and/or tuffs, rarely red-black banded lava.</p> <p>Structure: massive (m); normal (n), reverse (r), and varied (v) grading; lithic- and pumice-rich lenses (lens); clast concentration zones; elutriation pipes (pip); rare clast alignment and imbrication (i); 0.02 – 25 m thick.</p> <p>Lithification: unlithified – indurated.</p> <p>Stratigraphic occurrence: Alitagtag Formation, Antonio Carpio Units, Balagbag Formation, Bucu Formation, BuroI Formation, Calumpang Formation, Indang Formation, Pasong Formation, Tadlac Cave Formation, Tagaytay Units and unnamed.</p>	<p>Deposited from a granular fluid-based PDC with a fluid escape-dominated flow-boundary zone, supported by elutriation pipes¹. Steady and uniform deposition, with periods of unsteadiness and non-uniformity during deposition of clast-rich lenses, representing clast segregation e.g. pumice rafts or levees, fine ash elutriation¹. Normal and reverse grading indicates waning and waxing conditions¹.</p>	 <p>25<75% matrix</p>
Massive lapilli-tuff with accretionary lapilli (mLTacc)	<p>Lithology: variable proportions of pumice and/or (dense, fluidal) scoria lapilli, blocks and bombs, mostly subordinate similar sized lithic clasts, and whole and fragmented accretionary lapilli (acc) matrix-supported in poorly sorted ash tuff; lithic assemblage: fresh/weathered glassy, aphanitic or porphyritic lavas and/or tuffs, rare hydrothermally altered clasts.</p> <p>Structure: massive (m); normal (n) and reverse (r) grading; 0.1 – 10 m thick.</p> <p>Lithification: unlithified – indurated.</p> <p>Stratigraphic occurrence: Antonio Carpio Units, Balagbag Formation, Bucu Formation, BuroI Formation, Pasong Formation and unnamed.</p>	<p>Deposited from a granular fluid-based PDC with a fluid escape-dominated flow-boundary zone¹. Normal and reverse grading indicates waning and waxing conditions¹. Moisture levels high enough so that ash cores formed in upper part of current or co-ignimbrite plume that fall into current, accrete layers of fine ash before depositing^{2,3}. High aggradation rate, otherwise accretionary lapilli more likely to be destroyed⁴. Accretionary lapilli fragments indicate they were hard enough to fracture in a brittle way.</p>	 <p>25<75% matrix acc lap</p>
Diffuse cross-bedded lapilli-tuff (dxBLT)	<p>Lithology: variable proportions of pumice and/or (dense, fluidal) scoria lapilli, blocks and bombs, and similar sized lithic clasts matrix-supported in a poorly sorted vitric tuff; lithic assemblage: fresh/weathered glassy, aphanitic or porphyritic lavas and/or tuffs, rare diorite and hydrothermally-altered clasts.</p> <p>Structure: diffuse cross-bedded (dx) throughout; rare clast alignment; normal (n), reverse (r) and varied (v) grading; some exposures are lithic-rich; rare elutriation pipes (pip); pumice-lithic- and fines-rich lenses (lens); 0.05 – 12 m thick.</p>	<p>Deposition from a granular fluid-based PDC with a fluid escape- (elutriation pipes form) to traction-dominant environment¹. Small-scale unsteadiness produces diffuse bedding² and larger-scale unsteadiness results in clast- and fines-rich lenses¹. Clast alignments support temporary granular shear components or granular-flow dominant</p>	 <p>25<75% matrix diffuse cross-bedding</p>

	<p>Lithification: unlithified – indurated.</p> <p>Stratigraphic occurrence: Buco Formation, Buroi Formation, Calumpang Formation, Pasong Formation, Sampaga Formation, Tadlac Cave Formation, Tagaytay Units and unnamed.</p>	<p>boundary zone¹. Normal and reverse grading indicates waning and waxing conditions¹.</p>	
<p>Diffuse cross-bedded lapilli-tuff with accretionary lapilli (dxbLTacc)</p>	<p>Lithology: variable proportions of pumice and/or (dense, fluidal) scoria lapilli, blocks and bombs, fine – coarse lithic lapilli, and whole and fragmented accretionary lapilli (acc); lithic assemblage: fresh/weathered glassy, aphanitic or porphyritic lavas and/or tuffs, rare hydrothermally-altered clasts.</p> <p>Structure: diffuse cross-bedded (dxb) throughout; rare lithic alignment; 0.1 – 9 m thick.</p> <p>Lithification: unlithified – lithified.</p> <p>Stratigraphic occurrence: Buco Formation and unnamed.</p>	<p>Deposition from a granular fluid-based PDC with a fluid escape- to traction-dominant environment¹. Small-scale unsteadiness produces diffuse bedding². Clast alignments support temporary granular shear components or granular-flow dominant boundary zone¹. Moisture levels high enough so that ash cores formed in upper part of current or cognimbrite plume that fall into current accrete layers of fine ash before depositing^{2,3}. Accretionary lapilli fragments indicate they were hard enough to fracture in a brittle way.</p>	
<p>Cross-bedded lapilli-tuff (xbLT)</p>	<p>Lithology: variable proportions of pumice and/or scoria lapilli, blocks and bombs, and similarly-sized lithic clasts matrix-supported in vitric tuff; lithic assemblage: fresh/weathered glassy, aphanitic or porphyritic lavas and/or tuffs, rare hydrothermally-altered clasts.</p> <p>Structure: low- and high-angle cross-bedded (xb); rare normal (n) and reverse (r) grading; rare clast alignments; pumice-concentration zones; bedforms common; highly laterally discontinuous; 0.01 – 1 m thick.</p> <p>Lithification: unlithified – well lithified.</p> <p>Stratigraphic occurrence: Buco Formation, Pasong Formation and unnamed.</p>	<p>Deposition from a granular fluid-based PDC with a traction-dominated flow-boundary zone. Grain fabrics show increased shear and/or lower aggradation rates. Discontinuous beds imply a non-uniform current and clast-concentration zones support more subtle current unsteadiness compared to if clast-rich lenses were present¹. Normal and reverse grading indicates waning and waxing conditions¹.</p>	

<p>Cross-bedded lapilli-tuff with accretionary lapilli (xbLTacc)</p>	<p>Lithology: variable proportions of pumice and/or scoria lapilli, fine – medium lithic lapilli and whole and fragmented accretionary lapilli (acc) matrix-supported in a poorly sorted vitric tuff; lithic assemblage: fresh/weathered glassy, aphanitic lavas and/or tuffs. Structure: low- and high-angle cross-bedded (xb); rare lithic alignment; bedforms common; highly laterally discontinuous; 0.2 – 1 m thick. Lithification: poor. Stratigraphic occurrence: Buco Formation.</p>	<p>Deposition from a granular fluid-based PDC with a traction-dominated flow-boundary zone. Grain fabrics show increased shear and/or lower aggradation rates. Discontinuous beds imply a non-uniform current¹. Moisture levels high enough so that ash cores formed in upper part of current or cognimbrite plume that fall into current accrete layers of fine ash before depositing^{2,3}. Accretionary lapilli fragments indicate they were hard enough to fracture in a brittle way.</p>	 <p>25<75% matrix cross- bedding acc lap</p>
<p>Fines-poor massive lapilli-tuff (fpoormLT)</p>	<p>Lithology: abundant subrounded pumice and/or scoria lapilli, blocks and bombs with lithic clasts of similar sizes matrix-supported in a poorly sorted fine-medium lapilli-sized matrix; lithic assemblage: fresh/weathered glassy, aphanitic lavas and/or tuffs. Structure: massive (m); normal (n) and reverse (r) grading; may be laterally discontinuous; 0.05 – 2 m thick. Lithification: unlithified – indurated Stratigraphic occurrence: Antonio Carpio Units, Batangas Formation, Burol Formation, Pasong Formation and unnamed.</p>	<p>Deposited by concentrated, granular fluid-based PDCs with a predominantly end-member-type fluid escape-dominant flow-boundary zone as indicated by the lack of fines¹. Discontinuous beds and various grading patterns indicate current unsteadiness. Normal and reverse grading indicates waning and waxing conditions¹.</p>	 <p><25% matrix rounded pumice/ scoria</p>
<p>Fines-poor diffuse cross-bedded lapilli-tuff (fpoordxbLT)</p>	<p>Lithology: abundant subrounded pumice and/or scoria lapilli, blocks and bombs with lithic clasts of similar sizes matrix-supported in a poorly sorted fine-medium lapilli-sized matrix; lithic assemblage: fresh/weathered glassy, aphanitic lavas and/or tuffs. Structure: low- to high-angle diffuse cross-bedded (dxb) throughout; rarely normally (n) graded; may be lensoidal; 0.25 – 3 m thick. Lithification: unlithified – poorly lithified. Stratigraphic occurrence: Alitagtag Formation, Pasong Formation, Tagaytay Units and unnamed.</p>	<p>Deposited by concentrated, granular fluid-based PDCs with a fluid escape- to traction-dominant environment¹. Grading and lensoidal nature suggests unsteadiness in the current. Normal grading indicates waning conditions¹.</p>	 <p><25% matrix diffuse cross- bedding rounded pumice/ scoria</p>

Massive lithic breccia (mIBr)

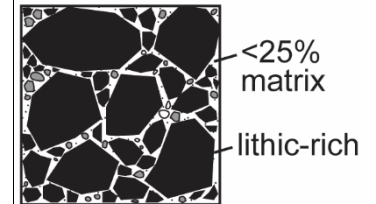
Lithology: lithic-rich; subordinate pumice and/or preferential dense, fluidal scoria lapilli, blocks and bombs, and abundant similarly-sized angular or subrounded lithic clasts matrix-supported in a poorly sorted lapilli-sized matrix; lithic assemblage: fresh/weathered glassy, aphanitic or porphyritic lavas and/or tuffs and hydrothermally altered clasts.

Structure: massive (m); rare reverse (r) grading; rare vertical changes in clast abundance; rare imbrication (i); may be laterally discontinuous; 0.15 – 2 m thick.

Lithification: unlithified – well lithified.

Stratigraphic occurrence: Pasong Formation, Tadalac Cave Formation and unnamed.

Lithic lag breccias, deposited in a similar way to mLT, the fluid escape-dominant flow-boundary zone enhancing fines elutriation. A decrease in current competence (e.g. at break in slope) caused dense clasts to preferentially deposit¹. Where deposits are discontinuous it implies current was non-uniform¹. Rare imbrication suggests a small granular shear component¹ and clast abundance changes reflect periods of unsteadiness². Normal and reverse grading indicates waning and waxing conditions¹.



Diffuse cross-bedded lithic breccia (dxblBr)

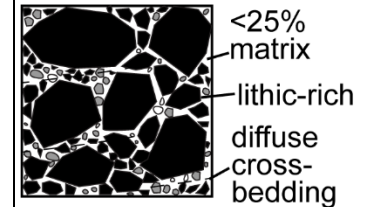
Lithology: lithic-rich; subordinate pumice and/or dense, fluidal scoria lapilli, blocks and bombs, and abundant similar sized angular or subrounded lithic clasts matrix-supported in a poorly sorted lapilli-sized matrix; lithic assemblage: fresh/weathered glassy, aphanitic or porphyritic lavas and/or tuffs and hydrothermally altered clasts.

Structure: diffuse cross-bedded (dx) throughout; rare normal (n) grading; may be laterally discontinuous; 0.3 – 1 m thick.

Lithification: unlithified – poorly lithified.

Stratigraphic occurrence: Indang Formation and Pasong Formation.

Lithic lag breccias, deposited in a similar way to mLT, the fluid escape-dominant flow-boundary zone enhancing fines elutriation. The diffuse cross-bedding implies current experienced periods of unsteadiness². A decrease in current competence (e.g. at break in slope) caused dense clasts to preferentially deposit¹. Where deposits are discontinuous it implies current was non-uniform¹. Normal grading indicates waning conditions¹.



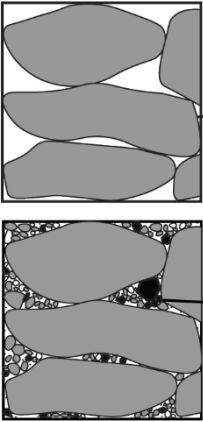
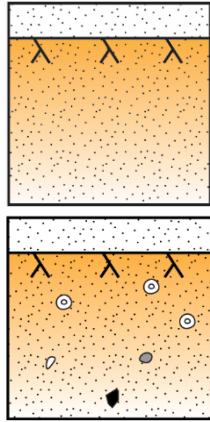
<p>Agglomerate (Ag)</p>	<p>Lithology: dominant block and bomb-sized (spatter-type) scoria, framework- or matrix-supported; matrix (if present) is coarse ash and lapilli-sized scoria with subordinate, smaller lithic coarse ash, lapilli and blocks; lithic assemblage: fresh/weathered glassy, aphanitic or porphyritic lava, tuffs, hydrothermally altered clasts.</p> <p>Structure: massive (m); 1 – 7 m thick.</p> <p>Lithification: welded or non-welded.</p> <p>Stratigraphic occurrence: Pasong Formation and unnamed.</p>	<p>Deposited in a similar way to mLT with a fluid escape-dominant flow-boundary zone enhancing fines elutriation. A decrease in current competence (e.g. at break in slope) caused dense clasts to preferentially deposit¹. Matrix presence and vertical and/or lateral changes into dxbLT or mLT support flow origin^{9,10}. Where there is no matrix component, limited exposure, and limited/no lithic material a fall origin cannot be ruled out if deposit is close enough to a potential source.</p>	 <p>(spatter-type) scoria</p> <p>matrix</p>
<p>Palaeosol (ps)</p>	<p>Lithology: rare altered lapilli-sized pumice and/or whole and fragmented accretionary lapilli (acc) in a fine-grained, poorly sorted orange, brown or beige tuff matrix.</p> <p>Structure: massive (m), calcrete structures present in some palaeosols make them look parallel-bedded (//); intense orange coloured palaeosols have drying cracks; light orange palaeosols have a powder-like texture; gradational lower contact; sharp upper contact; may be laterally discontinuous; 0.02 – 5.0 m thick.</p> <p>Lithification: moderately lithified – well lithified.</p> <p>Stratigraphic occurrence: Alitagtag Formation, Antonio Carpio Units, Balagbag Formation, Batangas Formation, Buco Formation, Burol formation, Calumpang Formation, Indang Formation, Pasong Formation, Sampaga Formation, Tagaytay Units, unnamed.</p>	<p>Indicates a period of non-deposition, which usually coincides with a break in volcanic activity. Laterally discontinuous, thin soils represent shorter breaks compared to thicker, orange soils (Chapter 1).</p>	

Table 3.1 (p. 91-99): descriptions and interpretations of lithofacies identified around Taal Caldera Volcano. A key for the cartoon representations is presented in the 'massive tuff' row of the table. Flow-boundary zones described in the interpretation referenced in Fig. 3.3. References cited in table: ¹Branney and Kokelaar, 2002; ²Brown and Branney, 2004; ³Scarpati et al., 2020; ⁴Mueller et al., 2018; ⁵Van Eaton and Wilson, 2013; ⁶Brown and Branney, 2013; ⁷Brown et al., 2010; ⁸Rosi, 1992; ⁹Druitt et al., 1989; ¹⁰Mellors and Sparks, 1991.

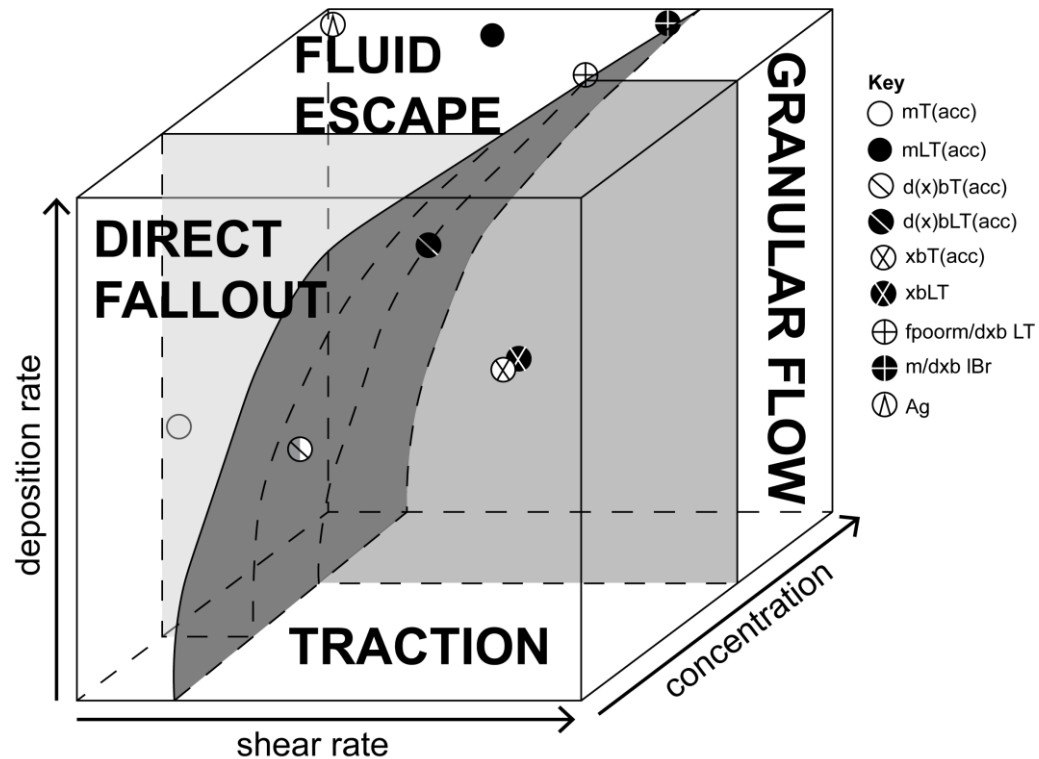


Fig. 3.3: The impacts of changing deposition rate, shear rate and concentration on flow-boundary zones (Branney and Kokelaar, 2002). Different facies identified in this study have been placed in an approximate location on the diagram.

3.3.1 Ash aggregates and vesiculated tuff

Ash aggregation can occur via agglomeration (i.e. particle adhesion) and/or accretion (i.e. small grains progressively adhere to a larger grain layer-by-layer; Brown et al., 2010); evidence for both these mechanisms is seen at Taal in the various ash aggregates found in Taal's prehistoric deposits. Juvenile pumice and scoria and very rarely lithic clasts, in (lapilli-) tuffs are frequently covered in a whole or partial ash coat (e.g. Allen, 2005). These clasts are referred to as cored pellets or coated clasts respectively (Table 3.2) and are formed in pyroclastic density currents via accretion. They are rare in the older Tadalac Cave and Alitagtag formations, but the norm in the Pasong, Burol, Balagbag and Buco formations.

In the Buco and Pasong formations, cored pellets and coated clasts occur together with accretionary lapilli, unlike the ignimbrites on Tenerife where accretionary lapilli occur together with cored accretionary lapilli and coated pellets (Brown et al., 2010). Ash coatings on clasts are usually a few millimetres thick, but can be <3 cm on smaller clasts, while they can be absent on larger clasts. Ash coats are usually well lithified and can hide the true shape of clasts they completely encompass, often making clasts appear more rounded than they are. It is likely that this accreted ash rim protected the smaller juvenile clasts during transport, reducing abrasion and therefore better preserving their original, relatively angular shape.

In the Pasong Formation's scoria agglomerates and the Indang Formation's spatter-rich indurated lapilli-tuffs, fluidal bombs can contain ash coats up to 3 cm thick, which can include fine lapilli material (Fig. 3.4A). This ash coat is not thought to form via accretion, but sintering because of the larger grain sizes found in the ash coat. Sintering of matrix to hot juvenile bombs has even been hypothesised to speed up deposition from PDCs because matrix material deposits prematurely if it sinters to hot juvenile clasts (Trigila and Walker, 1980). Although it could be argued that this matrix coat has become lithified due to diagenesis in the Indang ignimbrite, this is unlikely to be the case for the scoria

agglomerates of the Pasong Formation because the matrix not near the scoria bombs is unlithified. If matrix had become attached to scoria bombs due to diagenesis, it seems unlikely that only matrix next to scoria bombs would lithify.

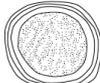
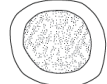
Type of Aggregate	Typical Size	General Description	Interpretation
 <p>particle cluster</p>	10 μ m – 10 cm	irregular shape, fragile so often disintegrate upon deposition but may be cemented together; loosely-packed together ^{1,2} ; not identified at Taal	dry fall conditions (>5 wt.% liquid) ²
 <p>ash pellet</p>	<1 – 20 mm	very weakly developed or complete lack of internal structure ¹ ; may have thin outer film of fine ash; deposit usually clast-supported ²	grows in saturated conditions (15 – 20 wt.% liquid) ² , fall deposit ¹ (either co-ignimbrite or primary)
 <p>coalesced ash pellets</p>	< 5 mm (individual pellet)	dense, vesicular ash beds with internally massive aggregates that have partially or completed coalesced ²	as above, but plastically deformed upon deposition ²
 <p>coated clast</p>	0.05 – 100 mm	a lithic, pumice or crystal core is partially covered in fine ash forming a fragile aggregate; ash particles likely fall off during deposition ¹	clast accretes partial layer of fine ash within PDC
 <p>accretionary lapilli (Lacc + Ufacc)</p>	2 – 40 mm	fine ash or matrix core surrounded by several concentric laminations of (ultra)fine ash; laminations may crosscut each other; individual brittle disintegration when deposited ^{1,2}	ash pellets accrete one or multiple rims of material in sub-saturated conditions (<10 – 15 wt.% liquid) ²
 <p>cored accretionary lapilli</p>	5 – 25 mm	a lithic or pumice core surrounded by several concentric laminations of fine ash; brittle disintegration when deposited ¹	as above, but core is made up of a clast ²
 <p>cored pellet</p>	2 – 25 mm	a pumice or lithic core covered in one lamination of fine ash; quite fragile ¹	as above, but only one rim is accreted
 <p>coated ash pellet</p>	2 – 6 mm	ash core covered in one lamination of fine ash; quite fragile ¹	as above, but core is an ash pellet

Table 3.2: Ash aggregate types, typical sizes, descriptions and possible interpretations, based on ¹Brown et al. (2010, 2012) and ²Van Eaton and Wilson (2013) and this study. Accretionary lapilli include both layered accretionary lapilli (Lacc) and ultrafine rim-type accretionary lapilli (Ufacc; Van Eaton and Wilson, 2013).

Some pyroclastic deposits at Taal contain accretionary lapilli and (coated) ash pellets (Table 3.2). Accretionary lapilli are most common and can appear in the thick ignimbrites associated with the Pasong and Buco formations, as well as in thinner tuffs. They range in size from 3 mm to 4 cm and are (sub)rounded or elongate in shape. They are lithified and difficult to break except for those in an almost clast-supported bed at the top of the Indang Formation (Fig. 3.4B).

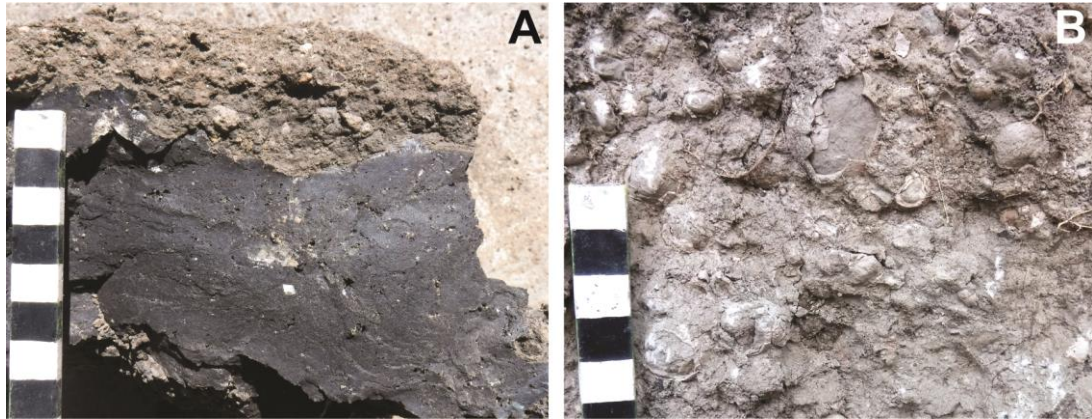


Fig. 3.4: (A) Thick ash- and lapilli-sized matrix rim attached (likely sintered) to a fluidal, juvenile bomb in a scoria agglomerate (Ag) of the Pasong Formation. (B) Fragile accretionary lapilli within the almost clast-supported bed (mTacc) at the top of the Indang Formation.

In thin section most accretionary lapilli have an ash core (Fig. 3.5C), although where the core ends and accreted ash layers begin can be difficult to tell if the grain size of the core is similar to the accreted laminae (Fig. 3.5A, D).

Surprisingly, ash pellets with relatively little fine ash are more commonly found in matrix-rich deposits (Fig. 3.5C) where they and accretionary lapilli represent the only clast types. These ash pellets also contain relatively large pumices, which could be seen as cores, but ash does not concentrically accrete around them (Fig. 3.5C). A more moisture-rich environment may allow coarser ash to stick together, while the number of rims accreted around a core depends on whether aggregation conditions change rapidly or not, and how long an aggregate remains in the ash-rich accretion environment (Mueller et al., 2018).

Accretionary lapilli (Table 3.2), not ash pellets, are identified in relatively matrix-poor lapilli-tuffs. Accretionary lapilli record different ash sizes in concentric layers, which may appear lensoidal (Fig. 3.5A); there is no preferential appearance of fine or coarse ash closer or farther from the accretionary lapilli

core in these examples. Clast and vesicle alignment within the ash rims can be used as evidence of concentric accretion, which is otherwise not always obvious in coarser ash laminae (Fig. 3.5B). These vesicles are hypothesised to form either through gas entrapment during their formation, from gas released by included juvenile material, and/or through the re-vaporisation of binding fluids (Lorenz, 1974; Sheridan and Wohletz, 1983B; Schumacher and Schmincke, 1991). Those aggregates with more vesicles were likely hotter (e.g. Fig. 3.5B), making it more likely that binding fluids would re-vaporise (Schumacher and Schmincke, 1991).

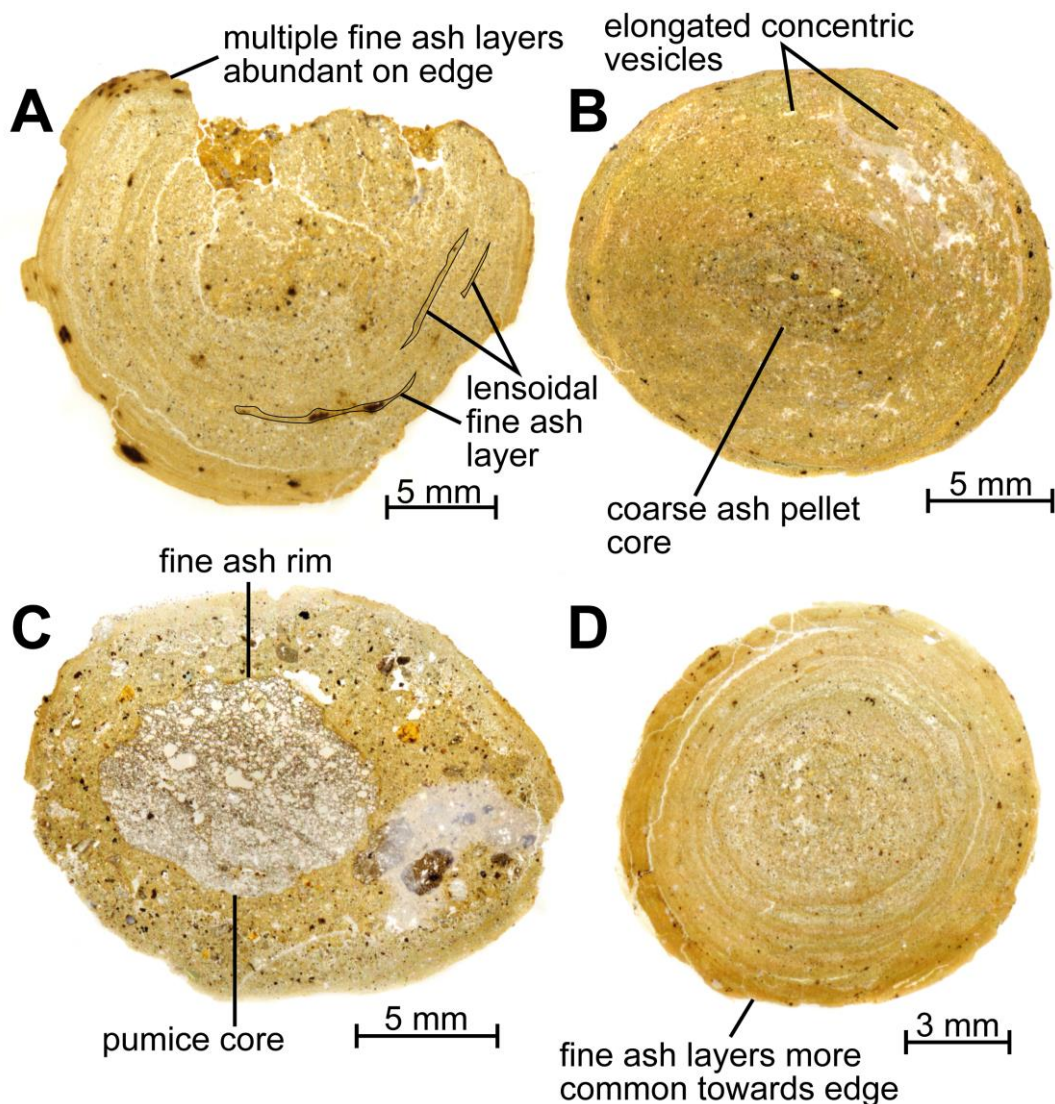


Fig. 3.5: Photos of ash aggregates scanned on a flatbed scanner. **(A)** An accretionary lapillus from a massive lapilli-tuff with lensoidal fine ash layers. **(B)** An accretionary lapillus from a massive lapilli-tuff with a coarse ash pellet core and elongate concentric vesicles. **(C)** A cored pellet from a massive tuff with a pumice core and fine ash rim, surrounded by coarser ash. **(D)** An accretionary lapillus from a massive lapilli-tuff with multiple concentric ash rims with fine ash rims becoming more abundant towards the edge of the accretionary lapillus.

Subrounded to rounded ash pellets are also found in clast-supported beds (Tpel), most frequently within unnamed deposits. They represent either openwork ash pellet layers, particle clusters or coalesced ash pellets (e.g. Brown et al., 2010; Fig. 3.6A, B). Individual ash pellets in these beds are usually a few mms in diameter and can transition into vesiculated ash beds with subrounded – elongate vesicles (<2 mm in size; Fig. 3.6C, D). The large range of ash aggregates at Taal, similar to the range seen in the Oruanui deposits, New Zealand (Van Eaton and Wilson, 2013), indicates a complex involvement of moisture in eruptions and during deposition, with conditions ranging from sub-saturated (e.g. accretionary lapilli; Fig. 3.4B) to saturated (e.g. amalgamated pellets; Fig. 3.6).

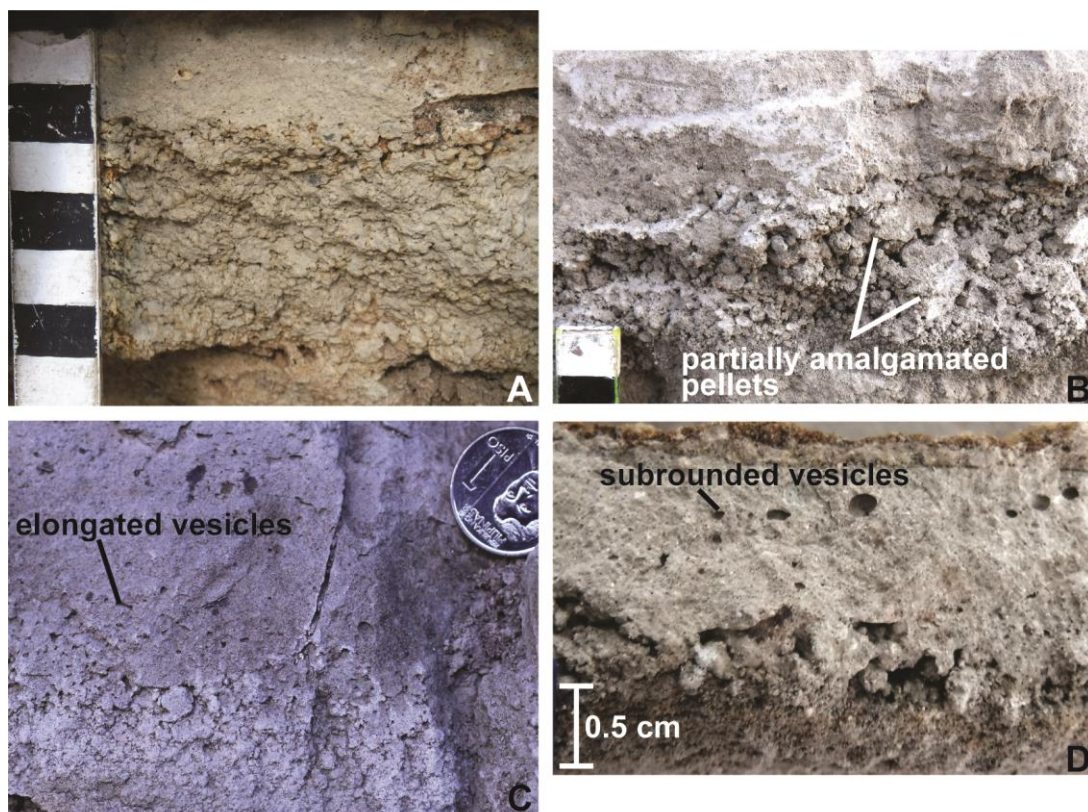


Fig. 3.6: (A) A layer of ash pellet tuff (Tpel) overlain by a massive tuff (mT) in the Pasong Formation. (B) A layer of ash pellet tuff (Tpel) with amalgamated pellets overlain by a massive tuff (mT) in the Balagbag Formation. (C) A layer of ash pellet tuff (Tpel) overlain by a vesiculated tuff (Tves) with elongated vesicles in an unnamed deposit. (D) A layer of ash pellet tuff (Tpel) overlain by a vesiculated tuff (Tves) with subrounded vesicles in an unknown deposit.

3.3.2 Fluidal juvenile bomb-bearing ignimbrites

Fluidal juvenile bombs (e.g. Mellors and Sparks, 1991) are black, dense and poorly vesicular scoria bombs and lapilli and are the main component in scoria agglomerates and can also occur sparsely within lithic breccias and (fines-poor) lapilli-tuffs (Table 3.1; Fig. 3.7). A fluidal juvenile bomb-bearing ignimbrite first appears in the Indang Formation (Fig. 3.7A); the Pasong Formation comprises multiple fluidal juvenile bomb-bearing ignimbrites and a spatter agglomerate (Fig. 3.7B, D); the Buco Formation consists of a fluidal juvenile bomb-bearing ignimbrite and there are several scoria agglomerates that remain unclassified.

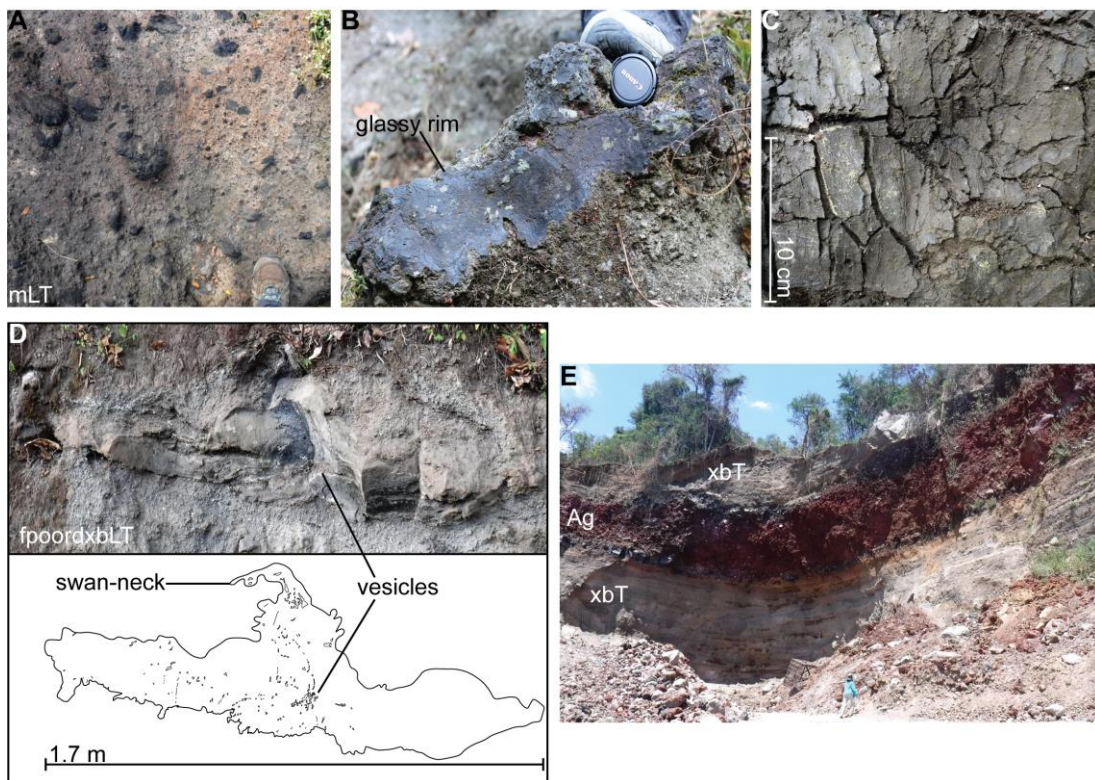


Fig. 3.7: (A) Fluidal juvenile bomb-rich massive lapilli-tuff (mLT) of the Indang Formation. (B) A fluidal juvenile bomb within a mLT with a glassy outer rim in the Pasong Formation. (C) Breadcrust texture on the outside of a fluidal juvenile bomb from an unknown agglomerate. (D) Fluidal juvenile bomb within a fines-poor diffuse cross-bedded lapilli-tuff (fpoordxbLT) of the Pasong Formation showing a swan-neck structure and vesicles, which are most abundant near the centre of the clast. (E) An unknown agglomerate with minimal lithic clasts near the northern shore of Lake Taal has an oxidised red colour in its centre.

Individual fluidal juvenile bombs are up to 2 m in size and may have a red, oxidised appearance (Fig. 3.7E) similar to the spatter agglomerate and the Siwi ignimbrite from the Yenkahe Caldera, Vanuatu (Firth et al., 2015). In both lapilli-

tuffs and agglomerates, fluidal juvenile bombs show internal shear structures in the form of stretched and aligned vesicles, which tend to appear within the outer rims of clasts as also observed in the Upper Scoria 1C member from Santorini, Greece (Mellors and Sparks, 1991) and in lithic breccias and ignimbrites from the Villa Senni caldera-forming eruption from Colli Albani, Italy (Vinkler et al., 2012). At Taal, vesicles in fluidal juvenile bombs may be most abundant in the outer rim (small vesicles) or core (larger vesicles; Fig. 3.7D), or they create bands of high and low vesicularity in the clast. Vesicles are absent from the outer rim if it has a glassy texture (e.g. Pasong and Buco formations; Fig. 3.7B), similar to fluidal juvenile bombs found in the lithic breccias of the Campanian deposits, Italy (Rosi et al., 1996). Glassy outer rims on fluidal juvenile bombs within ignimbrites of Summer Coon volcano, USA, were hypothesised to infer quenching with colder non-juvenile and coarse ash juvenile components within pyroclastic density currents (Valentine et al., 2000), but quenching was hypothesised to have occurred during interaction of hot juvenile material with water during the Pavey Ark ignimbrite eruption, Scafell caldera, UK (Kokelaar et al., 2007).

Fluidal juvenile bombs from Taal Caldera Volcano have variously developed breadcrust or cauliform textures (e.g. Branney and Kokelaar, 2002; Fig. 3.7C) like in the Upper Scoria 1 member from Santorini, Greece (Mellors and Sparks, 1991), the lithic breccias and ignimbrites from the Villa Senni eruption, Colli Albani (Vinkler et al., 2012) and the Adeje Formation ignimbrite in Tenerife, Spain (Dávilla-Harris et al., 2013). In the Indang and Pasong formations, individual fractures produced by breadcrust textures may be infilled with matrix material. Breadcrust textures form when the outer rim of a clast cools more quickly compared to the interior, which continues degassing and expanding, cracking the cooled, brittle rim (Fisher and Schmincke, 1984). Although the outer rim cooled quickly, clasts likely remained hot enough to sinter matrix material to the edges of the clasts in the Indang and Pasong formations (Section 3.3.1), and to produce clasts with fragile shapes like swan-necks (e.g. Kokelaar et al., 2007; Fig. 3.7D).

Lithic clasts (igneous, sedimentary) included within fluidal juvenile bombs are often considered a characteristic feature (e.g. Branney and Kokelaar, 2002; Dávilla-Harris et al., 2013) and are recorded at Taal (Fig. 3.8). Although the inclusion of lithic clasts may provide evidence that fluidal juvenile bombs were hot and fluidal during transport, lithic clasts could also have been included at the source when all erupting magma was still fluidal. At Taal, evidence for the latter is seen where lithic inclusions are found in poorly vesicular scoria in ignimbrites without fluidal juvenile bombs (such as the Burol and Balagbag formations). Lithic inclusions are often more abundant in phreatomagmatic deposits because of their highly explosive interaction with country rock (Fisher and Schmincke, 1984). Therefore lithic inclusions, both in fluidal juvenile bombs and other juvenile clasts, can provide evidence of a hydrovolcanic eruption (Mellors and Sparks, 1991), and thus supports the idea that fluidal juvenile bombs are associated with flooded caldera volcanoes (Branney and Kokelaar, 2002).

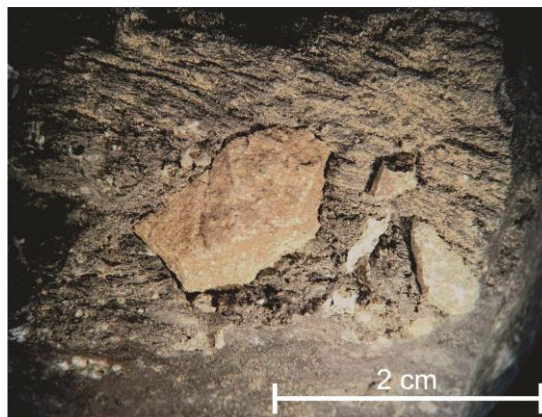


Fig. 3.8: Lithic clasts (weathered lava) included in a fluidal juvenile bomb from a massive lapilli-tuff of the Buco Formation.

3.3.3 Bedforms

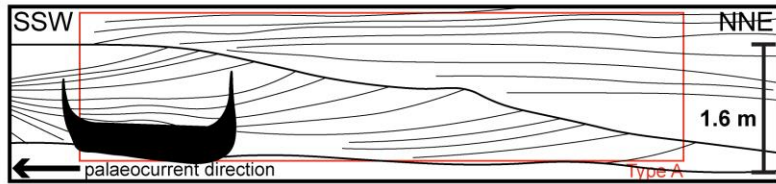
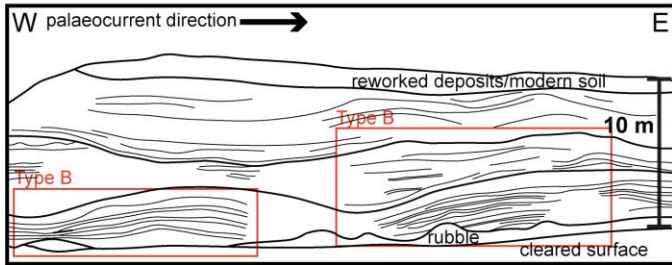
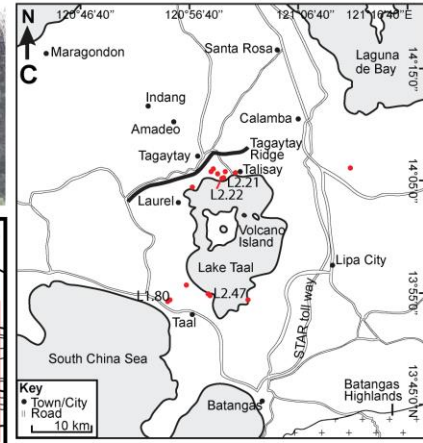
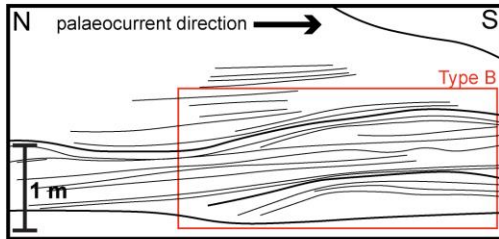
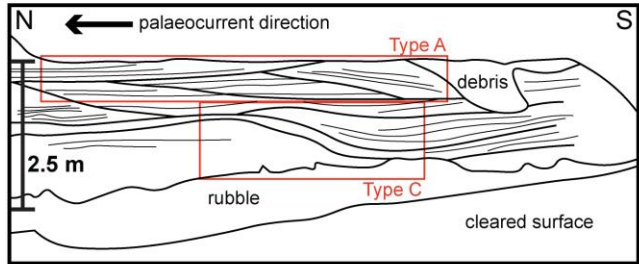
Dune-bedforms (descriptive term only: single sedimentary structures formed by meter-scale bed undulations; includes both antidunes and chute-and-pool structures; Douillet, 2021), associated with cross-bedded facies, occur in the Pasong and Buco formations (Fig. 3.9). Contacts between stratasesets as well as individual strata can be erosive (Fig. 3.9). Dune-bedforms at Taal share many of the reference characteristics of dune-bedforms elsewhere, which include:

backsets (i.e. stoss-side stratasets), stoss-side truncations, steeper stoss-sides, fully-aggrading structures (i.e. structures that demonstrate continuous deposition from stoss to lee side), and vertical truncations covered with a massive unit (Douillet, 2021 and references therein).

Where little cross-cutting erosion has occurred, Type B (Fig. 3.10; Douillet, 2021), relatively symmetrical, fully-aggrading dune-bedforms are identified in the Buco Formation (Fig. 3.9D). Where the stoss-side is both steeper and thicker, PDCs may have been moist since moisture is thought to encourage preservation of the stoss-side beds (Waters and Fisher, 1971; Moorhouse and White, 2016). Steep, thick stoss-sides are a common feature of some historical phreatic/Taalial Taal deposits, namely the 1965 'pyroclastic surge' deposits found on Volcano Island (Moore, 1967; Waters and Fisher, 1971). Moist PDCs also commonly grade from planar stratification to dunes (Moorhouse and White, 2016), as also previously identified in the Buco Formation (Geronimo, 1988), which may be described as a low-angle structure from type A, with some subtle type C truncations (Figs. 3.9B; 3.10; Douillet, 2021).

More end-member type A and type C structures are also found in the Buco Formation at meter and centimetre scales (Figs. 3.9; 3.10). In previous work, however, the bedforms in the Buco Formation were mostly interpreted as antidunes (Geronimo, 1988). Although type A structures may be interpreted as antidunes (Douillet, 2021), other dune-bedforms are here interpreted as chute-and-pool structures (Fig. 3.9). Chute-and-pool structures typically suggest an upper flow regime (Waters and Fisher, 1971; Schmincke et al., 1973; Cole, 1991), however, if PDCs are travelling in the supercritical regime (i.e. PDC stores more kinetic than potential energy), low-energy, waning PDC conditions can also form chute-and-pool structures (Douillet, 2021).

Fig. 3.9 (p. 110): Buco Formation bedforms **(A)** Type C dune-bedform (Douillet, 2021) at base of deposit with a steeper southern side. The lateral inconsistency of bedform laminae with low-angle, crosscutting type A structures (Douillet et al., 2021) near the top shows the erosive nature of PDCs. **(B)** Subtle type B structures (Douillet et al., 2021). **(C)** Map with dune-bedform localities. Photos from L2.22 [14° 05.007'N 120°59.548'E], L1.80 [13° 53.900' N 120° 55.190' E], L2.21 [14° 04.977'N 120°59.610'E], and L2.47 [13° 54.588'N 120°58.901'E]. **(D)** Large-scale dune-bedforms are a fairly symmetrical example of type B structures (Douillet, 2021) with a slightly steeper eastern side. **(E)** Stratasets with different component abundances crosscutting each other, forming large-scale type A structures (Douillet, 2021).



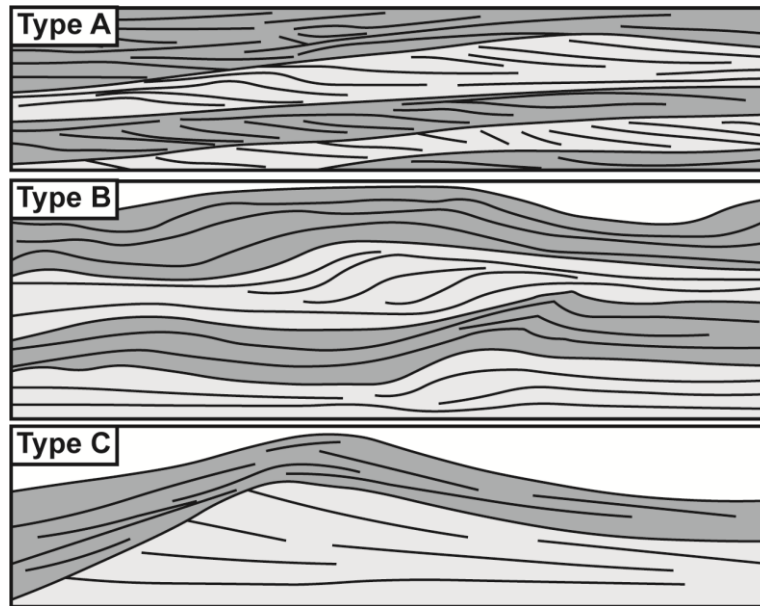


Fig. 3.10: Schematics adapted from Douillet (2021) demonstrating Types A, B and C structures. Flow directions from left to right.

Stoss sides of dune-bedforms are often steeper and more likely to be truncated than lee sides (Fig. 3.9; Belousov and Belousova, 2001; Douillet, 2021). These features allow more confident identification of the stoss side of dune-bedforms in the Taal deposits, and can give an initial, tentative suggestion of a possible Buco eruption source. Previous work placed the Buco eruption source to the east of Volcano Island (Geronimo, 1988), which this study agrees with. Additional evidence of a lack of ballistic projectiles in the bedform laminae at Taal, usually a common feature of these kinds of cross-bedded deposits close to source (e.g. Sohn and Chough, 1989; Pardo et al., 2009), supports the placement of the Buco eruption source several kilometres away from the modern lakeshore (e.g. Taddeucci et al., 2017 and references therein).

The PDCs that deposited the Buco dune-bedforms were more likely to be fully dilute (e.g. Schmincke et al., 1973; Wohletz and Sheridan, 1979; Allen, 1982; Walker, 1984; Cas and Wright, 1987; Cole, 1991; Douillet et al., 2013), although recent experimental work has shown that denser granular-fluid based flows are also capable of forming bedforms (Smith et al., 2020). Taal dune-bedforms are generally matrix-rich, however, and do not laterally grade into massive lapilli-tuffs, which supports the dilute nature of their depositing PDCs (e.g. Branney and Kokelaar, 2002). The Buco Formation dune-bedforms were deposited by

multiple PDCs, each strataset perhaps representing the passing of one pyroclastic density current (Schmincke et al., 1973). Evidence for this includes significant changes in the componentry of stratasets, for example, along the southern shore of Lake Taal one strataset contains abundant black pumice, while the strataset above consists mostly of fine ash and accretionary lapilli-rich layers (Fig. 3.9E). However, such a significant change in componentry is rare and without any field exposures of flow-unit boundaries (e.g. ash pellet tuffs) this hypothesis is difficult to prove.

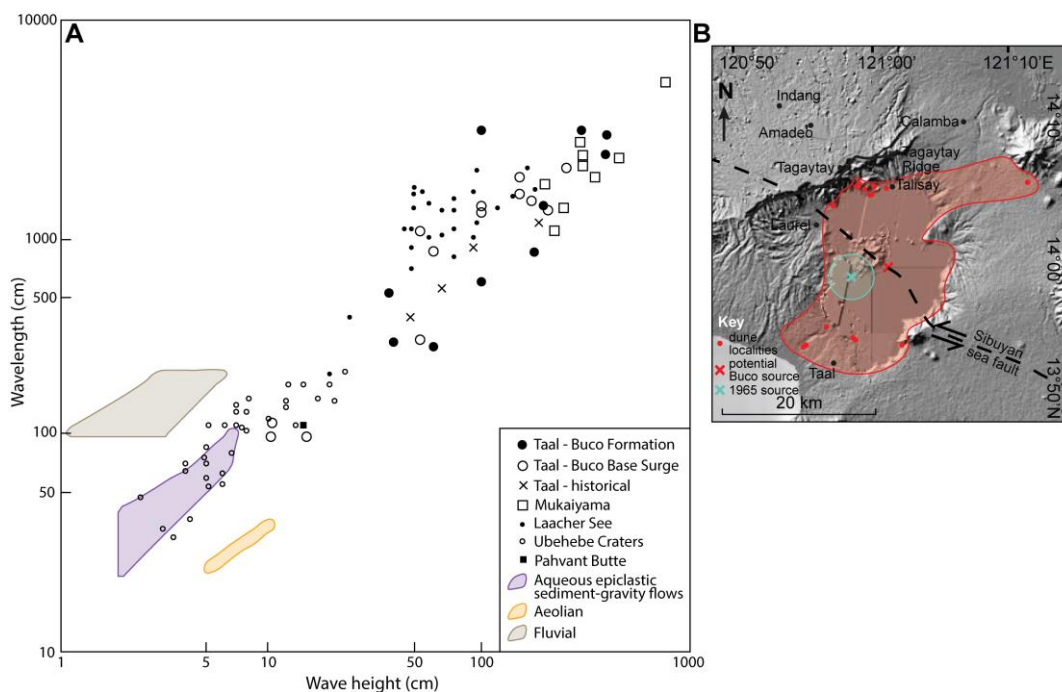


Fig. 3.11: (A) Taal's Buco Formation data from this study compared with Taal's 'Buco Base Surge' (Geronimo, 1988); Mukaiyama (Yokoyama and Tokunaga, 1978); subaerial moist PDCs: Taal 1965, 1966 historical deposits (Waters and Fisher, 1971), Laacher See (Schmincke et al., 1973), Ubehebe Craters (Crowe and Fisher, 1973); aqueous sediment-gravity flow: Pahvant Butte (White, 1996); subaerial dry PDCs (Sheridan and Updike, 1975; Cole, 1991); aqueous epiclastic sediment-gravity flows (Walker, 1967; Skipper, 1971; Prave and Duke, 1990; Mulder et al., 2009); aeolian flow deposits (Hooper et al., 2012); fluvial flow deposits (Middleton, 1965; Rust and Gibling, 1990; Fielding, 2006). **(B)** Minimal area covered by bedforms from Taal's Buco Formation compared with area covered by bedforms from 1965 eruption (Moore et al., 1966).

Strataset formation is favoured by dry PDCs (Walker, 1984; Dellino et al., 2004; Sohn and Park, 2005), although the structural characteristics of dune-bedforms are argued by some to be the same as in moist PDC deposits (Douillet, 2021). PDCs at Taal are unlikely to have been moisture-saturated, however, because no sediment slumping or dewatering structures are visible (Dellino et al., 1990).

Other studies have argued that moisture-rich currents produce wider variations in dune wavelength (Moorhouse and White, 2016), however, most of the variation in dune wavelength seen at Taal is lateral and most likely reflects a waning current (Waters and Fisher, 1971; Lajoie et al., 1992; Druitt, 1992; Brand and Clarke, 2012; Douillet, 2021). Dune-bedforms measured in the Buco Formation cover a range of dimensions, but generally plot towards the larger end of the spectrum when compared to other dune-bedform-producing eruptions. The largest recorded dune-bedforms are similar to those from the Mukaiyama eruption, Japan, which is recorded as a VEI 4 eruption (Fig. 3.11; GVP, 2021A). Although this VEI may suggest the Buco Formation was of a similar size to the 1965 eruption at Taal, also a VEI 4 (Delos Reyes et al., 2018), the Buco Formation's maximum dune-bedform size is larger and they have a wider spatial distribution compared to dune-bedforms from 1965 (Fig. 3.11; Moore et al., 1966).

3.3.4 Clast textures

Preliminary clast textural data (based on 1 to 3 samples per named formation) suggests that the youngest named formation, the Buco Formation, contains ~90% blocky – subrounded, non-vesicular grains (Fig. 3.12A), which is much more than older formations (the Pasong, Tadalac Cave and Alitagtag formations). The Pasong Formation contains only ~25% non-vesicular grains, while both the Tadalac Cave and Alitagtag formations contain ~50% non-vesicular grains. Where grains are vesicular, individual vesicles are on average smaller in the Pasong Formation compared to the Tadalac Cave and Alitagtag formations as indicated by the dominance of micropumice (Fig. 3.12B) over bubble wall shards (Fig. 3.12C) in the Pasong Formation. Where micropumice is visible in the Tadalac Cave and Alitagtag formations, however, it tends to show elongated vesicles (Fig. 3.12D) rather than the more rounded vesicles seen in the Pasong Formation. Since all formations do contain vesicular grains, magma exsolution occurred during all eruptions. Vesicular grains are rarer in the Buco Formation and individual vesicles are smaller in the Pasong formation, therefore magma fragmentation may have been initiated by water interacting with magma

(e.g. Rausch et al., 2015). However, the current limited clast textures data does not provide sufficient evidence on its own to confirm or deny this hypothesis.

Grains in the Alitagtag sample have limited adhering particles, suggesting limited moisture presence during particle transport (Zimanowski et al., 2015), while adhering particles are common in the Pasong and Tadalac Cave samples and very abundant in the Buco Formation (~95% of grains in the Buco Formation have adhering particles; Fig. 3.12A). Particles from the Buco and Pasong formations also show hydration skins or overgrowth films with abundant cracks and pitting (Fig. 3.12E), supporting the availability of moisture during transportation; the Buco Formation also contains particles with moss-like patterns (Fig. 3.12F), providing rare evidence of direct interaction between water and magma at source during eruption (Austin-Erickson et al., 2008; Zimanowski et al., 2015). Overall, therefore, the Buco Formation shows more evidence of water interacting with magma during eruption (i.e. moss-like patterns) and during deposition (i.e. adhering particles, hydration skins, pitting) compared to the older Pasong, Tadalac Cave and Alitagtag formations.

Moss-like patterns are also common in two samples from two different beds (each representing an eruption-unit) in the Tagaytay Units, which are dominated by non-vesicular grains that also show hydration skins and abundant adhesion, suggesting magma fragmentation may have been driven by water interacting with magma at the source (e.g. Rausch et al., 2015) and that water influenced deposition. A different sample from a separate bed (representing an eruption-unit) in the Tagaytay Units, however, is made up of almost exclusively vesicular grains and lacks any hydration skins or adhering particles, suggesting this eruption was likely driven by magma exsolution and experienced minimal water interaction during deposition. The Tagaytay Units represent a series of smaller-scale eruptions (Chapter 2), therefore the varying particle morphologies between different eruption-units suggests that Taal Caldera Volcano experiences varying extents of magma – water interaction during eruption and deposition for smaller-scale eruptions as well as large, ignimbrite-forming eruptions like the Pasong Formation.

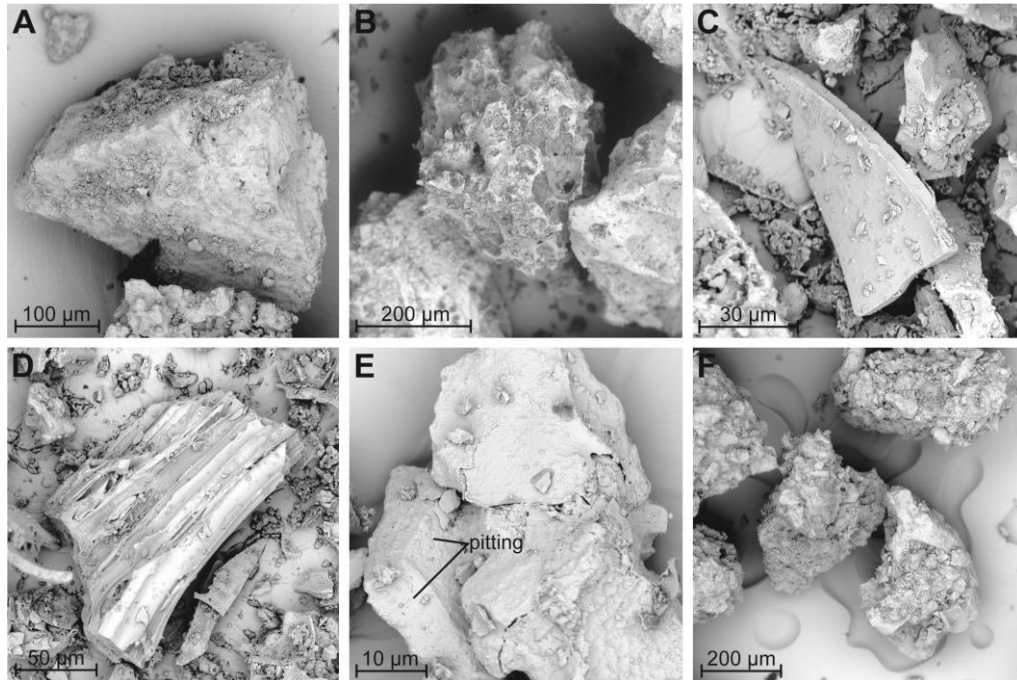
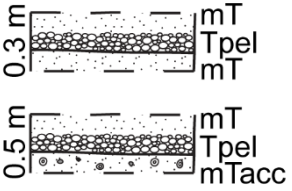


Fig. 3.12: (A) A blocky grain with adhering grains from the Buco Formation. (B) Micropumice with rounded vesicles in the Pasong Formation. (C) An ash shard from the Alitagtag Formation, similar to those seen in the Pasong Formation. (D) Tubular pumice from the Alitagtag Formation. (E) Hydration skin with cracks and pitting in the Buco Formation. (F) Moss-like clast in the Buco Formation.

3.4 Vertical lithofacies associations at Taal Caldera Volcano

Vertical lithofacies associations were first investigated qualitatively by placing all field logs next to each other and picking out the most common vertical facies associations. For this purpose, all logs were used regardless of whether they could be linked to a named formation in the stratigraphy to get the best overview of the types of vertical facies transitions produced by eruptions from Taal Caldera Volcano. These vertical lithofacies associations are described and interpreted in a facies associations table (Table 3.3).

		Units (82%), with less significant appearances in the Antonio Carpio Units (6%) and unknown deposits (5%), and the Alitagtag (<1%), Balagbag (1%), Buco (1%), Calumpang (2%) and Pasong (2%) formations.	depositional behaviour, or eruption columns experiencing multiple phases of ash deposition.	
Diffuse cross-bedding linked to massive beds (dxbm)	dxblT, mLT, dxblTacc, mLTacc	dxblT(acc) appears above, below, or interbedded with mLT(acc). 58% of occurrences show mLT(acc) transitioning into dxblT(acc), with 42% being the other way around. These transitions are almost exclusively gradational and they are seen more than once at 50% of localities. Diffuse cross-bedded lapilli-tuff facies are rarely seen without massive lapilli-tuff facies. They are most common in the Buco Formation (34%), followed by unknown deposits (29%), the Pasong Formation (24%), and the Buroi (9%) and Calumpang (3%) formations.	This facies association represents fluctuations between a fluid escape-dominated (massive facies) and more traction-dominated flow-boundary zone (diffuse cross-bedded facies). The fact that dxblT(acc) are rarely seen without mLT(acc) suggests that PDCs are unlikely to sustain a single flow-boundary zone for a prolonged period of time.	<p>A vertical sequence of facies with thicknesses indicated on the left: 2 m mLTacc, 1 m dxblTacc, 2 m mLT, 1 m dxblT diffuse cross-bedding, and 2 m mLT. The diagram shows a transition from massive facies (mLTacc) to diffuse cross-bedded facies (dxblTacc) and back to massive facies (mLT).</p>
Interbedding of massive and cross-bedded non and accretionary lapilli-	mT, mTacc, xbT, xbTacc, mLT, mLTacc, xbLT, xbLTacc	mT and mTacc are often interbedded, or they are interbedded with themselves. The same association exists for the cross-bedded equivalent facies. Occasionally the coarser versions of these facies also appear in the sequence. On 50% of occasions	This association represents fluctuations between accretionary lapilli-forming conditions and non-accretionary lapilli-forming conditions and/or preservation potential. These could include changes in	<p>A vertical sequence of facies with thicknesses indicated on the left: 0.2 m mT, 1 m mLTacc, 0.5 m mTacc, 0.6 m mLT, 0.5 m mTacc, and 0.2 m mT. The diagram shows alternating layers of massive facies (mT, mTacc) and cross-bedded facies (mLT, mLTacc).</p>

bearing facies (nac)		<p>non-accretionary lapilli-bearing facies transition into accretionary lapilli-bearing facies, while 32% of the time the relationship is reversed. Only 12% of occurrences show an accretionary lapilli-bearing facies changing into another accretionary lapilli-bearing facies, while 6% of the time the equivalent relationship is seen for non-accretionary lapilli-bearing facies. These transitions are mostly gradational when massive facies are involved, but are more likely to be sharp for cross-bedded facies. 29% of times this association is found in the Buco Formation; unknown deposits, the Balagbag Formation and the Antonio Carpio Units account for 28%, 19% and 15% respectively. Lower occurrences are found in the BuroI, Calumpang, Pasong and Sampaga formations.</p>	<p>moisture (Brown et al., 2012), or a reduction in PDC concentration (i.e. less large clasts) that may otherwise encourage accretionary lapilli break-up (Mueller et al., 2018). Overtime conditions in the PDC become more favourable to accretionary lapilli formation and/or preservation.</p>	
Ash pellet tuffs mainly associated with tuffs (pt)	Tpel, mT, mTacc, mLT, mLTacc, ps, Tves, dxBT, fpoormL	<p>mT overlies Tpel 59% of the time and underlies Tpel 39% of the time. mTacc is the second most common over- and underlying facies, with 27% and 25% respectively. Palaeosols underlie Tpel 14% of the time; while dxBT and mLTacc underlie Tpel 7% of</p>	<p>Pellet-bearing tuffs are most likely deposited from co-ignimbrite plumes once a PDC has passed. Where mT(acc) underlies Tpel, it could represent the last, dilute portion of a passing PDC. If mT overlies Tpel it</p>	 <p>0.3 m mT Tpel mT</p> <p>0.5 m mT Tpel mTacc</p>

the time, and fpoormL and mLT 4%. Overlying facies are less versatile, only including mLT and Tves, both 7%. Contacts between facies are more likely to be gradational, but may be sharp. This association is most often found in unknown deposits (43%), followed by the Pasong Formation (16%) and the Balagbag Formation (14%). The association is also found in the Alaminos (9%), Batangas (3%) and Buco formations (5%), and the Tagaytay (7%) and Antonio Carpio Units (3%).

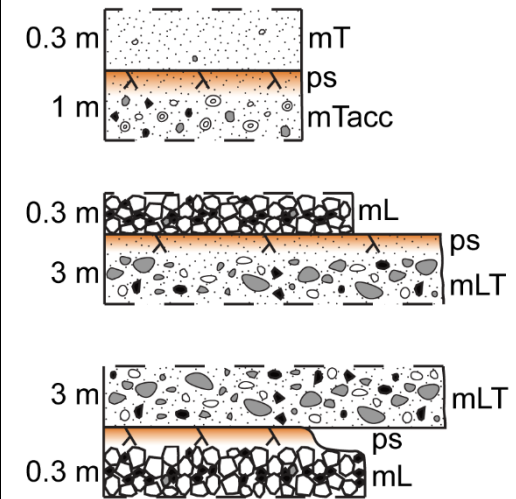
likely represents the final fallout from a co-ignimbrite plume, when ash is too limited to accrete and deposit as pellets. Alternatively, increased moisture content could have caused the disaggregation of any pellets upon impact (Van Eaton and Wilson, 2013). Where mTacc is overlying, a new PDC is hypothesised to have passed. The presence of Tpel above palaeosols implies that PDCs pass (near to) certain localities without depositing any material, leaving only deposits from their co-ignimbrite plumes.

Palaeosols are most commonly overlain by non-accretionary lapilli-bearing facies and underlain by accretionary lapilli-bearing facies (**snacs**)

ps, mT, mL, mL_T, mTacc, //T, dxblBr, fpoordxl, dxblT, mlBr, Tpel, dxblTacc, mL_Tacc

87% of palaeosols are overlain by a non-accretionary lapilli-bearing facies (Fig. 3.22). The three most common overlying facies are mT, mL and mL_T. Out of all transitions to a palaeosol, however, only 48% are underlain by non-accretionary lapilli-bearing facies. The three most common underlying facies are mTacc, mL_T and mL. A multitude of other facies appear above and below palaeosols, but most of these are much less common (**Fig. 3.13**). Underlying facies almost exclusively grade into the palaeosols, while sharp contacts tend to exist with facies overlying palaeosols. 47% of this association occurs in unknown deposits, with a further 17% in the Tagaytay Units and 11% in the Antonio Carpio Units. The following formations also contain this association, but in much smaller abundances: Alitagtag, Balagbag, Batangas, Buco, Buroi, Calumpang, Indang, Pasong, and Sampaga formations.

Conditions for accretionary lapilli formation and/or preservation are more likely to occur towards the end of PDCs, because currents become more dilute in their waning stages, making it less likely that any accretionary lapilli will be destroyed prior to deposition. The presence of accretionary lapilli in a deposit can be seen as part of the evidence to suggest an eruption has come to an end at Taal Caldera Volcano. This association also suggests that accretionary lapilli are unlikely to be formed and/or deposited early on in most eruptions from Taal Caldera Volcano.



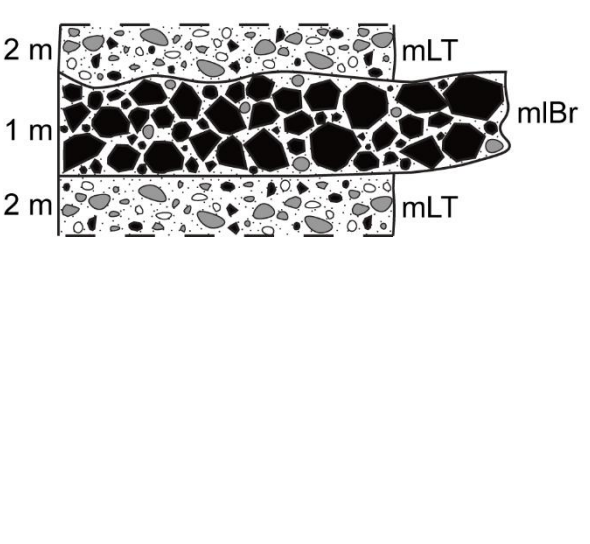
<p>Massive lithic breccia most often associated with massive lapilli-tuff (blt)</p>	<p>mIBr, mLT, dxblT, mTacc, ps, fpoormL</p>	<p>mIBr is always overlain by mLT or dxblT; 86% of the time it is mLT. mIBr is underlain by a wider variety of facies, but 50% of the time this is still mLT. The other underlying facies are equally represented by mTacc, ps and mL. Contacts with facies underlying mIBr are often sharp, while contacts with overlying mLT are erosive. 40% of this facies association occurs in unknown deposits, while 27% is found in the Pasong and Tadalac Cave formations, and a further 7% in the Tagaytay Units.</p>	<p>This transition to and from mIBr represents a change in current parameters, most likely a change in velocity or clast abundance (Branney and Kokelaar, 2002). The fact that mIBr changes into mLT or dxblT more often than the other way around suggests PDCs were more likely to wane rather than wax, or decrease in clast abundance rather than increase, over time once the current had started.</p>	
--	---	--	---	---

Table 3.3: Facies associations recognised within the prehistoric deposits of Taal Caldera Volcano. Average thicknesses for facies included in these associations and most common contacts between the facies are shown in the cartoon representations. Although a large dataset was used (~1000 data points), any preservation bias is difficult to account for, therefore future studies may reveal more exposures and potentially change these abundance percentages. This study finds it unlikely, however, that the facies associations themselves would change drastically.

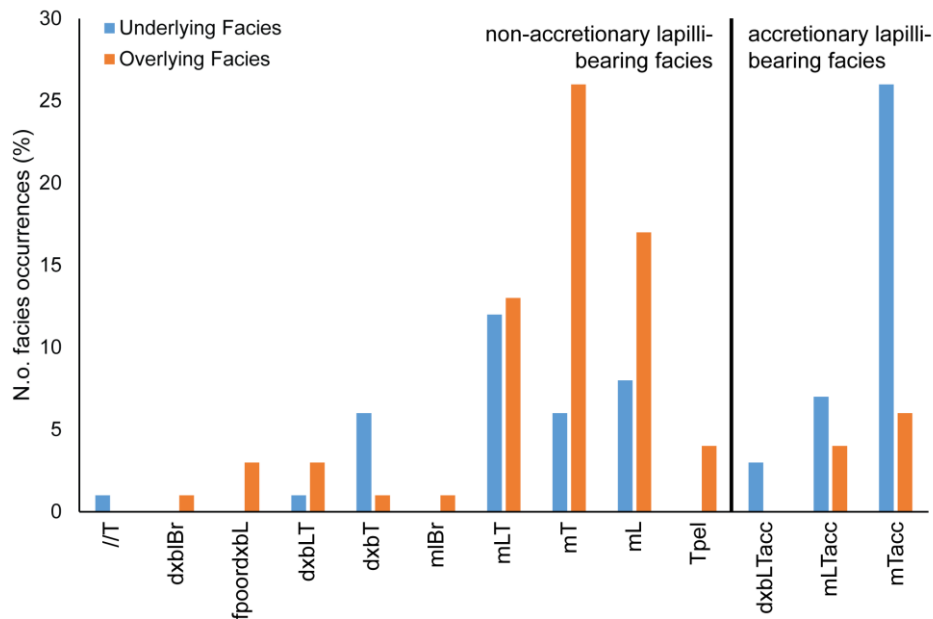


Fig. 3.13: The palaeosols are most commonly overlain by non-accretionary lapilli-bearing facies and underlain by accretionary lapilli-bearing (snacs) lithofacies association (**Table 3.3**) shown on a plot of facies under- and overlying palaeosols, split by accretionary lapilli presence. Overall it is clear that palaeosols are more likely to be overlain by non-accretionary lapilli-bearing facies, while they are more likely to be underlain by accretionary lapilli-bearing facies. The most significant overlying facies are massive tuff (mT) and massive lapillistone (mL), while the most significant underlying facies is massive tuff with accretionary lapilli (mTacc). This result is significant because it may allow identification of the end of an eruption (i.e. accretionary lapilli-bearing facies) in the pyroclastic record even if palaeosols are rarely exposed.

3.5 Markov Chain Analysis

3.5.1 Methods

To statistically investigate vertical facies transitions, Markov Chain Analysis was employed in this study. A process may be referred to as Markovian if a random variable depends on its history (Schwarzacher, 1975). By assuming there is no randomness in a system, it is possible to deduce whether certain elements are impacted by non-random processes, which can then be interpreted (Tewari and Khan, 2017). In order to perform Markov Chain Analysis a sequence must be divided into discrete steps (Schwarzacher, 1975). This is possible with stratigraphic sequences such as turbidites, upon which Markov Chain Analysis was first conducted (Vistelius, 1949). In this study, Markov Chain Analysis will distinguish preferred vertical facies transitions (Xu and MacCarthy, 1998). Commonly, this analysis is applied to sedimentary basins with data based on

field logs (e.g. Tewari and Khan, 2017; Onyekuru et al., 2019); this study is one of the few where this type of analysis has been applied to pyroclastic deposits (the others being Wohletz and Sheridan, 1979 and Sohn and Chough, 1989). The use of Markov Chain Analysis on pyroclastic deposits is appropriate because they are deposited by sedimentary processes and contain sedimentary bedding and features (Schwarzacher, 1975). Several different methods for Markov Chain Analysis have been established and adapted through the years, which has led to the following (Xu and McCarthy, 1998): the Gingerich-Harper method (Gingerich, 1969; Harper, 1984), the Powers-Easterling method (Powers and Easterling, 1982), and the Selley-Türk method (Selley, 1970; Türk, 1979). The first two tend to utilise embedded matrices, while the Selley-Türk method always uses a non-embedded matrix. The Selley-Türk method further tests for randomness using a normalised difference model, similarly to the Powers-Easterling method; the use of binomial probability values is preferred by the Gingerich-Harper method (Xu and McCarthy, 1998).

In the field, facies are observed to overlies themselves (i.e. a massive lapilli-tuff may be overlain by another massive lapilli-tuff). Therefore, this study initially selects the Selley-Türk method (Selley, 1970; Türk, 1979; Xu and McCarthy, 1998) because the non-embedded matrix allows facies to be overlain by themselves. Firstly, a transition count matrix (f_{ij}) was made using field observations, where vertical sections were divided up into beds and/or facies. Next, the predicted data array (e_{ij}) was calculated using:

$$e_{ij} = \frac{R_i C_j}{T} \quad (1)$$

where R_i is the row total of facies i , C_j is the column total of facies j , and T is the total numbers of transitions for all facies (Xu and McCarthy, 1998). The difference matrix (d_{ij}) was then made by subtracting the number of each individual cell in f_{ij} from the same cell in e_{ij} . This matrix shows which facies transitions occur more frequently than would be expected if transitions were random. To test further for significance and randomness, a normalised difference matrix (Türk, 1979) is calculated (nd_{ij}) using:

$$nd_{ij} = \frac{f_{ij} - e_{ij}}{\sqrt{e_{ij}}} \quad (2).$$

Values from individual cells were then compared to published normalised difference values to determine which were significant (≥ 1.65 ; Miller, 1989; Waltham, 1994; Xu and McCarthy, 1998). To confirm results from the matrix as a whole were significant, a chi-square value was calculated. The chi-square test provides one number that defines whether there is a significant difference between observed facies transitions (based on field data) and the facies transitions calculated in the independent trials matrix (i.e. if all observed data was random and not related to each other). This is calculated as follows:

$$x_v^2 = \sum_{ij} \frac{(f_{ij} - e_{ij})^2}{e_{ij}} \quad (3)$$

where v = degrees of freedom:

$$v = (m - 1)^2 \quad (4)$$

where m = number of facies (Xu and McCarthy, 1998). An alpha level (significance level) of 0.1 was chosen for this study (Xu and McCarthy, 1998; Tewari and Khan, 2017).

Markov Chain Analysis was repeated using the Gingerich-Harper method because it was used in the lithofacies study of the Suwolbong tuff ring on Cheju Island, Korea (Sohn and Chough, 1989). Results were compared to those of the Selley-Türk method, which allowed an evaluation of both the two methods and Markov Chain Analysis in general from a volcanological standpoint. The Gingerich-Harper method is slightly different from the Selley-Türk method. The transition count matrix (f_{ij}) is created in the same way, but the predicted data array (e_{ij}) is calculated using:

$$e_{ij} = \frac{C_j}{(T - C_i)} \quad \text{or} \quad e_{ij} = \frac{R_j}{(T - R_i)} \quad (5)$$

where C_j is the column total of facies j , C_i is the column total of facies i , R_j is the row total of facies j , R_i is the row total of facies i , and T is the total numbers of transitions for all facies (Xu and MacCarthy, 1998). In addition, the Gingerich-Harper method then calculates a transitional probability matrix using:

$$P_{ij} = \frac{f_{ij}}{R_i} \quad (6)$$

where f_{ij} is the total number of transitions from facies i to j (Xu and MacCarthy, 1998). The difference matrix is then calculated using this transitional probability matrix:

$$D_{ij} = P_{ij} - e_{ij} \quad (7).$$

Any positive values in the difference matrix represent facies transitions that occur more frequently than expected if any facies transitions were random. To test which of these differences is significant, the Gingerich-Harper method uses a binomial probability matrix:

$$P_N(n) = \sum_{n=n_{obs}}^{n=N} C(N, n) p^n q^{N-n} \quad (8)$$

where n_{obs} is the number of successes (i.e. observations of a particular facies transition) observed in N trials, p is the probability of success in a single trial based on the predicted data array, q is $1-p$, and $C(N, n)$ is calculated using:

$$C(N, n) = \frac{N!}{(N-n)!n!} \quad (9; \text{Xu and MacCarthy, 1998}).$$

However, in this study, the function BINOM.DIST.RANGE on Microsoft Excel was used to calculate the binomial probability matrix, because it performs the same calculations as equations (8) and (9), but allows the binomial probability to be calculated much faster. Like in the Selley-Türk method, the chi-square test was then conducted. The equation for the chi-square test with reference to the Gingerich-Harper method is slightly different, however, and is as follows:

$$\chi_v^2 = \sum_{ij} \frac{(f_{ij} - R_i e_{ij})^2}{R_i e_{ij}} \quad (10)$$

where v still equals degrees of freedom:

$$v = (m - 1)^2 \quad (11)$$

with m being the total number of facies (Xu and MacCarthy, 1998).

3.5.2 Results

In volcanic terms Markovity suggests that there are preferred eruptive sequences. Knowing what these are could help predict how future eruptions will progress. For example, if massive lapilli-tuffs significantly overlie pumice fall deposits, it suggests that after every pumice fall phase the volcano experiences a pyroclastic density current (PDC) phase. Such information is invaluable for hazard planning and evacuation procedures.

Markov Chain Analysis was conducted using the generalised vertical section (GVS; Appendix C). Only data from the GVS was used because the aim of

Markov Chain Analysis here is to establish any preferred eruptive sequences for Taal Caldera Volcano. If a dataset including all localities was used, then the same facies transition may be counted more than once (i.e. the same facies transition in the same eruption-unit may be exposed in the field more than once), which would then bias the analysis. Although using only facies transitions from the GVS reduces the amount of data, the chi-square test ensures results are statistically significant.

Several assumptions were made in using this approach. Firstly, it was assumed that the GVS represents a complete record of each eruption-unit. Although this is unlikely to be the case for every eruption-unit, all geological studies must contend with a depositional, preservation and exposure bias that is challenging to overcome and quantify. Despite this, sufficient data has been collected in this study to make Markov Chain Analysis results significant (see chi-square test values below) and therefore even if interpretations of individual eruption-units may change as more evidence comes to light, this study still makes a new and substantial contribution by being the first to attempt to statistically evaluate lithofacies associations at Taal Caldera Volcano. Secondly, all facies involved in the analysis have been split to the same categorical level. That is to say, lapillituffs are split into relevant bedding categories, i.e. massive, diffuse cross-bedded and cross-bedded, just like tuffs, lithic breccias and lapillistones. This was done because extreme changes in depositional processes (e.g. a change from fall to flow deposition) are assumed to be rarer than less extreme changes (e.g. a change at the flow-boundary zone of a depositing PDC). Therefore, these less extreme changes would be represented in the lithofacies more frequently, making it important that all facies are recorded at a similar level of detail.

The chi-square test for the Selley-Türk method provides a value of 200, which is significant at a 0.1 alpha level with 169 degrees of freedom. The relationships between facies found around Taal Caldera Volcano are thus significant, supporting the presence of Markovity (e.g. Schwarzacher, 1975). There are 40 facies transitions that occur more commonly than expected for a random distribution, but only 15 of these are significant (i.e. ≥ 1.65 in normalised

difference matrix). The chi-square test for the Gingerich-Harper method provides a value of 190, which is just under the critical level (i.e. significance level) of 192 for a 0.1 alpha level with 169 degrees of freedom. Since there is only a difference of 2 between the calculated value (190) and the critical level (192), results from the Gingerich-Harper method are still useful, especially to compare to results from the Selley-Türk method. The Gingerich-Harper method finds that there are 39 facies transitions that occur more often than expected for a random distribution, but only 13 of these are significant (i.e. binomial probability is ≤ 0.10 ; Xu and MacCarthy, 1998). All significant facies transitions identified by the Gingerich-Harper method are also identified by the Selley-Türk method.

The facies relationship diagram shows three separate groups of facies transitions, meaning it is not possible to travel from each facies to every other facies on the relationship diagram (Fig. 3.14). The first (A) links multiple relatively coarse facies (breccias and lapilli-tuffs) together (Fig. 3.14). Interestingly, the significant associations only exist between facies of the same coarseness or the same bedding (i.e. massive or diffuse cross-bedded). For example, fines-poor diffuse cross-bedded lapilli-tuff (fpoordxbLT) only associates with diffuse cross-bedded lapilli-tuff (dxbLT), which then connects to massive lapilli-tuff (mLT) and massive lapilli-tuff with accretionary lapilli (mLTacc). There is no direct path between fines-poor diffuse cross-bedded lapilli-tuff (fpoordxbLT) and any massive lapilli-tuff (mLT) or massive lithic breccia (mLBr). The only two facies that significantly change into each other are diffuse cross-bedded lapilli-tuff (dxbLT) and massive lapilli-tuff (mLT); all other facies connect to each other in one direction (Fig. 3.14).

The second group (B) connects several relatively fine facies (tuffs), as well as palaeosols (ps) and massive lapillistone (mL, representing pumice fall deposits). No coarse facies (breccias and lapilli-tuffs) are present in this group (Fig. 3.14). No two facies are significantly overlain by each other (i.e. connections on the facies relationship diagram only go one way). The facies most involved in significant associations is massive tuff (mT), which is significantly overlain by massive lapillistone (mL) and ash pellet tuff (Tpel). The connection with ash

pellet tuff (Tpel) appears to start a cycle, which connects massive tuff (mT) to ash pellet tuff (Tpel), followed by massive tuff with accretionary lapilli (mTacc), palaeosol (ps) and diffuse cross-bedded tuff (dxbT), before coming back to massive tuff (mT; Fig. 3.14). The only facies not in this cycle is massive lapillistone (mL; Fig. 3.14).

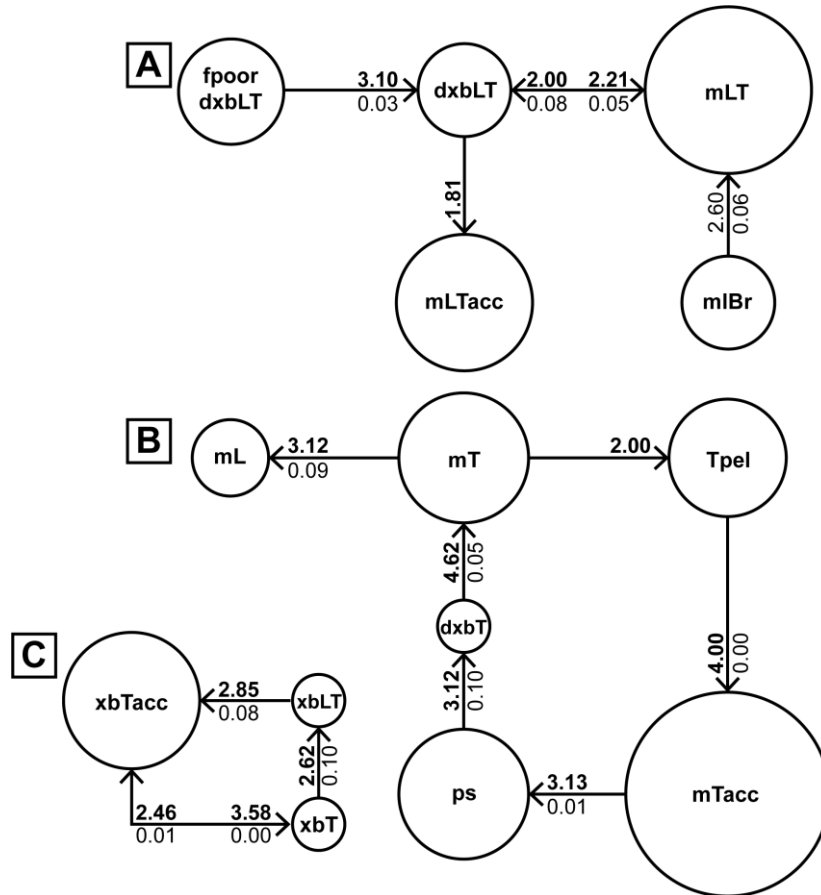


Fig. 3.14: Facies relationship diagram based on both the Selley-Türk method (**bold text** used for normalised difference values on arrows) and the Gingerich-Harper method (regular text used for binomial probability values on arrows). Where only a bold value is present, the association was only identified as significant by the Selley-Türk method. The circles represent relative abundances of each facies in the dataset. Three different groups are recognised (A, B and C). Lithofacies as follows: fines-poor diffuse cross-bedded lapilli-tuff (fpoordxbLT), diffuse cross-bedded lapilli-tuff (dxblT), massive lapilli-tuff (mLT), massive lapilli-tuff with accretionary lapilli (mLTacc), massive lithic breccia (mlBr), massive lapillistone (mL), massive tuff (mT), ash pellet tuff (Tpel), massive tuff with accretionary lapilli (mTacc), palaeosol (ps), diffuse cross-bedded tuff (dxbt), cross-bedded tuff with accretionary lapilli (xbTacc), cross-bedded lapilli-tuff (xbLT), cross-bedded tuff (xbT).

A cycle is similarly seen in the last group (C; Fig. 3.14). The cycle starts at cross-bedded tuff (xbT), which is significantly overlain by cross-bedded lapilli-tuff (xbLT), which is then overlain by cross-bedded tuff with accretionary lapilli

(xbTacc), which leads back to cross-bedded tuff (xbT). Group C, like group A, contains a set of facies (cross-bedded tuff with accretionary lapilli, xbTacc, and cross-bedded tuff, xbT) that significantly change into each other (Fig. 3.14). Unlike all the other groups, group C contains both fine and coarse flow deposits (tuffs and lapilli-tuffs), but consists of a singular type of bedding, namely cross-bedding (Fig. 3.14).

3.5.3 Interpretations

The fact that deposits from Taal Caldera Volcano show Markovity suggests that the depositional processes during an eruption are not random and whatever facies deposits next is directly related to the underlying facies. The facies relationship diagram splits coarse and fine facies apart in groups A and B respectively (Fig. 3.14), which implies that the overlying of one coarse facies by another, and similarly one fine facies by another, is more common than would be expected in a random system. In a volcanological context, group A highlights the frequent internal variations within the flow-boundary zone of PDCs (e.g. Branney and Kokelaar, 2002), with changes in clast concentration particularly more common than expected (e.g. lithic breccia being overlain by a lapilli-tuff).

In group B (Fig. 3.14), the cycle represented by a palaeosol, diffuse cross-bedded tuff, massive tuff, ash pellet tuff and massive accretionary lapilli-tuff is significant because it includes a palaeosol. This suggests that this cycle could represent an eruption-unit that is more commonly observed than predicted. If this is the case, then a dilute flow phase represents the start of the eruption (diffuse cross-bedded tuff overlies a palaeosol), followed by a change to a more direct fallout-dominant flow-boundary zone (massive tuff overlies diffuse cross-bedded tuff). Following this, fallout from the co-ignimbrite plume starts (ash pellet tuff overlies massive tuff) before a second relatively dilute PDC passes in which accretionary lapilli are able to form and/or deposit (massive accretionary lapilli-tuff overlies ash pellet tuff) before the eruption ceases and a palaeosol forms (palaeosol overlies massive accretionary lapilli-tuff; Fig. 3.14). Although this facies cycle may represent an eruption-unit, it is more likely to be seen in the field at distal localities as opposed to proximal localities, unless the eruption

is relatively small. It highlights that the presence of at least two flow phases, even at relatively distal localities, is more common than expected. Furthermore, the only facies palaeosols overlies more often than predicted is massive tuff with accretionary lapilli, which suggests that massive tuff with accretionary lapilli most commonly represents the final phase of activity of an eruption (i.e. a dilute, direct fallout-dominant flow-boundary zone PDC), supporting the conclusions of qualitative vertical lithofacies associations analysis (Table 3.3).

Group C (Fig. 3.14) demonstrates that cross-bedded facies are much more likely to associate with each other than predicted. The interchange between accretionary lapilli-bearing facies is particularly common, suggesting conditions allowing the formation and/or deposition of accretionary lapilli frequently fluctuates in PDCs depositing cross-bedded facies.

3.5.4 Effectiveness of Markov Chain Analysis

The difference between the Selley-Türk and Gingerich-Harper methods will first be evaluated. The methods do not differ in their identification of significant facies associations at Taal; the Selley-Türk method only highlights two additional significant facies associations. The overall significance of the results, as identified by the chi square test, is achieved at a lower alpha level (0.1) for the Selley-Türk method compared to the Gingerich-Harper method. This is likely due to the overall smaller dataset (65 compared to 70) used for the Gingerich-Harper method, because it does not allow facies to associate with themselves. Herein lies the main problem this study identifies with the Gingerich-Harper method. Within a volcanological depositional environment, it can be expected that the same facies overlies each other. For example, a massive lapilli-tuff may overlie another massive lapilli-tuff in the field because two separate PDCs have passed and deposited material in the same locality without any other material depositing in between, which provides important information about the number of PDCs produced during one eruption. Ignoring these facies associations provides a biased interpretation of the eruptive and depositional processes at the studied volcano. Therefore, this study recommends the use of the Selley-Türk method when using Markov Chain Analysis on pyroclastic deposits.

There are some limitations when using Markov Chain Analysis in a volcanological context. Firstly, only facies transitions within known stratigraphy can be used in the dataset so the same facies transitions are not repeated in the dataset, which can be done using the GVS like in this study, or if the stratigraphy is better constrained, could be done using data from different exposures from the same eruption-unit. The latter is only possible if individual flow or fall units can be well correlated across the depositional area. If there are excellent lateral exposures in the field, then lateral facies associations could also be investigated using Markov Chain Analysis (e.g. Sohn and Chough, 1989). A potential drawback of this type of statistical analysis is that it only considers a single facies transition because Markov Chain Analysis tests whether the deposition of one facies is related to the facies directly below it only (i.e. Markovity), not to any other facies below it. It is most useful for volcanologists, however, to build up a complete picture of the eruptive and depositional behaviour of a volcano, which requires construction of multiple facies transitions within one eruption-unit since it is unlikely that an eruption-unit will only consist of one facies transition. In addition, certain facies associations may not be picked up as being statistically significant, but could be significant in a volcanological context. Statistics can provide extra weighting to any observed facies associations and can highlight particularly important individual facies transitions for the volcano in question. Therefore, this study recommends that statistical analysis is combined with qualitative and quantitative analysis of the field data (e.g. Sohn and Chough, 1989), which has been done in this study.

3.6 Eruption and depositional styles at Taal Caldera Volcano

3.6.1 Depositional styles interpreted from vertical facies associations

Pumice fall deposits around Taal Caldera Volcano are almost exclusively found along Tagaytay Ridge within the Tagaytay Units. When considering named deposits (i.e. those identified in the GVS) the lithofacies parallel-bedded lapillistone and diffuse cross-bedded lapillistone are only identified within the

Tagaytay Units (Table 3.1). The Tagaytay Units also contain 82% of the tuff repetitions or single occurrences without any accretionary lapilli-bearing or vesiculated tuff (tr) facies association, 17% of the palaeosols overlain by non-accretionary lapilli-bearing facies and underlain by accretionary lapilli-bearing facies (snacs) facies association, and 33% of the pumice fall deposits overlain by coarse, massive facies or a palaeosol (fm) facies association (Table 3.3). Therefore, fall deposition was the preferred depositional style of eruptions belonging to the Tagaytay Units.

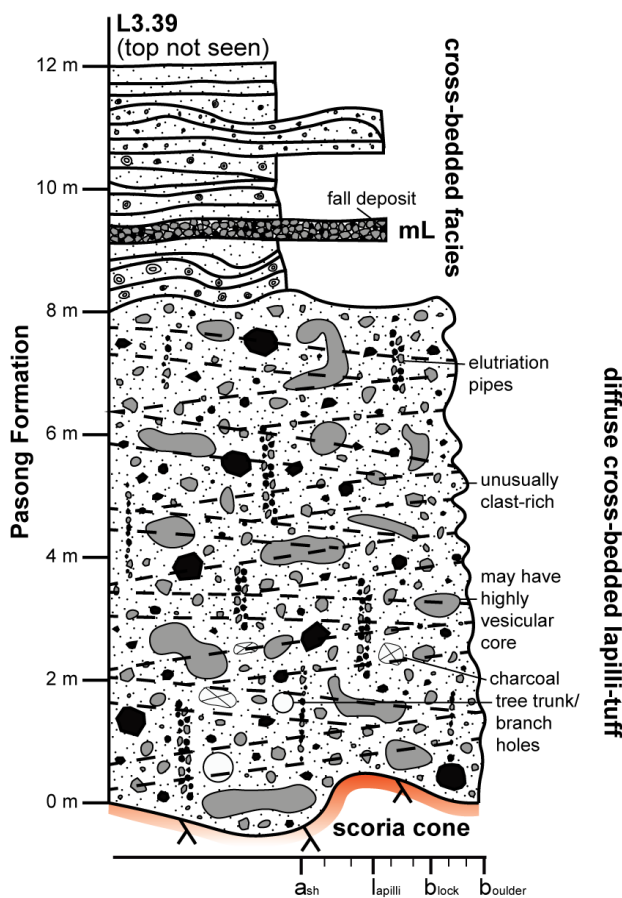


Fig. 3.15: Log of a Pasong Formation exposure at L3.39 [13° 54.631'N 121°10.745'E] with a pumice fall deposit (massive lapillistone, mL) within the cross-bedded sequence of the Pasong Formation.

Pumice fall deposits are more rarely identified on the ignimbrite plains in association with ignimbrite-forming eruptions. Pyroclastic density currents can erode pumice fall deposits, leaving little or no record of any fall activity in the pyroclastic record, as demonstrated by the locally eroded pumice fall deposit underlying the Alitagtag ignimbrite (Chapter 2). More often pumice fall deposits occur within the cross-bedded sequences within the Buco and Pasong formations (i.e. not the climactic phases of caldera-forming eruptions) and do not under- or overlie- the massive

lapilli-tuffs (Fig. 3.15; Chapter 2; Section 3.3.3). Therefore, it appears like smaller-scale eruptions (e.g. the Tagaytay Units and non-climactic phases of caldera-forming eruptions) are more likely to experience pumice fall deposition as opposed to the climactic phases of ignimbrite-forming eruptions from Taal Caldera Volcano, which favour flow deposition over fall deposition. However, it

should be noted that pumice may have fallen directly into pyroclastic density currents and therefore the amount of pumice fall deposition experienced during caldera-forming eruptions may have been underestimated.

At Taal, the majority of field evidence of fall deposition is represented by ash pellet tuffs (Tpel). Ash pellet tuffs can provide evidence of fall deposition from a vent-derived eruption column (Wilson and Walker, 1985) or from a co-ignimbrite plume after the passing of a PDC (Brown and Branney, 2004; Brown et al., 2010; Dávila-Harris et al., 2013). The former could have occurred during eruptions whose deposits show palaeosols underlying ash pellet tuffs (Table 3.3), but most often ash pellet tuffs around Taal Caldera Volcano are underlain by massive tuff with accretionary lapilli or massive tuff (the latter identified as significant by Markov Chain Analysis, Fig. 3.14). This field evidence suggests that a PDC passed, depositing massive tuff (with accretionary lapilli), before a co-ignimbrite plume deposited an ash pellet tuff. The ash pellet tuffs mainly associated with tuffs (pt) facies association also shows that ash pellet tuffs are also commonly overlain by massive tuffs (Table 3.3). Where massive tuffs gradationally overlie ash pellet tuffs, they likely represent ash layers where pellets have disaggregated upon deposition (e.g. Brown et al., 2010) or pellets can no longer form in the co-ignimbrite plume (e.g. Mueller et al., 2016).

Where PDCs are produced during climactic phases of ignimbrite-forming eruptions from Taal Caldera Volcano, the diffuse cross-bedding linked to massive beds (dxbm) facies association (Table 3.3) and Markov Chain Analysis (Fig. 3.14) highlight the significance of transitions of diffuse cross-bedded lapilli-tuff (dxblT) to and from massive lapilli-tuff (mLT). Although the gradational transitions between diffuse cross-bedded lapilli-tuff (dxblT) and massive lapilli-tuff (mLT) is commonly observed in the field at other volcanoes (e.g. Branney and Kokelaar, 2002; Brown et al., 2003; Báez et al., 2020; Scarpati et al., 2020), this is the first study in which this relationship is shown to be statistically more common than expected (Fig. 3.14). Subtle, temporary unsteadiness (e.g. Branney and Kokelaar, 2002; Brown and Branney, 2004) was common during deposition at the base of Taal's PDCs, especially in the Pasong and Buco formations in which the diffuse cross-bedding linked to massive beds (dxbm)

association is recorded most frequently out of the named formations (Table 3.3).

Transitions from diffuse cross-bedded lapilli-tuff (dxbLT) to massive lapilli-tuff (mLT) are described as gradational in the literature (Branney and Kokelaar, 2002), which is reflected in the Taal deposits (Table 3.3). A complete switch to a traction-dominant flow-boundary zone to produce cross-bedded facies does not happen frequently at Taal Caldera Volcano, unless this type of flow-boundary zone is dominant as soon as the PDC starts as shown by the isolation of the cross-bedded facies in the Markov Chain facies relationship diagram (Group C; Fig. 3.14). Even though cross-bedded facies are deposited by turbulent, erosive, possibly multiple pyroclastic density currents (e.g. Schmincke et al., 1973; Németh and Cronin, 2009), the overall depositional regime is stable. For example, a PDC may change from depositing a lapilli-tuff instead of a tuff, but both the lapilli-tuff and tuff are cross-bedded.

3.6.2 Eruption styles at Taal Caldera Volcano

Taal Caldera Volcano experienced multiple large-scale eruptions for which caldera collapse can be inferred (Chapter 2), however, there are limited lithic breccia exposures, which are typically abundant during caldera collapse (e.g. Druitt and Sparks, 1984; Rosi et al., 1996; Bear et al., 2009; Valentine, 2020). However, with the eruption sources for Taal's prehistoric eruptions likely being somewhere within Lake Taal, to the southeast of Volcano Island in the case of the Buco Formation (Fig. 3.11), most lithic material produced during caldera collapse likely fell into the collapsing structure and thus now lies below Lake Taal (e.g. Wilson and Walker, 1985). This hypothesis is supported by the presence of brecciated lithic clasts in lapilli-tuffs from the Buroi and Balagbag formations. Fluidal juvenile bombs, where they occur as proximal agglomerates, may be another indicator of caldera-collapse (e.g. Mellors and Sparks, 1991; Rosi et al., 1996; Palladino and Simei, 2005; Kokelaar et al., 2007; Firth et al., 2015; Rooyakkers et al., 2020). Fluidal juvenile bombs were identified in the agglomerates of the Pasong Formation, therefore potentially providing evidence of caldera collapse during the Pasong Formation. Although no agglomerates

were identified in the Indang and Buco formations, their ignimbrites (and lithic breccia in the case of the Indang Formation) are fluidal juvenile bomb-rich and it is possible that their proximal agglomerates are not exposed. Therefore, fluidal juvenile bomb-rich ignimbrites in the Buco and Indang formations can tentatively also provide evidence of caldera collapse during the Buco and Indang formations.

The distribution of the rare lithic breccias that are exposed and spatter-rich agglomerates along the base of Tagaytay Ridge coincides with a fault that trends along the northern shore of Lake Taal (Fig. 3.16), which roughly coincides with the topographic outline of Taal Caldera Volcano (Punongbayan et al., 1995; Fig. 3.16). Since lithic breccias and spatter-rich deposits, specifically spatter agglomerates, are proximal facies of ignimbrites (Branney and Kokelaar, 2002), their placement along the Tagaytay Ridge fault indicates activation of, and eruption along, caldera faults, which often occurs during caldera collapse (e.g. Geyer and Martí, 2014).

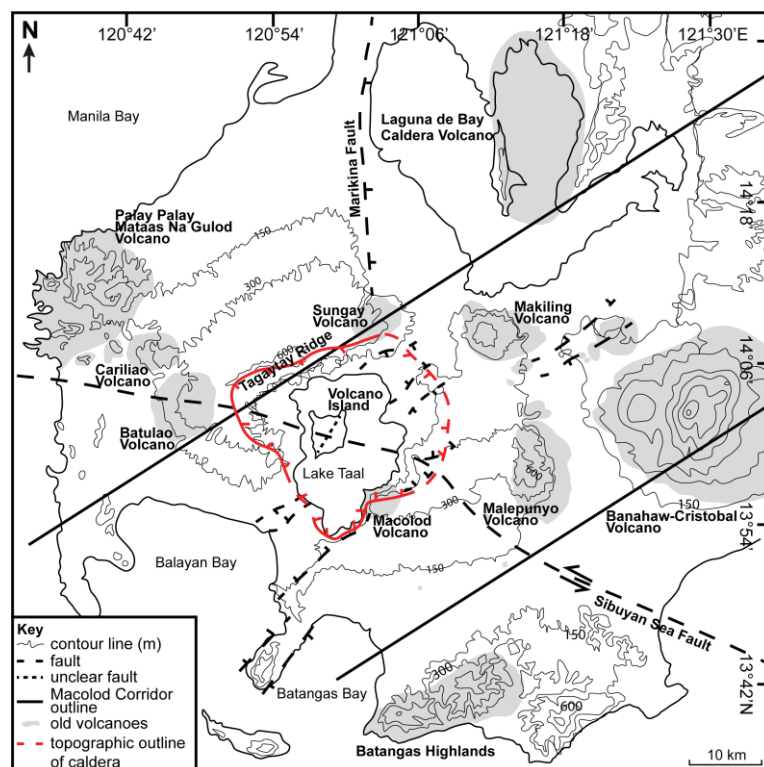


Fig. 3.16: Map of Taal Caldera Volcano with faults in the area, including those associated with the topographic outline of the caldera (e.g. along Tagaytay Ridge) based on Punongbayan et al. (1995).

The massive lithic breccia associated with massive lapilli-tuff (blt) association (Table 3.3) indicates that caldera-forming eruptions from Taal Caldera Volcano do not experience caldera collapse at the start of their eruptions. Instead, the presence of a massive lapilli-tuff (mLT) underlying a lithic breccia (lBr) identifies a pre-caldera-collapse flow phase, which is exemplified by the Tadalac Cave Formation (Figs. 3.1, 3.17; L2.9 [13° 52.788'N 120°59.718'E]). The Buco Formation is an exception because a lithic breccia is identified above a palaeosol (Fig. 3.1; L2.76 [14° 06.600'N 120°57.579'E]). The palaeosol overlain by non-accretionary lapilli-bearing facies and underlain by accretionary lapilli-bearing (snacs) facies association (Table 3.3) suggests that typically, large-scale, ignimbrite-forming eruptions from Taal Caldera Volcano commence with either a dilute flow phase (represented by diffuse cross-bedded tuff (dxbT) and possibly massive tuff (mT) as identified by Markov Chain Analysis as significant, Fig. 3.14), concentrated flow phase (represented by massive lapilli-tuff, mLT) or a pumice fall phase (represented by parallel-bedded, diffuse cross-bedded and massive lapillistone).

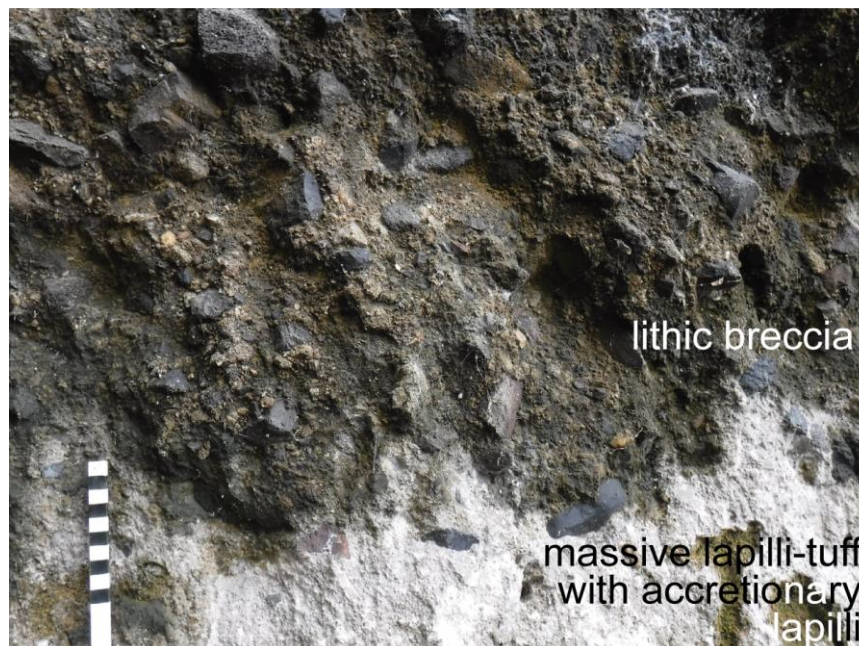


Fig. 3.17: A lithic breccia overlying a massive lapilli-tuff with accretionary lapilli in the Tadalac Cave Formation at L2.9 [13° 52.788'N 120°59.718'E]. Ruler split into 10 cm-sized sections for scale.

Rarely, Taal's caldera-forming eruptions started with a vent-derived buoyant eruption column (producing parallel-bedded, diffuse cross-bedded and massive lapillistone), although this is frequently observed at other calderas (e.g. Crater Lake Caldera, USA in Bacon, 1983; Santorini Caldera, Greece in Druitt et al., 1989; the Sutri eruption of Vico Volcano, Italy in Bear et al., 2009; Ilopango Caldera, El Salvador in Suñe-Puchol et al., 2019; the Xaltipan ignimbrite of the Los Humeros Volcanic Complex, Mexico in Cavazos-Álvarez and Carrasco-Núñez, 2020; Aira Caldera, Japan in Geshi et al., 2020). As indicated by the pumice fall deposits overlain by coarse, massive facies or a palaeosol (fm) facies association (Table 3.3), the buoyant eruption column then likely collapsed and produced a concentrated PDC that deposited massive lapilli-tuff before it waxed to produce rarer lithic breccia (IBr; Fig. 3.18) or another coarse facies such as fines-poor diffuse cross-bedded lapilli-tuff (fpoordxbLT).

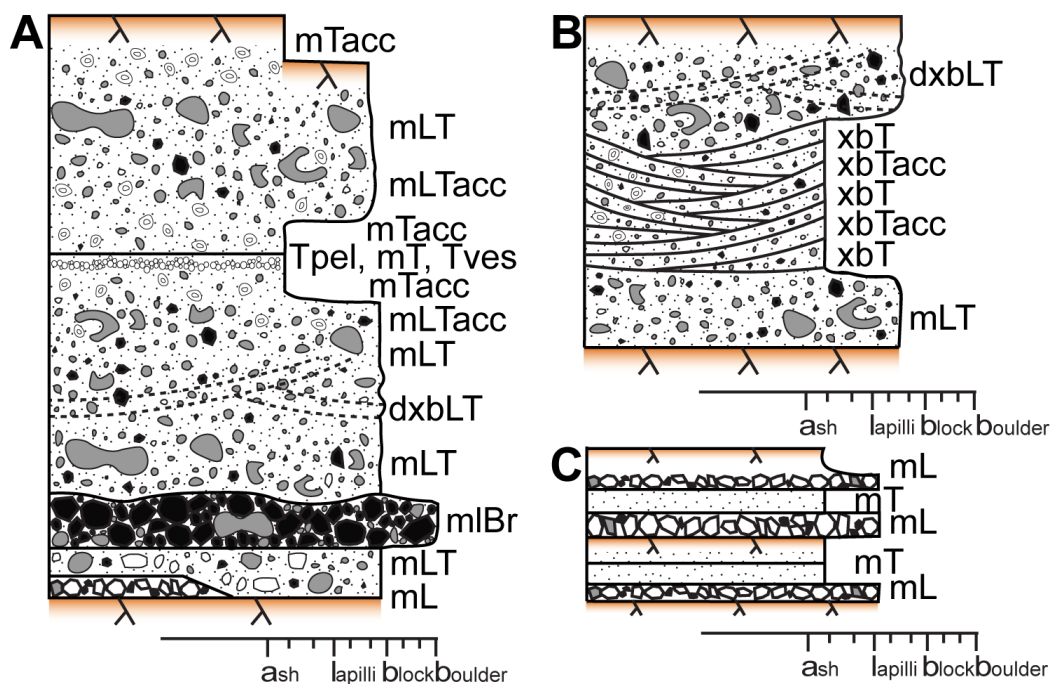


Fig. 3.18: A compilation of common eruption sequences from Taal Caldera Volcano based on lithofacies and Markov Chain Analysis. **(A)** A typical larger-scale, caldera-forming eruption, **(B)** smaller-scale activity within caldera-forming eruptions, **(C)** sequences of smaller-scale eruptions independent of caldera-forming eruptions.

More commonly, large-scale, ignimbrite-forming eruptions could not sustain a vent-derived buoyant eruption column and immediately produced a PDC (Fig. 3.18). The PDC proceeded to wane and deposit massive lapilli-tuff (mLT) and

diffuse cross-bedded lapilli-tuff (dxblT; Section 3.6.1) on top of previously deposited lithic breccia (lBr) and/or fines-poor diffuse cross-bedded lapilli-tuff (fpoordxbLT; Fig. 3.18), as indicated by the massive lithic breccia associated with massive lapilli-tuff (blt) association (Table 3.3) and the Markov Chain data (Fig. 3.14).



Fig. 3.19: Massive lapilli-tuff overlying a palaeosol, while a massive tuff with accretionary lapilli gradationally underlies a palaeosol. Another massive lapilli-tuff gradationally underlies the massive tuff with accretionary lapilli at L3.41 [14° 13.084'N 120°59.070'E].

Eventually, conditions in the PDC were such that accretionary lapilli were able to form and/or deposit, therefore a massive lapilli-tuff with accretionary lapilli (mLTacc) is deposited, followed by a massive tuff with accretionary lapilli (mTacc) before the PDC ceased (Fig. 3.18) and a palaeosol might have formed (e.g. Fig. 3.19). The presence of accretionary lapilli at the top of flow-units and eruption-units is recorded at other volcanoes (Brown et al., 2010; Van Eaton and Wilson, 2013), but this is the first study where statistics have confirmed this observation (i.e. the significant relationship

between massive tuff with accretionary lapilli (mTacc) and palaeosols (ps) in Fig. 3.14).

The presence of flow-unit boundaries (e.g. ash pellet tuffs) within eruption-units (Table 3.3) suggests that eruptions from Taal Caldera Volcano are likely to

experience multiple flow events. Therefore, ash pellet tuffs (Tpel), not palaeosols, are commonly found overlying massive tuff with accretionary lapilli and massive tuff (Fig. 3.18; Table 3.3), the former also recorded in ignimbrites on Tenerife (Brown et al., 2010). If abundant moisture was present in a co-ignimbrite plume, pellets may have disaggregated upon deposition (Rosi, 1992; Brown et al., 2010), which explains why on occasion massive tuff (mT) or vesiculated tuff (Tves), both possibly representing disaggregated pellets, overlie ash pellet tuff (Tpel) in the field (Fig. 3.18; Table 3.3).

The interbedding of massive and cross-bedded non- and accretionary lapilli-bearing facies association (nac) (Table 3.3; Fig. 3.18) suggests that following the deposition from a co-ignimbrite plume, generally, a second PDC passes and deposits massive tuff with accretionary lapilli (mTacc; Markov Chain results, Fig. 3.14) before waxing and depositing massive lapilli-tuff (mLT) or massive lapilli-tuff with accretionary lapilli (mLTacc). The interbedding of massive and cross-bedded non- and accretionary lapilli-bearing facies (nac) association also suggests that conditions at the flow-boundary zone can fluctuate between depositing and not depositing accretionary lapilli, perhaps reflecting whether conditions in the more dilute parts of the PDC are favourable to accretionary lapilli formation. Once the eruption mass flux, and thus PDC, waned for the final time, the PDC likely deposited massive tuff with accretionary lapilli (mTacc) before a palaeosol formed on top (Figs. 3.18, 3.19). However, the palaeosols overlain by non-accretionary lapilli-bearing facies and underlain by accretionary lapilli-bearing facies (snacs) association (Table 3.3) suggests that the deposition of massive tuff with accretionary lapilli (mTacc) is not always preserved and massive lapilli-tuff (mLT) can directly underlie palaeosols (Fig. 3.18). Evidence of massive tuff with accretionary lapilli (mTacc) deposition could have either been eroded by another non-depositing PDC or reworked prior to soil formation.

Large-scale, ignimbrite-forming eruptions may experience phases of smaller-scale activity. This smaller-scale activity often comprises of multiple, relatively dilute PDCs producing cross-bedded facies. Markov Chain results highlight how much more common transitions within cross-bedded facies are as opposed to

transitions with massive or diffuse cross-bedded facies (Group C, Fig. 3.14), which is further reflected by the interbedding of massive and cross-bedded non- and accretionary lapilli-bearing facies (nac) association (Table 3.3). Where the cross-bedded version of the interbedding of massive and cross-bedded non- and accretionary lapilli-bearing facies (nac) association is seen in the field, it overlies either massive lapilli-tuff (mLT) or diffuse cross-bedded lapilli-tuff (dxbLT) and is overlain by diffuse cross-bedded lapilli-tuff (dxbLT; Fig. 3.18). Both these facies (i.e. massive lapilli-tuff and diffuse cross-bedded lapilli-tuff) are associated with granular fluid-based PDCs (Table 3.1) and ignimbrite-forming eruptions. These field relationships support the fact that Taal Caldera Volcano experiences phases of smaller-scale activity during its ignimbrite-forming eruptions.

The ignimbrite-forming eruptions themselves are punctuated by more frequent smaller-scale eruptions in otherwise quiescent intervals (e.g. the Tagaytay Units and historical eruptions) like also seen at the flooded Santorini Caldera, Greece (Druitt et al., 1989). These smaller-scale eruptions are different to those produced during ignimbrite-forming eruptions as described above. The Tagaytay Units are exemplified by the tuff repetitions (tr) facies association (Table 3.3; Fig. 3.18); a similar interbedded sequence is recorded in the deposits from the 1883 Krakatau eruption, although the interpreted flow deposits there are cross-stratified (Madden-Nadeau et al., 2021), while in the Tagaytay Units they are massive (Table 3.3; Fig. 3.18). The pumice fall deposits overlain by coarse, massive facies or a palaeosol (fm) facies association also occurs in the Tagaytay Units where palaeosols are immediately overlain by pumice fall deposits (mL; Table 3.3), thus suggesting that, contrary to the tuff repetitions (tr) facies association, the eruption column remained buoyant throughout the entire eruption. The presence of both the tuff repetitions (tr) and pumice fall deposits overlain by coarse, massive facies or a palaeosol (fm) facies associations in the Tagaytay Units shows that, although eruptions were of a smaller-scale than Taal's caldera-forming eruptions, not all eruptions were the same size. Similar evidence is seen in the smaller-scale historical eruptions

of Taal Caldera Volcano, where eruptions have ranged in size from VEI 1 – 5 (Delos Reyes et al., 2018).

3.6.3 Magma – water interaction at Taal Caldera Volcano

The pyroclastic record of Taal Caldera Volcano's prehistoric eruptions shows evidence of different degrees of magma – water interaction, both during eruption and deposition. The abundance and types of ash aggregates, both at a field and microscopic level, and presence of hardened (Brown et al., 2012) and vesiculated tuff (Rosi, 1992; Cole and Scarpati, 1993) suggests Taal's eruptions were sub-saturated to saturated at some stage (Table 3.2). The moisture required for (sub)saturated conditions may have an atmospheric source, however, and does not necessarily imply lake and/or groundwater interacted with magma at the eruption source (Németh and Kósik, 2020). For example, during the caldera-forming Campanian eruption of Campi Flegrei (Scrapti et al., 2020) and the 1991 Pinatubo eruption (Scott et al., 1996) rainfall provided the moisture required for ash aggregation. With the Philippines being a humid, tropical island with a rainy season, it is conceivable that either of these mechanisms or even the humid air (e.g. Volcán de Colima; Reyes-Dávila et al., 2016) could provide sufficient moisture to form ash aggregates. At Taal, however, aggregates are extremely abundant and appear close to source (e.g. Tomita et al., 1985), therefore it is proposed that moisture was sourced from Lake Taal or a relevant hydrothermal system. Further support for this hypothesis stems from the abundance of cored pellets and coated clasts in the Taal pyroclastic record, also a common feature in other deposits from hydrovolcanic eruptions such as the steam-rich PDC that deposited the fine pumiceous PDC deposit, Unit B, of the Phreatoplinian eruption of the Kos Plateau Tuff (Allen and Cas, 1998).

Ash accretion happens on a smaller scale as well, as exemplified by the ash adhesion microscopically observed in ash grain samples. Smaller particles stick to larger ones in almost all of the studied samples; this adhesion occurs due to the presence of moisture during transport, similarly to the growth of hydration skins or overgrowth films (Zimanowski et al., 2015). Where ash grains are non-

vesicular they are (sub)rounded or blocky, the latter being a key characteristic of passive hydrovolcanic particles (i.e. those particles formed by fragmentation due to stresses produced by magma-water interaction, but not in direct contact with the water; Büttner et al., 1999; Zimanowski et al., 2015). There is rarer evidence of active particles in ash samples, active particles being those that directly interacted with water during fragmentation (Austin-Erickson et al., 2008). Most commonly at Taal, active particles are represented by moss-like particles (e.g. Zimanowski et al., 2015); stepped features and quench cracks (e.g. Heiken, 1972; Büttner et al., 1999; Büttner et al., 2002) are uncommon.

The vesicular nature of many ash grains in Taal samples implies that most eruptions were driven by volatile exsolution (e.g. Self and Sparks, 1978; Barberi et al., 1988; Cioni et al., 1992; Houghton et al., 2003). Where an ash population shows a range of vesicle sizes, however, it is likely that at some stage water interacted with the vesiculating magma (e.g. Houghton and Wilson, 1989), although not at the same stage of vesiculation for all erupting magma (e.g. White and Valentine, 2016). Where bubble wall remnants are more common, vesicles were likely abundant and large prior to fragmentation (Rausch et al., 2015), but even in this case water interaction usually still produces more blocky shards (Graettinger et al., 2013). If bubbles remain small and rare during exsolution, the only way the magma may fragment is via interaction with water (Rausch et al., 2015). Therefore, those deposits containing both highly and varyingly vesicular as well as blocky, non-vesicular clasts relate to erupting magma that was already vesiculating and fragmenting prior to water contact. The deposits with poorly vesicular or smaller grains indicate water triggered the eruption. The former is more commonly seen at Taal and suggests that for most prehistoric eruptions, the eruption had already been set in motion and was only altered, not triggered, by water interaction. Therefore, it is inferred that any water that interacted with magma at Taal Caldera Volcano only altered the eruption style and products; water interaction did not trigger the large-scale, ignimbrite-forming eruptions as was also the case for the 1875 Phreatoplinian eruption of Askja Caldera (Carey et al., 2009).

A certain degree of water involvement during most eruptions is supported by the abundance of flow deposits, their stratigraphic association with each other (i.e. (lapilli)-tuffs are often vertically associated with similar deposits) and the interbedded nature of tuff (flow) and lapillistone (fall) deposits. All of these characteristics suggest prehistoric eruptions from Taal Caldera Volcano were unsteady with frequently collapsing eruption columns. This type of behaviour is common during hydrovolcanic eruptions (Van Eaton et al., 2012; Biró et al., 2020). The poorly lithified nature of most Taal ignimbrites suggests relatively cool PDCs, which could be explained by water involvement at the source (Wilson, 2001).

3.6.4 Temporal changes in eruption style

Over time, Taal appears to have undergone changes in dominant eruption style. Although not all lithofacies can be linked to named eruption-units, those that can suggest that moisture and water had a larger impact in the more recent eruptions, including historical eruptions. At Taal, this pattern is firstly evidenced by the abundance of dune-bedforms in the Buco Formation (Geronimo, 1988), and some in the Pasong Formation, as well as historical deposits (Moore, 1967; Lagmay et al., 2021). Most dune-bedforms imply high-velocity, dilute currents, indicative of small-volume hydrovolcanic eruptions (e.g. Druitt et al., 1989; Brown and Andrews, 2015). The dune-bedforms within the Buco Formation do not support moisture-saturated currents, instead the componentry of stratasets more likely suggests a combination of more moisture-rich (i.e. fine ash and accretionary lapilli-rich stratasets) and drier PDCs (i.e. matrix poor, pumice-rich stratasets; Section 3.3.3). A combination of magmatic and hydrovolcanic eruptions is typical of emergent, Surtseyan-style eruptions (Cole et al., 2001). Since the Buco eruption source is hypothesised to be near modern-day Volcano Island (Fig. 3.11), it is possible that these deposits may record the emergence of Volcano Island

Cored pellets and coated clasts are more common in the younger Buco and Pasong ignimbrites while almost non-existent in the older Indang, Tadalac Cave and Alitagtag ignimbrites (Fig. 3.1). In the older formations, accretionary lapilli also do not appear in the main ignimbrites, while they do in the main Buco ignimbrite and rarely in some of the Pasong ignimbrites (Fig. 3.1; Chapter 2). Magma – water interaction in the Buco Formation is further supported by fluidal juvenile clasts which display cauliform textures that are associated with hydrovolcanic eruptions (Fisher and Schmincke, 1984; Németh and Kósik, 2020), and in both the Buco and Pasong formations where fluidal juvenile clasts have glassy, chilled rims. Glassy rims indicate clast interaction with a cooling substance, potentially water (Németh and Kósik, 2020), although air (Benage et al., 2014) or a relatively cool PDC (Valentine et al., 2000) are also able to produce glassy rims. In the Indang Formation, spatter clasts do not exhibit glassy rims and the ignimbrite is more indurated than any other ignimbrites associated with Taal. Therefore, the older Indang eruption likely experienced less magma-water interaction compared to the younger Buco and Pasong eruptions.

Ash grain textures also support an increased involvement of water with time for the major, caldera-forming eruptions from Taal Caldera Volcano. The Buco Formation contains active particles (i.e. bits of melt that made direct contact with water at the source; Austin-Erickson et al., 2008) and passive particles (i.e. bits of melt that fragmented due to the stresses produced by other bits of melt explosively interacting with water; Zimanowski et al., 2015) in the form of moss-like patterned grains and abundant blocky, non-vesicular grains (e.g. Büttner et al., 1999, 2002). Extensive post-fragmentation water interaction is also implied by the abundance of adhering grains and hydration skins (Zimanowski et al., 2015) seen in both the Buco and to a lesser extent the older Pasong Formation. The Pasong Formation shows no active particles, but contains passive particles in the form of blocky, non-vesicular grains, which are much less abundant than in the Buco Formation, however, since vesicular grains dominate the Pasong samples. Grain adhesion is rare in the older Alitagtag Formation, but passive particles are present in the form of blocky, non-vesicular grains. Non-vesicular

grains in the Tadalac Cave and Alitagtag formations are more common than in the Pasong Formation, therefore the younger Pasong Formation may have experienced less extensive magma-water interaction during the eruption, but more post-eruption. However, due to the limited sample size and the minimal abundance difference between vesicular and non-vesicular grains, we do not feel confident concluding a wildly different magma-water interaction history for the Pasong, Tadalac Cave and Alitagtag formations based on ash grain textures alone. However, it does open up an interesting path for future investigation. Textural evidence does show a clear, significant increase in magma-water interaction both during and post-eruption in the Buco Formation compared to the older three.

Reasons for the temporal increased magma – water interaction during and post-eruption, from the oldest to youngest major eruptions, may include the lack of a caldera structure in the early history of Taal. Prior to the Alitagtag eruption, a caldera structure may not have existed and therefore a lake filling it may not have either. Earlier eruptions could have coincided with a glaciation (e.g. 20 Ma, 150 Ma, 250 Ma; Siddall et al., 2003), leading to lowered global sea levels. Land bridges existed between the many islands that now make up the Philippines during glaciations (Hosner et al., 2014), therefore it is possible that the palaeo-coastline was further seaward than today, making it less likely that significant quantities of water were present near Taal. Additionally, Taal lies within the relatively young extensional Macolod Corridor (e.g. Defant et al., 1988, 1989). It is possible that at the start of Taal's volcanic activity this rift-zone was in its infancy and thus the modern-day Lake Taal region had a higher elevation. As rifting continued, land would have subsided and become closer to sea level, eventually allowing the sea to intrude into the low-lying land. Better age constraints for Taal's prehistoric eruptions (3 samples currently submitted for Ar-Ar dating) will help determine which of these hypotheses, if any, may be a factor in the increasing importance of magma-water interaction. Alternatively, a temporal decrease in overall eruption mass flux for each of Taal's caldera-forming eruptions may have allowed water better access to erupting magma over time (e.g. Houghton et al., 2003). The lack of fall deposits and the difficulty involved in calculating eruption intensity from (poorly exposed) ignimbrites (e.g.

Pyle, 2015) means that it is currently challenging to determine whether there was a significant change in eruption intensity between the caldera-forming eruptions. The fact that all of the caldera-forming eruptions involved at least one ignimbrite and a likely caldera-collapse phase (Chapter 2), however, suggests the differences in intensity may not be significant enough to affect water access during these phases.

3.7 Explosive eruptions at flooded calderas

It is likely that all caldera-forming eruptions experience magma – water interaction to some degree, be that magma interacting with groundwater or surface water (Németh and Kósik, 2020). Finding evidence of this interaction and the extent of it in prehistoric eruption deposits remains extremely challenging (White and Valentine, 2016). Part of this problem may stem from the fact that only about one third of magma interacts with water during eruptions, therefore deposits may not always show clear indicators of magma – water interaction at source (Zimanowski et al., 1997). During large-scale, ignimbrite-forming eruptions from flooded caldera volcanoes this problem may be exacerbated by the high velocities at which magma usually moves towards the surface, making it challenging for water to interact with magma at all (e.g. Houghton et al., 2003). Based on observations of deposits from Taal Caldera Volcano and other examples, outcrop-scale evidence such as lithofacies associations, as well as clast textures that may be indicative of large-scale hydromagmatic eruptions (often referred to as Phreatoplinian; Self and Sparks, 1978) are discussed. Comparison volcanoes were selected to represent a breadth of flooded and non-flooded calderas from various tectonic settings, ages, and compositions.

3.7.1 Are flooded caldera deposits finer grained than non-flooded caldera deposits?

A classic indicator of effective magma – water interaction is an abundance of fine ash (Walker and Croasdale, 1972; Van Eaton et al., 2012), especially close to source (Branney, 1991; Houghton et al., 2015). Erupted material experiences

enhanced deposition due to ash aggregation or rain-flushing (Walker, 1981; Van Eaton and Wilson, 2013) allowing fine ash to deposit closer to source than it normally would. Although fine grained deposits are usually quoted as a general feature of hydrovolcanic eruptions, this appears to only be the case for fall deposits (e.g. Sparks et al., 1981; Nairn et al., 1995; Machida et al., 1996; Wilson, 2001). The Oruanui ignimbrite, New Zealand, is the only example of a massive, thick ignimbrite that is dominated by fine ash and is finer grained close to source compared to more distal localities (Self, 1983; Wilson, 2001). Other ignimbrites deposited from 'wet' eruptions tend to contain abundant bedforms (Kos Plateau Tuff, Greece; Minoan eruption, Greece; Bond and Sparks, 1976; Allen and Cas, 1998), and/or consist of multiple thin flow-units (Neapolitan Yellow Tuff, Italy; 1875 Askja eruption, Iceland; Sparks et al., 1981; Cole and Scarpati, 1993). Interestingly, the Taupo ignimbrite, which also erupted from the Taupo Volcanic Centre like the Oruanui ignimbrite, is coarser proximally than distally (Wilson and Walker, 1985). Ignimbrites from other flooded calderas usually show this same trend, even if fall deposits with abundant fines were produced during the same eruption (e.g. Wilson and Walker, 1985; Nairn et al., 1995; Machida et al., 1996; Ponomareva et al., 2004).

However, a lack of fines in pyroclastic deposits of explosive eruptions from flooded calderas does not necessarily mean abundant fines were not produced during the ignimbrite-forming phase of the eruptions. The presence of surface water can actually encourage the deposition of fines-poor ignimbrites if steam is produced when the PDC passes over water (Sigurdsson and Carey, 1989), which was likely the case at Taal Caldera Volcano where PDCs would have travelled some distance across Lake Taal. Steam encourages the elutriation of fine ash (Sigurdsson and Carey, 1989), a process which is especially efficient in fluid escape-dominated flow-boundary zones from which massive ignimbrites are deposited (Branney and Kokelaar, 2002). Excessive moisture may hinder elutriation (Branney and Kokelaar, 2002), but a turbulent flow regime can further support it (Cas et al., 2011). Elutriated fines overpass proximal localities and deposit further from source (e.g. Kokelaar et al., 2007). Several relatively thick (max 0.5 m) co-ignimbrite deposits (Tpel, Tves, possibly mT) are identified

around Taal Caldera Volcano supporting intense fines elutriation from some PDCs, despite much of this ash likely ending up in the seas surrounding Luzon.

As recorded in the Taal succession, the accretion of fine ash around juvenile clasts and ash pellets can be extensive and decreases the amount of loose fine ash in the matrix of relatively proximal pyroclastic deposits. Accretion and fines elutriation can thus make Taal ignimbrites seem relatively coarse-grained in the field. An alternative explanation for the relatively coarse Taal ignimbrites is that the magma discharge rate was too high during the ignimbrite-forming phase to allow efficient magma – water interaction (e.g. Maeno and Taniguchi, 2007).

3.7.2 Do fluidal juvenile bombs indicate magma – water interaction?

Large fluidal juvenile bombs have been identified in ignimbrites and associated proximal agglomerates, agglutinates and lithic breccias, which, together with other lines of field evidence (e.g. imbrication, gradation into massive lapilli-tuffs), shows that they were transported in a flow (e.g. Mellors and Sparks, 1991). The exact mechanism of their formation is still being debated (Branney and Kokelaar, 2002) and includes: disruption of a degassed lava lake or dome by water and/or more gas-rich magma (Mellors and Sparks, 1991), coincident fire fountaining and PDC eruptions (Rosi et al., 1996; Allen, 2005), varying ascent velocities in the conduit (Bear et al., 2009), water intruding into the magma chamber due to a drop in magmastatic pressure and forcing out gas-poor magma (Palladino and Simei, 2005; Kokelaar et al., 2007), and peripheral gas-poor magma erupting through ring faults (Palladino and Simei, 2005; Palladino et al., 2014; Firth et al., 2015). Within ignimbrites, fluidal juvenile bombs are commonly deposited together with pumice clasts (e.g. Druitt et al., 1989; Allen, 2005; Kokelaar et al., 2007; Bear et al., 2009; Rooyakkers et al., 2020), which implies that two fragmentation mechanisms were simultaneously active during the ignimbrite-forming eruption: brittle (producing ash and pumice) and viscous (producing fluidal bombs) fragmentation (Cashman and Scheu, 2015; Rooyakkers et al., 2020).

Fluidal juvenile bomb-rich deposits are frequently associated with flooded calderas and have been hypothesised to be an indicator of water involvement in caldera-forming eruptions (Druitt et al., 1989; Mellors and Sparks, 1991; Branney and Kokelaar, 2002; Kokelaar et al., 2007). A trigger, such as water, is thought to be needed to erupt the gas-poor magma represented by fluidal juvenile bombs, which may otherwise not have been erupted (Mellors and Sparks, 1991). At Taal, fluidal juvenile bombs are present in three of the younger caldera-forming eruptions (i.e. the Indang, Pasong and Buco eruptions), all of which appear to have interacted with water to varying extents during their eruptions (Section 3.6.4). Not all studies agree that water interaction drives the eruption of the gas-poor magma represented by fluidal juvenile bombs (e.g. Bear et al., 2009), but most link the occurrence of fluidal juvenile bombs with the caldera collapse phase of eruptions. In this case, the caldera collapse is the trigger that allows gas-poor magma to erupt (Rosi et al., 1996; Palladino and Simei, 2005; Kokelaar et al., 2007; Firth et al., 2015; Rooyakkers et al., 2020).

However, if caldera collapse alone is the prerequisite for fluidal juvenile bomb production, then why do not all caldera-forming eruptions produce fluidal juvenile bombs, such as the Mazama eruption, Crater Lake, USA (rhyodacite, Bacon and Lanphere, 2006) and the Holocene Cerro Blanco eruption, Argentina (rhyolite – rhyodacite, Báez et al., 2020)? Evidence from Taal deposits suggests magma composition could be a factor since the only caldera-forming deposit identified thus far without abundant fluidal juvenile bombs is dacitic (the most evolved), while the other 3 are (basaltic) andesite. Additional evidence of the production of fluidal juvenile bombs being linked to magma composition is provided by eruptions from the flooded caldera volcano Taupo, New Zealand (Wilson, 1985) and Atitlán, Guatemala (Rose et al., 1987), which experienced rhyolitic eruptions and extensive explosive magma-water interaction, but produced no fluidal juvenile bombs. Other (flooded) caldera volcanoes whose pyroclastic deposits include fluidal juvenile bombs are less evolved, usually in the 54 – 63 wt.% SiO₂ range (e.g. Druitt et al., 1989; Mellors and Sparks, 1991; Rosi et al., 1996; Valentine et al., 2000; Bear et al., 2009; Caulfield et al., 2011;

Vinkler et al., 2012; Firth et al., 2015), with rare exceptions pushing into the dacitic classification (Rooyakkers et al., 2020).

It therefore seems that magma must be (partially) in the (basaltic) andesite range for fluidal juvenile bombs to erupt. More mafic magmas are less likely to cross the glass transition (towards colder temperatures), preventing brittle deformation, even at high eruption rates because their structural relaxation time is too big (Gonnermann, 2015). However, structural relaxation time also depends on magma viscosity and therefore there could be other factors that determine whether magma fragments in a brittle or viscous manner (e.g. degassing history, magma ascent rate; Cashman and Scheu, 2015; Gonnermann, 2015). At volcanoes where the composition of fluidal juvenile bombs and pumice is the same, a non-compositional factor must account for the different fragmentation styles. However, the hypothesis that there must be a (basaltic) andesite magma component in eruptions to allow fluidal juvenile bombs formation remains valid (i.e. a homogeneous rhyolitic magma will not erupt spatter clasts).

It is therefore hypothesised that fluidal juvenile bombs were produced during Taal's caldera-forming eruptions when a source of relatively mafic, degassed magma was available, strongly encouraged by, but not requiring water interaction. Although this hypothesis could be applied to other flooded caldera volcanoes (e.g. Krafla Caldera in Rooyakkers et al., 2020), there are exceptions, most notably Masaya Caldera, which experienced one of the only recorded basaltic caldera-forming eruptions in the world, but produced no fluidal juvenile bombs (Pérez et al., 2020). Therefore, it remains important to consider each volcano individually.

3.7.3 Implications of magma – water interaction on ignimbrite induration

If a significant volume of water is involved in an eruption it can cool PDCs down enough to prevent welding (Monzier et al., 1994; Nairn et al., 1995; Wilson, 2001), which is exemplified by the Oruanui ignimbrite, New Zealand, and the Los Chocoyos Ash, Guatemala, where completely unwelded ignimbrites of at

least 200 m are observed (Rose et al., 1987; Wilson, 2001). Although welded ignimbrites may be associated with flooded calderas such as in the Lower Pumice 1 and Cape Riva deposits from Santorini Caldera, Greece, they are rare and the welding is only partial (Druitt et al., 1989).

At Taal, most ignimbrites are non-lithified and rarely indurated (Fig. 3.2); induration may occur due to post-depositional alteration. Ignimbrites, especially those with water involvement at source, are prone to alteration and frequently undergo zeolitisation (Brown and Andrews, 2015). This process is clearly visible in the Campanian ignimbrite and the aptly named Neapolitan Yellow Tuff, both from caldera-forming eruptions from the flooded Campi Flegrei Caldera, Italy (Wohletz et al., 1995; de’Gennaro et al., 2000; Scarpati et al., 2020).

As a general rule, therefore, extensively non-welded, especially non- or poorly-lithified ignimbrites, which may show evidence of post-depositional alteration, is characteristic of a flooded caldera eruption. There are rare exceptions, notably the non-welded ignimbrites associated with the ‘dry’ caldera-forming eruptions from Los Humeros, Mexico (Zaragoza ignimbrite, also non-lithified; Carrasco-Núñez and Branney, 2005) and Cerro Blanco, Argentina (Báez et al., 2020).

3.7.4 Do flooded caldera pyroclastic deposits have indicative lithofacies associations?

Based on the low abundance of pumice fall deposits associated with the flooded Tavui volcano, Papua New Guinea, (McKee, 2015) and Kuwae volcano, Vanuatu (Monzier et al., 1994), it appears that flooded calderas produce less pumice fall deposits compared to non-flooded calderas. However, these examples seem to be an exception as the majority of flooded calderas, including Taal, produce pumice fall deposits (Sparks et al., 1981; Wilson and Walker, 1985; Druitt et al., 1989; Nairn et al., 1995; Lloyd et al., 1996; Machida et al., 1996; Ponomareva et al., 2004) and conversely, non-flooded caldera eruptions may lack abundant pumice fall deposits (Ellis et al., 2013; Báez et al., 2020).

Pumice falls usually signal the start of an explosive eruption at a flooded caldera, although the Taupo (New Zealand), Kuwae (Vanuatu), Kurile Lake (Russia) and Kos Tuff (Greece) eruptions started with hydrovolcanic phases (Wilson and Walker, 1985; Monzier et al., 1994; Allen, 2001; Ponomareva et al., 2004). Perhaps during the hydrovolcanic phases, eruptions were immediately inundated by surface water, either because of slow magma discharge rates or water gaining access to the magma through faults for example, while those eruptions able to produce Plinian eruption columns were able to prevent effective magma – water interaction at the start of the eruption. Although pyroclastic deposits at Taal Caldera Volcano show evidence of eruptions commencing with both pumice fall deposits and dilute PDCs (the palaeosols overlain by non-accretionary lapilli-bearing and underlain by accretionary lapilli-bearing (snacs) facies association), named caldera-forming formations only expose pumice fall deposits or massive lapilli-tuffs at their bases, thus suggesting caldera-forming eruptions from Taal Caldera Volcano did not start with the production of fully dilute PDCs.

Flooded calderas commonly experience contemporaneous pumice and hydrovolcanic ash falls, indicating shifts in eruption styles on relatively short timescales (e.g. Sparks et al., 1981; Pérez et al., 2020), and also frequently exhibit coeval fall and flow activity (e.g. Wilson, 2001). Although evidence for coeval fall and flow activity is also seen in pyroclastic deposits from non-flooded calderas such as the Bishop Tuff, USA (Wilson and Hildreth, 1997) and the Zaragoza ignimbrite, Mexico (Carrasco-Núñez and Branney, 2005), where pumice fall deposition occurs together with the main ignimbrite-forming stage of the eruption, perhaps a reflection of the relative steadiness of the eruption column (i.e. the eruption column can still sustain itself while the eruption is also undergoing extensive flow activity).

Hydrovolcanic eruptions tend to have much less steady columns (Van Eaton et al., 2012; Van Eaton and Wilson, 2013; Houghton et al., 2015) and thus pumice fall deposits are rarely seen in thick ignimbrites produced by flooded caldera volcanoes (Oruanui eruption, New Zealand, is an exception; Wilson, 2001),

even if the ignimbrite-forming phase is hypothesised to have experienced minimal explosive magma – water interaction at the eruption source (e.g. Campanian ignimbrite, Italy; Scarpati et al., 2020). Taal Caldera Volcano’s pyroclastic deposits currently similarly show no clear field evidence of pumice fall deposition during the main ignimbrite-forming phases.

The production of fully dilute PDCs is common at flooded caldera volcanoes (e.g. Sparks et al., 1981; Lloyd et al., 1996; Carey et al., 2010; Pérez et al., 2020), while this is rarely observed in such abundance during non-flooded caldera eruptions (e.g. Carrasco-Núñez and Branney, 2005; Edgar et al., 2017). Taal deposits reflect this, with the Buco Formation and Pasong Formation both containing at least one fully dilute PDC phase producing cross-bedded facies, while the Alitagtag Formation, which experienced less magma – water interaction (Section 3.6.4), does not. The Masaya (Nicaragua), Askja 1875 (Iceland), and Macauley Island (New Zealand) caldera-forming eruptions are extreme examples of flow deposit abundance because their flow phase produced only dilute PDCs, which frequently deposited accretionary lapilli-rich cross-bedded tuffs with possible dune structures (Sparks et al., 1981; Lloyd et al., 1996; Carey et al., 2010; Pérez et al., 2020). Somehow water was able to interact very effectively with magma during these eruptions.

3.8 Conclusions

- There are 23 different lithofacies in the prehistoric pyroclastic deposits at Taal Caldera Volcano (Table 3.1), which suggests that Taal had dynamic and varied eruption styles and depositional processes.
- Ash aggregates found in Taal’s prehistoric deposits indicate that at times, conditions during eruptions and/or depositional processes were sub-saturated (e.g. accretionary lapilli) to saturated (e.g. amalgamated pellets).

- Vertical lithofacies are grouped into 7 lithofacies associations (Table 3.3): (1) the pumice fall deposits overlain by coarse, massive facies or a palaeosol (fm) facies association, (2) the tuff repetitions (tr) facies association, (3) the diffuse cross-bedding linked to massive beds (dxbm) facies association, (4) the interbedding of massive and cross-bedded non- and accretionary lapilli-bearing (nac) facies association, (5) the ash pellet tuffs mainly associated with tuffs (pt) facies association, (6) the palaeosols overlain by non-accretionary lapilli-bearing facies and underlain by accretionary lapilli-bearing (snacs) facies association, and (7) the massive lithic breccia most often associated with massive lapilli-tuff (blt) facies association.
- Deposits from Taal Caldera Volcano show Markovity: facies that deposit are not random and directly relate to their underlying facies.
- Smaller-scale eruptions from Taal Caldera Volcano (e.g. the Tagaytay Units and non-climactic phases of caldera-forming eruptions) are more likely to experience pumice fall deposition as opposed to the climactic phases of ignimbrite-forming eruptions from Taal Caldera Volcano, which appear more likely to produce pyroclastic density currents than the smaller-scale eruptions.
- During deposition from a pyroclastic density current, subtle, temporary unsteadiness at the flow-boundary zone was common, but a complete switch to a traction-dominant flow-boundary zone was rare.
- When cross-bedded facies were deposited, the overall depositional regime was stable (i.e. cross-bedded facies are unlikely to pass upwards into diffuse cross-bedded or massive facies) despite the fact that individual units were likely deposited by turbulent, erosive, possibly multiple pyroclastic density currents.
- Non-accretionary lapilli-bearing facies are more likely to pass upwards into accretionary lapilli-bearing facies rather than the other way around,

which implies that once conditions in a depositing pyroclastic density current favoured the formation and/or deposition of accretionary lapilli, they were unlikely to reverse.

- Lithic breccias are always overlain by massive lapilli-tuffs (mLT), suggesting that pyroclastic density currents waned gradually and deposited massive lapilli-tuffs after lithic breccias before any finer grained facies (e.g. diffuse cross-bedded tuff).
- The lack of lithic breccias directly above a palaeosol suggests that large-scale eruptions from Taal Caldera Volcano were unlikely to experience immediate caldera collapse, as is the case for most caldera-forming volcanoes (Branney and Acocella, 2015).
- The distribution of lithic breccias and fluidal juvenile bomb deposits along the base of Tagaytay Ridge coincide with a fault and could provide evidence of the activation of, and eruption along, caldera faults during caldera collapse.
- The caldera-forming eruptions from Taal Caldera Volcano may experience phases of smaller-scale activity, often involving fully dilute pyroclastic density currents, which produce cross-bedded facies, including dune-bedforms, in between massive and diffuse cross-bedded lapilli-tuffs, while caldera-forming eruptions themselves are punctuated by smaller-scale eruptions like those represented by the Tagaytay Units and historical eruptions.
- The qualitative, quantitative and statistical analysis of vertical lithofacies associations have allowed three different common eruption sequences to be compiled for Taal Caldera Volcano's prehistorical eruptions (Fig. 3.20).

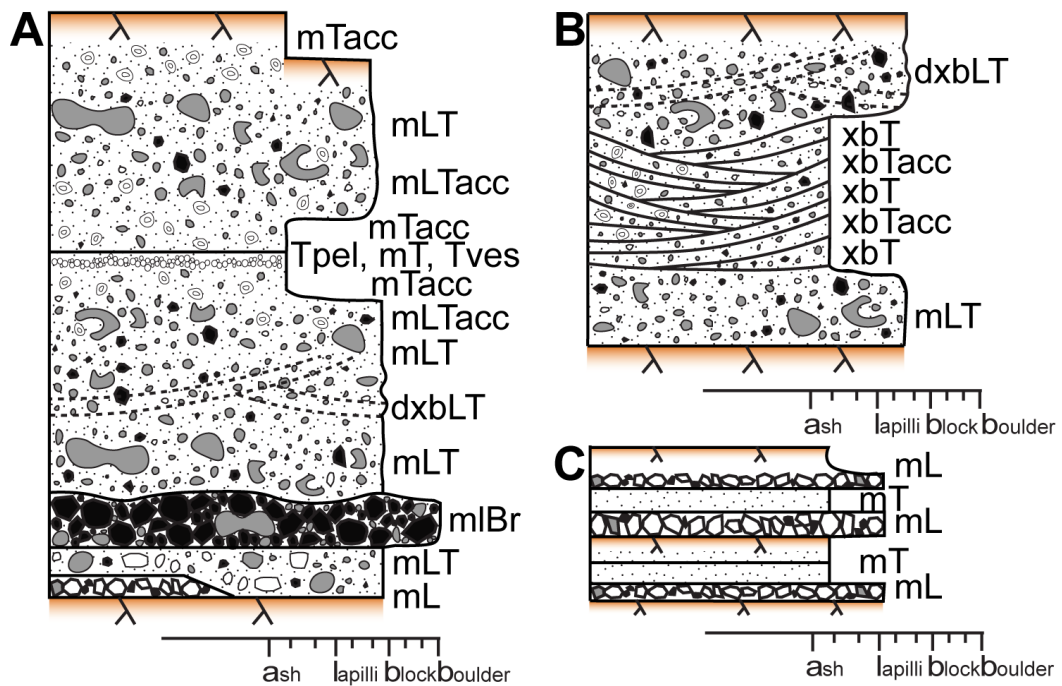


Fig. 3.20: A compilation of common eruption sequences from Taal Caldera Volcano based on lithofacies and Markov Chain Analysis. **(A)** A typical larger-scale, caldera-forming eruption, **(B)** smaller-scale activity within caldera-forming eruptions, **(C)** sequences of smaller-scale eruptions independent of caldera-forming eruptions.

- At Taal Caldera Volcano, pyroclastic deposits show more evidence of moisture availability during transport than direct interaction of magma and water at the source. However, where the latter did occur during large-scale, ignimbrite-forming eruptions, water interaction did not trigger the eruption, but only altered the eruption and/or depositional style.
- There is a suggested increase in the amount of magma – water interaction at source and during transport experienced by Taal’s prehistoric caldera-forming eruptions over time (i.e. the oldest Alitagtag Formation shows less evidence of magma – water interaction than the youngest Buco Formation). Possible explanations for this trend are a lake not existing during the infancy of Taal Caldera, changes in the palaeo-coastline, and/or the age of the Macolod Corridor rift-zone.

- Ignimbrites produced by flooded caldera eruptions are not exclusively finer-grained compared to their non-flooded counterparts. At Taal Caldera Volcano, and possibly other flooded caldera volcanoes, this lack of fines in the matrix of proximal pyroclastic deposits may be explained by the abundance of ash aggregation processes and a high loss of fine material during transport via elutriation, as well as the inability of magma to effectively interact with water at high discharge rates.
- Fluidal juvenile bombs at Taal Caldera Volcano show features that could support their explosive interaction with water (e.g. breadcrust textures and glassy clast rims), but water is unlikely a requirement for their formations. More likely, fluidal juvenile bombs were produced during caldera-forming eruptions if a source of relatively mafic, degassed magma was available, strongly encouraged by, but not requiring, water interaction.
- In general, extensively non-welded, especially non- or poorly-lithified ignimbrite, which may show evidence of post-depositional alteration/lithification, as seen at Taal Caldera Volcano, are characteristic of an explosive eruption from a flooded caldera volcano.
- Explosive eruptions from flooded caldera volcanoes may include both pumice and ash fall deposits and are more likely to be unsteady compared to non-flooded caldera eruptions, shifting eruption styles on relatively short timescales.
- Fully dilute pyroclastic density currents are commonly produced during flooded caldera eruptions like at Taal Caldera Volcano, but rarely seen at the same abundance levels in non-flooded caldera eruptions.

Chapter 4

The geochemical and petrographic characterisation and evolution of prehistoric eruptions from Taal Caldera Volcano

4.1 Introduction

To better identify the scale of large volcanic eruptions and their regional or global impacts, the chemical fingerprinting of on-land tephras from these eruptions is incredibly important in order to recognise them distally, especially in marine cores. For example, great success has been made, using such techniques, in identifying the Campanian eruption of Campi Flegrei throughout the Mediterranean and Eastern Europe (e.g. Smith et al., 2011A). Chemical fingerprinting also assisted in identifying a previously unclassified tephra layer in northern and southern polar ice core records as the 1257 AD eruption of the Rinjani Volcanic Complex, Indonesia (Lavigne et al., 2013). Furthermore, in areas where deposits are difficult to map or trace laterally, geochemical fingerprinting can help to distinguish individual eruption-units in the field, as in the Snake River Plain (e.g. Ellis et al., 2019) and with the Los Chocoyos Ash in Guatemala (Hahn et al., 1979). This is especially important in countries like the Philippines where ever-changing land use and the erosive tropical climate make accessibility to on-land deposits limited (de Maisonneuve et al., 2020). However, despite the limited on-land deposits, there is an abundance of marine core tephra layers around the Philippines (Ku et al., 2009) and in the wider region.

Taal Caldera, Philippines, is an example of a volcano that has produced at least 4, likely 7, prehistoric large-scale, caldera-forming eruptions (Fig. 4.1; Chapter 2), but on which there has been only limited geochemical characterisation (Listanco, 1994; Martinez and Williams, 1999). By better understanding the geochemical fingerprints of specific eruption-units from Taal Caldera, the spatial impact of any one of these eruptions can be better defined and new eruption-

units may be revealed. An increased comprehension of the magmatic system feeding Taal Caldera may also provide insight into future eruption styles and where in its caldera cycle Taal Caldera is presently situated.

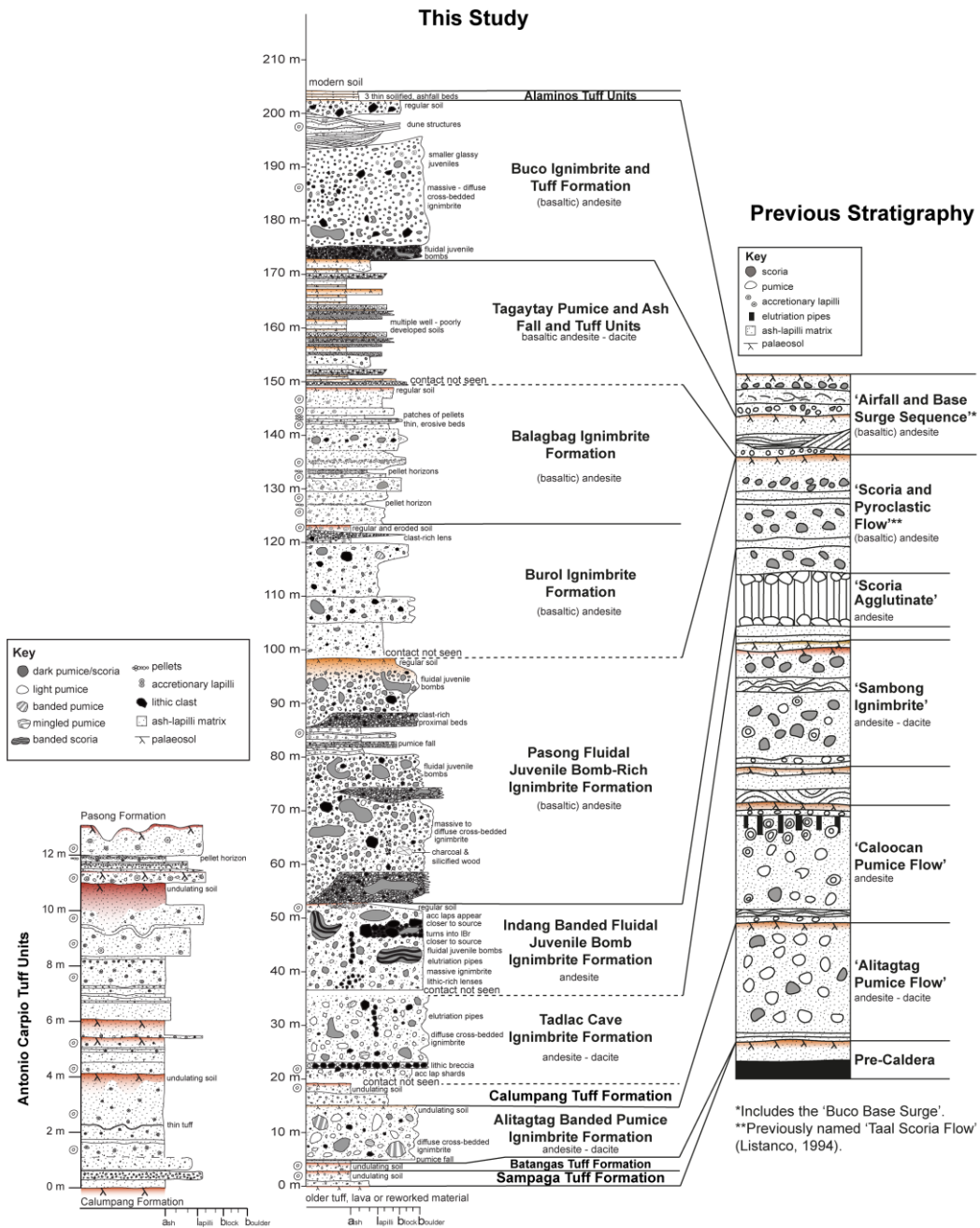


Fig. 4.1: The previous stratigraphy established by Listanco (1994) and partly renamed by Martinez and Williams (1999) correlated where possible with the new stratigraphy established during this study (Chapter 2). Listanco (1994) identified the following as caldera-forming eruptions: ALI, CAL, SAM and SPF. Major, possibly caldera-forming eruptions are: Alitagtag, Indang, Pasong and Buco formations, and likely the Tadalac Cave, BuroI and Balagbag formations. The chemical composition of each eruption-units (formation), where available, is included for both the previous (Listanco, 1994) and new stratigraphy.

4.1.1 Taal Caldera eruptive history and geochemistry

Juvenile whole rock geochemistry, based on the previously published stratigraphy (Fig. 4.1; Listanco, 1994), shows that Taal's prehistoric deposits range from basaltic andesite to dacite in composition (Listanco, 1994; Martinez and Williams, 1999). Listanco (1994) also makes some attempts to differentiate eruption-units in his stratigraphy based on the compositions of plagioclase phenocrysts (Listanco, 1994).

Using major and trace element data, Listanco (1994) identified two trend lines on Harker plots within the caldera-forming eruptions, which were interpreted as evidence of magma mixing (Fig. 4.2; Listanco, 1994). Magma mixing in the Taal magmatic system was hypothesised to be confined to independently evolving melt batches (Miklius et al., 1991; Listanco, 1994) originating from a heterogeneous mantle (Miklius et al., 1991). Tapping of these different melt batches is thought to explain the chemical differences in the caldera-forming eruptions identified by Listanco (1994). The compositions of the caldera-forming eruptions has been compared to historical eruptions from Volcano Island (Miklius et al., 1991; Listanco, 1994). Initially, limited samples from what were assumed to represent prehistoric (caldera-forming) eruptions retrieved from

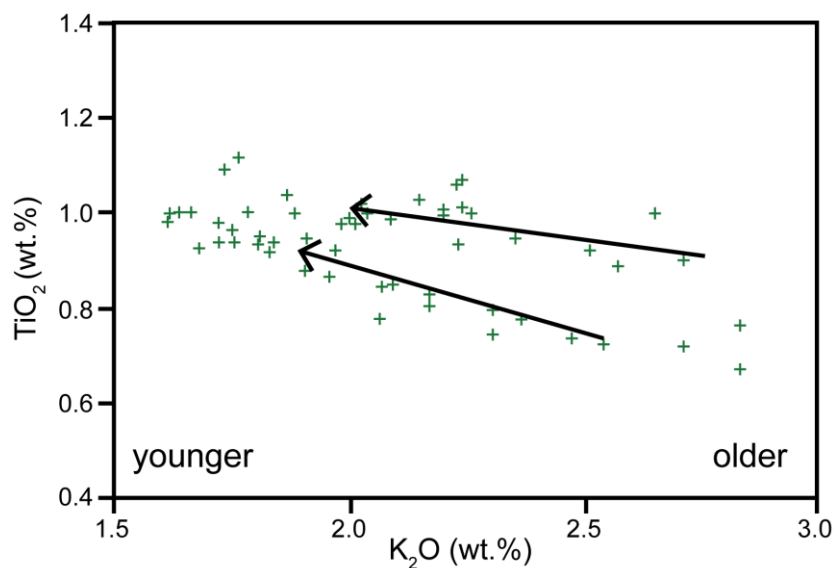


Fig. 4.2: Graph adapted from Listanco (1994) showing Taal caldera samples. Two different trend lines were interpreted from the data by Listanco (1994). Trend lines point towards younger formations.

Tagaytay Ridge and Napayung Island, could be clearly distinguished from historical Volcano Island samples (Miklius et al., 1991). However, Listanco's (1994) more extensive dataset showed overlap between the two datasets (Fig. 4.2). The main focus of all these previous studies (Miklius et al., 1991; Listanco, 1994; Mukasa et al., 1994) was on the chemical distinction and characterisation of historical deposits from Volcano Island. Even Listanco (1994), who published the largest prehistorical dataset thus far, often grouped all prehistoric samples together. In addition, the work does not discuss chemical variation within individual eruption-units in any detail and does not attempt to chemically distinguish the different caldera forming eruption-units from each other (Listanco, 1994). This current gap in the geochemical understanding of Taal Caldera Volcano will be addressed in this study.

4.1.2 Regional geochemistry

Volcanic activity in the region around Taal Caldera Volcano (Fig. 4.3) is driven by the subduction of the South China Sea plate below the Philippine Sea plate along the Manila Trench (Fig. 4.3; Defant et al., 1989; Defant et al., 1991; Delmelle et al., 1998; Castillo and Newhall, 2004). The Manila Trench is divided into the northern Bataan segment, split into a west and east segment, and the southern Mindoro segment, divided by the NE-SW trending Macolod Corridor, within which Taal Caldera lies (Fig. 4.3). The Macolod Corridor is hypothesised to be an area of rifting caused by shearing between the Philippine fault and the southern section of the Manila Trench (Förster et al., 1990; Galgana et al., 2007). Volcanism within the Corridor may thus be related to rifting (Defant and Ragland, 1988). The entire arc has a calc-alkaline signature with typical arc phenocryst assemblages (pyroxene, plagioclase, titanomagnetite, rare amphibole; Defant et al., 1991), but the Macolod Corridor and Mindoro segment show particular enrichment in radiogenic Sr isotopes compared to the Bataan segments (see figure 16 in Defant et al., 1991), while both the Macolod Corridor, Mindoro segment and the East Bataan segment are enriched in large ion lithophile elements (LILE) and light rare earth elements (LREE) when compared to the West Bataan segment (see figures 2, 3 and 4 in Defant et al., 1991). For the Macolod Corridor, the LILE enrichment is thought to be related to

small degrees of partial melting of a mantle source due to rifting, or to the incorporation of crustal material from the Palawan-Mindoro Block during subduction (Chapter 1, Fig. 1.1), the latter of which also holds true for the Mindoro segment (Fig. 4.3; Defant et al., 1988; Defant et al., 1989).

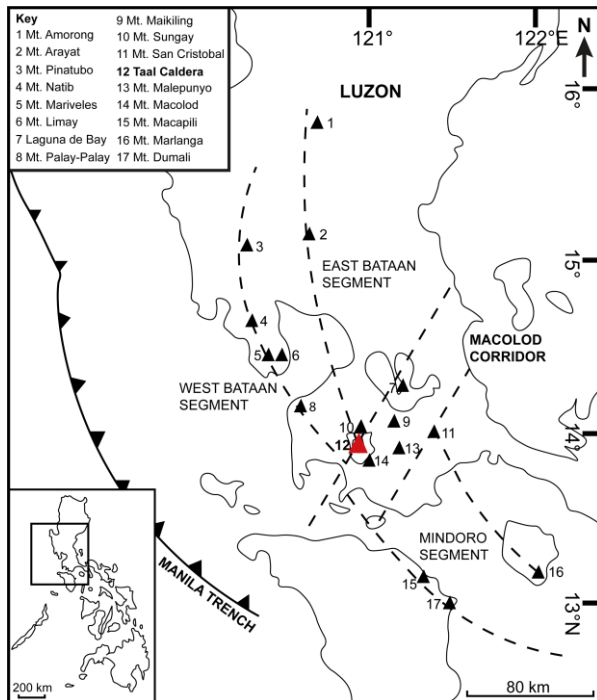


Fig. 4.3: Taal Caldera Volcano (red triangle) located in the Macolod Corridor in Southwest Luzon. The Manila Trench and different segments of the Luzon Arc are highlighted, as well as multiple key volcanic centres within each segment. Based on Defant et al. (1991).

Although previous work has investigated the chemistry of volcanic units both within the Luzon Arc (Defant et al., 1988, Defant et al., 1989; Defant et al., 1991; Listanco, 1994; DuFrane et al., 2006; Ku et al., 2009) and the Macolod Corridor (Listanco, 1994; Mukasa et al., 1994; Vogel et al., 2006), no study has compared an extensive dataset of Taal's prehistoric deposits with all the different volcanic centres within the Macolod Corridor or to other segments of the Luzon Arc. When any Taal samples are included in studies, they

frequently include only historical samples, often lavas, from Volcano Island and only rare prehistoric samples (Miklius et al., 1991; Mukasa et al., 1994). In these studies, prehistoric samples only refer to those sampled along Tagaytay Ridge and on Napayung Island (Fig. 1.2); rare stratigraphic context is provided and samples are not linked to any specific eruption-unit. Only Listanco (1994) and Martinez and Williams (1999) performed chemical analysis on named Taal prehistoric eruption-units placed in stratigraphic context. When compared to other volcanoes in the region, Taal samples, including historic samples, are all combined and investigated as one dataset (Listanco, 1994; Mukasa et al., 1994; Vogel et al., 2006). Therefore, this study will focus on the new prehistoric dataset collected for this work and will compare it to published datasets for

different volcanic centres within the Macolod Corridor. This will provide an overview of any temporal chemistry trends within the region and determine whether Taal's prehistoric deposits can be sufficiently discriminated from other regional pyroclastic deposits. In addition, Taal's prehistoric deposits will be plotted with volcanic units from volcanoes on other segments of the Luzon Arc (Fig. 4.3) to investigate whether Taal's prehistoric samples all plot within a field defined for the Macolod Corridor (Defant et al., 1988; Defant et al., 1989; Defant et al., 1991; Miklius et al., 1991; Vogel et al., 2006).

4.1.3 Aims and objectives

This chapter aims to chemically and petrographically characterise and fingerprint each named formation of the Taal succession:

- Taal's chemical signature is first placed in a regional context to investigate if Taal deposits can be chemically distinguished from other regional volcanoes.
- Named formations from the Taal Group are petrographically and geochemically characterised to investigate any internal variations.
- Harker diagrams are used to identify any potential fractionation or mixing trends within the Taal Group magmas.
- Linear discriminant analysis on the JMP statistical program is employed to support or identify elements or elemental combinations that could be used to distinguish eruption-units. The great strength of this method is that it combines multiple elements, which individually may minimally discriminate different units, but when combined are able to discriminate units much more successfully (Huff, 1983; Kramer et al., 2001); this method, or similar, statistical methods have been used by other studies to characterise volcanic eruption-units (e.g. Borchardt et al., 1972; De Silva and Francis, 1989; Kramer et al., 2001; Wulf et al., 2008; Lanzo et al., 2010).
- Using this data, the best individual elements for discrimination are determined.
- Named formations are then organised temporally to determine whether Taal's chemical signature has changed over time.

- Finally, Taal's chemical characteristics are compared to those of other global calderas to highlight parallels, or differences, between them and any emerging trends with regards to the chemistry of caldera-forming eruptions.

4.2 Methods

4.2.1 Field sampling and XRF analysis

Fieldwork was conducted across 3 separate field seasons, lasting 13 weeks in total. 126 samples were collected for X-ray fluorescence (XRF) analysis and 21 samples for thin sectioning. Certain formations lack geochemical data because samples could not be collected. Juvenile clasts only were sampled where possible. Where ignimbrites contained only rare, small (<1 cm) juvenile clasts, a bulk (matrix) sample was taken. Bulk material has been used in geochemical correlation of volcanic units (e.g. Hahn et al., 1979; De Silva and Francis, 1989), but will be compared to juvenile material of the same unit where possible to confirm it can be used for geochemical characterisation.

Most juvenile samples had an outer rim of matrix material (usually fine ash), ranging from 1 mm to 1 cm in thickness. To ensure juvenile material only was included in further analyses, this matrix material was removed after drying using a DREMEL model 3000 drill. For larger clasts (3 cm or more), a large sandpaper drill bit was used first. Clasts were then placed in an ultrasonic bath for at least 30 minutes before being placed in an aluminium tray and put into a LEEC drying cabinet at around 40°C overnight. Once dry, clasts were looked at again and, if needed, a smaller drill bit was used to remove as much remaining matrix as possible. Clasts were put into an ultrasonic bath again and dried. For smaller, more delicate clasts, only the small drill bit was used. Clasts with abundant loose, fine ash within their outer rim were put into an ultrasonic bath first before drilling. Where samples did not require cleaning, they were still placed in the drying cabinet to remove any excess moisture. After cleaning, all samples were coarsely crushed with a hardened steel fly press, milled into a

fine powder in agate-lined pots in a planetary mill, and prepared for XRF analysis, which was performed on the University of Leicester PANalytical Axios Advanced XRF spectrometer. Major elements were analysed from fused glass beads that were made from ignited powders with a sample to flux (80% Li metaborate and 20% Li tetraborate) ratio of 1:5. Trace elements were determined on 32 mm diameter pressed powder pellets. The pellet was made from mixing 7 g of sample powder with 12 – 15 drops of a 7% PVA solution pressed at 10 tons per square inch.

4.2.2 Data quality

To test the quality of elements, elements which were recorded as a value less than a certain number (e.g. <1.3 ppm) in the XRF dataset were removed from the dataset (Appendix D; Cs, Ni, Sb, Se, Sn and W). Two further quality tests were then conducted with the remaining elements. These include: 1. plotting elements against their respective loss on ignition (LOI); and 2. isocon analysis. Error bars of individual data points were also calculated to test the precision of the data based on standards acquired by XRF analysis. All tests are explained further in the following paragraphs. Samples are analysed by named formation, each representing a single eruption-unit. Since the Tagaytay Units and unknown samples contain multiple eruption-units they are likely to display a relatively wide geochemical range. As such, any hypothesised element mobilisation may just be a reflection of this wide geochemical range. Therefore, the Tagaytay Units and unknown samples will not be used to identify mobilised elements.

Quality test 1: loss on ignition (LOI)

Concentrations were plotted by element against their LOI values, grouped by formation (Fig. 4.4). If individual samples record higher LOI values, it is more likely that elements were mobilised in this sample. If certain elements were mobilised in samples with relatively high LOI values, their concentrations are expected to fall outside the range of concentrations recorded by samples with

relatively low LOI values. A LOI value of 2 wt.% was set as a baseline above which elements were more likely to remobilise (Fig. 4.4) because each formation (except the Buroi Formation) includes at least one sample with a LOI value of >2 wt.%. The less mobile an element is thought to be, the more reliable the element will be considered in this study. Elements were assigned as mobile if samples with a LOI of >2 wt.% plotted significantly outside of the concentration range displayed by samples with a LOI of <2 wt.% (Fig. 4.4); elements were assigned as potentially mobile if any sample concentrations, regardless of their LOI, plotted significantly outside of the concentration range displayed by other samples of the same formation (Fig. 4.4); elements were assigned as immobile if all sample concentrations fell within the same range regardless of their LOI values (Fig. 4.4). Mobile elements comprise MgO, CaO, P₂O₅, As, Co, Cr, Pb and U, while the only potentially mobile element is Cu (Fig. 4.4; Table 4.2).

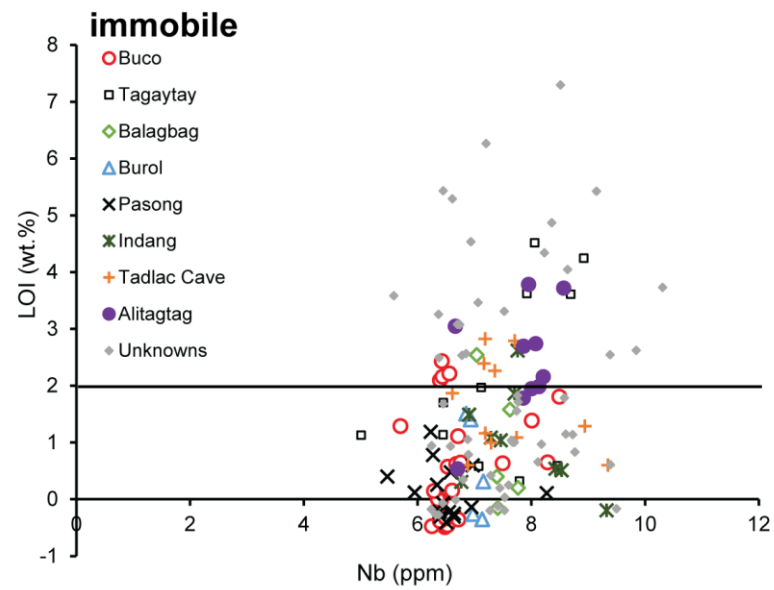
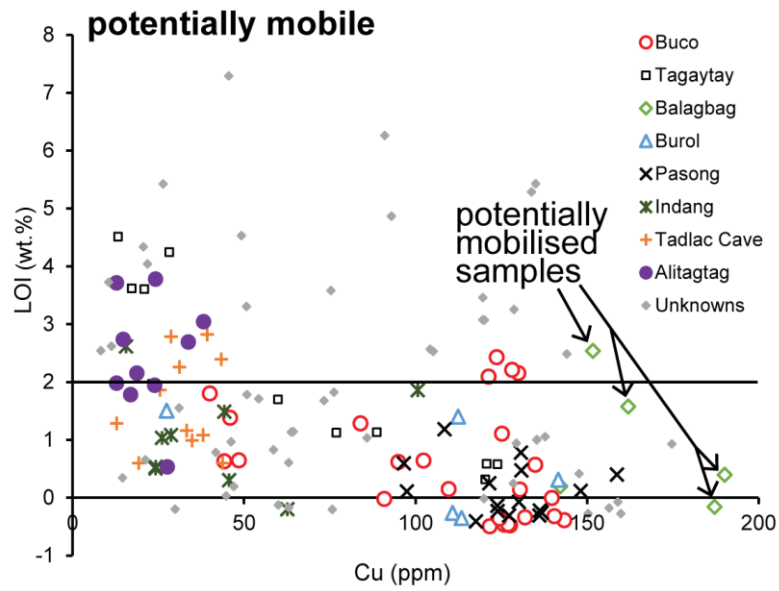
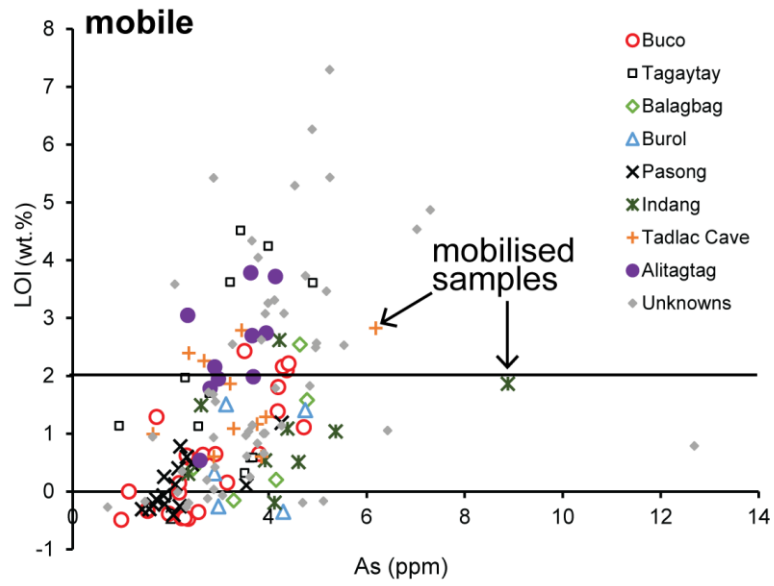


Fig. 4.4 (p. 167): Examples of a mobile element, As, a potentially mobile element, Cu, and an immobile element, Nb. The Tagaytay and unknown samples are plotted on to show their wider range of concentrations compared with other formations. The LOI value of 2 wt.% is highlighted on the graphs. On the As plot, two samples, a Tadalac Cave sample with a LOI >2 wt.% and an Indang sample with a LOI <2 wt.%, plot relatively far away from samples of the same formation with lower LOIs. Balagbag samples on the Cu plot in varying places and obvious outliers not seen on any other elemental plots.

Quality test 2: isocon analysis

The relative mobility of elements was analysed per formation using isocon analysis (Grant, 1986), which has previously been used in pyroclastic deposits to investigate effects of fossil fumaroles (e.g. Papike et al., 1991). Mobile elements will be regarded as less reliable in this study. To prevent any random errors that may be present in a single sample, the average concentrations of three samples (or two where the total number of samples was ≤ 5) with the lowest LOI values and three samples with the highest LOI values within each formation were calculated. To draw the isocon (a straight line through the origin with a gradient based on the location of immobile elements), the average concentrations needed to be scaled otherwise the graph would appear distorted.

To scale the data, the average concentrations for the three samples with the lowest LOI were given an arbitrary, whole, even number ranging from 6 – 66 (6 was chosen as the lowest arbitrary whole number based on the method described in Grant, 2005). Major elements were given the highest arbitrary numbers (66 – 48) and trace elements the lower arbitrary numbers (46 – 6; Table 4.1). Trace elements were assigned numbers in alphabetical order (i.e. Ba has the highest number and Zr the lowest number) with the exception of As and Cr, which were assigned the numbers 8 and 6 respectively because of their large concentration range (i.e. the difference between the average high LOI concentration of average low LOI concentration was large; Table 4.1). The arbitrary numbers were then divided by the average low LOI concentrations for each element to create a 'scale factor' (Table 4.1). Scale factors are different for each element. The average high LOI concentrations for each element were then

multiplied by their relevant scale factors to work out the average scaled high LOI concentrations (Table 4.1). The average scaled high LOI concentrations (y-axis) were then plotted against the arbitrary numbers assigned to the average low LOI concentrations (x-axis), which allowed the isocon to be drawn (Fig. 4.5).

Sample	As (ppm)	Ba (ppm)	Ce (ppm)	Co (ppm)	Cr (ppm)
T59	2.4	454.7	37.2	24.2	8.2
T66	2.9	505.6	44.1	22.8	2.7
T69 - DARK	3.8	625.7	55.2	11.1	<0.7
T69 - LIGHT	4.2	620.7	59.0	15.6	<0.7
T2.40	3.5	557.0	40.6	22.9	8.3
T2.42	1.0	454.2	42.0	27.9	14.9
T2.43	2.4	447.8	45.7	25.9	13.9
T2.46	4.3	478.7	37.1	24.2	7.0
T2.47	4.4	447.8	37.0	26.6	12.4
T2.50A	2.3	461.7	36.8	28.6	10.2
T2.50A-R	2.2	451.4	39.2	27.0	7.6
T2.50B	2.6	460.8	37.7	27.0	2.7
T2.52	4.4	462.9	39.8	26.7	5.7
T2.53	2.3	482.7	43.4	25.8	5.2
T2.54	2.2	466.0	43.5	25.4	7.0
T2.56	3.2	469.7	49.1	26.1	4.8
T2.61	1.5	451.2	42.7	26.5	3.3
T2.78	4.2	627.4	54.4	14.6	<0.68
T2.81	2.7	514.5	42.4	19.2	<0.69
T2.82	1.7	368.0	26.7	24.3	3.4
T2.101	4.7	449.0	39.3	24.9	6.0
T3.4	2.2	432.3	39.4	24.3	2.1
T3.10	1.5	456.2	37.2	26.5	7.2
T3.11A	1.1	439.5	43.9	25.0	6.3
T3.11B	2.0	443.4	39.2	27.0	13.5
Avg. low LOI	1.8	445.9	42.3	24.9	5.1
Avg. high LOI	4.1	494.5	38.2	24.6	9.2
Arbitrary number	8	46	44	42	6
Scale factor	4.4	0.1	1.0	1.7	1.2
Scaled avg. high LOI	17.8	51.0	39.8	41.4	10.7

Table 4.1: Example of scaling for the Buco Formation for elements As, Ba, Ce, Co and Cr.

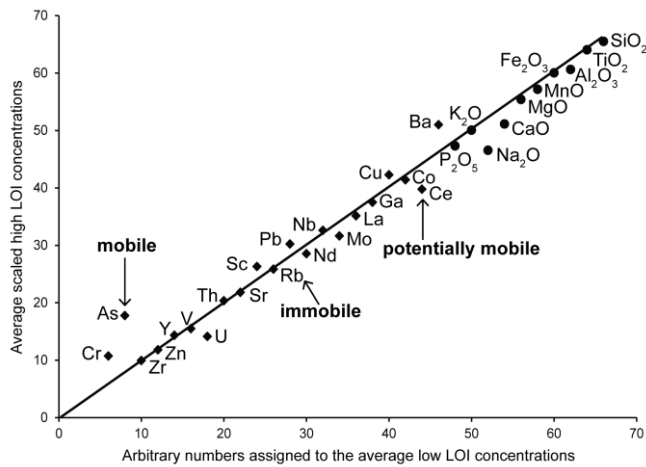


Fig. 4.5: The isocon analysis for the Buco Formation. Examples of a mobile, potentially mobile, and immobile element are identified on the plot.

The isocon was drawn taking into consideration the typical behaviour of relevant elements and the potential alteration processes experienced by samples from Taal (i.e. hydrothermal mobilisation is much more likely than any metamorphism). Although there is a degree of bias involved with this process,

Grant (2005) finds it preferable to a purely statistical approach because the latter assumes general element immobility (Baumgartner and Olsen, 1995), which is more than likely not to be the case. The traditionally immobile TiO_2 , Nb and Zr (Rollinson, 1993) are used as reference points for the isocon because they represent points at the end, middle and start of the isocon respectively (Fig. 4.5). If elements plot on the isocon, it is unlikely they have been mobilised. If elements plot above the isocon, they have been added, whereas if they plot below the isocon, they have been leached (Grant, 2005). It is possible for elements to appear mobile if they have been added if a lot of other elements were leached.

A separate plot and isocon was made for each named formation. Elements were classified as immobile if they plotted on the isocon for most formations; elements were classified as potentially mobile if they did not plot on the isocon for most formations, but were considered close enough to be within potential subjective error incurred during the drawing of the isocon (e.g. Ce in Fig. 4.5); elements were classified as mobile if they plotted significantly far away from the isocon for most formations (i.e. not within potential subjective error incurred during the drawing of the isocon; e.g. As in Fig. 4.5). This method highlights the following elements as mobile: MgO, CaO, P_2O_5 , As, Co, Cr, Cu, Mo and Pb,

while the following elements are classified as potentially mobile: TiO₂, Fe₂O₃, MnO, Na₂O, Ce, Cu, Mo, and U (Table 4.2).

Precision test: error bars using standards

Error bars were calculated for each element using the standard that covered most of the data range displayed by the Taal dataset (Appendix E). For major elements this was the Bardon Hill microgranodiorite (BH-1) and for trace elements this was the CRB – basalt (BCR-1). Precision was calculated as percentage standard deviation and accuracy as percentage uncertainty. For the precision calculations, XRF data for standards was collected for each run of Taal samples (3 in total) and 3 runs before and after each Taal run (21 data points per standard). Error bars were plotted as 2 sigma (2 times the percentage standard deviation) on each elemental plot that follows in this chapter. Error bars were only plotted on the data point that best matched the composition of the standard used.

Overall element mobility and quality

The overall mobility of each element was determined by combining both mobility tests (element vs. LOI and isocon analysis; Table 4.2). If elements were classified as mobile or of poor quality by at least one of the tests, they were considered 'mobile' in this study (Table 4.2). If elements were classified as potentially mobile by at least one test, they were considered 'potentially mobile' in this study (Table 4.2). If elements were classified as immobile for both tests, they were considered 'immobile' in this study (Table 4.2).

Element	Element vs. LOI	Isocon	Overall mobility	Element	Element vs. LOI	Isocon	Overall mobility
SiO ₂			immobile	Ga		M	mobile
TiO ₂		PM	potentially mobile	La			immobile
Al ₂ O ₃			immobile	Mo		PM	potentially mobile
Fe ₂ O ₃		PM	potentially mobile	Nb			immobile
MnO		PM	potentially mobile	Nd			immobile
MgO	M	M	mobile	Pb	M	M	mobile
CaO	M	M	mobile	Rb			immobile
Na ₂ O		PM	potentially mobile	Sc			immobile
K ₂ O			immobile	Sr			immobile
P ₂ O ₅	M	M	mobile	Th			immobile
As	M	M	mobile	U	M	PM	mobile
Ba			immobile	V			immobile
Ce		PM	potentially mobile	Y			immobile
Co	M	M	mobile	Zn			immobile
Cr	M	M	mobile	Zr			immobile
Cu	PM	PM	potentially mobile				

Table 4.2: A summary table with the mobility allocations for each element for each reliability test, followed by an overall mobility classification. M – mobile, PM – potentially mobile, if no letters are present the element was immobile according to that test.

4.2.3 Geochemical variation within datasets

Data were grouped into formations, each representing a single eruption-unit. Before determining whether geochemical data could distinguish different formations, each formation was characterised (e.g. De Silva and Francis, 1989) because intra-formation variance needed to be small enough if formations were to be chemically distinguished from each other (Merriam and Bischoff, 1975). To investigate the chemical variation within formations, they were split by

stratigraphic height. Separate groups were created within each formation based on stratigraphic height (e.g. the Alitagtag Formation was split into a pumice fall group, a lower ignimbrite group, and an upper ignimbrite group; Section 4.3.2). Groups were often composed of multiple localities and therefore contained some inherent uncertainty. How the stratigraphic height was divided depended on the formation and how easily different stratigraphic sections could be identified in the field. Each formation was analysed graphically and statistically using the JMP program.

4.2.4 JMP statistical analysis

Statistical analysis on the JMP program was first performed to quantify any variation within formations using different stratigraphic height groupings (Section 4.3.2). After this, each formation was considered as an individual group and compared to other formations to determine if there were any statistically-significant differences between them (Section 4.3.3).

The ANOVA test

The analysis of variance (ANOVA) test was conducted first and determines whether there were significant differences between the means of ≥ 3 groups (McDonald, 2014). The groups in this case were either the stratigraphic height groups within each formation (Section 4.2.3; e.g. Fig. 4.7) or entire individual formations (Section 4.3.3). The ANOVA test was conducted for each element and determined whether at least two group means were significantly different from each other for the chosen element, but did not specify which groups this involved. The ANOVA test was selected over similar statistical tests (e.g. the t-test) because it is more robust. The t-test, like the ANOVA test, determines whether there is a significant difference between group means, but only compares two groups at a time. Multiple t-tests would therefore need to be run to compare multiple groups together. During one run of a t-test the chance of a type-1 error (the chance that the test identifies a significant difference when there is not one) is ~5% (McDonald, 2014). When a second t-test is then run on

the same dataset, this error doubles, and triples for a third t-test, etc. The ability of the ANOVA test to compare multiple groups at once means the chance of a type-1 error occurring remains minimal, thus making it more robust than the t-test. Alpha levels, or p-values, for the ANOVA test were set at 0.05. The p-value quantifies whether any observed variance between group means is due to chance. If p-values are low (≤ 0.05), any variance between group means is significant and not due to chance (McDonald, 2014).

The Tukey-Kramer HSD test

If the ANOVA test revealed statistically-significant differences between the means of one or more groups, a Tukey-Kramer HSD (honestly significant difference) test was conducted to identify the significantly different groups. The Tukey-Kramer HSD test calculates the minimum significant difference (MSD) for each pair of group means, which depends on the total number of groups, the amount of data in each group, and the variation within each group. If the difference between the means of two groups is larger than the calculated MSD, this difference is significant (McDonald, 2014). The Tukey-Kramer HSD test was selected for its strictness and robustness compared to the t-test, which could also have been employed for this analysis (McDonald, 2014). Alpha levels for the Tukey-Kramer HSD test were again set at 0.05.

Linear discriminant analysis (only performed to compare formations to each other)

Linear discriminant analysis (LDA) was conducted only to compare different formations with each other using the JMP program. Linear discriminant analysis was not used to investigate inter-formational variation because the total number of data points and groups within each formation (maximum 4) were not deemed sufficient to warrant LDA. Linear discriminant analysis in this case would not contribute useful information that could not be determined from the ANOVA and Tukey-Kramer tests.

During linear discriminant analysis, elements for which the majority of samples recorded concentrations below XRF detection (Appendix D) were not included in any runs of the analysis. Linear discriminant analysis plots all elements on several combined axes (canons), each of which represents a linear combination of all elements in the dataset, and aims to maximise separation between formations. The Wilks' Lambda test provides a p-value for the entire LDA. If this p-value is less than 0.05, results are significant.

The probability of whether an individual sample was classified correctly to its assigned formation during linear discriminant analysis, and whether the 95% confidence ellipses plotted for each formation intersected with the ellipses of other formations, provided an idea as to how well a formation could be distinguished from another. For example, if all individual samples from the Alitagtag Formation were also statistically classified as the Alitagtag Formation based on their chemistry, and if the 95% confidence ellipse of the Alitagtag Formation did not overlap with the ellipse of any other formation, the Alitagtag Formation is statistically well distinguished from all other formations in the Taal Group.

Only the two axes (canons) which provide the greatest variation between formations are plotted by JMP. These canons create a biplot with data points colour coded to their formation and a 95% confidence ellipse drawn for each formation. Since only two canons are displayed, this can mean that, for example, a data point that graphically plots within the 95% confidence ellipse of the Alitagtag Formation on the biplot, statistically belongs to the Indang Formation when all canons are considered. The conical structure data was analysed in this study to determine which elements accounted for most of the variation on each canon, and thus accounted for the variation seen between formations (Appendix F).

Linear discriminant analysis is useful because it can take many elements into account when attempting to distinguish formations from each other. Statistical analysis such as LDA may provide the only way to distinguish different

formations, and thus eruption-units, in an area where single elements, or a single ratio, is not able to do so.

4.3 The Taal Group in a regional context

Before attempting to characterise formations in the Taal Group and differentiate between them, formations are compared to the chemistries of regional volcanoes to confirm that all formations are from the Taal Group and are unlikely to belong to a different volcano. Laguna de Bay is of particular importance because it is the only other flooded caldera volcano in the region of a similar size to Taal (Fig. 4.6); other volcanoes are stratovolcanoes (Palay-Palay Mataas Na Gulod, Sungay, Macolod, Makiling, Malepunyo and San Cristobal), scoria cones (Anilao Hill, Rosario Hill and Mayabobo) or maars (Alligator Maar; Fig. 4.6).

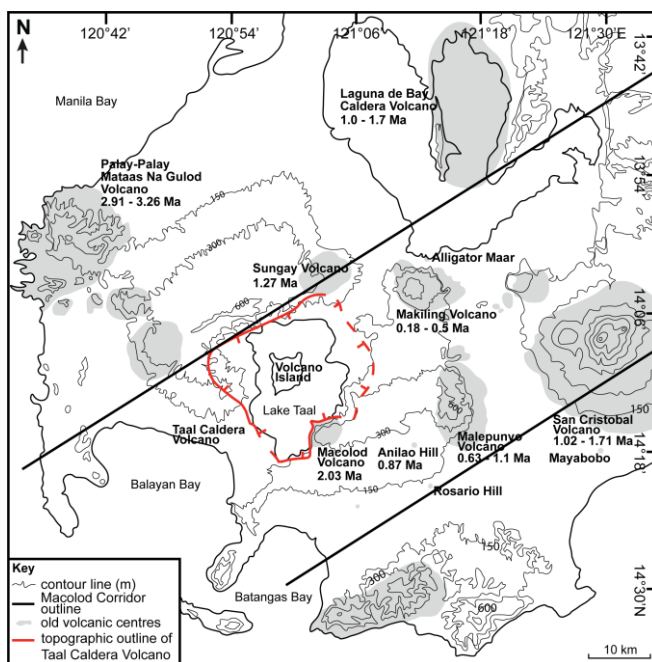


Fig. 4.6: Regional map of Taal Caldera Volcano (topographic caldera outline in red), Volcano Island and surrounding volcanoes. Labeled volcanoes are used for the regional study. Figure adapted from Listanco (1994) with topographic caldera outline from Punongbayan et al., 1995.

When considering major oxides (e.g. K_2O , Fig. 4.7), the large majority of samples overlap with fields of other Macolod Corridor volcanoes. Laguna de Bay shows a much wider range of K_2O values compared to any of Taal's prehistoric eruptions (Fig. 4.7), therefore it is unlikely that any samples from Laguna de Bay were misidentified as being from Taal Caldera Volcano. This is

further supported by the fact that no samples from prehistoric Taal Caldera Volcano eruptions plot within the Laguna de Bay field for Zr (Fig. 4.7). The stratovolcanoes Mt. Sungay and Mt. Macolod, both located on the topographic Taal Caldera outline, as well as various scoria cones and Mt. Palay-Palay, do not overlap with any prehistoric samples from Taal Caldera Volcano (Fig. 4.7).

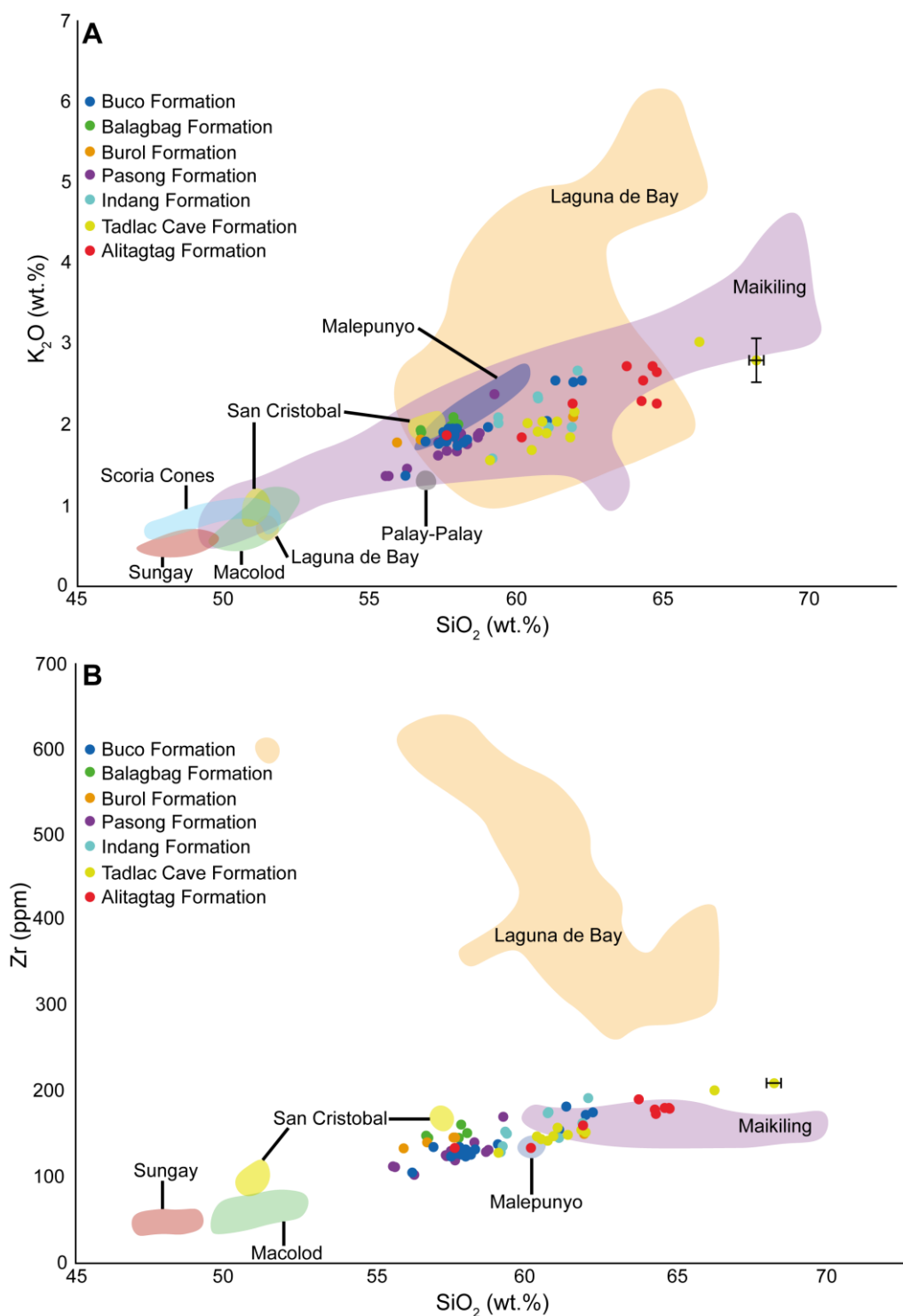


Fig. 4.7: (A) All named formations compared to chemistry fields for peripheral volcanoes in the Macolod Corridor on a K_2O vs. SiO_2 Harker diagram. (B) The same Taal data points compared to more minimal chemistry fields for peripheral volcanoes because of less published data on a Zr vs. SiO_2 Harker diagram (Defant et al., 1988, 1989, 1991; Miklius et al., 1991; Knittel and Oles, 1994; Knittel et al., 1997; Vogel et al., 2006). Taal's prehistoric formations are written in stratigraphic order from youngest (Buco Formation) to oldest (Alitagtag Formation). All referenced data and data from this study is whole-rock juvenile data and thus directly comparable. Error bars are 2 sigma and not drawn where they are smaller than the data points.

Both prehistoric and historic Taal samples follow a relatively classic island arc basalt trend on multi-element plot (Tatsumi et al., 1986), with almost all elements, except Ti, enriched compared to MORB (Fig. 4.8). The large ion lithophile elements (LILEs) are particularly enriched (Fig. 4.8). A sample from one of the most recent eruptions from Taal's Volcano Island, in January 2020, falls within the confines of Taal's prehistoric eruptions for most elements (Fig. 4.8). Other samples from the Macolod Corridor (Laguna de Bay and San Cristobal volcanoes) show slight differences in concentrations of individual elements, but also show a general subduction signature (Pearce, 1982). The same holds true for other sections of the Luzon Arc (Figs. 4.3, 4.8).

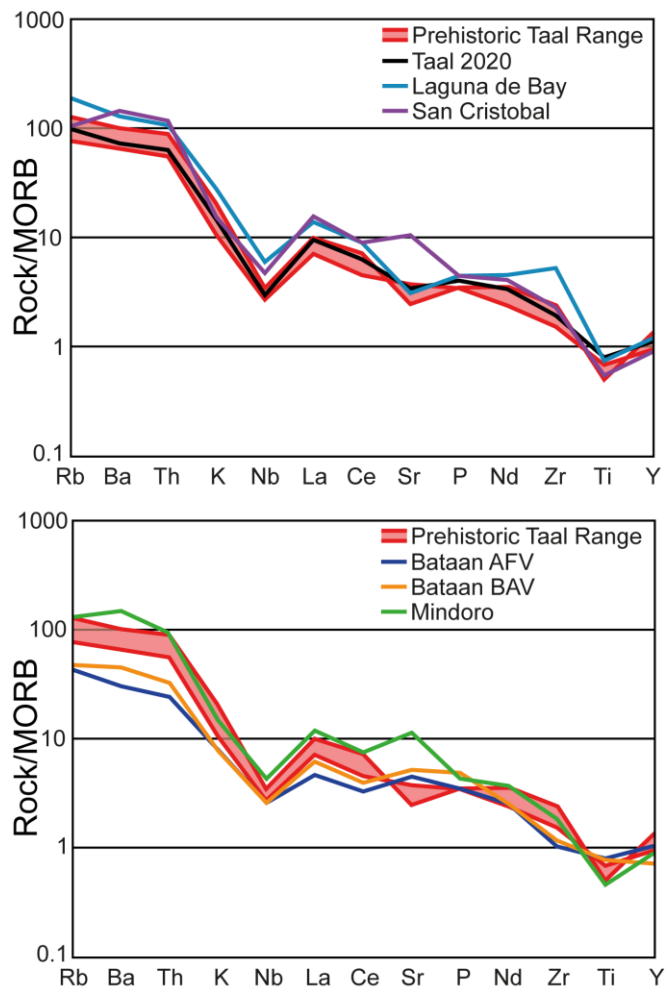


Fig. 4.8: Multi-element plots comparing Taal's most primitive and evolved prehistoric juvenile samples and a sample from the 2020 eruption of Taal's Volcano Island with Laguna de Bay and San Cristobal on one plot, and the three different segments of the Luzon Arc. The Laguna de Bay sample is an average taken from Vogel et al. (2006); the following data is based on single samples, which were the only samples with relevant elemental data: San Cristobal is sample 171; Bataan AFV is based on Mt. Natib, sample 71 (Defant et al., 1991); Bataan BAV is based on Mt. Arayat, sample 168 (Defant et al., 1991); Mindoro is based on Dumali, sample 195 (Defant et al., 1991). All referenced data and data from this study is whole-rock juvenile data and thus directly comparable.

Taal samples from this study support the finding that Taal Caldera Volcano magmas are calc-alkaline (Defant et al., 1988), similarly to the rest of the Luzon Arc (Fig. 4.9). The western Bataan segment is the only exception because its field pushes into the low-K range (Fig. 4.9), which supports previous observations that the western Bataan segment has lower K_2O contents compared to Taal and other arc segments (Defant et al., 1988; Miklius et al., 1991). However, the Bataan West field does overlap with all other fields except the Mindoro segment (Fig. 4.9). All named formations from the Taal Group plot within the Macolod Corridor field, with the exception of a single Tadalac Cave sample and two Alitagtag samples (Fig. 4.9). Therefore, all of Taal's prehistoric eruptions identified in the stratigraphy introduced in this thesis (Chapter 2) generally match the chemical identity of the Macolod Corridor (Fig. 4.9).

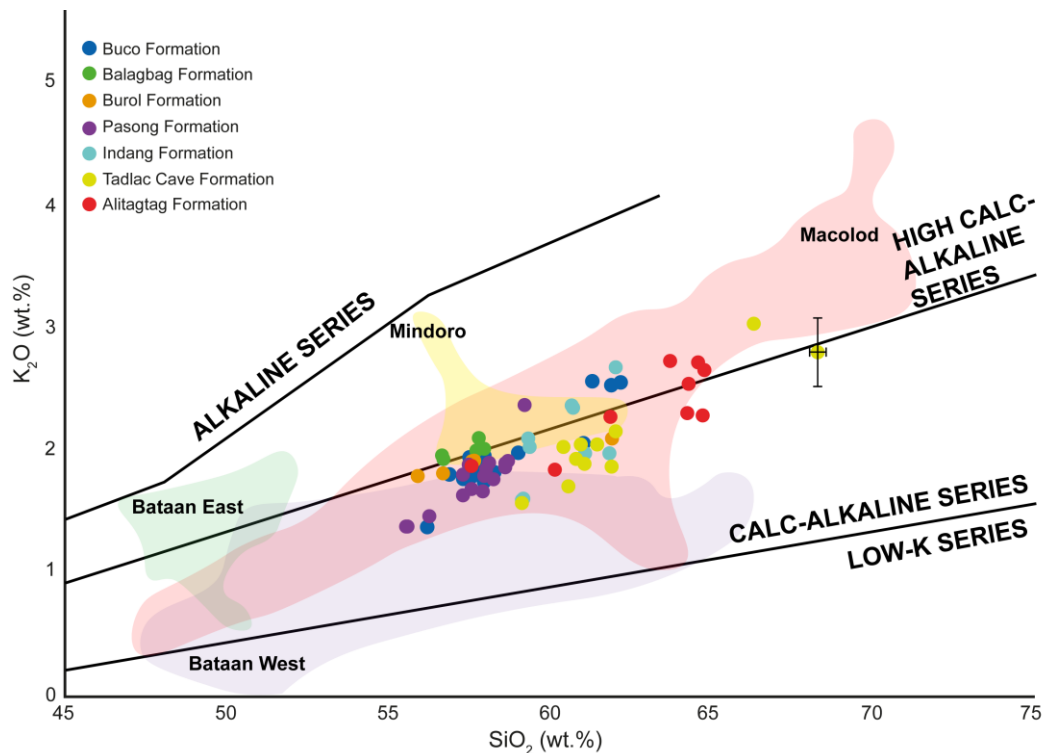


Fig. 4.9: Alkaline series grouping for Taal samples with arc segment fields (including the Macolod Corridor). The Macolod Corridor field does not include Laguna de Bay samples. This plot builds on work from Defant et al., (1989, 1991) who drew volcanic fields for these segments on Harker plots using a limited dataset. This dataset is much broader and focuses on how named prehistoric eruption-units from Taal Caldera relate to drawn fields. Data from: Bataan East Field (Defant et al., 1991; Bau and Knittel, 1993), Bataan West Field (Defant et al., 1988, 1991; Knittel and Oles, 1994; Bernard et al., 1996; Castillo and Punongbayan, 1996; Luhr and Melson, 1996; Pallister et al., 1996), Mindoro Field (Mukasa et al., 1987; Defant et al., 1988, 1991), and the Macolod Field (Defant et al., 1988, 1989; 1991; Miklius et al., 1991; Knittel and Oles, 1994; Knittel et al., 1997; Vogel et al., 2006). Taal named formations are in stratigraphic order from youngest (Buco Formation) to oldest (Alitagtag Formation). All referenced data and data from this study is whole-rock juvenile data and thus directly comparable. Error bars are 2 sigma.

4.4 Characterising the Taal Group

Each named formation is analysed for internal variation, both petrographically and geochemically. Petrographic results will be presented first, followed by geochemical results. Findings are then summarised by named formation and unit before they are compared with each other to identify any significant differences between them. After this, unknown samples will be placed in a named formation or unit based on their geochemistry if possible. It should be noted at this stage that petrographic and geochemical characteristics need to be treated with some caution because the data sets, particularly the petrographic data set, are quite small and there is no certainty that this characterisation is truly representative of the entire eruption-unit. Nevertheless, only limited work geochemical and petrographic work has been done on named prehistoric eruption-units from Taal Caldera Volcano (Listanco, 1994; Martinez and Williams, 1999), therefore despite minimal data sets the results from this study are still important in progressing understanding of the geochemical and petrographic characteristics of Taal Caldera Volcano.

4.4.1 Petrographic characterisation

All samples are dominated by glass and vesicles with a small number of phenocrysts and microphenocrysts. It is generally difficult to observe abundant clearly identifiable minerals, but minerals and textures that were observable are described below.

The Alitagtag Formation

The Alitagtag Formation contains white and black pumice. Their difference may be textural, with white pumice containing more highly stretched vesicles compared to black pumice. However, this observation does not hold true for all

samples. Crystallinity is low in all pumice samples and is not dependent on pumice colour. Plagioclase dominates, making up 50 – 60% of the crystal population, while pyroxene makes up 30 – 40%, and oxides 10%.

Orthopyroxene is the more common pyroxene (70 – 95% of all pyroxenes) for all but one pumice sample (T2.11; Appendix B), where clinopyroxene dominates (80% of all pyroxenes). All samples have two crystal size modes: phenocrysts and microcrysts. Microcrysts are usually hard to identify because of their small size, but look mostly like plagioclase laths. Plagioclase phenocrysts commonly exhibit simple twinning and oscillatory zoning, while pyroxenes show only simple twinning, if any.

The Tadalac Cave Formation

The Tadalac Cave Formation, like the Alitagtag Formation, contains white and black pumice. Texturally, the white pumice contains more highly stretched vesicles, has a smaller modal vesicle size and is marginally more vesicular than the black pumice. Although in thin section the glass component is colourless for both pumice types, these vesicular differences may account for their colour difference in hand specimen. In terms of crystallinity, both pumice types are similar, with white pumice containing slightly less plagioclase compared to black pumice. White pumice has 35% plagioclase, 25% clinopyroxene, 25% orthopyroxene and 15% oxides, while black pumice contains 45% plagioclase, 25% orthopyroxene, 20% clinopyroxene and 10% oxides. In both white and black pumice, plagioclase and pyroxene commonly show simple twinning and more rarely lamellar twinning, and show abundant resorption textures. Plagioclase also often exhibits undulose extinction and oscillatory zoning. Glomerocrysts occur in both pumice types and importantly, both are dominated by phenocrysts of plagioclase, pyroxene and oxides, with barely any microcrysts visible under the optical microscope.

The Indang Formation

The sampled juvenile clast from the Indang Formation is a poorly vesicular, black, spatter clast (see Chapter 3). This poor vesicularity is reflected in thin section; any vesicles present are well rounded. The sample is crystal poor at 5 – 10 vol.%. The crystal assemblage consists of 70% phenocrysts and only 30% microcrysts. Within the phenocryst population, plagioclase is the most common phase (80%) followed by clinopyroxene (14%), orthopyroxene (6%), and oxides (<1%). Plagioclase commonly exhibits both simple and lamellar twinning, exsolution textures, and gradational, sectoral and oscillatory zoning. They make up almost 100% of the microcryst population. Pyroxenes show simple twinning and sometimes exsolution textures, are rare as microcrysts, but are generally smaller in size than plagioclase phenocrysts.

The Pasong Formation

The 5 juvenile samples from the Pasong Formation show a variation in crystal phase abundances and sizes and can be split into 3 groups. The first (T3.20, T3.21; Appendix B) is crystal poor (<10%), containing 50 – 59% plagioclase, 30 – 35% clinopyroxene, 10 – 15% orthopyroxene, and $\leq 1\%$ oxides. These crystals vary in size along a continuous range (i.e. no distinct modes) and no glomerocrysts are present. The second (T3.16, T3.12; Appendix B) is even more crystal poor (≤ 3 vol.%) than the first and contains markedly more plagioclase (70%) compared to group 1. Their clino- and orthopyroxene abundances (17.5% each) are thus appropriately lower than group 1, while oxides are slightly more common (5%). Glomerocrysts are present in group 2, as are two modal sizes: phenocrysts and microcrysts. Group 3 (T19; Appendix B) represents an amalgamation of groups 1 and 2, but it is more crystal-rich (15 vol.%) than both of them. Its crystal phases have similar proportions to group 1, but, like group 2, it contains glomerocrysts and has two modal crystal sizes. In all groups plagioclase often exhibits simple or lamellar twinning, as well as gradational zoning and less commonly oscillatory zoning and exsolution

textures. Pyroxenes both frequently contain blebs of the other pyroxene and can show simple or sectoral twinning.

The Burol Formation

Both juvenile samples from the Burol Formation are crystal poor (<5%) and moderately vesicular in thin section. The two juvenile samples taken from the Burol Formation were sampled from two different lapilli-tuffs and demonstrate differences as well as similarities. One contains equal numbers of stretched and well-rounded vesicles (T2.96; Appendix B), while the other is dominated by well-rounded vesicles (T2.97; Appendix B). The former's crystal population consists of plagioclase (65%), clinopyroxene (23%), orthopyroxene (2%) and oxides (10%), while the latter is dominated by clinopyroxene (67%), also containing plagioclase (30%) and oxides (3%). In both samples these can occur as phenocrysts (within glomerocrysts) or as microcrysts, although T2.96 contains only minimal microcrysts. Plagioclase exhibits gradational and sectoral zoning and simple twinning, while pyroxenes show rimmed birefringence and rare simple twinning and oscillatory zoning in both samples.

The Balagbag Formation

The juvenile sample from the Balagbag Formation is poorly to moderately vesicular, with vesicles having either an elongate or well-rounded shape. Crystals make up <3% of the sample and consist of plagioclase (40%), clinopyroxene (50%), orthopyroxene (5%) and oxides (5%). Almost all crystals are phenocrysts, which may occur as glomerocrysts. Microcrysts are very rare and too small to identify in the glassy matrix. Plagioclase frequently exhibits lamellar twinning, alteration rims, and oscillatory zoning, while the pyroxenes can also show alteration rims or alteration along common intra-crystal cracks, as well as simple twinning.

The Buco Formation

Samples from the Buco ignimbrite show relatively consistent petrographic features. They are moderately to poorly vesicular with well-rounded vesicles. There is limited evidence of vesicle stretching, with vesicle coalescence responsible for the largest vesicles. All three analysed samples are extremely crystal poor (<2%). The phenocryst assemblage that exists is made up of predominantly plagioclase (80 – 90%), with 9% orthopyroxene, and <1% clinopyroxene and oxides. There is no other formation within the Taal sequence where clinopyroxene is this rare. Although microcrysts are present, they are rare and seem to mainly consist of plagioclase laths. Plagioclase phenocrysts tend to exhibit lamellar twinning, patched zoning, and may be heavily fractured (sometimes along cleavage planes). Orthopyroxene is similarly heavily fractured and shows patched zoning, but no twinning. All observed phenocrysts are broken up, i.e. there are no complete phenocrysts in any of the samples, and may occur as glomerocrysts.

Glomerocrysts also exist in samples from the cross-bedded section of the Buco Formation, but these samples do not show the same features as those from the ignimbrite and show much more variation between samples. Dark coloured samples are moderately to poorly vesicular, while colourless samples in thin section are more highly vesicular. All vesicles are sub-rounded, with any larger vesicles the result of coalescence. All cross-bedded Buco samples are crystal-poor, but much more crystal-rich than the Buco ignimbrite samples at 5 – 10%. Crystals occur as both microcrysts and phenocrysts. The abundance of microcrysts accounts for the relatively high overall crystal abundance and consist of plagioclase and clinopyroxene, although their identification can be difficult due to their small size. Unlike the Buco ignimbrite samples, pyroxenes are more abundant in the phenocryst assemblage of the cross-bedded samples (60 – 65%). Clinopyroxene appears to be the dominant of the two pyroxenes, which also contrasts with the Buco ignimbrite. Plagioclase is the next dominant phase (40 – 54%), followed by very rare oxides (<1%). The textures of the crystals are similar to the Buco ignimbrite, including gradational zoning, twinning, and fracturing.

Summary

Petrographically, formations show very little internal variation. All juvenile material is crystal poor and has a crystal population made up of plagioclase, pyroxene and oxides - a common island arc assemblage (Davidson et al., 2007). The phenocryst assemblages alone do not vary between different formations, and therefore on their own will not be useful for differentiating different formations. However, the abundances of various phases and microcrysts vs. phenocrysts percentages do vary between different formations, which can be helpful when used together with geochemical or field evidence.

4.4.2 Geochemical characterisation

The Alitagtag Formation

Samples from the Alitagtag Formation are split into 3 different stratigraphic groups: (1) the basal fall deposit, (2) the lower ignimbrite and (3) the middle - upper ignimbrite (referred to as upper ignimbrite, which includes those samples taken from an exposure of the Alitagtag ignimbrite (L1.62; [14° 03.968' N 120° 53.658' E]; Appendix A) without stratigraphic context, i.e. no upper or lower units exposed). The sample set includes a matrix sample and both black and white pumice, but no banded pumice, which is also present in the Alitagtag Formation. The basal pumice fall sample has a SiO₂ composition of 64.29 wt.%, a Fe₂O₃ composition of 5.59 wt.% and immobile element of Y (37.0 ppm; Fig. 4.10). All these elements were selected because they are representative of the range of behaviour displayed by all elements across the Alitagtag Formation and may be important in distinguishing formations from each other (Section 4.5.3). The lower ignimbrite samples have a SiO₂ composition of 60.18 – 61.90 wt.% with Fe₂O₃ compositions of 6.97 – 8.29 wt.% with immobile Y values of 33 – 34.5 ppm, while the upper ignimbrite samples have a SiO₂ range of 57.62 – 64.80 wt.%, a Fe₂O₃ range of 5.09 – 7.66 wt.% and a Y concentration of 32.0 – 39.8 ppm (Fig. 4.10). The basal pumice fall sample always plots within the same chemical range as the upper ignimbrite, but never overlaps with lower

ignimbrite samples (Fig. 4.10). However, the lower and upper ignimbrite do have overlapping samples (Fig. 4.10). There is no clear vertical geochemical trend seen in the Alitagtag Formation, but the relatively large chemical range suggests the erupting magma may have been heterogeneously mixed.

Samples within both the upper and lower ignimbrite groups do not always plot together (Fig. 4.10) because the groups contain samples from both black and white pumices. Black pumice has a lower minimum silica content (57.62 wt.%) compared to white pumice (63.76 wt.%). However, white and black pumice sampled from the Alitagtag ignimbrite at L1.62 (Appendix A) have very similar silica content (64.29 – 64.80 wt.%). The fall deposit only consists of white pumice and thus fittingly has a relatively high SiO₂ content compared to the ignimbrite sample sets (Fig. 4.10).

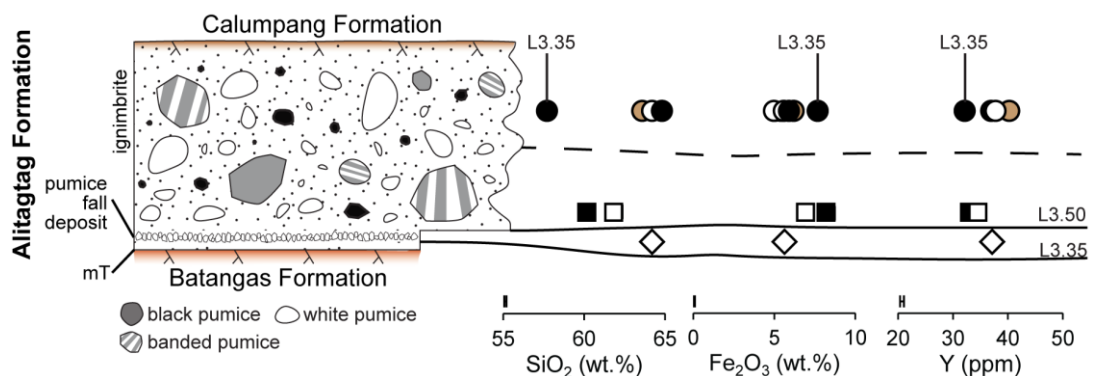


Fig. 4.10: Samples split into 3 groups based on their stratigraphic height (fall deposit as diamond, lower ignimbrite as squares, upper ignimbrite as circles) for SiO₂, Fe₂O₃ and Y, which represent the range of behaviour shown by different elements. Black pumice samples are shown with a black symbol, white pumice samples are shown with a white symbol, and one bulk matrix sample is shown with a brown symbol. Black pumices from L3.50 [13° 47.067'N 121°05.509'E] and L3.35 (Appendix A; [13° 45.226'N 121°06.037'E]) do not have the same composition as white pumice sampled at the same locality. Error bars are 2 sigma.

The geochemical range within the Alitagtag Formation is not large enough to result in any elements being identified as significantly different between all three groups using JMP statistical analysis. Only La was significantly different (p-value: 0.0342 from Tukey-Kramer test) between the pumice fall and lower ignimbrite group. However, since the pumice fall deposit group consists of only

one sample, and the lower ignimbrite of only two samples, this difference could be an artefact of the small population size. The reason that no elements are statistically different between the upper and lower ignimbrite groups is because samples of the lower silica black pumice are found in both the lower and upper ignimbrite groups, which means that the geochemical characteristics of these two groups are very similar.

To investigate whether the observed graphical difference between black and white pumice translates into a statistically significant difference, the Alitagtag Formation dataset was again split into three groups: (1) L1.62 (Appendix A; [14° 03.968' N 120° 53.658' E]), whose pumice is all of roughly equal composition despite their different colours; (2) black pumice from L3.35 [13° 45.226' N 121° 06.037' E] and L3.50 (Appendix A; [13° 47.067' N 121° 05.509' E]); and (3) white pumice from L3.35 and L3.50. All elements, except for Al₂O₃, MnO, K₂O, Nd and Sc show a statistically significant difference between the L1.62 group and the black pumice group, while only SiO₂, Ba, Cu, Nb, Rb, Sr, Y and Zr display such a difference between the black and white pumice groups (Fig. 4.11). This supports the graphical observation that black pumice is significantly, chemically distinct from other samples for most elements. Where white and black pumice does overlap in composition (i.e. at locality 1.62), this is likely due to mild chemical zoning within the ignimbrite.

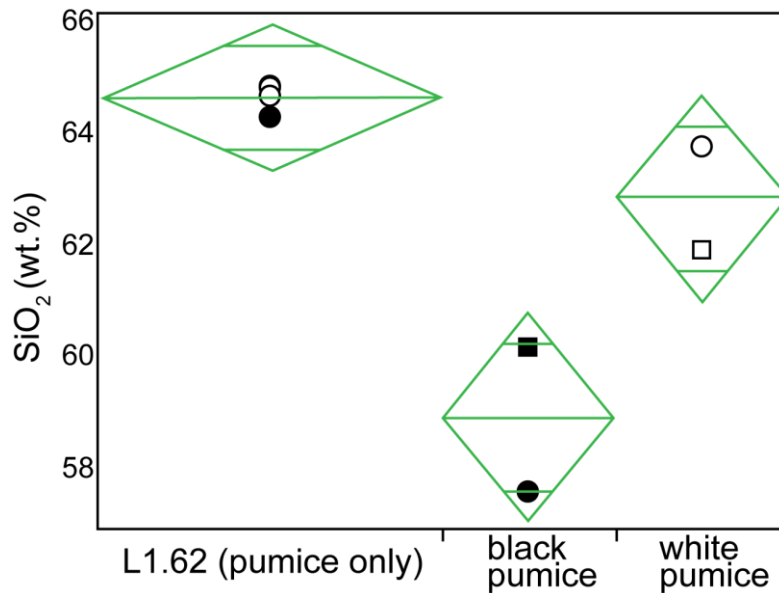


Fig. 4.11: An ANOVA diamond plot showing results for SiO₂ between the L1.62 group (containing both white and black pumice of similar composition), the black pumice group, and the white pumice group. Symbols as in Fig. 4.10. Significant differences are found between the L1.62 and black pumice groups (p-value: 0.0030) and the black pumice and black pumice groups (p-value: 0.0267). P-values are calculated by the Tukey-Kramer test. In ANOVA diamond plots, the middle line through the diamond represents the group mean; the tips of the diamond represent the 95% confidence interval; the small upper and lower lines are the overlap marks, if overlap marks from one group are closer to the mean of another group, then those two groups are not significantly different (e.g. L1.62 and white pumice). The x-axis is proportional to the sample size, therefore groups with larger sample sizes will take up more space on the x-axis, and thus have a wider diamond. A smaller sample size will have a narrower diamond, reflecting the larger confidence interval resulting from smaller sample sizes. These descriptions can be applied to all ANOVA plots used in this study.

The Tadalac Cave Formation

Samples from the Tadalac Cave Formation were taken from either the lower or upper part of the ignimbrite (upper meaning the highest reachable point of the ignimbrite in the field since the top of the ignimbrite was not exposed). The lower ignimbrite has a SiO₂ composition of 60.37 – 68.21 wt.% with Y concentrations of 33.3 – 40.3 ppm, Zn concentrations of 78.9 – 94.6 ppm, and Pb concentrations of 15.7 – 66.9 ppm (Fig. 4.12). The upper ignimbrite, on the other hand, has a SiO₂ composition of 59.10 – 66.27 wt.% with Y concentrations of 30.4 – 40.9 ppm, Zn concentrations of 83.0 – 90.2 ppm, and Pb concentrations of 14.8 – 22.2 ppm (Fig. 4.12). These elements represent the

range of geochemical behaviour shown by all elements for the Tadalac Cave Formation.

Samples from the lower and upper ignimbrite overlap for all elements except Pb, where two samples from the lower ignimbrite do not overlap with any samples from the upper ignimbrite (Fig. 4.12). These two non-overlapping samples were sampled from an exposure close to lake level, therefore they likely experienced preferential alteration which mobilised Pb (supporting the classification of Pb as a mobile element in Table 4.2). Interestingly, unlike for the Alitagtag Formation, there is a negligible chemical difference between white and black pumice from the Tadalac Cave Formation (i.e. both pumice colours plot together on Fig. 4.12). However, one sample from the upper ignimbrite and one from the lower ignimbrite sample sets do not plot together with other samples from their respective sample sets for all other elements (e.g. SiO₂, Y, Fig. 4.12) except for Zn where all samples from the upper ignimbrite do plot together (Fig. 4.12). The outlying samples have similar compositions and are a glassy obsidian clast in the lower ignimbrite and a dense, vesicular clast in the upper ignimbrite. Although they may represent juvenile clasts, the majority of juvenile samples within the Tadalac Cave Formation have a much lower silica content, therefore the two outlying samples may be accidental clasts. However, the current data set is too minimal to prove or disprove this with high confidence levels.

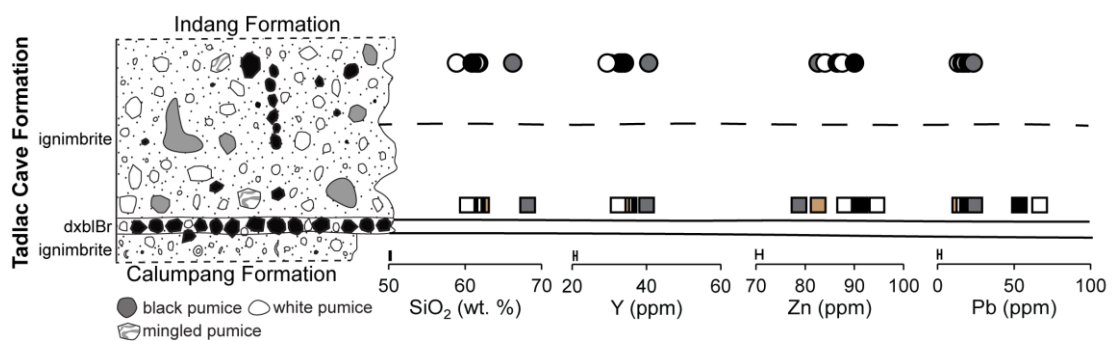


Fig. 4.12: Ignimbrite samples split by stratigraphic height (lower ignimbrite as squares and upper ignimbrite as circles). Black pumice represented by a black symbol, white pumice represented by a white symbol, a bulk sample represented by a brown symbol and accidental clasts (obsidian and dense vesicular) represented by grey symbols. Error bars are 2 sigma.

The compositional similarity of the two accidental clasts means that there is no statistically significant difference between the upper and lower ignimbrite groups identified using the JMP statistical program. This remains the case even if the two accidental clast samples are removed from the dataset. A further statistical test was done with the two accidental clasts as a separate group to confirm that these are statistically significantly different from both white and black pumice. This hypothesis was proven true for all elements, except for immobile TiO_2 , Al_2O_3 , Nd, and Zn (Fig. 4.13). This test also statistically supported the chemical similarity of white and black pumice from the Tadolac Cave Formation (Fig. 4.13).

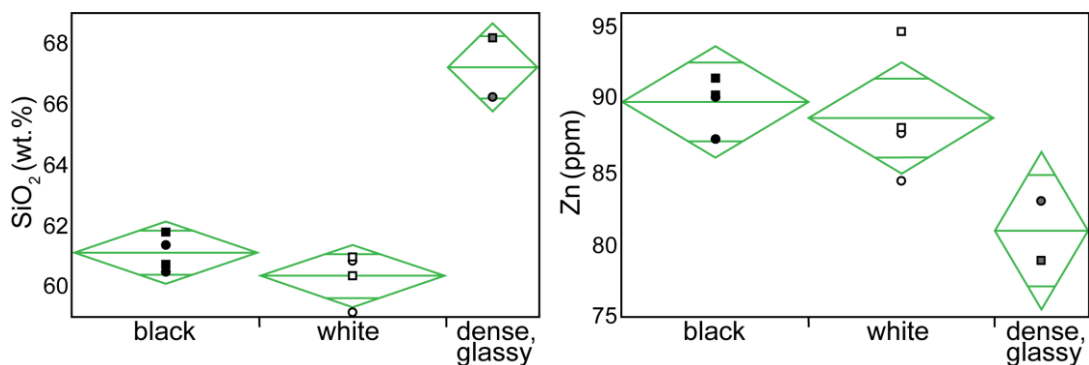


Fig. 4.13: An example of an element (SiO_2) showing a significant difference between both black pumice and accidental clasts (p-value: 0.0002) and white pumice and accidental clasts (p-value: <0.0001). An example of an element (Zn) that shows no significant difference between any groups. Data points are labelled as in Fig. 4.12. P-values are calculated by the Tukey-Kramer test.

The Indang Formation

Samples from the Indang Formation were divided into three groups based on their stratigraphic height: lower, middle and upper. The lower and middle groups contain only samples from the Indang ignimbrite, while the upper group also includes a juvenile sample from a lithic breccia. The lower group has a TiO_2 composition of 0.90 – 0.93 wt.%, a Fe_2O_3 composition of 8.13 – 8.81, a Sc concentration of 22.2 – 24.9 ppm, and a Y concentration of 31.3 – 34.1 ppm (Fig. 4.14). The middle group has a lower TiO_2 composition (0.72 – 0.81 wt.%) and a lower minimum Fe_2O_3 composition (6.68 wt.%, maximum is 8.35 wt.%), with a Sc concentration of 21.6 – 23.6 ppm and a Y concentration of 32.0 – 38.7 ppm (Fig. 4.14). Finally, the upper group has TiO_2 and Fe_2O_3 compositions of

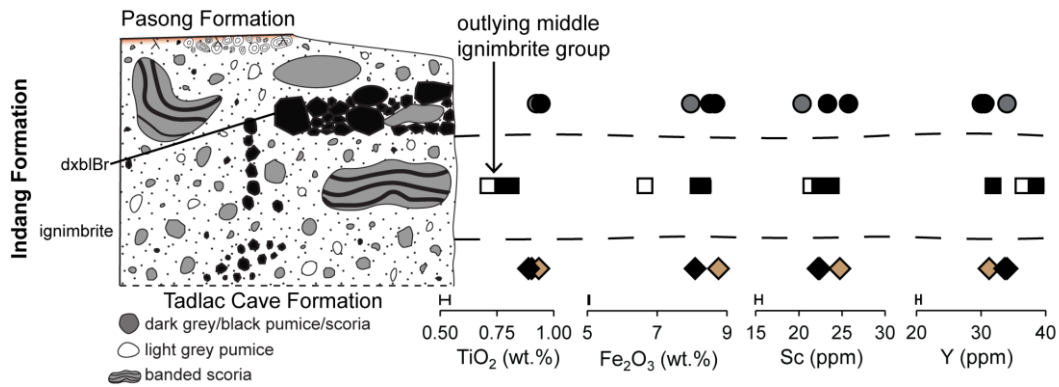


Fig. 4.14: Stratigraphic height groupings for the Indang Formation: (1) lower ignimbrite (samples taken within 2 m of an underlying palaeosol; represented by diamonds), middle ignimbrite (samples taken more than 2 m below an overlying palaeosol; represented by squares), and upper ignimbrite (samples taken within 2 m of an overlying palaeosol; represented by circles). The total sample set consists of: a lithic breccia (grey symbol), a light grey juvenile clast (white symbol), a matrix sample (brown symbol), and black scoria clasts (black symbols). Error bars are 2 sigma.

0.93 – 0.95 wt.% and 8.01 – 8.74 wt.% respectively, and Sc and Y concentrations of 20.4 – 25.7 ppm and 30.4 – 34.2 ppm respectively (Fig. 4.14). Most elements show a singular outlier, which is usually the lithic breccia sample (T2.64; e.g. Sc, Y in Fig. 4.14; Appendix B), but this is not always the case (e.g. Fe₂O₃ in Fig. 4.13). The middle group has particularly low TiO₂ values, which means the middle group does not overlap with the lower or upper group for TiO₂ (Fig. 4.14). No other element differentiates the stratigraphic groups like this, which is supported by statistical analysis conducted on JMP, where TiO₂ was the only element showing a statistically significant difference between the middle group, and lower and upper groups (Fig. 4.15; p-values: 0.008 between upper and middle ignimbrite groups, and 0.0021 between lower and middle ignimbrite groups, calculated by the Tukey-Kramer test).

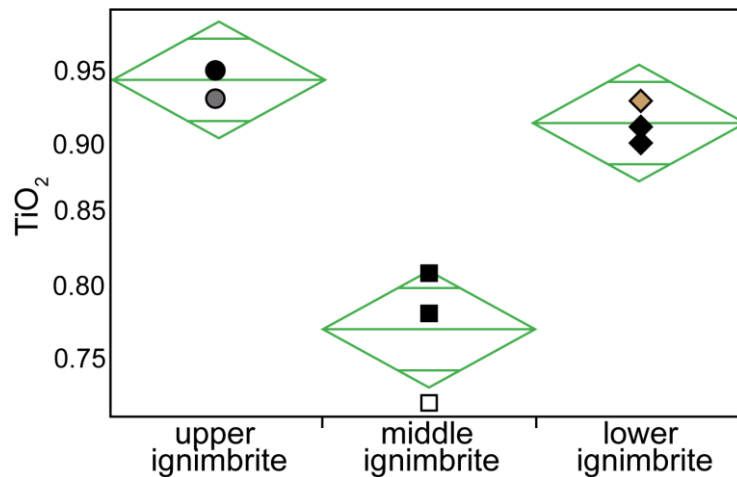


Fig. 4.15: The ANOVA plot for TiO₂ showing a significant difference between the middle ignimbrite group and the upper and lower ignimbrite groups. Symbols as described in Fig. 4.14.

The Pasong Formation

Samples for the Pasong Formation were divided into four stratigraphic groups: (1) the base (an underlying palaeosol is visible), (2) upper base (sample taken below cross-bedded tuffs seen in between ignimbrites; Fig 4.15), (3) lower top (sample taken above cross-bedded tuffs seen in between ignimbrites; Fig. 4.15), and (4) top (an overlying palaeosol or reworked deposits are visible). All elemental behaviour can be represented by TiO₂, Nd and Y (Fig. 4.16). The base group has a TiO₂ composition of 0.93 – 0.99 wt.% with a Nd concentration of 19.3 – 20.1 ppm and a Y concentration of 27.7 – 27.8 ppm (Fig. 4.16). The upper base group has a lower TiO₂ composition of 0.82 – 0.93 wt.%, a wider range of Nd concentrations (18.5 – 21.5 ppm), but a narrower range of Y concentrations (27.2 – 28.7 ppm; Fig. 4.16). The lower top group has a TiO₂ composition similar to the base group (0.94 – 0.95 wt.%), but a lower Nd concentration compared to both the base and upper base groups (13.3 – 15.8 ppm).

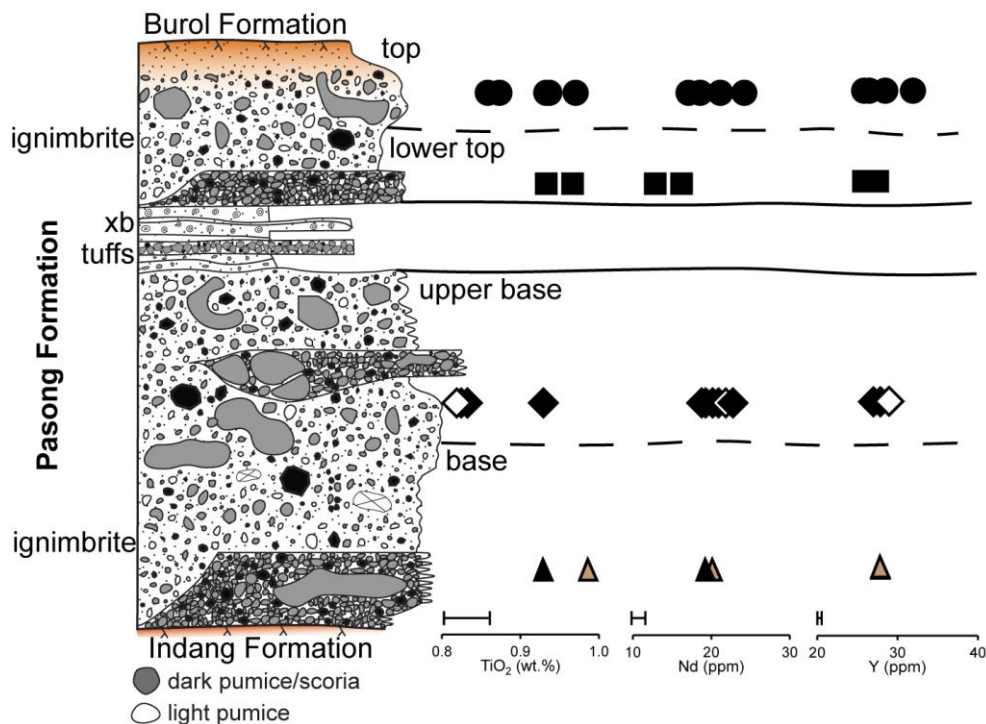


Fig. 4.16: Stratigraphic height groupings for the Pasong Formation: (1) base (represented by triangles), upper base (represented by diamonds), lower top (represented by squares), and top (represented by circles). The total sample set consists of: black scoria clasts (black symbol), a light grey juvenile clast (white symbol) and a matrix sample (brown symbol). Small internal variations within each group are represented by TiO₂, Nd and Y plots, however, no overall trend with stratigraphic height is evident. Error bars are 2 sigma.

Meanwhile, the Y concentration (25.9 – 27.4 ppm) for the lower top group has a lower minimum value (i.e. 25.9 ppm) compared to the base and upper base groups, similar to the top group (Y concentrations of 25.9 – 31.8 ppm; Fig. 4.16). The top group has a Y concentration higher than any other stratigraphic group, just like its Nd concentration (17.3 – 24.0 ppm). The TiO₂ composition for the top group, however, falls within the range covered by all other stratigraphic groups (0.86 – 0.97 wt.%). Despite the TiO₂, Nd and Y variations between the different stratigraphic groups, none of them show a clear trend with stratigraphic height. The only stratigraphic group that lacks overlap with another is the lower top group, which has Nd concentrations below the minimum Nd concentrations of the top group and upper base group (Fig. 4.16). This lack of overlap is reflected in results from the JMP statistical program in which Nd is the only element that show a significant difference. As expected, this difference is between both the top and lower top group (p-value: 0.0093) and the lower top and upper base group (p-value: 0.0173; Fig. 4.17).

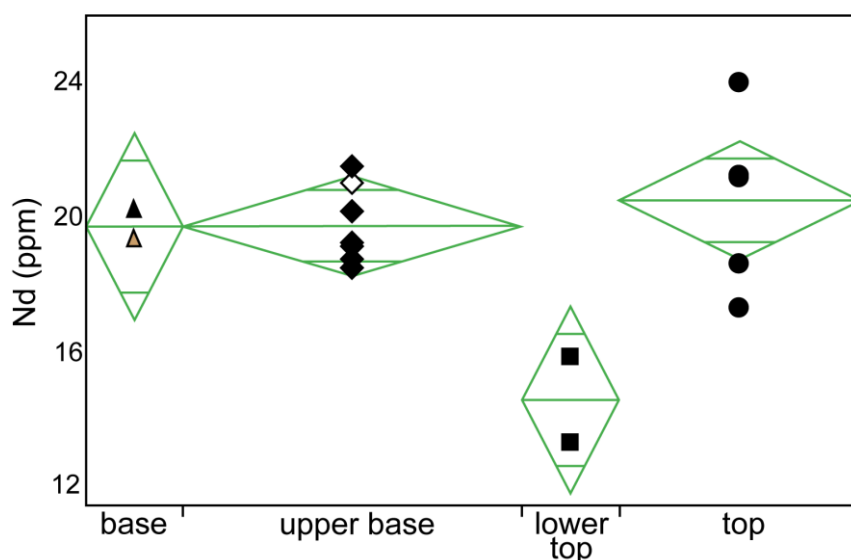


Fig. 4.17: The ANOVA plot for Nd showing a significant difference between the lower top group and the top group, and the lower top group and the upper base group. Symbols as described in Fig. 4.16.

The Burol Formation

There are five samples from the Burol Formation, which is not enough to split the dataset into groups and present a meaningful statistical result. Instead, samples will be qualitatively analysed by stratigraphic height only. The lower ignimbrite group has a TiO_2 composition of 1.03 wt.%, which is higher than the TiO_2 compositions for both the upper ignimbrite group (0.83 – 0.95 wt.%) and the lapillistone group (0.95 wt.%; Fig. 4.18). The upper ignimbrite group has a relatively low Sc concentration (16.9 – 27.2 ppm) compared to the lower ignimbrite (28.4 ppm) and lapillistone group (27.4 – 27.9 ppm; Fig. 4.17). The lower ignimbrite group on the other hand has the lowest Y concentration (30.2 ppm) out of the three groups. The upper ignimbrite group in comparison has a Y concentration of 30.6 – 31.9 ppm, while the lapillistone group has an even higher Y concentration of 32.1 – 33.4 ppm (Fig. 4.18). This Y trend might imply chemical grading within the Burol Formation (Fig. 4.18), however, with only five samples, more are needed to confirm or deny this hypothesis.

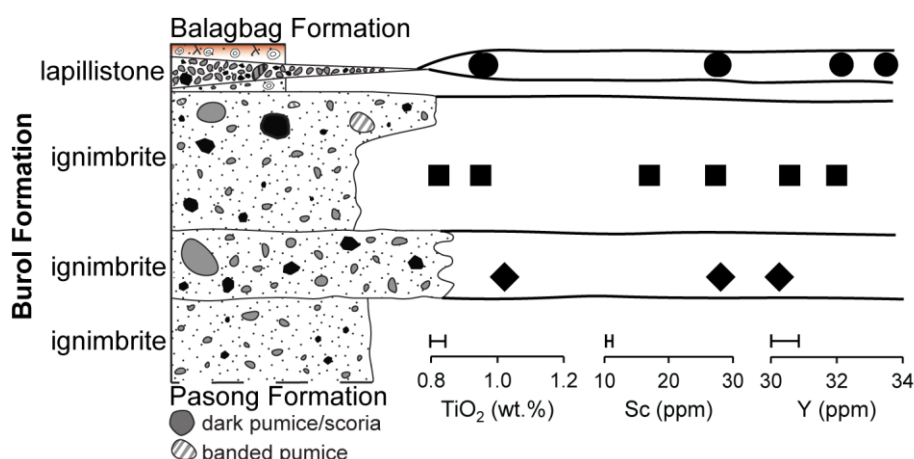


Fig. 4.18: Samples split by stratigraphic height. Lapillistone samples represented by circles, upper ignimbrite samples by squares, and lower ignimbrite samples by diamonds. TiO₂, Sc and Y are representative of the behaviour displayed by other elements. Error bars are 2 sigma.

The Balagbag Formation

There are insufficient samples from the Balagbag Formation to conduct a meaningful statistical analysis, but samples can be qualitatively analysed by stratigraphic height. The upper ignimbrite group has the lowest Fe₂O₃ concentration (9.81 wt.%), while the tuffs and pellets group (10.15 – 10.59 wt.%) and the lower and middle ignimbrite groups (10.09 wt.% and 10.47 wt.% respectively) have a similar Fe₂O₃ range (Fig. 4.19). Similarly, the upper ignimbrite group has the lowest Sc concentration (24.9 ppm), followed by the lower ignimbrite group (26.0 ppm), the middle ignimbrite group (27.2 ppm) and the tuffs and pellets group (27.8 – 28.2 ppm; Fig. 4.19). Contrastingly, the lower ignimbrite group has the highest Y concentration of 39.1 ppm, while the other groups have lower concentrations ranging from 30.9 ppm – 32.1 ppm. Although elemental concentrations may thus vary between stratigraphic groups, there is no trend with stratigraphic height visible (Fig. 4.19).

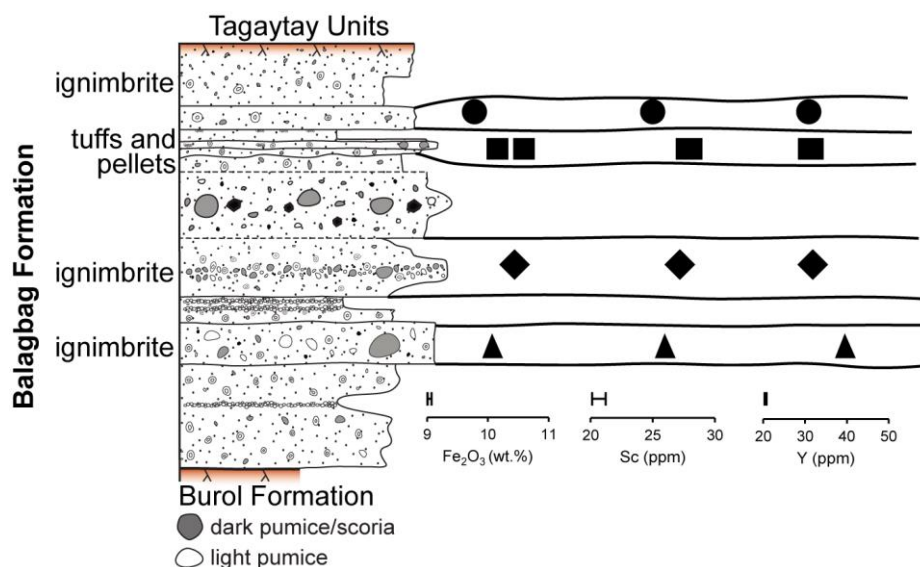


Fig. 4.19: Samples split by stratigraphic height. Upper ignimbrite samples represented by circles, tuffs and pellets samples by squares, middle ignimbrite samples by diamonds and lower ignimbrite samples by triangles. Lower and upper ignimbrite samples may be offset from the middle three samples for certain elements. Fe₂O₃, Sc and Y are representative of the behaviour displayed by other elements. Error bars are 2 sigma.

The Buco Formation

Only two samples from the same exposure can be grouped into different stratigraphic height categories (L3.22; [14° 06.440'N 121°11.044'E]; Appendix A). Other samples are from different localities and are stratigraphically placed as best as possible. The dataset is divided into four stratigraphic groups: (1) lithic breccia, (2) lower ignimbrite, (3) upper ignimbrite, and (4) cross-bedded (Fig. 4.19). The lithic breccia has a SiO₂ composition of 61.07 wt.%, which is higher than both the lower (56.21 – 58.30 wt.%) and upper ignimbrite groups (58.01 – 58.15 wt.%). The cross-bedded group is the only one with a higher SiO₂ composition (56.91 – 62.22 wt.%) than the lithic breccia group (Fig. 4.19). This is being driven by the three high SiO₂ samples that have been highlighted as outliers within the cross-bedded group (Fig. 4.20). These three high SiO₂ samples have similarly different Sc concentrations, namely lower (17.5 – 18.7 ppm) compared to the rest of the cross-bedded group (23.5 – 31.8 ppm). The upper and lower ignimbrite groups have Sc concentrations that fall into the range of the cross-bedded group (24.6 – 27.5 ppm and 24.1 – 30.2 ppm

respectively), similarly to the lithic breccia sample (23.1 ppm). The lithic breccia sample has the highest Y concentration (33.4 ppm), however, except for the high SiO₂ samples from the cross-bedded group (34.7 – 35.5 ppm). The rest of the cross-bedded group have lower Y concentrations of 26.9 – 30.4 ppm and the upper and lower ignimbrite groups have a similar concentration (27.4 – 27.9 ppm and 25.0 – 30.0 ppm; Fig. 4.20).

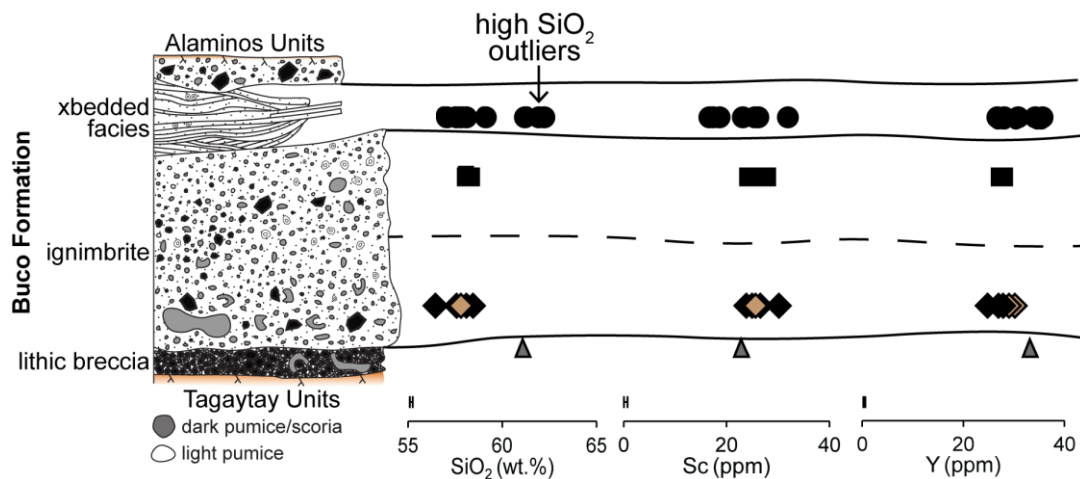


Fig. 4.20: Samples split into four groups based on their stratigraphic height for SiO₂, Sc and Y. These elements are representative of the different chemical trends seen across the Buco Formation. The cross-bedded (xbedded) group are represented by circles, the upper ignimbrite by squares, the lower ignimbrite by diamonds, and the lithic breccia by a triangle. Juvenile samples have black symbols, matrix samples brown symbols, and the lithic breccia sample a grey symbol. The high SiO₂ outliers from the cross-bedded group are highlighted. Error bars are 2 sigma.

To test whether any stratigraphic groups show any statistically significant differences between each other for different elements, they were analysed in their stratigraphic groups on the JMP program. The lithic breccia group is significantly different from all other groups for TiO₂ (Fig. 4.21), while for Cu the lithic breccia and cross-bedded groups are significantly different from both ignimbrite groups. A wider range of elements (Ce, Nb, Nd, Rb, Sr, Th, V, and Y; Fig. 4.21) shows a significant differences between the lower ignimbrite group and the cross-bedded group, which is likely driven by the three high SiO₂ outlying samples (Fig. 4.21) identified in the cross-bedded group.

The JMP statistical program was again used to investigate whether significant differences still exist between the stratigraphic groups if the lithic breccia group

and the three outlying samples from the cross-bedded group are removed. Results show that there are no more significant differences between any stratigraphic groups, therefore the lithic breccia group and three outlying samples from the cross-bedded group account for the variation shown within the Buco Formation (Fig. 4.21).

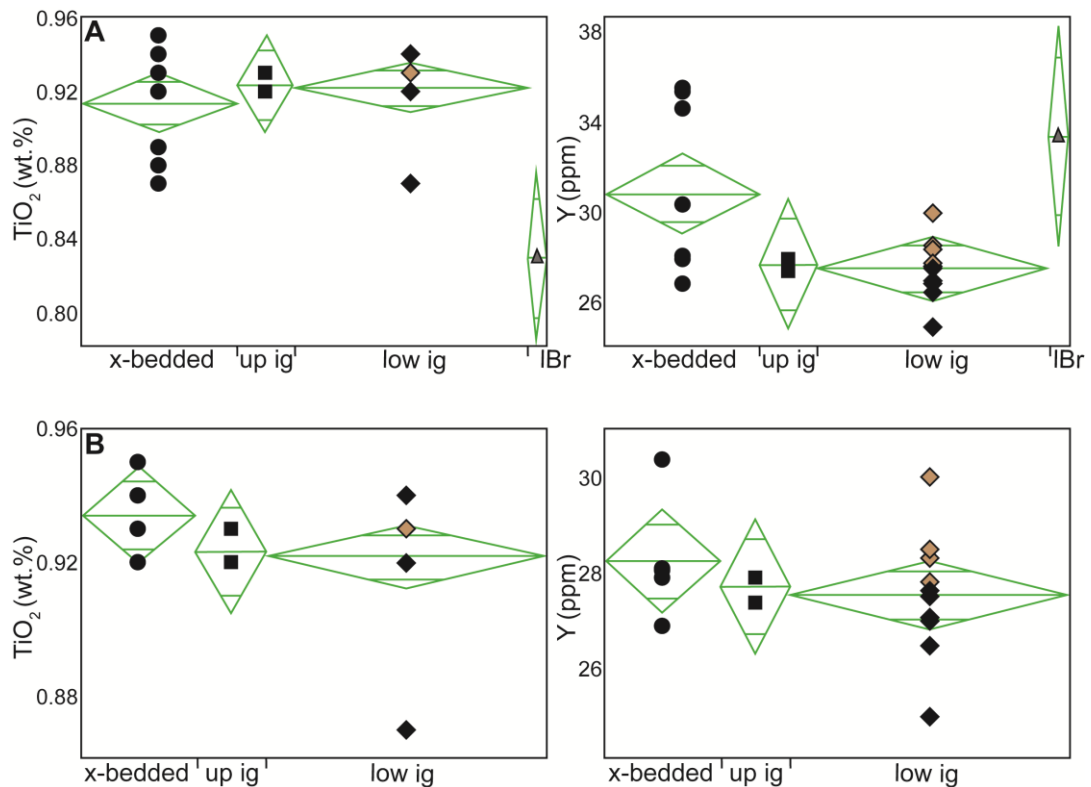
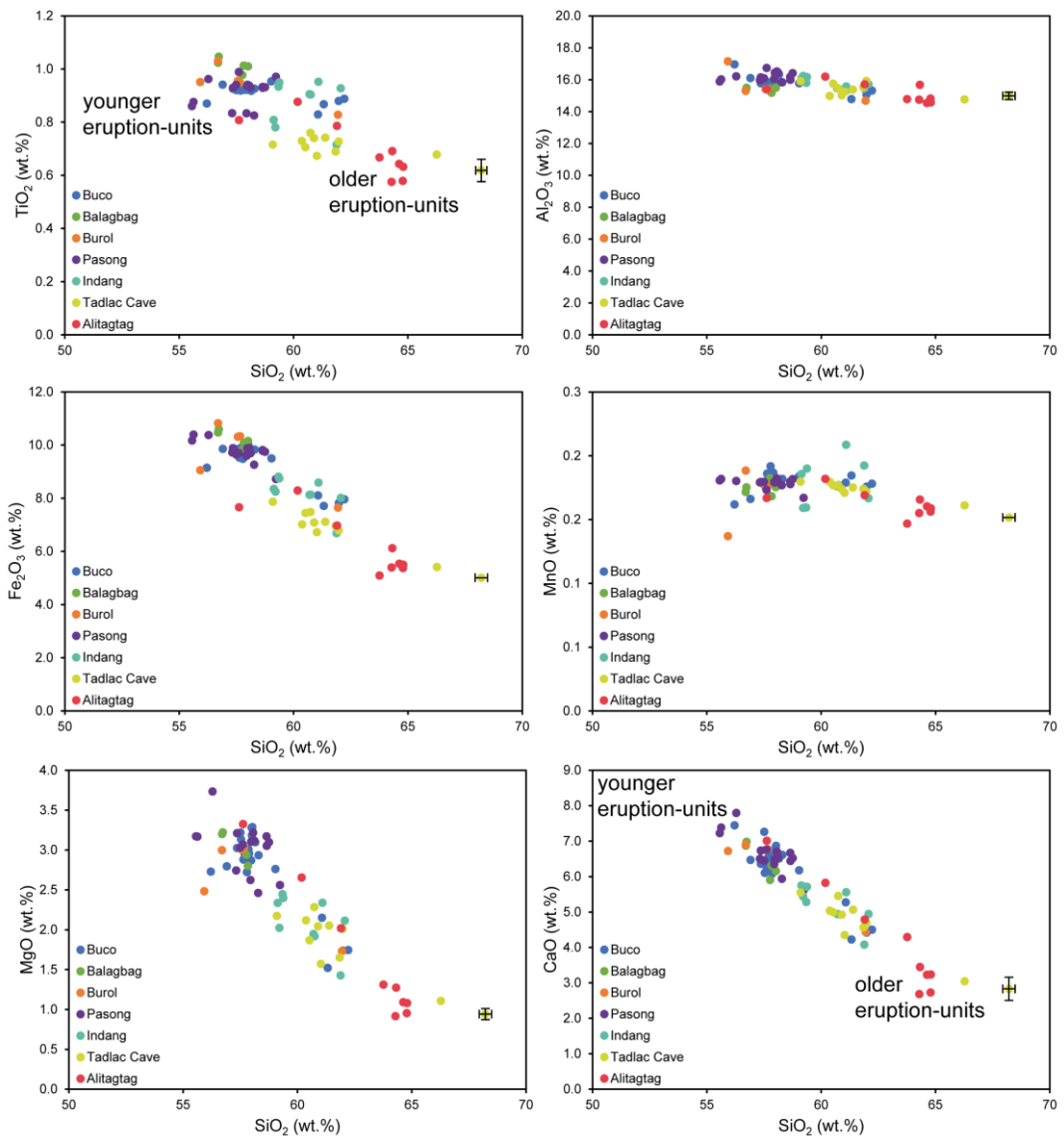


Fig. 4.21: (A) ANOVA plots for TiO₂ and Y with all samples. Significant differences between the IBr and the cross-bedded (x-bedded) group (p-value: 0.0089), the upper ignimbrite group (p-value: 0.0074), and the lower ignimbrite group (p-value: 0.0035) for TiO₂, while significant differences between the cross-bedded and lower ignimbrite group (p-value: 0.0291) are found for Y. P-values calculated by the Tukey-Kramer HSD test. **(B)** ANOVA plots for TiO₂ and Y without cross-bedded outliers and the IBr group. No significant differences are found between any groups. Symbols match those in Fig. 4.20.

4.5 Differentiating named formations within the Taal Group

4.5.1 Major element geochemistry

When all formations are combined on the Harker diagrams, they all plot roughly along the same trend line. This trend line decreases as the melt evolves for TiO_2 , Fe_2O_3 , MgO and CaO while it stays subhorizontal for Al_2O_3 and MnO , and increases for Na_2O and K_2O , while no clear trend is visible for P_2O_5 (Fig. 4.22). The decrease in TiO_2 , Fe_2O_3 and MgO reflect fractionation of Fe-Ti oxides (e.g.



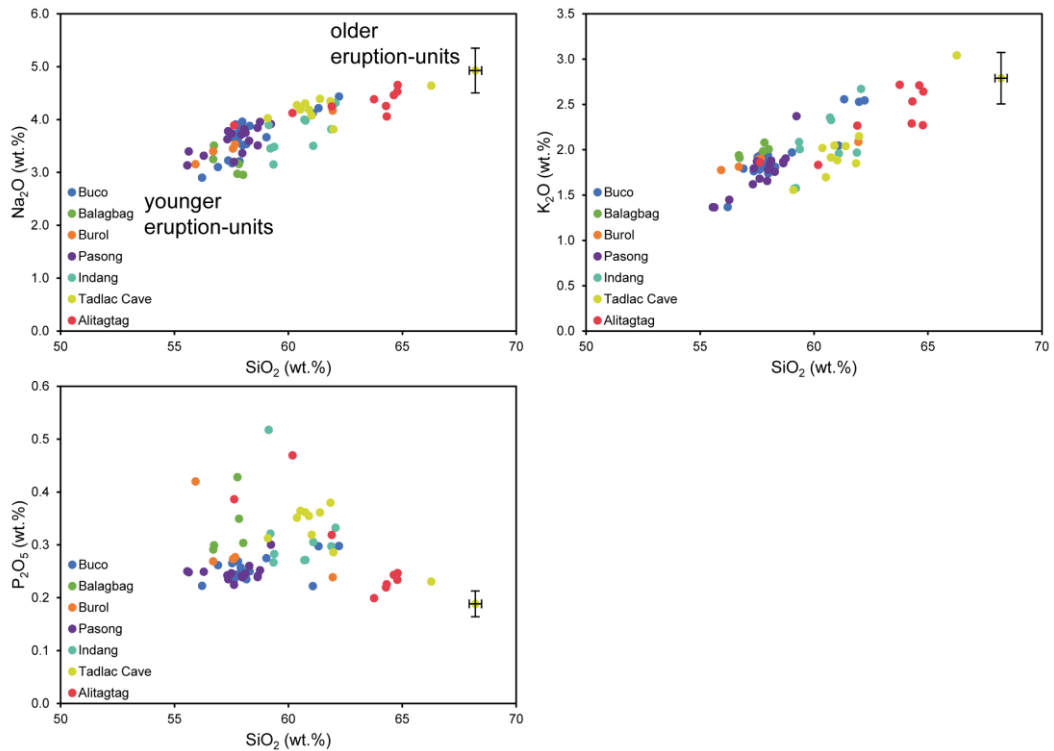


Fig. 4.22 (p.200-201): Harker plots for all major oxides. Error bars are 2 sigma. Error bars are not drawn where they are smaller than the size of data points.

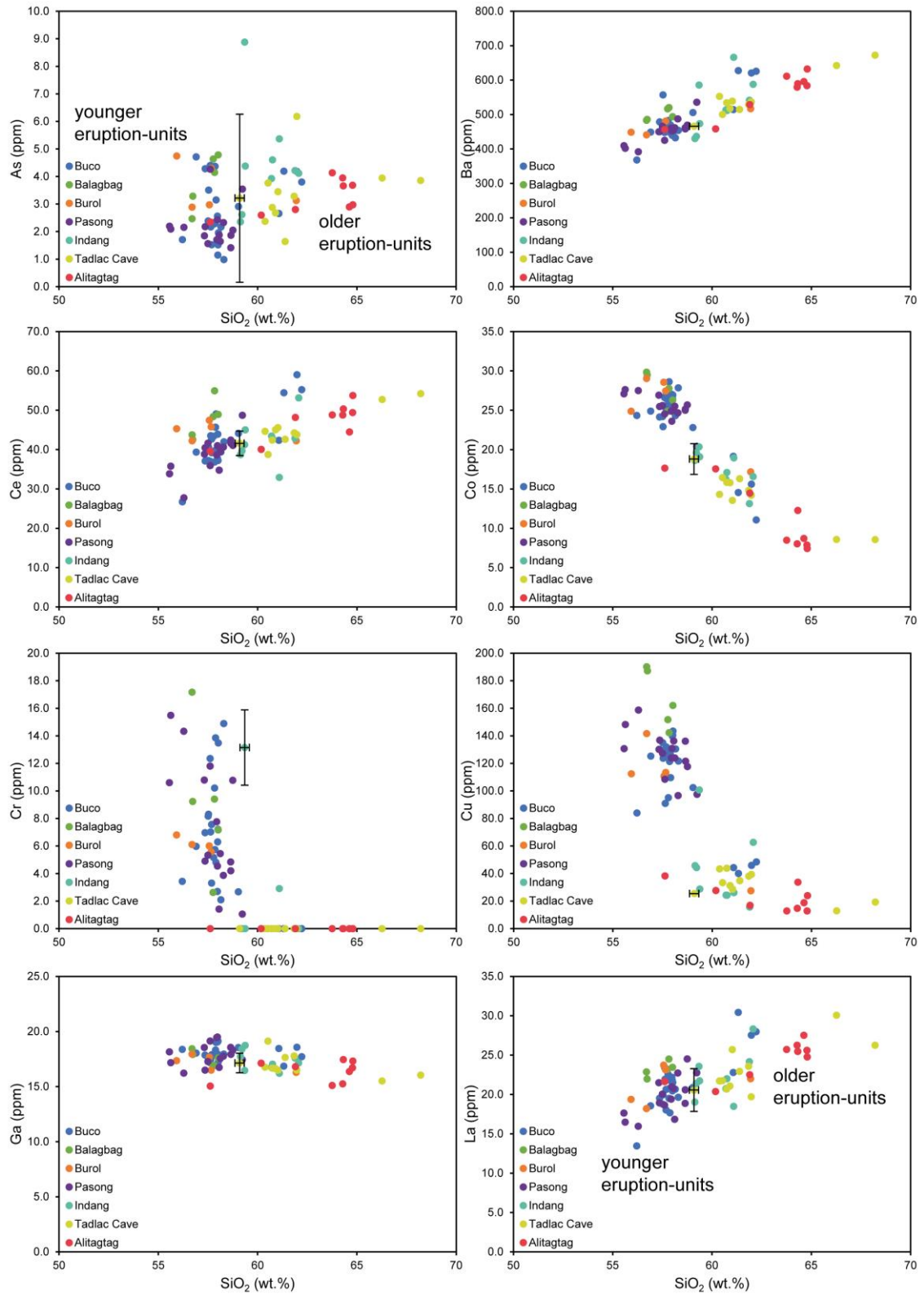
Elburg, 2010; Fig. 4.22) and other mafic phases such as pyroxene. The decrease of CaO may represent the fractionation of plagioclase, but the increase in Na₂O and K₂O suggests a lack of fractionation of any relatively felsic phases (Fig. 4.22). Stratigraphically, eruption-units appear to be becoming less evolved over time (i.e. the Alitagtag Formation has a higher SiO₂ content than the Buco Formation; Section 4.5.4), thus suggesting that the magmas feeding eruptions from Taal Caldera Volcano are not sourced from a single continuously evolving source. If they were, we would expect the youngest eruption-units to be the most evolved.

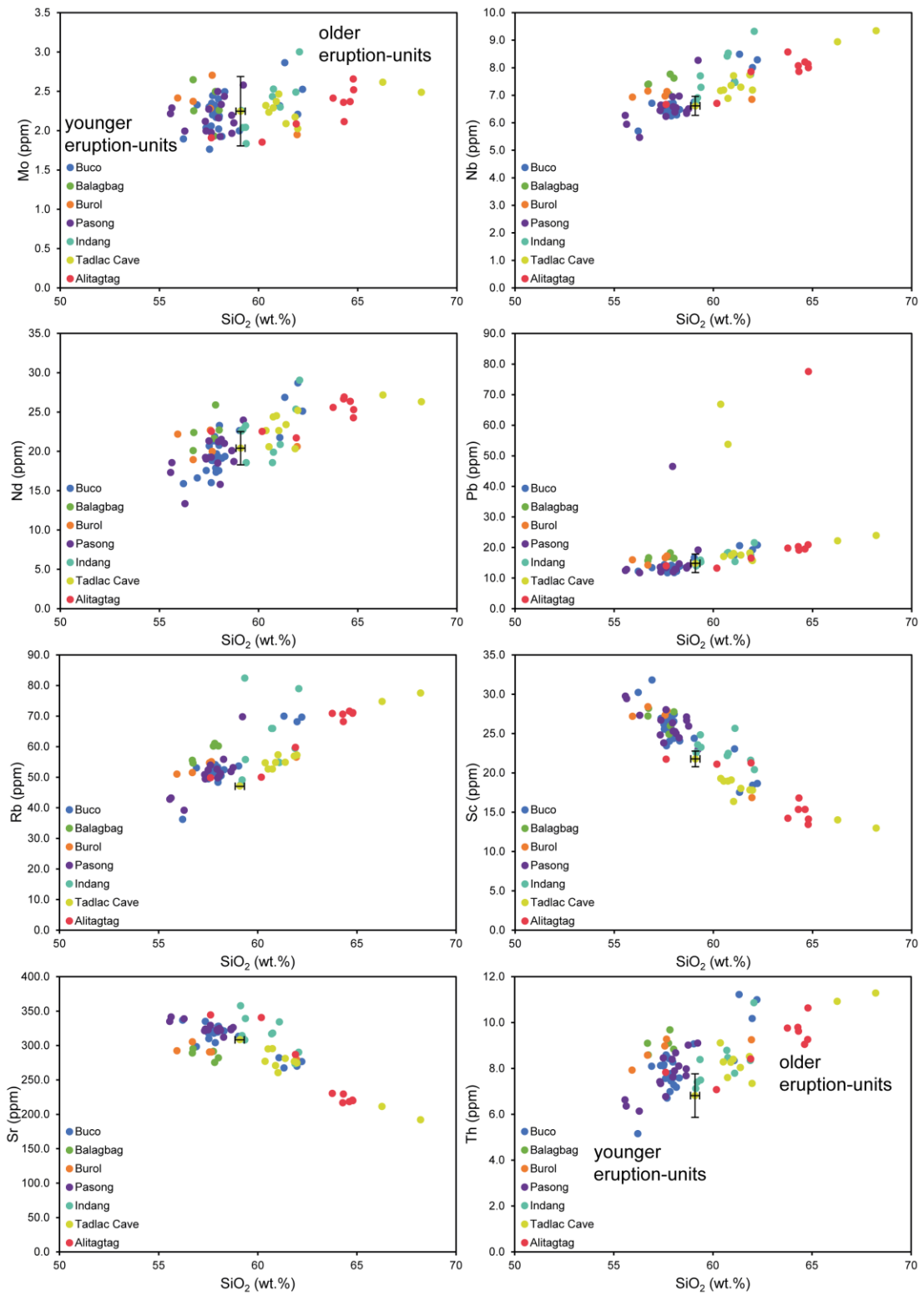
4.5.2 Trace element geochemistry

All Taal samples lie along relatively well defined trend lines with As, Ce, La, Mo, Nd, Rb, Th, U, and V showing slightly more spread than other elements. This spread and observed increases of As and U as melts become more evolved need to be interpreted cautiously because of the relatively large error bars

calculated for As and U. Almost all trace elements behave incompatibly and increase in abundance as melt becomes more evolved (As, Ba, Ce, La, Nb, Nd, Pb, Rb, Th, U, Y and Zr; Fig. 4.22). Trend lines for Ga, Mo and Zn remain flat until ~63 wt.% SiO₂ for Ga when Ga concentrations slightly decrease, ~60 wt.% SiO₂ for Mo when Mo concentrations slightly increase, and ~63 wt.% SiO₂ for Zn when Zn concentrations slightly decrease (Fig. 4.23). These changes occur approximately at the same SiO₂ concentrations, perhaps suggesting more compatible phases have been used up by this point, and therefore less compatible phases like Ga and Zn are starting to move into crystallising phases. Only Co, Cr, Cu, Sc, Sr and V display compatible behaviours and decrease in abundance as melt becomes more evolved (Fig. 4.23). Cr decreases very quickly, reaching zero by ~60 wt.% SiO₂, emphasising the early fractionation of abundant magnetite. This early magnetite fractionation also leads to sulphite saturation at depth, which can explain the steep decrease shown by Cu as SiO₂ increases (Fig. 4.23; Jenner et al., 2010).

This decreasing concentrations of Sc, Sr and V with increasing SiO₂ could reflect the fractionation of all the mineral phases seen in the crystal assemblages of the Taal Group, namely plagioclase, pyroxene and Fe-Ti oxide (possibly magnetite). Plagioclase is compatible with Sr (e.g. Humphreys et al., 2019) and thus its fractionation can account for the decreasing Sr (Fig. 4.23). The fractionation of pyroxenes can account for the decreasing Sc concentrations (e.g. Bachmann et al., 2012; Nielsen et al., 2017) while the decreasing V concentration can reflect the fractionation of magnetite (e.g. Asan, 2020; Fig. 4.23). The sharp drop in V concentration compared to Sc and Sr again indicates that magnetite fractionation played a key role during the formation of all Taal magmas. It is emphasised again that younger eruption-units are less silicic than older eruption-units, showing that magmas feeding eruptions from Taal Caldera Volcano have not evolved from a single, consistently evolving source.





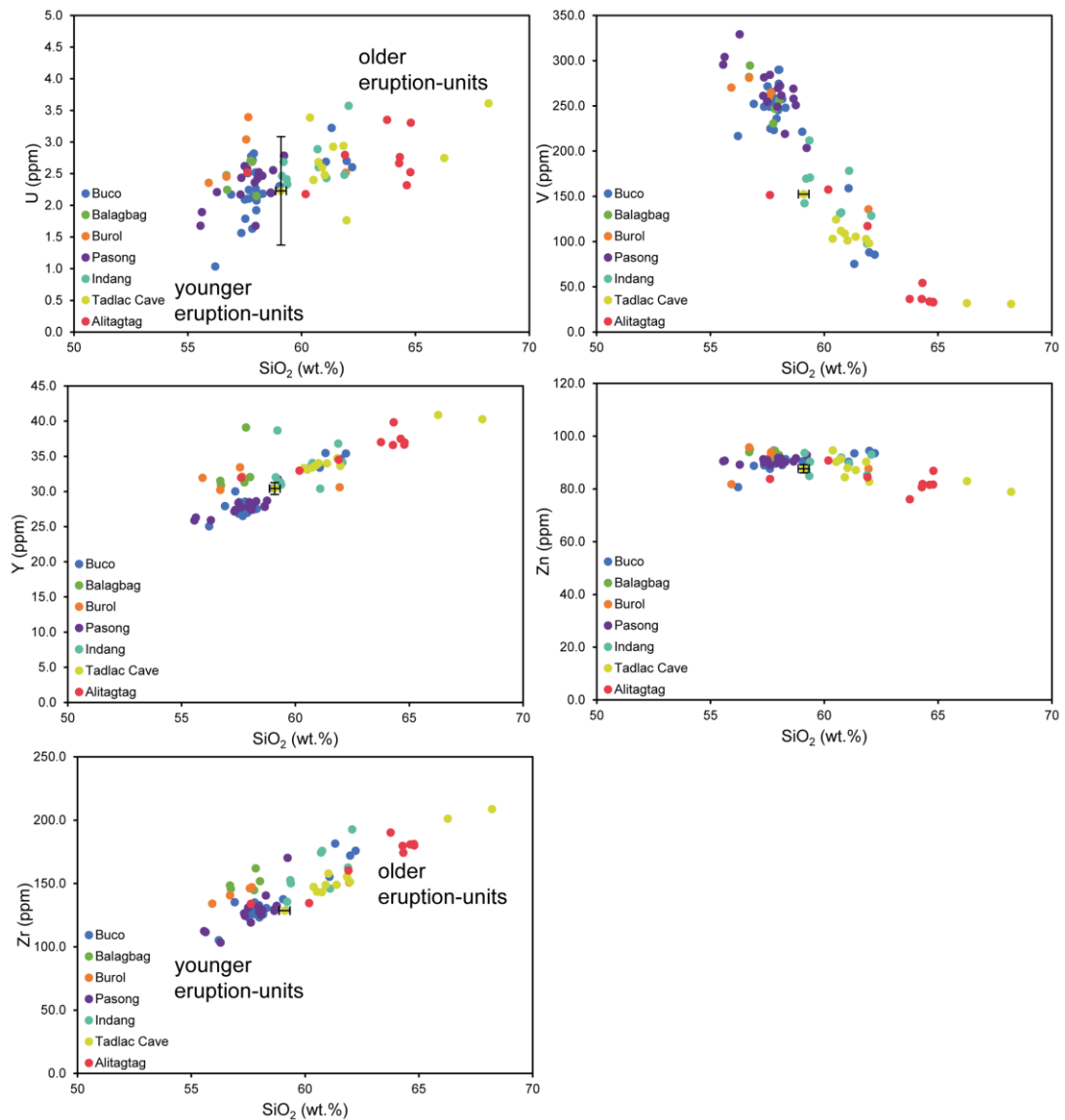


Fig. 4.23 (p. 203-205): Harker plots for all trace elements. Error bars are 2 sigma. Error bars are not drawn where they are smaller than data points.

Since results show that it is not a single continuously evolving magma source that provides the melts for all the prehistoric eruption-units, simple models were made to test whether each individual magma was formed by pure fractional crystallisation from a primitive source or whether mixing was likely required. This was achieved by plotting elements with tight linear trends (Y, Zr) and those showing a decrease in concentration as melts evolve (Sc, Sr, V) against immobile element Rb (Fig. 4.24). It is not currently possible to ascertain whether assimilation was involved because no isotope data is available and the

composition of the subsurface around Taal Caldera Volcano is poorly exposed and defined (Listanco, 1994).

An average crystal assemblage based on all samples from the Taal Group was established to use for fractional crystallisation (Fig. 4.24) because there were only limited samples for each formation and thus crystal assemblages described in this study may not be representative of entire individual formations. Overall fractional crystallisation curves are a better fit for the older, more evolved Alitagtag and Tadalac Cave formations, particularly regarding V concentrations (Fig. 4.24). Although Sc and Sr concentrations for the Alitagtag and Tadalac Cave formations do not plot on the fractional crystallisation curve (Fig. 4.24), if the starting composition for these two formations had slightly higher Sc and Sr concentrations the fractional crystallisation curve may fit. Importantly, the Alitagtag and Tadalac Cave formations lend themselves more to a hyperbolic curve such as that resulting for incompatible elements from fractional crystallisation.

The other formations on the other hand only fall on fractional crystallisation lines for the incompatible elements Y and Zr (Fig. 4.24). It would be difficult to fit a hyperbolic curve to the concentrations of these formations for Sc, Sr and V. The trend line for these formations is much more linear and therefore lends itself more to a mixing line (Fig. 4.24). Although the mixing line created using the least and most evolved compositions from the Taal Group does not pass through all data points from the Buco, Balagbag, Burol, Pasong and Indang formations, a linear mixing line using two other compositions could. It is likely that the compositions mixing together were not the same for all formations, particularly the Indang Formation, which has a much shallower linear trend line compared to the Buco, Balagbag, Burol and Pasong formations.

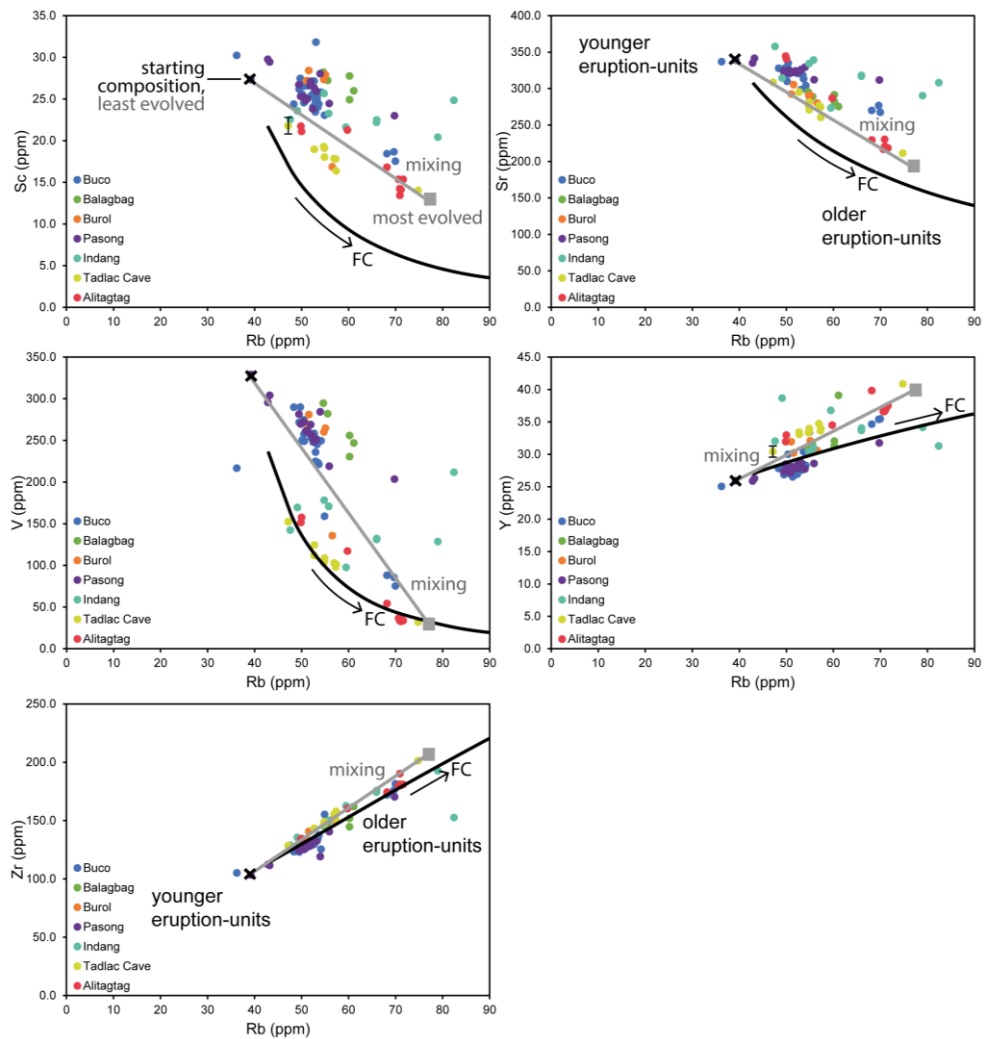


Fig. 4.24: Biplots of key elements plotted against the incompatible element Rb. Fractional crystallisation curves use the least evolved sample (Pasong Formation, T3.21; appendix B) as starting composition and are drawn for an assemblage of: orthopyroxene (15%), clinopyroxene (20%), plagioclase (55%) and magnetite (10%). Partition coefficients based on Luhr and Carmichael (1980), Bacon and Druitt (1988), Ewart and Griffin (1994). Mixing lines are drawn using the least evolved sample and most evolved sample (Tadalac Cave Formation, T2.5; Appendix B). Error bars are 2 sigma. Error bars are not drawn where they are smaller than data points.

Magma mixing is a common process where large-volume intermediate magmas are produced in arc settings (e.g. Eichelberger, 1975; Reubi and Blundy, 2009; Kent, 2014; Blum-Oeste and Wörner, 2016; Klaver et al., 2018). There is also non-chemical evidence for magma mixing and mingling in the Taal Group including mingled and banded pumice (Perugini and Poli, 2012) in the Alitagtag and Burol formations, resorption textures (e.g. Hibbard, 1991) in the Tadalac Cave Formation, and banded scoria (i.e. flow structures in Perugini and Poli, 2012) in the Indang Formation. Previous work has identified magma mixing within the Pasong Formation as well (Listanco, 1994), therefore magma mixing

is likely a dominant process during magma genesis at Taal Caldera Volcano as previously postulated by Listanco (1994). The older Alitagtag and Tadalac Cave formation melts were developed largely by fractional crystallisation with minor mixing, while all for the younger formations magma mixing was more dominant.

4.5.3 Distinguishing formations

Investigations into the major and trace element geochemistry has shown that not all formation melts may have formed in the same way. Samples from individual formations tend to mostly cluster together, although there is some spread. The general clustering of samples suggests that there may be elements that allow the chemical distinction of different formations from each other. Graphically, it is relatively easy to discriminate the older Alitagtag and Tadalac Cave formations from all other formations because of their more evolved composition (Figs. 4.22, 4.23). Major oxides TiO_2 and Fe_2O_3 also seem to provide enough spread between the Alitagtag, Tadalac Cave and Indang formations to differentiate them from each other and the four younger formations (Fig. 4.22). The trace element Cu is excellent at discriminating the younger Buco, Balagbag, Burol and Pasong formations from the older Indang, Tadalac Cave and Alitagtag formations (Fig. 4.23). The Balagbag and Burol formations also seem to be separated from all other formations by their lower Sr concentrations and higher Y and Zr concentrations (Fig. 4.23). It appears impossible to chemically differentiate between the Buco and Pasong formations.

To make these interpretations more robust and highlight any other elements that may be good at discriminating formations from each other, linear discriminant analysis (LDA) was conducted on the JMP program. This method takes all the different elements into consideration at the same time and emphasises the differences between the formations. Multiple runs of LDA were performed to explore the differences brought about by element mobility. Multiple elements were initially used for each run because a larger number of elements will make it more likely that formations will be able to be distinguished from each

other. There were three different elemental groups run: (run 1) immobile elements only, (run 2) immobile and potentially mobile elements, and (run 3) all elements (see Section 4.2.2 for data reliability explanation). Although formations can display internal chemical variation with some outlying samples recognised (Section 4.4.2), due to the small sample sizes it is important to include these outliers because if more samples are collected in future the outliers may prove to be more common than currently thought. Therefore, no outliers were removed from any datasets run through the JMP program.

Run 1 used the most robust dataset (i.e. immobile elements only) and allowed the distinction of the Alitagtag, Tadalac Cave and Indang formations from the other formations (Fig. 4.25), which supports the graphical hypothesis that the Alitagtag and Tadalac Cave formations could be differentiated from all other formations. The Indang formation was not graphically observed to sufficiently differ from other formations on Harker plots (Figs. 4.22, 4.23). The 95% confidence ellipses of the Alitagtag, Tadalac Cave and Indang formations did not overlap with any other formation group, therefore they are significantly different from all other formations. However, the 95% confidence ellipses for the Alitagtag and Tadalac Cave formations overlapped with each other and one sample from each formation was misclassified (outlier T2.7 from the Tadalac Cave Formation and outlier T3.22 from the Alitagtag Formation; Section 4.3.2), which was also the case during run 2, while only T2.7 was misclassified during run 3. Therefore, the Alitagtag and Tadalac Cave formations are chemically similar and unless their outlying clasts (i.e. the high SiO₂ clasts from the Tadalac Cave Formation, Fig. 4.13, and the low SiO₂ black pumice from the Alitagtag Formation, Fig. 4.11) are not taken into account they cannot be distinguished from each other. The Alitagtag and Tadalac Cave formations can therefore not be chemically distinguished from each other, which contradicts the graphical interpretation based on major and trace element plots.

The Balagbag and Buroi formations could only be distinguished from each other and the Pasong and Bucu formations in runs 2 and 3 because in run 1 their 95% confidence ellipses overlapped and samples were misclassified (Fig. 4.25), which suggests that the chemical difference between these formations is driven

by a potentially mobile element. This result supports the hypothesis made from Harker plots that Cu (a potentially mobile element) is the only element able to differentiate the Balagbag and Burol formations, but graphically it appeared that the Balagbag and Burol formations could be distinguished from the Buco and Pasong formations using immobile elements Sr, Y and Zr, which statistically does not appear to be the case. No LDA runs were able to distinguish the Pasong and Buco formations from each other; (Fig. 4.25) all runs often statistically misclassified them as each other, which supports the hypothesis made graphically that the Pasong and Buco formations could not be chemically distinguished from each other.

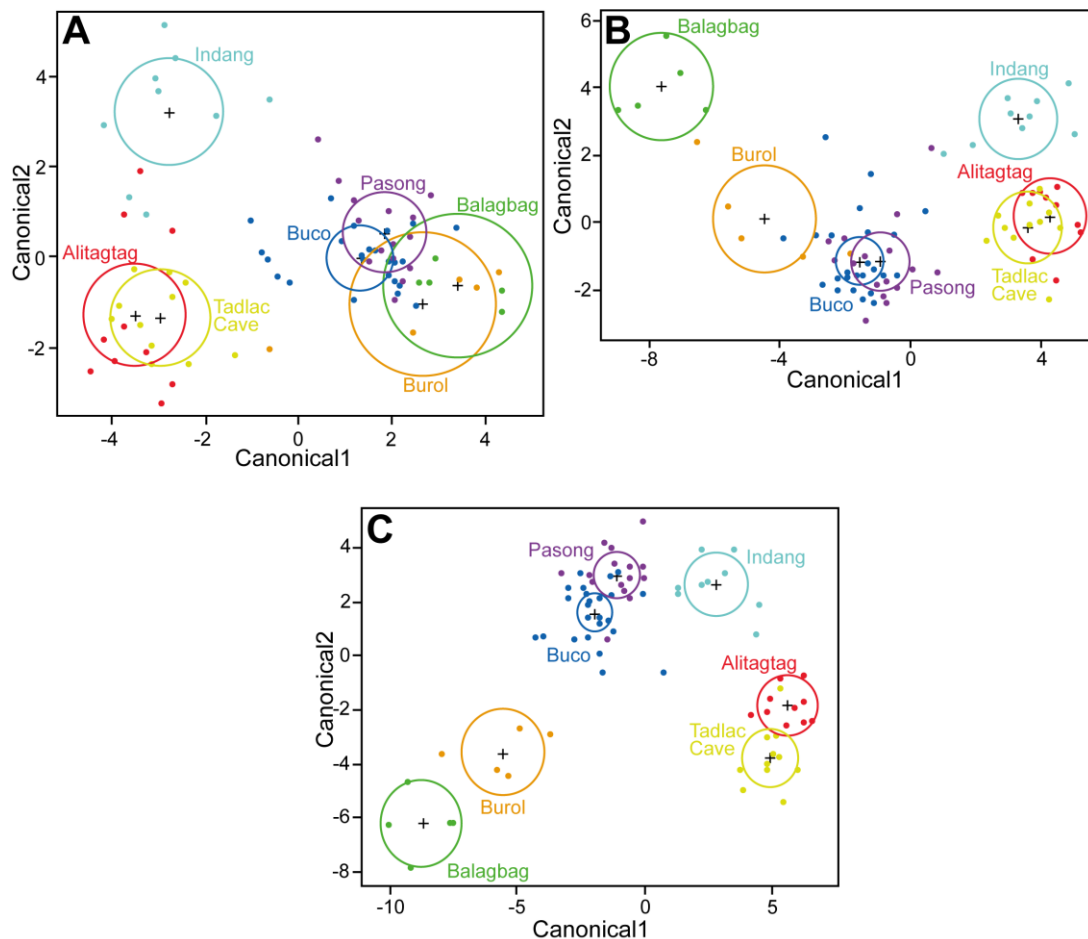


Fig. 4.25: The LDA plots show the two canonicals that show the maximum separation between formations. The '+' symbol represents the mean of individual formations. Samples from all formations are plotted in different colours, which match the colour of the 95% confidence ellipse for that formation. Plots show the following: **(A)** immobile elements, **(B)** immobile and potentially mobile elements, and **(C)** all elements.

Since most formations could be distinguished using the immobile and potentially mobile dataset, this dataset was further investigated to determine which individual elements were best to distinguish formations from each other. To achieve this, the canonical weightings of each element (based on the canonical structure dataset on JMP and the p-values from the Tukey-Kramer HSD tests) were used to determine which elements accounted for most of the variation between the different formations. The lower the p-value was and/or the higher the absolute canonical weighting was, the more important an element was with regards to distinguishing formations from each other.

An initial selection of elements was made comprising elements that were within the top five of canonical weightings for the first two canons (the most significant) and showed >5 significant differences (p-value <0.05) between formations was made (Appendix F). The elements in this selection were: TiO₂, Fe₂O₃, Cu, Sc, V, Nb, Y and Zr, many of which were also graphically identified as significant on Harker plots (Figs. 4.22, 4.23). The selection of elements was then narrowed down by trial-and-error, creating bivariate plots on excel until the best single element to place on each graph axes was identified. The bivariate plots that graphically best separated most formations were: Y vs. Fe₂O₃ and Sc vs. Y (Fig. 4.26). The bivariate plot Cu vs. SiO₂ was also useful because it graphically separated the Balagbag and Burol formations from each other, similarly to the Cu Harker plot (Fig. 4.23). Several formations from the Taal Group can therefore be distinguished using juvenile geochemistry, similarly to certain

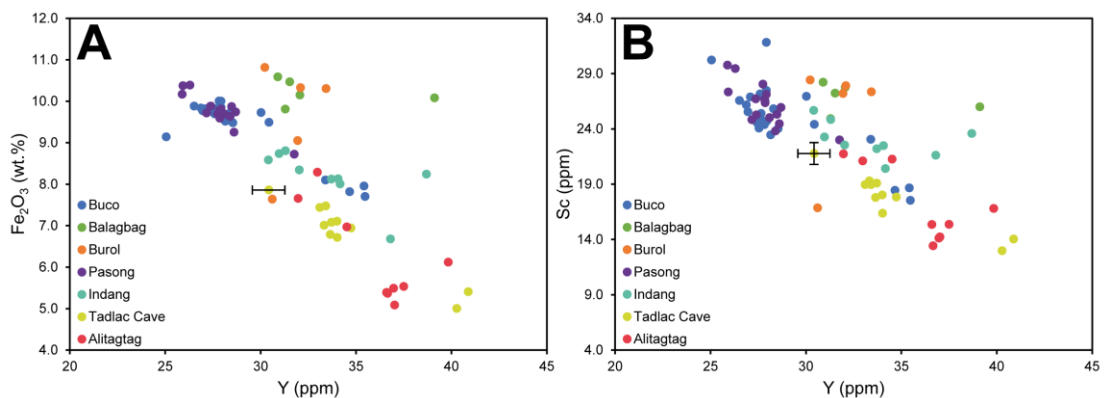


Fig. 4.26: (A) The Fe₂O₃ vs. Y bivariate plot allowing visual distinction between most formations. **(B)** The Sc vs. Y bivariate plot is the best to visually distinguish formations using immobile elements only. Neither plots allow the Buco and Pasong formations and the Balagbag and Burol formations to be distinguished from each other. Error bars are 2 sigma. Error bars are not plotted where they are smaller than data points.

deposits from the Snake River Plain, USA (Morgan et al., 1984; Ellis et al., 2019) and the Central Andes, Northern Chile (De Silva and Francis, 1989). The elements most useful in this distinction strongly depends on the volcanic system; there does not appear to be a common combination for a specific region, let alone globally, e.g. rare earth elements are not useful in the Central Andes, Northern Chile (De Silva and Francis, 1989), but are good discriminators in nearby Arequipa, Southern Peru (Lebti et al., 2006).

It is appreciated that the bulk juvenile geochemistry of samples will likely be less evolved than their juvenile glass chemistry due to the presence of phenocrysts (Smith et al., 2005), however, since all Taal samples are phenocryst-poor (Section 4.4.1) this is not expected to make a significant difference at Taal (Hahn et al., 1979; De Silva and Francis, 1989; de Maisonneuve and Bergal-Kuvikas, 2020). Despite the scarcity of phenocrysts, their potential effect on juvenile chemistry collected in this study may become important when comparing proximal juvenile chemistry to very distal tephra, perhaps of limited abundance, from sea or lake cores where glass shards are the dominant component (Smith et al., 2011A). Although such detailed glass chemistry work may be able to distinguish different tephra units at some volcanoes (Smith et al., 2011A), this may not be the case for the Buco and Pasong formations for example, which have an incredibly similar chemistry. In this case, it may be necessary to analyse crystal compositions, which have been successfully used at Toba, Indonesia (Smith et al., 2011B) and in the Snake River Plain, USA (Ellis et al., 2019) to differentiate eruption-units that were undistinguishable using glass chemistry.

4.5.4 The temporal geochemical evolution of Taal Caldera Volcano

The composition of Taal's eruptive products ranges from dacite to basaltic andesite, with prehistoric ignimbrite-forming eruptions seemingly becoming less evolved over time (Fig. 4.27) with the past four eruptions having relatively similar silica compositions (i.e. the Pasong, Burol, Balagbag and Buco

formations). This trend can also be observed with data from previous work (Listanco, 1994; Martinez and Williams, 1999), but it is not explicitly commented upon. Other elements that reflect the fractionation of plagioclase, pyroxene and magnetite as well as the incompatible element Y, show an increase or decrease from the oldest Alitagtag Formation to the younger Indang Formation, while all these elements remain relatively constant for the four youngest formations (Pasong, Burol, Balagbag and Buco formations; Fig. 4.27). Mixing is thought to have been the dominant mechanism involved during magma evolution for the five youngest formations (Indang – Buco formations), which thus suggests that mixing has become more important at Taal Caldera Volcano over time, a hypothesis that is supported by the relatively similar average compositions of

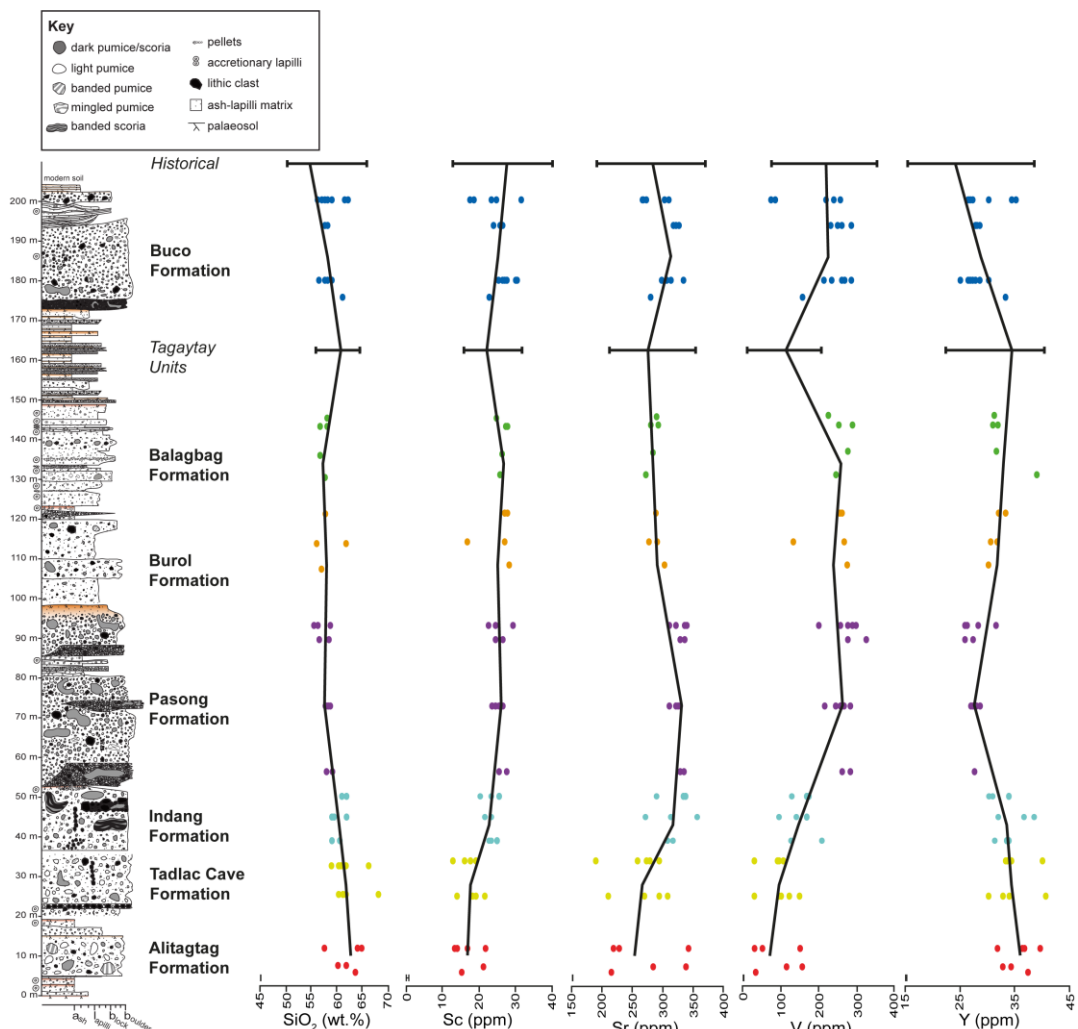


Fig. 4.27: Temporal changes within the Taal Group for key elements, including the Tagaytay Units, which consist of multiple eruption-units, and historical eruption-units alongside the general vertical section for the Taal Group. Data points are split up stratigraphically as done in Section 4.4.2 where relevant. Each graph shows a line connecting the average values of different formations and units. Error bars shown at the bottom of the graph are 2 sigma.

the four youngest units. The evolution of the Indang magma is also hypothesised to have been dominated by mixing (Section 4.5.2) despite its composition being relatively different to any other formation.

Historical eruptions from Volcano Island show a large compositional range, spanning, and sometimes exceeding, that of all prehistoric eruptions (Fig. 4.27), although a large proportion of historical eruptions are more primitive than ignimbrite-forming eruptions. A similar pattern is seen for the prehistoric Tagaytay Units, which, like historical eruptions, represent a series of relatively small eruptions (Fig. 4.27). This trend suggests that smaller-scale eruptions are of similar composition to larger-scale eruptions, as also seen in the Jeju Island Volcanic Field, South Korea (Brenna et al., 2012). Since relatively evolved compositions thus also make up some historical eruptions, more evolved melts must still be able to be formed in the present day. Therefore the lower SiO₂ compositions displayed by the youngest four formations cannot be explained by evolved melts not being able to form, which supports the hypothesis that mixing was key in their magma evolution.

However, the generally more primitive nature of many of the smaller-scale historical eruptions could indicate that Taal Caldera Volcano is in the post-collapse stage of its caldera cycle, since this stage is identified by more frequent eruptions with more primitive compositions (Shane et al., 2005; Bachmann et al., 2012; Gelman et al., 2013; Barker et al., 2014; Forni et al., 2018). Taal would thus follow the trend of Campi Flegrei, Italy (Forni et al., 2018) and the Taupo and Okataina Volcanic Zones, New Zealand, although most of the latter's more primitive eruptions are still significantly more evolved than those at Taal and Campi Flegrei (Smith et al., 2005). If eruptions at Taal Caldera Volcano start to become more evolved and less frequent, it may be an indicator that a new caldera cycle is starting (Forni et al., 2018). With Taal's general temporal trend towards more primitive compositions, however, there may not be a large difference between smaller-scale mafic eruptions, and the compositions of those slightly larger eruptions that occur during the pre-caldera collapse stage of the cycle. In addition, those pre-caldera eruptions, especially within 5 – 30 kyr of a caldera-forming eruption, usually have a similar

composition to the caldera-forming eruption (Bachmann and Huber, 2016). Therefore at Taal, eruptions throughout the caldera cycle may all have relatively similar compositions on average, which makes it challenging to gauge in which part of its caldera cycle Taal presently lies, based on the geochemistry of its eruptions alone.

4.5.5 Geochemistry of large, caldera-forming eruptions

Plinian eruptions are more likely to have an evolved composition ($\text{SiO}_2 > 60$ wt.%); there are only a handful of Plinian basaltic eruptions recorded in the last 2.5 Ma (Cioni et al., 2015). When it comes to explosive caldera-forming eruptions, this number is even less frequent because large, ignimbrite-forming eruptions tend to be relatively silicic (Bachmann and Bergantz, 2008; Wotzlaw et al., 2013). Masaya Caldera is an example of a volcano that has experienced an explosive caldera-forming basaltic eruption (Pérez et al., 2020), as has Niufou'ou volcano in Tonga, while later components of an eruption of Ambrym volcano on Vanuatu were also basaltic (Walker, 1993; Robin et al., 1993). Compositions of Taal's caldera-forming eruptions seem to fall in between these two extremes, covering a relatively large range from basaltic andesite to dacite (Fig. 4.28). These compositions are not the most primitive when compared to the compositions of VEI 7 eruptions from the past 10,000 years (Newhall et al., 2018) and multiple other caldera-forming eruptions (Fig. 4.28).

Ambrym volcano, Vanuatu, records the most primitive compositions, while the 4.2 ka Cerro Blanco eruption, Argentina, has the most evolved composition. Taal samples are relatively alkaline compared to most other volcanoes, although all samples from the Rinjani (Indonesia), Changbaishan (China – North Korea), Tambora (Indonesia) and Campanian (Italy) deposits have higher K_2O compositions compared to Taal, the latter three (partially) entering the alkaline series (Fig. 4.28). The Kurile Lake (Russia) and Mazama, Crater Lake (USA) eruptions are the only two whose fields extend into the low-K series (Fig. 4.28).

Although some caldera eruptions record a limited compositional range, the Rinjani, Indonesia eruption, does not follow this trend (Fig. 4.28). Eruptions like Mazama (USA), Ambrym (Vanuatu), and Kikai (Japan) clearly demonstrate the Bunsen-Daly gap (Bunsen, 1851; Daly, 1925, 1933) with their bimodal SiO₂ compositions (Fig. 4.28). Similar bimodal compositions, although across a smaller SiO₂ range, are seen for the Alitagtag, Buce, Buroi and Tadalac Cave formations from Taal (Fig. 4.28). This is quite common, however, because more primitive magma is thought to be the thermal driving force behind large-scale eruptions, and thus this magma can be partly, although scarcely, represented in the eruption deposit (Lowenstern and Hurwitz, 2008; Miller and Wark, 2008). The relatively primitive Pasong Formation from Taal is unique because any other caldera eruptions that have compositions in the basaltic andesite range also contain magma with a dacitic – rhyolitic composition (Fig. 4.28).

Individual Taal eruptions have a relatively small range in composition, both in terms of silica and potassium. This is compared to the Kurile Lake (Russia), Fisher (USA) and Minoan (Greece) eruptions, which display a large, continuous range of SiO₂, while the Changbaishan (China – North Korea), Cerro Blanco (Argentina) and Campanian (Italy) eruptions show a large, continuous range of K₂O (Fig. 4.28). Overall, there are more differences than similarities between all these caldera-forming eruptions and no geochemical trend can link all of them together.

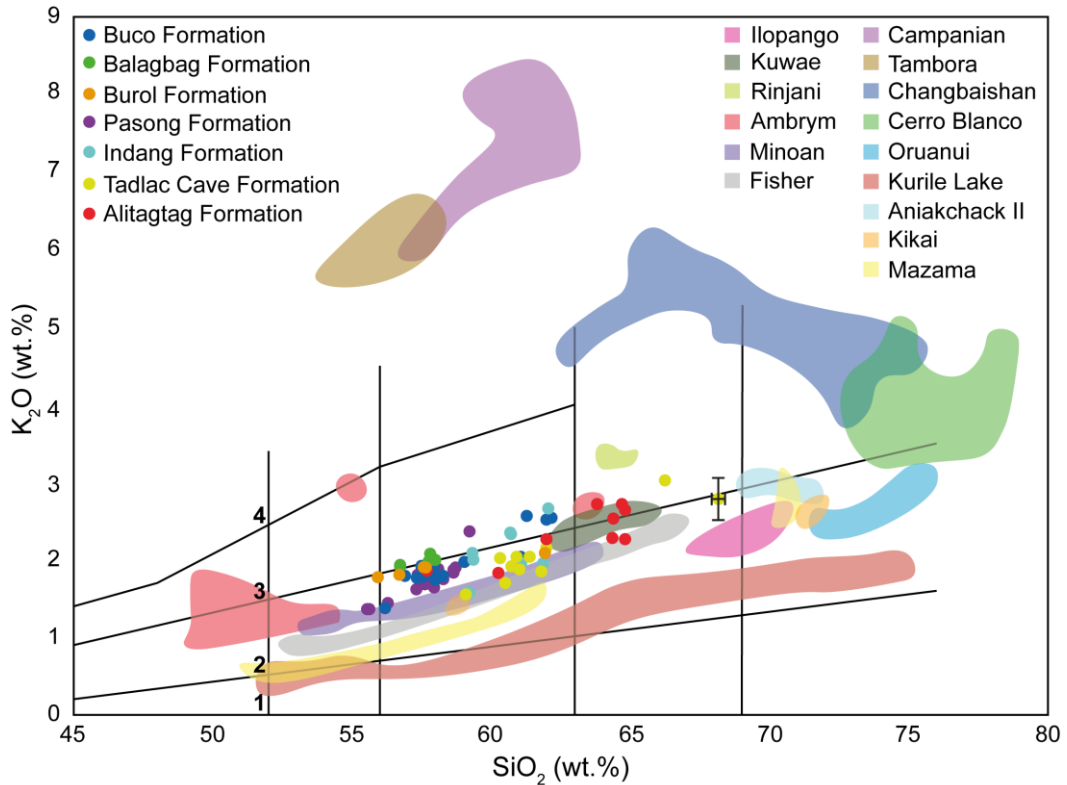


Fig. 4.28: K_2O Harker plot for all named formations compared with several VEI 7 eruptions from the past 10,000 years (Newhall et al., 2018) and multiple other caldera-forming eruptions compared to Taal's prehistoric, possibly caldera-forming eruptions (i.e. all named formations). The published eruptions used for comparison were selected based on data availability and with the aim of covering the largest geochemical range possible. Eruptions are: the Ilopango Tierra Blanca Joven eruption (Pedrazzi et al., 2019); the 1425 Kuwae eruption (Monzier et al., 1994; Robin et al., 1994); the 1257 Rinjani/Samalas eruption (Vidal et al., 2015); Ambrym Caldera (Robin et al., 1993); the Minoan eruption, Santorini* (Druitt et al., 1989); Fisher Caldera (Stelling et al., 2005); the Campanian eruption, Campi Flegrei* (Fedele et al., 2016); the 1815 Tambora eruption (Sigurdsson and Carey, 1989); the Changbaishan-Tianchi Millennium eruption (Pan et al., 2020); the 4.2 ka BP Cerro Blanco eruption (Fernandez-Turiel et al., 2018); the Oruanui eruption, Taupo* (Wilson et al., 2006); the 7600 BP Kurile Lake eruption (Ponomareva et al., 2004); the Aniakchak II eruption* (Riehle et al., 1987; Begét et al., 1992; Blackford et al., 2014); the 7.3 ka Kikai Caldera eruption (Maeno and Taniguchi, 2007); the Mazama, Crater Lake eruption* (Bacon, 1986); *normalised to 100%. Cerro Blanco, Aniakchack II and part of the Tambora data is juvenile glass chemistry and thus may not be directly comparable with the whole-rock Taal dataset. All other referenced data is whole-rock juvenile data and thus comparable. (1) Low-K series; (2) Calc-alkaline series; (3) High calc-alkaline series; (4) Alkaline series; based on Ewart (1982). Taal's prehistoric formations written in stratigraphic order from youngest (Buco Formation) to oldest (Alitagtag Formation). Error bars are 2 sigma.

4.6 Conclusions

- The Taal Group can be chemically distinguished from regional volcanoes, importantly from the other caldera volcano in the region, Laguna de Bay.
- Formations from the Taal Group are crystal-poor and contain plagioclase, pyroxene and oxides.
- The Taal Group ranges from basaltic andesite to dacite in composition.
- Individual formations show internal chemical variation, but none show significant evidence of stratigraphic chemical grading and no internal variation is large enough to impact the ability of formations to be successfully chemically distinguished from each other, except for the Tadalac Cave and Alitagtag formations.
- The Taal Group shows chemical evidence of pyroxene, plagioclase and magnetite fractionation in both major and trace element data.
- The magma evolution for the oldest two formations was dominated by fractional crystallisation processes, while mixing dominated the magma evolution for the younger formations.
- All eruption-units in the Taal Group, except the Buco and Pasong formations and the Tadalac Cave and Alitagtag formations, can be chemically distinguished from each other, which is statistically supported by Linear Discriminant Analysis (LDA).
- The best individual elements to differentiate between all formations are Y or Sr plotted against Fe_2O_3 , while Cu is the only element that can be distinguished between the Burol and Balagbag formations.

- Taal's large prehistoric eruptions have become less evolved over time and magma mixing appears to be a more dominant process in magma evolution over time.
- Smaller-scale prehistoric eruptions (i.e. the Tagaytay Units) and historical eruptions span across and exceed the entire compositional range of the prehistoric, ignimbrite-forming eruptions.
- Based on geochemistry alone, the relatively primitive nature of the most recent caldera-forming eruptions at Taal make it difficult to infer in which part of the caldera cycle Taal might be.
- The entire Taal Group is relatively alkaline compared to other caldera-forming and/or VEI 7 eruptions and most formations have bimodal compositions like several other caldera-forming eruptions.
- Taal's Pasong Formation is unique in that eruptions from referenced caldera volcanoes with material in the basaltic andesite range also contain dacitic – rhyolitic material, but the Pasong Formation does not.
- Individual formations at Taal have a relatively small range in composition in terms of both silica and potassium, even if they have a bimodal composition.

Chapter 5

Summary, implications and further work

5.1 Summary of main conclusions

This study is the first investigation into Taal Caldera Volcano's prehistoric eruptions since that of Martinez and Williams (1999). Although identified as a 'Decade Volcano' (Torres et al., 1995), little work has been done to resolve Taal's prehistoric stratigraphy. The present study has developed the stratigraphy and characterised several eruption-units. The key findings of the study are summarized below (1-15):

(1) A new stratigraphic framework for Taal Caldera Volcano's prehistoric explosive eruptions is presented (Fig. 5.1). This increases the number of major explosive eruptions (those with volumes of $>5 \text{ km}^3$ DRE) recorded from 4 (Geronimo, 1988; Listanco, 1994; Martinez and Williams, 1999) to 7.

(2) The oldest pyroclastic eruption-unit is the Sampaga Formation ($>670 \text{ ka}$; Ar-Ar date from Punongbayan et al., 1995) and the most recent major eruption-unit is the Buco Formation ($<6 \text{ ka}$; C-14 dates from Listanco, 1994 and Martinez and Williams, 1999).

(3) The recurrence time for major explosive eruptions is not precisely constrained and ranges between 670 k and 330 k years, although in the past 6000 years 2 definite major eruptions have taken place, which could imply major eruptions are starting to occur more frequently. More age data is desperately needed to gain a more accurate understanding of the frequency of Taal's major eruptions.

(4) New volume estimates for the major explosive eruptions are significantly larger than previous estimates. The Pasong eruption is estimated to be 90 km^3 ($M = 7.4$) three times the previous estimate (Listanco, 1994), and the Buco

Formation is estimated to have been 28 km³ (M = 6.8), a near ten-fold increase on the previous estimate (3 km³; Listanco, 1994). The revised magnitude estimates are based upon outflow sheets, inferred palaeotopographies and inferred pyroclastic density current runouts and include a fall deposit volume where appropriate. They do not include caldera fills.

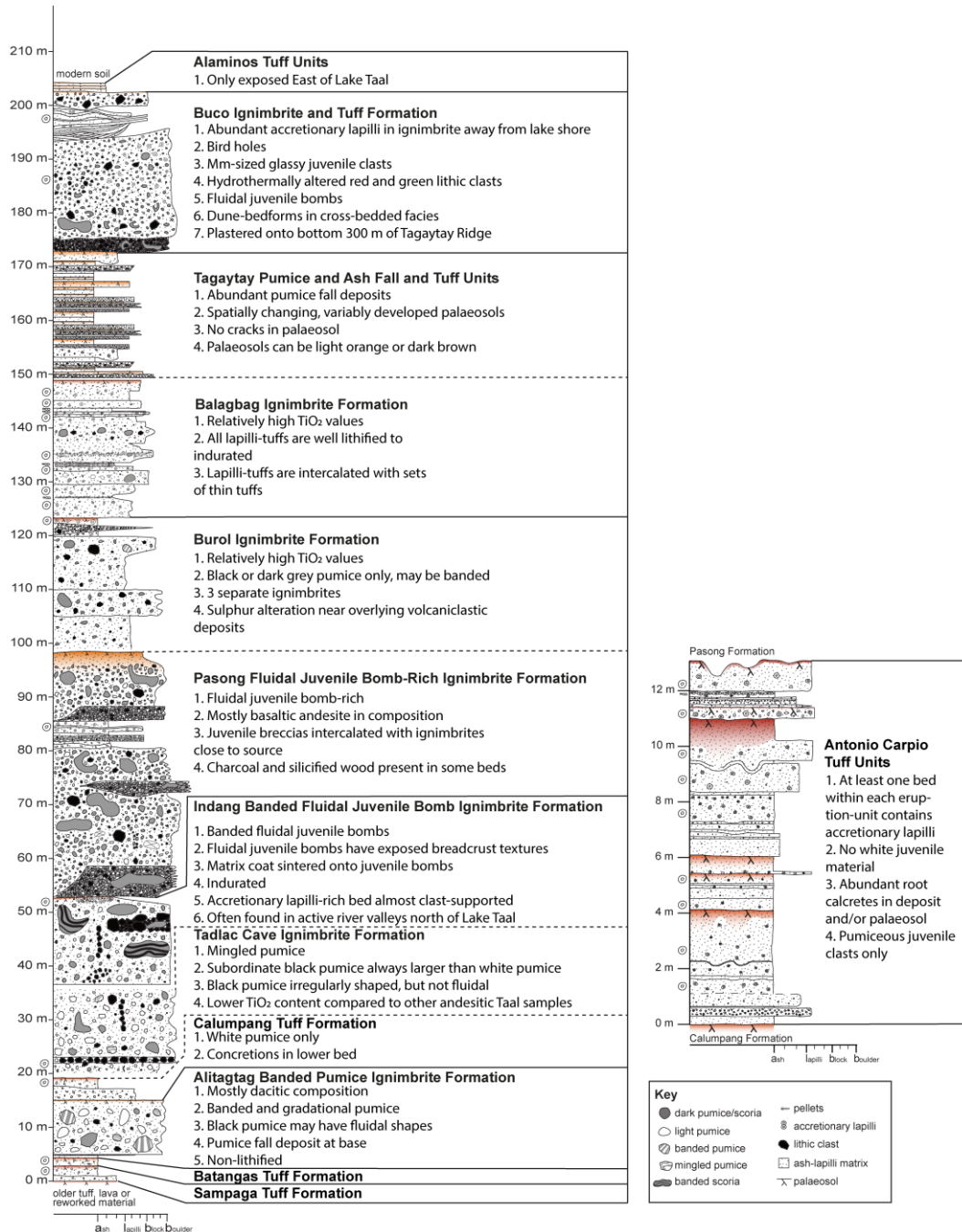


Fig. 5.1: A new generalised vertical section (GVS) of Taal Caldera Volcano's prehistoric eruptions. The stratigraphic position of the Antonio Carpio Tuff units within the GVS remains unresolved, but may belong between the Calumpang and Pasong formations. Key identifiable features for each formation and relevant units are stated.

(5) All 7 major eruptions were large enough to have involved caldera collapse. The location of individual collapse structures within the broader Taal caldera is not resolved, but their sizes likely ranged from 72 km² to 340 km². Even the maximum caldera collapse area (i.e. 340 km²) does not coincide with the 650 km² total that makes up Lake Taal, thus supporting the hypothesis that Taal Caldera Volcano is a nested (composite) caldera structure. Limited lithic breccias and more extensive fluidal juvenile bomb-rich deposits support caldera collapse for 4 of the major eruptions (Buco, Pasong and Indang formations – fluidal juvenile bombs and lithic breccia, Tadalac Cave Formation – lithic breccia), although the majority of lithic breccias are likely hidden below Lake Taal.

(6) Prehistoric deposits from Taal Caldera Volcano comprise 23 different lithofacies (Table 3.1) grouped into 7 lithofacies associations (Table 3.3). Lithofacies associations and Markov Chain Analysis revealed key facies relationships: (1) massive and diffuse cross-bedded facies commonly transition into each other, suggesting subtle, temporary unsteadiness at the flow-boundary zone of a pyroclastic density current was common, (2) non-accretionary lapilli-bearing facies are more likely to pass upwards into accretionary lapilli-bearing facies rather than the other way around, suggesting that once conditions in a pyroclastic density current favoured the formation and/or deposition of accretionary lapilli, they were unlikely to reverse, (3) lithic breccias are always overlain by massive lapilli-tuffs, suggesting that pyroclastic density currents waned gradually and deposited massive lapilli-tuffs after lithic breccias before any finer grained facies. Lithofacies associations and Markov Chain Analysis furthermore allowed the establishment of three common eruption sequences from Taal Caldera Volcano (Fig. 5.2).

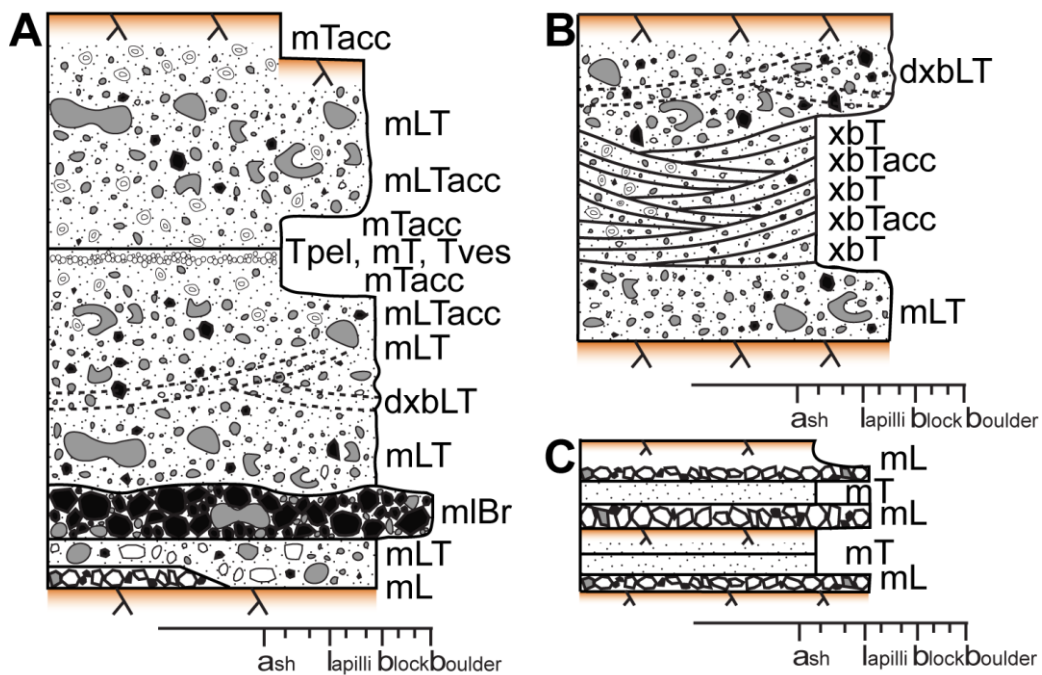


Fig. 5.2: A compilation of common eruption sequences from Taal Caldera Volcano based on lithofacies and Markov Chain Analysis. **(A)** A typical larger-scale, caldera-forming eruption, **(B)** smaller-scale activity within caldera-forming eruptions, **(C)** sequences of smaller-scale eruptions independent of caldera-forming eruptions.

(7) Major prehistoric eruptions range in composition from basaltic andesite to dacite and show evidence of plagioclase, pyroxene and magnetite fractionation, which is reflected in their petrography. All major eruption-units, except the Buco and Pasong formations and the Tadalac Cave and Alitagtag formations, can be chemically distinguished from each other. The best individual elements to chemically distinguish eruption-units are Y or Sr plotted against Fe_2O_3 , while Cu is the only element that can distinguish the Burol and Balagbag formations from each other.

(8) At least two phases of minor, but more frequent, explosive eruptive activity were interspersed with Taal's major eruptions. Two such phases in particular, are recorded by the Tagaytay Units and the Alaminos Units, and a possible third set is recorded by the Antonio Carpio Units, with unresolved stratigraphic position (Fig. 5.1). The Sampaga, Calumpang and Batangas formations represent individual minor eruptions. The recurrence time of eruptions recorded

by the Tagaytay Unit is estimated to be <146 years, which is a longer time interval than the 18-year recurrence interval estimated for historical eruptions of Volcano Island, likely because not all minor eruptions were preserved beyond the large caldera lake.

(9) The Tagaytay Units and historical eruptions span across and exceed the entire compositional range of the prehistoric major eruptions; historical eruptions may be basaltic, while the least evolved composition of a prehistoric major eruption is basaltic andesite (e.g. the Pasong Formation).

(10) Smaller-scale eruptions such as the Tagaytay Units (Fig. 5.2) and the non-climactic phases of major, caldera forming-eruptions (Fig. 5.2) are more likely to experience pumice fall deposition. The non-climactic phases of major, caldera-forming eruptions contain abundant cross-bedded facies, some with dune-bedforms, which Markov Chain Analysis shows to rarely be overlain by massive or diffuse cross-bedded facies, therefore suggesting that the overall depositional regime was stable (i.e. flow-boundary zone remains traction-dominant).

(11) Pyroclastic deposits from Taal Caldera Volcano show more evidence of moisture availability during transport than direct interaction of magma and water at the eruption source. Where the latter did occur, explosive water interaction with magma did not trigger the eruption, but only altered the eruption and/or depositional style of eruptions, leading to sub-saturated or saturated conditions during phases of some eruptions.

(12) Over time, it appears that the amount of water involved during major eruptions increased (i.e. the oldest Alitagtag Formation shows less evidence of magma – water interaction than the youngest Buco Formation). Chemically, eruption-units also show a temporal trend, namely, they appear to become more mafic over time (i.e. the oldest Alitagtag Formation has less mafic compositions compared to the youngest Buco Formation). Additionally, magma mixing appears to be a more dominant process in magma evolution in younger eruption-units (i.e. Indang, Pasong and Buco formations), while fractional

crystallisation processes appear to dominate magma evolution in older eruption-units (i.e. Alitagtag and Tadalac Cave formations).

(13) The Taal Group is relatively alkaline with a limited silica and potassium range compared to caldera-forming eruptions and/or VEI 7 eruptions from referenced caldera volcanoes, although most Taal formations have bimodal compositions like several referenced caldera-forming eruptions.

(14) The relatively mafic chemistry of fluidal juvenile bombs from Taal Caldera Volcano and other referenced caldera volcanoes suggests that although fluidal juvenile bombs show features that could support their explosive interaction with water (e.g. breadcrust textures and glassy clast rims), they were produced during caldera-forming eruptions if a source of relatively mafic, degassed magma was available, strongly encouraged by, but not requiring, water interaction.

(15) Additional suggestions were formed about explosive eruptions at flooded calderas based on field evidence from Taal's pyroclastic deposits and referenced examples: (1) extensively non-welded, especially non- or poorly-lithified ignimbrite, which may show evidence of post-depositional alteration/lithification seem characteristic of an explosive eruption at flooded calderas; (2) explosive eruptions from flooded calderas may include both pumice and ash fall deposits and are more likely to be unsteady compared to non-flooded caldera eruptions, shifting eruption styles on relatively short timescales; (3) fully dilute pyroclastic density currents are commonly produced during explosive eruptions from flooded caldera volcanoes, but rarely seen at the same abundance levels in non-flooded caldera eruptions.

5.2 Hazard implications

Hazards from Taal's volcanic activity include pyroclastic density currents, tephra falls, ballistic projectiles, lava flows, tsunamis and seiches, toxic gas emission, earthquakes, fissure openings, subsidence, lahars, flooding, liquefaction, volcanic lightning and atmospheric shock waves (Delos Reyes et al., 2018). All of these have been observed throughout Taal's historical record, during which at least 1500 people lost their lives. Many lakeshore towns were destroyed during historical eruptions, causing their re-establishment elsewhere (e.g. Taal Town; Delos Reyes et al., 2018). The new settlements are continuously growing. The 2020 eruption, although relatively small (VEI 4; GVP, 2021), caused the evacuation of the population within a 14 km radius of Volcano Island. It is estimated about 460,000 people live within this area (OCHA, 2020), while 2.4 million reside within a 30 km radius (Table 5.1; Fig. 5.3; GVP, 2021), the area that may require evacuation during a caldera-forming eruption from Taal Caldera Volcano. Luckily, the January 2020 eruption only produced ash fall, and due to the timely evacuation called by PHIVOLCS, barely any deaths were reported. However, ash reached the capital Manila causing the international airport to close, damage to at least 22,000 homes, and the economic damage to the agricultural and fishing industry alone is estimated at US\$ 62 million (OCHA, 2020). The impact of even a relatively small eruption like this highlights the vulnerability of the densely populated regions surrounding Lake Taal.

Hazard maps currently exist for hydrovolcanic 'pyroclastic surges', ballistic projectiles, tsunamis and fissures from Volcano Island (Fig. 5.3; PHIVOLCS, 2020). These hazard maps are based on historical eruptions and cover a limited region, reaching a maximum distance of 12 km from the lakeshore in the low-lying south-western area (Fig. 5.3). Hazard maps do not reflect the significantly larger area that could be affected by an eruption the size of a major prehistoric eruption (Fig. 5.3). Only the population living within the 'at risk' areas identified by the hazard maps, (i.e. residents living on Volcano Island and the shores of Lake Taal) seem aware of the volcanic hazards they are exposed to. While

speaking to local governments and citizens during several months of fieldwork, it became apparent that many were not aware they were living on the ignimbrite plains of Taal Caldera Volcano, which is especially concerning for those living beyond Tagaytay Ridge, who may feel that they are not at risk to pyroclastic density currents produced by Taal. However, this study has highlighted the mobility of pyroclastic density currents produced by Taal Caldera Volcano, with at least two previous eruptions (the Indang and Pasong eruptions), likely more, producing pyroclastic density currents that surpassed Tagaytay Ridge.

City	Population	City	Population
Balayan	90 K	Metro-Manila	14 M
Batangas City	350 K	Naic	110 K
Calamba	390 K	Nasugbu	120 K
Dasmariñas	580 K	San Pablo City	250 K
Laurel	40 K	Tagaytay	70 K
Lemery	90 K	Talisay	45 K
Lipa	390 K		

Table 5.1: Large, highly populated cities surrounding Taal Caldera Volcano, many of them within the inundation area of PDCs produced during the prehistoric Pasong eruption (Fig. 5.3).

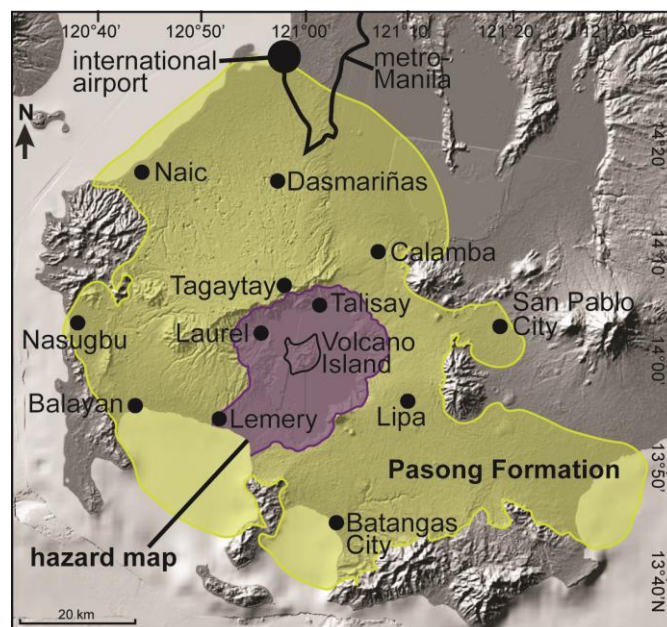


Fig. 5.3: Map displaying the current hazard map for 'base surges' and buffer zone in purple from the published PHIVOLCS hazard map. In yellow is the deposit extent for the prehistoric Pasong eruption. Batangas City, and several other cities, are highlighted (Table 5.1).

It is of course difficult to prepare residents for eruptions which may only occur once every few thousand years when smaller-scale eruptions happen much more frequently. However, one key result that has come out of this study is how common pyroclastic density current deposits are in the Taal Group (Chapters 2, 3). Pyroclastic density current deposits are found up to 30 km from the lakeshore, where they can still be several meters thick, in areas where residents appear largely unaware that they could be at risk to pyroclastic density currents from Taal Caldera Volcano.

A key exposure near the densely populated port city, Batangas City (Fig. 5.3; which includes the Buco, Pasong, Alitagtag, Calumpang and Sampaga formations and the Antonio Carpio Tuff Units), revealed 14 eruption-units, all of which included at least one ignimbrite. Although these eruption-units are unlikely to all relate to caldera-collapse events, even thin pyroclastic density current deposits are a cause for concern because pyroclastic density currents destroy everything in their path, even if they leave no deposit. This danger was highlighted by the May 8th 1902 eruption of Mt. Pelée on the island of Martinique where a dilute pyroclastic density current swept through the town of St. Pierre, killing all but 3 of the 30000 residents but leaving only a few cm of deposit (Self and Blake, 2008). This study therefore emphasises the fact that evidence of past pyroclastic density currents in the field may be scarce for several eruptions and thus any eruption frequency calculations carried out, especially for minor eruptions, are likely underestimates. The recurrence time of major eruptions at Taal may be uncertain, but there is a large chance one will happen again. Therefore, the authorities need to follow the example being set by Naples, Italy, and Auckland, New Zealand, where emphasis is being placed on the evacuation of thousands, if not millions, of people over a short timescale (Loughlin et al., 2015).

Post-eruption, there are concerns of secondary hazards because the majority of pyroclastic deposits from Taal Caldera Volcano are poorly lithified (Chapter 3), which makes them more prone to reworking, especially in a tropical environment like the Philippines. The 1991 Plinian eruption of Mt. Pinatubo exemplifies this because abundant lahars were produced in the years following

the eruption. Lahars affected over a million people living around Mt. Pinatubo and devastated the economy as acres of farmland were destroyed (Janda et al., 1996). Residents not originally affected by the eruption can still be at-risk to these secondary hazards like lahars. For the larger, caldera-forming eruptions from Taal Caldera Volcano (e.g. the Pasong eruption), this would expand the at risk region further into the densely populated, low-lying, area that makes up Metro-Manila (Fig. 5.3; Table 5.1).

5.3 Further work

The area covered by the Taal Group is large and challenging, but excellent temporary exposures occur at new road cuts, construction sites and quarries. However, these exposures rarely persist many years, due to the tropical environment and rapid urbanisation, thus it is paramount that field teams visit, document and sample new exposures as soon as they are created. Collaboration will be key in this endeavour due to the complexity of the deposits and their sporadic exposures. New exposures may provide the key to better understanding prehistoric eruptions from Taal Caldera Volcano, but it is essential that this new information is combined with previous work. With this in mind, it is crucial that any unpublished data can be accessed by teams looking to work on Taal Caldera Volcano.

The dating of eruption-units should be considered a priority by authorities and scientists to achieve a better understanding of the eruption frequency of Taal's major eruptions. Taal's rocks are challenging to date because of their general lack of charcoal and young age, making it difficult to use dating techniques like Ar-Ar. Recent Ar-Ar dating techniques, however, have improved and been able to date rocks <1 Ma (Preece et al., 2018). Therefore, this study hopes to achieve meaningful results from the 3 samples submitted for dating (Chapter 2) and hopes samples from additional eruption-units will be submitted in future studies. The abundant palaeosols found in between Taal's tephra may also be

considered as a potential dating option in future (e.g. Evans, 1982; Lian and Shane, 2000; Guilbaud et al., 2022).

This study was only the second to produce a stratigraphy for all of Taal Caldera Volcano's prehistoric eruptions. Although this study has taken strides forward in terms of the understanding of Taal Caldera Volcano, there is still a way to go before there is a level of knowledge similar to better studied calderas such as Campi Flegrei, Italy (e.g. Scarpati et al., 1993; Scarpati et al., 2020) and Santorini, Greece (e.g. Druitt et al., 1989; Myers et al., 2021). It is sincerely hoped that this study inspires volcanologists to continue the fieldwork and lab work to further improve the stratigraphic framework and understanding of this dangerous flooded caldera volcano.

Appendices

Appendix A: locality table

Tables of localities divided by field season, including which samples were collected there and their GPS coordinates.

FIELD SEASON 1

Locality (L)	Samples (T)	GPS coordinates
1.20	1	14° 08.508' N 121° 01.236' E
1.21	53, 54, 55, 56	14° 07.575' N 121° 00.890' E
1.22		14° 03.981' N 120° 51.250' E
1.23	2.89, 2.90	14° 03.159' N 120° 52.685' E
1.24	34, 77, 78	14° 11.786' N 120° 51.817' E
1.25	27, 28, 29, 30, 31, 32	14° 11.663' N 120° 51.890' E
1.26		14° 11.368' N 120° 53.480' E
1.27	17	14° 12.200' N 120° 56.185' E
1.28	13, 14, 15, 16	14° 12.146' N 120° 56.327' E
1.29		13° 56.853' N 120° 53.005' E
1.30	2, 3	13° 53.184' N 121° 00.867' E
1.31		13° 53.172' N 121° 00.825' E
1.33		13° 55.581' N 120° 56.970' E
1.34		13° 55.346' N 120° 56.784' E
1.35	4	13° 53.331' N 121° 00.313' E
1.36	5, 6	13° 53.354' N 121° 00.412' E
1.37		13° 53.662' N 121° 01.283' E
1.38	18	14° 10.161' N 120° 55.548' E
1.39	19, 20	14° 10.358' N 120° 55.596' E
1.40	23, 24, 25	14° 04.728' N 120° 52.992' E
1.41	7, 38	14° 03.558' N 120° 53.878' E
1.42		14° 04.330' N 120° 56.993' E
1.43	8, 9, 10, 11	14° 05.257' N 120° 54.644' E
1.44	12	14° 04.793' N 120° 54.578' E
1.45		14° 05.976' N 120° 51.887' E
1.46		14° 08.546' N 120° 51.293' E
1.47		14° 12.114' N 120° 53.905' E
1.48		14° 12.149' N 120° 54.879' E
1.49		14° 12.208' N 120° 56.126' E
1.50	21, 22, C1, C2, C3, C4	14° 07.938' N 120° 56.049' E
1.51		14° 08.119' N 120° 56.753' E
1.52		14° 08.100' N 120° 56.042' E
1.53		14° 08.736' N 120° 56.700' E

Locality (L)	Samples (T)	GPS coordinates
1.54		14° 06.508' N 120° 49.827' E
1.55		14° 07.776' N 120° 49.845' E
1.56		14° 07.847' N 120° 50.569' E
1.57		14° 01.571' N 120° 56.694' E
1.58	26, 79	14° 07.753' N 120° 53.568' E
1.59		14° 07.775' N 120° 53.736' E
1.60		14° 07.630' N 120° 53.462' E
1.61	33	14° 11.729' N 120° 51.893' E
1.62	35, 36	14° 03.968' N 120° 53.658' E
1.63	37	14° 03.633' N 120° 53.835' E
1.64		14° 05.799' N 120° 55.132' E
1.65	52	14° 05.776' N 120° 55.022' E
1.66	39	14° 05.677' N 120° 54.973' E
1.67	40, 41	14° 05.605' N 120° 54.886' E
1.68		14° 05.536' N 120° 54.817' E
1.69	42, 51B	14° 05.515' N 120° 54.920' E
1.70	43, 44, 45	14° 05.571' N 120° 55.041' E
1.71	46, 47, 48	14° 05.568' N 120° 55.068' E
1.72	49, 50, 51A	14° 05.610' N 120° 55.023' E
1.73		14° 05.614' N 120° 55.004' E
1.74		14° 05.628' N 120° 55.021' E
1.75		14° 05.627' N 120° 54.968' E
1.76	57, 58	14° 07.654' N 121° 00.857' E
1.77		14° 05.968' N 120° 59.662' E
1.78		14° 05.676' N 120° 59.717' E
1.79	59, 60	14° 05.569' N 120° 59.684' E
1.80		13° 53.900' N 120° 55.190' E
1.81		13° 53.908' N 120° 55.218' E
1.82	61, 62, 63	13° 53.833' N 120° 55.130' E
1.83	64	13° 53.869' N 121° 01.925' E
1.84	65	13° 53.896' N 121° 01.948' E
1.85	66, 67, 68, 69, 70	13° 54.393' N 121° 02.228' E
1.86	71, 72, 73	14° 05.005' N 120° 53.959' E
1.87		14° 04.990' N 120° 53.934' E
1.88	74	14° 04.991' N 120° 53.910' E
1.89	75, 76	14° 04.973' N 120° 53.888' E
1.90	80	14° 04.979' N 120° 53.881' E
1.91		14° 04.979' N 120° 53.873' E
1.92		14° 05.021' N 120° 53.869' E
1.93		14° 05.044' N 120° 53.878' E
1.94		14° 05.090' N 120° 53.851' E
1.95		14° 05.174' N 120° 53.841' E
1.96		14° 05.192' N 120° 53.810' E

Locality (L)	Samples (T)	GPS coordinates
1.97		14° 05.213' N 120° 53.833' E

FIELD SEASON 2

Locality (L)	Samples (T)	GPS coordinates
2.1		14° 11.014'N 120°47.563'E
2.2		14° 10.506'N 120°48.147'E
2.3		14° 10.645'N 120°47.175'E
2.4		14° 10.454'N 120°46.908'E
2.5		14° 12.241'N 120°46.747'E
2.6	2.88	14° 14.030'N 120°46.951'E
2.7		14° 12.468'N 120°45.312'E
2.8	2.1	13° 53.602'N 121°01.185'E
2.9	2.2, 2.3, 2.4, 2.5, 2.6, 2.7, 2.8, 2.9	13° 52.788'N 120°59.718'E
2.10	2.76A, 2.76B, 2.77, 2.78	13° 52.549'N 120°59.577'E
2.11		13° 56.334'N 121°02.417'E
2.12		13° 55.253'N 120°51.327'E
2.13		13° 59.767'N 120°50.437'E
2.14		13° 56.359'N 120°49.090'E
2.15	2.85	13° 59.672'N 120°50.068'E
2.16		14° 16.406'N 120°46.214'E
2.17		14° 16.341'N 120°45.530'E
2.18		14° 15.775'N 120°46.982'E
2.19		14° 11.148'N 120°45.496'E
2.20		14° 05.425'N 121°00.591'E
2.21		14° 04.977'N 120°59.610'E
2.22		14° 05.007'N 120°59.548'E
2.23		14° 05.227'N 120°59.121'E
2.24		13° 58.761'N 120°57.223'E
2.25		14° 00.303'N 120°56.989'E
2.26		14° 00.882'N 120°57.313'E
2.27	2.10, 2.11, 2.12, 2.13	14° 03.968'N 120°53.659'E
2.28	2.14, 2.15	14° 03.629'N 120°53.837'E

Locality (L)	Samples (T)	GPS coordinates
2.29	2.16	14° 03.562'N 120°53.882'E
2.30	2.17, 2.18, 2.19, 2.45, 2.46, 2.47	14° 05.239'N 120°58.196'E
2.31	2.36, 2.37	14° 01.742'N 121°03.087'E
2.32		14° 02.100'N 121°02.756'E
2.33	2.38, 2.39	14° 01.885'N 121°02.559'E
2.34		14° 01.652'N 121°02.831'E
2.35		14° 01.770'N 121°02.862'E
2.36	2.48	14° 01.824'N 121°02.537'E
2.37	2.49	14° 01.821'N 121°02.595'E
2.38		14° 02.215'N 120°53.611'E
2.39		14° 04.841'N 120°57.684'E
2.40	2.50A, 2.50B, 2.51, 2.52	14° 05.485'N 120°58.483'E
2.41		14° 05.481'N 120°58.544'E
2.42		14° 05.503'N 120°58.512'E
2.43		14° 05.680'N 120°58.503'E
2.44		14° 05.699'N 120°58.492'E
2.45		14° 05.788'N 120°58.363'E
2.46	2.55	13° 54.752'N 120°58.943'E
2.47	2.56	13° 54.588'N 120°58.901'E
2.48	2.57	13° 53.742'N 121°01.926'E
2.49		13° 53.796'N 121°01.838'E
2.50	2.58	13° 53.711'N 121°01.923'E
2.51	2.59, 2.60	13° 54.280'N 121°02.122'E
2.52	2.61	14° 05.970'N 120°58.148'E
2.53		14° 05.970'N 120°58.103'E
2.54	2.62	14° 06.051'N 120°58.202'E
2.55		14° 06.101'N 120°58.188'E
2.56		14° 06.173'N 120°58.174'E
2.57	2.63, 2.64, 2.65, 2.66	14° 06.206'N 120°58.190'E
2.57B		14° 09.865'N 120°43.081'E
2.58		14° 08.686'N 120°47.263'E

Locality (L)	Samples (T)	GPS coordinates
2.59		14° 08.497'N 120°46.282'E
2.60		14° 08.345'N 120°47.224'E
2.61	2.67	14° 06.226'N 120°58.245'E
2.62		14° 06.225'N 120°58.275'E
2.63		14° 06.300'N 120°58.333'E
2.64		14° 06.366'N 120°58.315'E
2.65	2.68, 2.69, 2.70	14° 06.355'N 120°58.182'E
2.66	2.71, 2.72, 2.73	14° 06.324'N 120°58.005'E
2.67		14° 06.384'N 120°57.969'E
2.68	2.74	14° 06.496'N 120°58.005'E
2.69		14° 06.473'N 120°57.873'E
2.70		14° 06.463'N 120°57.824'E
2.71		14° 06.477'N 120°57.624'E
2.72		14° 06.402'N 120°57.478'E
2.73	2.75, 2.97, 2.98, 2.99, 2.100, 2.101	13° 53.559'N 120°58.816'E
2.74	2.79, 2.80, 2.102, 2.103, 2.104, 2.105, 3.24A, 3.24B	14° 05.319'N 120°57.778'E
2.75		14° 06.531'N 120°57.549'E
2.76	2.81	14° 06.600'N 120°57.579'E
2.77		14° 06.619'N 120°57.665'E
2.78		14° 06.664'N 120°57.858'E
2.79	2.82	14° 06.724'N 120°57.913'E
2.80		14° 06.945'N 120°58.042'E
2.81		14° 06.942'N 120°57.944'E
2.82	2.83, 2.84	14° 01.256'N 120°57.210'E
2.83	2.86, 2.87	14° 11.895'N 120°52.198'E
2.84		14° 04.328'N 120°51.572'E
2.85	2.91, 2.92	13° 52.686'N 120°59.338'E
2.86		13° 52.795'N 120°59.108'E
2.87	2.93, 2.94, 2.95	13° 52.853'N 120°59.072'E
2.88		13° 53.207'N 120°58.846'E

Locality (L)	Samples (T)	GPS coordinates
2.89	2.96	13° 53.380'N 120°58.851'E

FIELD SEASON 3

Locality (L)	Samples (T)	GPS coordinates
3.1	3.1	14° 13.074'N 120°58.569'E
3.2	2020 sample	14° 12.880'N 120°58.553'E
3.3		14° 11.904'N 120°58.927'E
3.4		14° 12.500'N 120°59.150'E
3.5		14° 12.059'N 120°59.259'E
3.6		13° 53.790'N 121°17.332'E
3.7		13° 54.987'N 121°14.545'E
3.8	3.2a, 3.2b	13° 55.157'N 121°14.234'E
3.9	3.3a, 3.3b	13° 55.201'N 121°13.672'E
3.10		13° 57.586'N 121°12.566'E
3.11	3.4	13° 58.998'N 121°12.655'E
3.12		13° 59.443'N 121°12.742'E
3.13	3.5	13° 44.719'N 121°14.469'E
3.14	3.6	13° 45.348'N 121°12.599'E
3.15		13° 42.747'N 121°12.733'E
3.16	3.7	13° 43.527'N 121°12.920'E
3.17		13° 43.636'N 121°12.866'E
3.18(1)	3.8a, 3.8b, 3.8c, 3.8d	13° 43.333'N 121°12.805'E
3.18(2)		13° 43.186'N 121°12.638'E
3.19	3.9a, 3.9b	13° 43.858'N 121°12.458'E
3.20	3.10	14° 03.406'N 121°14.565'E
3.21		14° 03.445'N 121°15.053'E
3.22	3.11	14° 06.440'N 121°11.044'E
3.23		14° 06.469'N 121°10.864'E
3.24		13° 57.076'N 121°09.310'E
3.25		14° 11.088'N 121°09.686'E
3.26		14° 02.767'N 120°41.786'E
3.27		14° 03.804'N 120°43.254'E

Locality (L)	Samples (T)	GPS coordinates
3.28	3.12	13° 59.770'N 120°46.879'E
3.29	3.13	13° 57.230'N 120°46.318'E
3.30	3.14a, 3.14b	13° 57.410'N 121°05.191'E
3.31		13° 58.459'N 121°04.906'E
3.32		13° 44.365'N 121°10.575'E
3.33		13° 45.083'N 121°08.682'E
3.34		13° 45.130'N 121°08.263'E
3.35	3.17, 3.18, 3.19a, 3.19b	13° 45.226'N 121°06.037'E
3.36		13° 54.539'N 121°10.995'E
3.37	3.15	13° 54.620'N 121°10.874'E
3.38		13° 54.912'N 121°10.876'E
3.39	3.16	13° 54.631'N 121°10.745'E
3.40		14° 13.089'N 120°59.506'E
3.41		14° 13.084'N 120°59.070'E
3.42		14° 11.113'N 121°00.067'E
3.43		14° 13.059'N 121°00.658'E
3.44		14° 14.299'N 121°03.165'E
3.45		14° 01.731'N 121°13.827'E
3.46		13° 47.118'N 121°05.461'E
3.47		13° 44.614'N 121°11.212'E
3.48	3.20	13° 44.391'N 121°05.886'E
3.49		13° 46.418'N 121°05.758'E
3.50	3.21, 3.22, 3.23	13° 47.067'N 121°05.509'E
3.51		14° 10.218'N 121°12.042'E
3.52		14° 10.424'N 121°10.716'E
3.53		14° 09.700'N 121°08.979'E

Appendix B: sample table

A table focused on individual samples, including the sample type, which formation the sample belongs to and which lab methods have been employed to analyse the sample.

Sample (T)	Sample type	Formation or Units	Geochemistry	Granulometry	Petrography	SEM
1	Lava	Mt. Sungay				
4-WB	White juvenile	Tadlac Cave	X			
4-WT	White juvenile	Tadlac Cave	X			
4-BB	Black juvenile	Tadlac Cave	X			
4-BT	Black juvenile	Tadlac Cave	X			
5	Bulk matrix – consolidated	Tadlac Cave				
7	Bulk matrix – consolidated	Unknown				
8A	Black juvenile	Unknown			X	
8B	Black juvenile	Unknown			X	
9	Black juvenile	Unknown	X			
10	White juvenile	Unknown	X			
11	Bulk matrix	Unknown		X		X
12	Lava	Unknown			X	
13	Black juvenile	Pasong	X			
14	Bulk matrix – consolidated	Pasong				
15	Light grey juvenile	Pasong	X			
16	Accretionary lapilli	Pasong			X	
17	Bulk matrix	Pasong		X		X
18	Lithic clasts	Pasong				
19	Black juvenile	Pasong			X	
21	Juvenile	Pasong	X	X		
22	Lithic clasts	Pasong				
24	White juvenile	Tagaytay	X			
25	Bulk matrix	Tagaytay	X			X
27	Black juvenile	Indang	X		X	
28	Light grey juvenile	Indang	X			
31	Black juvenile	Indang	X			
32	Lithic clasts	Indang				
33	Bulk matrix – consolidated	Pasong				
34	Bulk matrix – consolidated with accretionary lapilli	Pasong			X	
35	White juvenile	Alitagtag	X			
36	Black juvenile	Alitagtag	X			
37	Bulk fall deposit	Unknown		X		X
38	Bulk matrix – consolidated	Unknown			X	
40	Bulk matrix – consolidated	Unknown				

Sample (T)	Sample type	Formation or Units	Geochemistry	Granulometry	Petrography	SEM
41	Accretionary lapilli	Unknown			X	
42	White juvenile	Tagaytay	X			
45	Lava	Unknown			X	
46	Bulk matrix	Reworked		X		X
47	Juvenile	Unknown	X			
48	Juvenile	Unknown	X			
49	Bulk fall deposit	Tagaytay	X			
50	Bulk matrix – consolidated	Tagaytay				
51A	Bulk fall deposit	Tagaytay	X			
51B	Bulk matrix	Tagaytay		X		X
52	Black juvenile	Unknown			X	
53	Lava	Mt. Sungay				
54	Juvenile	Unknown	X			
55	Accretionary lapilli	Unknown			X	
57	Accretionary lapilli	Unknown			X	
58	Juvenile	Unknown	X			
59	Juvenile	Buco	X			
61	Bulk matrix	Pasong		X		
62	Black juvenile	Pasong	X			
63	Black juvenile	Pasong	X			
64	Lava	Mt. Macolod			X	
65	Bulk matrix	Unknown				X
66	Juvenile	Buco	X			
67	Accretionary lapilli	Buco			X	
69	Juvenile	Buco	X			
70	Black juvenile	Buco	X			
71	Black juvenile	Unknown	X			
72	Lithic clasts	Unknown				
73	Bulk matrix – consolidated	Unknown				
74	Bulk matrix	Unknown			X	
75	Juvenile	Unknown	X			
76	Bulk matrix	Unknown		X		X
79	Black juvenile	Pasong	X			
80	Lithic clasts	Unknown				
2.1	Bulk matrix	Unknown	X			
2.2	Lithic clasts	Tadlac Cave				
2.3	Juvenile	Tadlac Cave	X			
2.4	White juvenile	Tadlac Cave	X		X	
2.5	Lithic clasts (obsidian)	Tadlac Cave	X			
2.6	Bulk matrix	Tadlac Cave	X	X		X
2.7	Lithic clasts (dense scoria)	Tadlac Cave	X			
2.8	Black juvenile	Tadlac Cave	X		X	
2.9	White juvenile	Tadlac Cave	X		X	
2.10	Bulk matrix	Unknown	X	X		
2.11	Light grey juvenile	Alitagtag	X		X	

Sample (T)	Sample type	Formation or Units	Geochemistry	Granulometry	Petrography	SEM
2.12	Bulk matrix	Alitagtag	X	X		X
2.13	Black juvenile	Alitagtag	X		X	
2.14	Bulk fall deposit	Unknown	X			X
2.15	Bulk matrix	Unknown	X	X		X
2.16	Juvenile	Unknown	X			
2.17	Juvenile	Unknown	X		X	
2.18	Juvenile	Unknown	X		X	
2.19	Juvenile	Unknown	X			
2.20	Juvenile	Unknown	X			
2.21	Juvenile	Pasong	X			
2.22	Juvenile	Pasong				
2.23	Bulk matrix – consolidated	Unknown				
2.24	Bulk matrix – consolidated	Unknown	X			
2.25(12)	Bulk matrix	Unknown	X			
2.25(19)	Bulk matrix	Unknown	X			
2.26	Bulk matrix	Unknown	X			
2.27	Bulk fall deposit	Unknown	X			
2.28	Bulk matrix	Unknown				
2.29	Bulk matrix	Unknown	X			
2.30	Bulk matrix	Unknown	X			
2.31	Bulk matrix	Unknown	X			
2.32	Bulk matrix – consolidated	Unknown	X			
2.33	Juvenile	Indang	X			
2.34	Bulk matrix	Indang			X	
2.35	Banded juvenile	Indang	X			
2.36	Lithic clasts	Unknown			X	
2.37	Juvenile	Unknown	X			
2.38A	Juvenile	Unknown	X		X	
2.38B	Juvenile	Unknown	X			
2.39	Lava	Unknown				
2.40	Bulk matrix	Buco	X			
2.41	Bulk matrix	Buco		X		X
2.42	Juvenile	Buco	X			
2.43	Juvenile	Buco	X			
2.44	Lithic clasts	Buco				
2.45	Bulk matrix	Unknown	X	X		
2.46	Bulk matrix	Buco	X			
2.47	Bulk matrix	Buco	X			X
2.48	Juvenile	Unknown	X		X	
2.49	Juvenile	Unknown	X		X	
2.50A	Juvenile	Buco	X		X	
2.50B	Juvenile	Buco	X			
2.51	Lithic clasts	Buco				
2.52	Bulk matrix	Buco	X	X		X
2.53	Juvenile	Reworked	X		X	
2.54	Juvenile	Buco	X		X	
2.55	Lithic clasts	Burol				
2.56	Juvenile	Burol	X		X	
2.57	Bulk matrix – consolidated	Unknown	X			

Sample (T)	Sample type	Formation or Units	Geochemistry	Granulometry	Petrography	SEM
2.58	Bulk matrix	Unknown	X			
2.59	Lava	Mt. Macolod				
2.60	Bulk matrix – consolidated; lithic clasts	Unknown				
2.61	Juvenile	Buco	X			
2.62	Bulk matrix	Unknown	X			
2.63	Lithic clasts	Indang				
2.64	Juvenile	Indang	X		X	
2.65	Bulk matrix	Indang	X			
2.66	Bulk matrix	Pasong	X			X
2.67	Juvenile	Pasong	X			
2.68	Bulk matrix	Tagaytay	X			X
2.69	Bulk matrix	Tagaytay	X			
2.70	Bulk matrix	Tagaytay	X	X		X
2.71	Juvenile	Unknown	X			
2.72	Juvenile	Unknown	X			
2.73	Juvenile	Unknown	X			
2.74	Bulk matrix	Tagaytay	X			
2.75	Juvenile	Burol	X			
2.76A	Juvenile	Balagbag	X			
2.76B	Bulk matrix	Balagbag	X			
2.77	Bulk matrix	Balagbag	X			
2.78	Juvenile	Buco	X			
2.79A	Juvenile	Unknown	X			
2.79B	Juvenile	Unknown	X			
2.80	Juvenile	Unknown	X			
2.81	Juvenile	Pasong	X			
2.82	Juvenile	Pasong	X			
2.83	Bulk matrix	Tagaytay	X	X		
2.84	Juvenile	Unknown	X			
2.85	Juvenile	Unknown	X			
2.86	Juvenile	Pasong	X			
2.87	Juvenile	Unknown	X			
2.88	Juvenile	Indang	X			
2.89	Bulk fall deposit	Tagaytay	X			
2.90	Juvenile	Unknown	X			
2.92	Juvenile	Burol	X			
2.93	Juvenile	Unknown	X			
2.94	Juvenile	Unknown	X		X	
2.95	Juvenile	Unknown	X		X	
2.96	Juvenile	Burol	X		X	
2.97	Juvenile	Burol	X		X	
2.98	Juvenile	Burol	X			
2.99	Juvenile	Balagbag	X			
2.100	Juvenile	Balagbag	X		X	
2.101	Juvenile	Buco	X		X	
2.103	Bulk matrix	Unknown				
2.104A	Juvenile	Unknown	X		X	
2.104B	Juvenile	Unknown	X			
2.105	Juvenile	Unknown	X		X	
3.1	Juvenile	Pasong	X			
2020ash	Bulk fall deposit	2020 eruption	X			X
3.2A	Juvenile	Pasong	X			

Sample (T)	Sample type	Formation or Units	Geochemistry	Granulometry	Petrography	SEM
3.2B	Silicified wood	Pasong			X	
3.3A	Juvenile	Unknown	X		X	
3.3B	Juvenile	Unknown	X			
3.4	Juvenile	Buco	X		X	
3.4A	Accretionary lapilli	Buco			X	
3.4B	Accretionary lapilli	Buco			X	
3.5	Intrusion	Tolos batholith			X	
3.6	Intrusion	Tolos batholith			X	
3.7	Bulk matrix	Unknown			X	
3.8A	Bulk matrix	Unknown			X	
3.8B	Dark grey juvenile	Unknown	X			
3.8C	Intrusion	Unknown			X	
3.8D	Intrusion	Unknown			X	
3.9A	Bulk matrix	Unknown			X	
3.9B	Juvenile	Unknown	X			
3.10	Juvenile	Buco	X		X	
3.11A	Juvenile	Buco	X			
3.11B	Juvenile	Buco	X		X	
3.12	Juvenile	Pasong	X		X	
3.13	Juvenile	Pasong	X			
3.14A	Juvenile	Pasong	X		X	
3.14B	Juvenile	Unknown	X		X	
3.15	Juvenile	Lipa scoria cone lava			X	
3.16	Juvenile	Pasong	X		X	
3.17	Bulk fall deposit	Alitagtag	X			
3.18	Calcrete	Antonio Carpio			X	
3.19A	White juvenile	Alitagtag	X			
3.19B	Black juvenile	Alitagtag	X			
3.20	Juvenile	Pasong	X		X	
3.21	Juvenile	Pasong	X		X	
3.22	Black juvenile	Alitagtag	X		X	
3.23	White juvenile	Alitagtag	X		X	
3.24A	Juvenile	Unknown	X		X	
3.24B	Juvenile	Unknown	X		X	

Appendix C: Markov Chain Analysis data

Table C1 – Facies transition data based on the named formations from the GVS

Facies codes for all tables in appendix C are as follows: fpoordxbLT (fines-poor diffuse cross-bedded lapilli-tuff), dxblT (diffuse cross-bedded lapilli-tuff), dxbT (diffuse cross-bedded tuff), mL (massive lapillistone), mlBr (massive lithic breccia), mLT (massive lapilli-tuff), mLTacc (massive lapilli-tuff with accretionary lapilli), mT (massive tuff), mTacc (massive tuff with accretionary lapilli), ps (palaeosol), Tpel (ash pellet tuff), xblT (cross-bedded lapilli-tuff), xbt (cross-bedded tuff), and xbtacc (cross-bedded tuff with accretionary lapilli).

Facies	Overlying Facies	Formation
mLT	ps	Buco
xbTacc	mLT	Buco
xbT	xbTacc	Buco
xbTacc	xbT	Buco
xbT	xbTacc	Buco
xbTacc	xbT	Buco
xblT	xbTacc	Buco
xbT	xblT	Buco
xbTacc	xbT	Buco
xbTacc	xbTacc	Buco
mLT	xbTacc	Buco
dxblT	mLT	Buco
mLT	dxblT	Buco
mlBr	mLT	Buco
ps	mlBr	Tagaytay-Buco
mTacc	ps	Balagbag
mTacc	mTacc	Balagbag
Tpel	mTacc	Balagbag
mT	Tpel	Balagbag
mLTacc	mT	Balagbag
mTacc	mLTacc	Balagbag
mTacc	mTacc	Balagbag
mLT	mTacc	Balagbag

Facies	Overlying Facies	Formation
mTacc	mLT	Balagbag
mLTacc	mTacc	Balagbag
mTacc	mLTacc	Balagbag
Tpel	mTacc	Balagbag
mTacc	Tpel	Balagbag
Tpel	mTacc	Balagbag
mTacc	Tpel	Balagbag
mLTacc	mTacc	Balagbag
mTacc	mLTacc	Balagbag
Tpel	mTacc	Balagbag
mLTacc	Tpel	Balagbag
ps	mLTacc	Burol-Balagbag
mTacc	ps	Burol
fpoordxbLT	mTacc	Burol
mLTacc	fpoordxbLT	Burol
dxblT	mLTacc	Burol
dxblT	dxblT	Burol
mLT	dxblT	Burol
mLT	ps	Pasong
dxblT	mLT	Pasong
mLTacc	dxblT	Pasong
dxblT	mLTacc	Pasong
fpoordxbLT	dxblT	Pasong
xbT	fpoordxbLT	Pasong
xbT	xbT	Pasong
mL	xbT	Pasong
xbT	mL	Pasong
xbT	xbT	Pasong
xbTacc	xbT	Pasong
xbTacc	xbTacc	Pasong
xbT	xbTacc	Pasong
dxblT	xbT	Pasong
mLT	dxblT	Pasong
dxblT	mLT	Pasong
dxbl	dxblT	Pasong
ps	dxbl	Indang-Pasong
mTacc	ps	Indang
mIBr	mTacc	Indang

Facies	Overlying Facies	Formation
mLT	mIBr	Indang
mIBr	mLT	Tadlac
mLTacc	mIBr	Tadlac
mTacc	ps	Calumpang
mLT	mTacc	Calumpang
ps	mLT	Alitagtag-Calumpang
mLT	ps	Alitagtag
pmL	mLT	Alitagtag
mT	pmL	Alitagtag
ps	mT	Batangas-Alitagtag
mTacc	ps	Batangas
Tpel	mTacc	Batangas
mTacc	ps	Sampaga
mT	mTacc	Sampaga
dxBT	mT	Sampaga
ps	dxBT	Sampaga

Tables C2 – Markov Chain Selley-Türk method data tables

Transition count matrix

	fpoordxbLT	dxblLT	dxblT	mL	mIBr	mLT	mLTacc	mT	mTacc	ps	Tpel	xbLT	xbT	xbTacc	TOTAL
fpoordxbLT		2							1						3
dxblLT		1				3	2						1		7
dxblT								1							1
mL						1							1		2
mIBr						2			1						3
mLT		3			1				2	3				1	10
mLTacc	1	1			1			1	2		1				7
mT				1					1		1				3
mTacc						1	3		2	6	2				14
ps	1		1		1	1	1	1							6
Tpel									5						5
xbLT														1	1
xbT	1			1								1	2	3	8
xbTacc						1							4	2	7
TOTAL	3	7	1	2	3	9	6	3	14	9	4	1	8	7	70

Independent trials (probability) matrix

	fpoordxbLT	dxblT	dxblT	mL	mIBr	mLT	mLTacc	mT	mTacc	ps	Tpel	xbLT	xbT	xbTacc
fpoordxbLT	0.129	0.300	0.043	0.086	0.129	0.386	0.257	0.129	0.600	0.386	0.171	0.043	0.343	0.300
dxblT	0.300	0.700	0.100	0.200	0.300	0.900	0.600	0.300	1.400	0.900	0.400	0.100	0.800	0.700
dxblT	0.043	0.100	0.014	0.029	0.043	0.129	0.086	0.043	0.200	0.129	0.057	0.014	0.114	0.100
mL	0.086	0.200	0.029	0.057	0.086	0.257	0.171	0.086	0.400	0.257	0.114	0.029	0.229	0.200
mIBr	0.129	0.300	0.043	0.086	0.129	0.386	0.257	0.129	0.600	0.386	0.171	0.043	0.343	0.300
mLT	0.429	1.000	0.143	0.286	0.429	1.286	0.857	0.429	2.000	1.286	0.571	0.143	1.143	1.000
mLTacc	0.300	0.700	0.100	0.200	0.300	0.900	0.600	0.300	1.400	0.900	0.400	0.100	0.800	0.700
mT	0.129	0.300	0.043	0.086	0.129	0.386	0.257	0.129	0.600	0.386	0.171	0.043	0.343	0.300
mTacc	0.600	1.400	0.200	0.400	0.600	1.800	1.200	0.600	2.800	1.800	0.800	0.200	1.600	1.400
ps	0.257	0.600	0.086	0.171	0.257	0.771	0.514	0.257	1.200	0.771	0.343	0.086	0.686	0.600
Tpel	0.214	0.500	0.071	0.143	0.214	0.643	0.429	0.214	1.000	0.643	0.286	0.071	0.571	0.500
xbLT	0.043	0.100	0.014	0.029	0.043	0.129	0.086	0.043	0.200	0.129	0.057	0.014	0.114	0.100
xbT	0.343	0.800	0.114	0.229	0.343	1.029	0.686	0.343	1.600	1.029	0.457	0.114	0.914	0.800
xbTacc	0.300	0.700	0.100	0.200	0.300	0.900	0.600	0.300	1.400	0.900	0.400	0.100	0.800	0.700

Difference matrix

	fpoordxbLT	dxblT	dxblT	mL	mIBr	mLT	mLTacc	mT	mTacc	ps	Tpel	xbLT	xbT	xbTacc
fpoordxbLT	-0.129	1.700	-0.043	-0.086	-0.129	-0.386	-0.257	-0.129	0.400	-0.386	-0.171	-0.043	-0.343	-0.300
dxblT	-0.300	0.300	-0.100	-0.200	-0.300	2.100	1.400	-0.300	-1.400	-0.900	-0.400	-0.100	0.200	-0.700
dxblT	-0.043	-0.100	-0.014	-0.029	-0.043	-0.129	-0.086	0.957	-0.200	-0.129	-0.057	-0.014	-0.114	-0.100
mL	-0.086	-0.200	-0.029	-0.057	-0.086	0.743	-0.171	-0.086	-0.400	-0.257	-0.114	-0.029	0.771	-0.200
mIBr	-0.129	-0.300	-0.043	-0.086	-0.129	1.614	-0.257	-0.129	0.400	-0.386	-0.171	-0.043	-0.343	-0.300
mLT	-0.429	2.000	-0.143	-0.286	0.571	-1.286	-0.857	-0.429	0.000	1.714	-0.571	-0.143	-1.143	0.000
mLTacc	0.700	0.300	-0.100	-0.200	0.700	-0.900	-0.600	0.700	0.600	-0.900	0.600	-0.100	-0.800	-0.700
mT	-0.129	-0.300	-0.043	0.914	-0.129	-0.386	-0.257	-0.129	0.400	-0.386	0.829	-0.043	-0.343	-0.300
mTacc	-0.600	-1.400	-0.200	-0.400	-0.600	-0.800	1.800	-0.600	-0.800	4.200	1.200	-0.200	-1.600	-1.400
ps	0.743	-0.600	0.914	-0.171	0.743	0.229	0.486	0.743	-1.200	-0.771	-0.343	-0.086	-0.686	-0.600
Tpel	-0.214	-0.500	-0.071	-0.143	-0.214	-0.643	-0.429	-0.214	4.000	-0.643	-0.286	-0.071	-0.571	-0.500
xbLT	-0.043	-0.100	-0.014	-0.029	-0.043	-0.129	-0.086	-0.043	-0.200	-0.129	-0.057	-0.014	-0.114	0.900
xbT	0.657	-0.800	-0.114	0.771	-0.343	-1.029	-0.686	-0.343	-1.600	-1.029	-0.457	0.886	1.086	2.200
xbTacc	-0.300	-0.700	-0.100	-0.200	-0.300	0.100	-0.600	-0.300	-1.400	-0.900	-0.400	-0.100	3.200	1.300

All positive differences are highlighted in beige in the table. These represent facies transitions that occur more frequently than would be expected in a random system.

Normalised difference matrix

	fpoordxbLT	dxblT	dxblT	mL	mIBr	mLT	mLTacc	mT	mTacc	ps	Tpel	xbLT	xbT	xbTacc
fpoordxbLT	-0.36	3.10	-0.21	-0.29	-0.36	-0.62	-0.51	-0.36	0.52	-0.62	-0.41	-0.21	-0.59	-0.55
dxblT	-0.55	0.36	-0.32	-0.45	-0.55	2.21	1.81	-0.55	-1.18	-0.95	-0.63	-0.32	0.22	-0.84
dxblT	-0.21	-0.32	-0.12	-0.17	-0.21	-0.36	-0.29	4.62	-0.45	-0.36	-0.24	-0.12	-0.34	-0.32
mL	-0.29	-0.45	-0.17	-0.24	-0.29	1.46	-0.41	-0.29	-0.63	-0.51	-0.34	-0.17	1.61	-0.45
mIBr	-0.36	-0.55	-0.21	-0.29	-0.36	2.60	-0.51	-0.36	0.52	-0.62	-0.41	-0.21	-0.59	-0.55
mLT	-0.65	2.00	-0.38	-0.53	0.87	-1.13	-0.93	-0.65	0.00	1.51	-0.76	-0.38	-1.07	0.00
mLTacc	1.28	0.36	-0.32	-0.45	1.28	-0.95	-0.77	1.28	0.51	-0.95	0.95	-0.32	-0.89	-0.84
mT	-0.36	-0.55	-0.21	3.12	-0.36	-0.62	-0.51	-0.36	0.52	-0.62	2.00	-0.21	-0.59	-0.55
mTacc	-0.77	-1.18	-0.45	-0.63	-0.77	-0.60	1.64	-0.77	-0.48	3.13	1.34	-0.45	-1.26	-1.18
ps	1.46	-0.77	3.12	-0.41	1.46	0.26	0.68	1.46	-1.10	-0.88	-0.59	-0.29	-0.83	-0.77
Tpel	-0.46	-0.71	-0.27	-0.38	-0.46	-0.80	-0.65	-0.46	4.00	-0.80	-0.53	-0.27	-0.76	-0.71
xbLT	-0.21	-0.32	-0.12	-0.17	-0.21	-0.36	-0.29	-0.21	-0.45	-0.36	-0.24	-0.12	-0.34	2.85
xbT	1.12	-0.89	-0.34	1.61	-0.59	-1.01	-0.83	-0.59	-1.26	-1.01	-0.68	2.62	1.14	2.46
xbTacc	-0.55	-0.84	-0.32	-0.45	-0.55	0.11	-0.77	-0.55	-1.18	-0.95	-0.63	-0.32	3.58	1.55

All significant facies transitions (i.e. those ≥ 1.65) are written in bold.

Chi square matrix

	fpoordxbLT	dxblT	dxbt	mL	mIBr	mLT	mLTacc	mT	mTacc	ps	Tpel	xbLT	xbT	xbTacc	TOTAL
fpoordxbLT	0.1	9.6	0.0	0.1	0.1	0.4	0.3	0.1	0.3	0.4	0.2	0.0	0.3	0.3	12.3
dxblT	0.3	0.1	0.1	0.2	0.3	4.9	3.3	0.3	1.4	0.9	0.4	0.1	0.1	0.7	13.0
dxbt	0.0	0.1	0.0	0.0	0.0	0.1	0.1	21.4	0.2	0.1	0.1	0.0	0.1	0.1	22.4
mL	0.1	0.2	0.0	0.1	0.1	2.1	0.2	0.1	0.4	0.3	0.1	0.0	2.6	0.2	6.5
mIBr	0.1	0.3	0.0	0.1	0.1	6.8	0.3	0.1	0.3	0.4	0.2	0.0	0.3	0.3	9.3
mLT	0.4	4.0	0.1	0.3	0.8	1.3	0.9	0.4	0.0	2.3	0.6	0.1	1.1	0.0	12.3
mLTacc	1.6	0.1	0.1	0.2	1.6	0.9	0.6	1.6	0.3	0.9	0.9	0.1	0.8	0.7	10.5
mT	0.1	0.3	0.0	9.8	0.1	0.4	0.3	0.1	0.3	0.4	4.0	0.0	0.3	0.3	16.5
mTacc	0.6	1.4	0.2	0.4	0.6	0.4	2.7	0.6	0.2	9.8	1.8	0.2	1.6	1.4	21.9
ps	2.1	0.6	9.8	0.2	2.1	0.1	0.5	2.1	1.2	0.8	0.3	0.1	0.7	0.6	21.2
Tpel	0.2	0.5	0.1	0.1	0.2	0.6	0.4	0.2	16.0	0.6	0.3	0.1	0.6	0.5	20.5
xbLT	0.0	0.1	0.0	0.0	0.0	0.1	0.1	0.0	0.2	0.1	0.1	0.0	0.1	8.1	9.1
xbT	1.3	0.8	0.1	2.6	0.3	1.0	0.7	0.3	1.6	1.0	0.5	6.9	1.3	6.1	24.5
xbTacc	0.3	0.7	0.1	0.2	0.3	0.0	0.6	0.3	1.4	0.9	0.4	0.1	12.8	2.4	20.5
TOTAL	7.4	18.9	10.8	14.2	6.9	19.1	10.7	27.9	23.7	18.9	9.7	7.9	22.8	21.7	200.0

Tables C3 – Markov Chain Gingerich-Harper method data tables

Transition count matrix

	fpoordxbLT	dxblT	dxblT	mL	mIBr	mLT	mLTacc	mT	mTacc	ps	Tpel	xbLT	xbT	xbTacc	TOTAL
fpoordxbLT		2							1						3
dxblT						3	2						1		6
dxblT								1							1
pmL						1							1		2
mIBr						2			1						3
mLT		3			1				2	3				1	10
mLTacc	1	1			1			1	2		1				7
mT				1					1		1				3
mTacc						1	3			6	2				12
ps	1		1		1	1	1	1							6
Tpel									5						5
xbLT														1	1
xbT	1			1								1		3	6
xbTacc						1							4		5
TOTAL	3	6	1	2	3	9	6	3	12	9	4	1	6	5	65

The Gingerich-Harper method does not allow a facies to overlie itself, therefore these squares are blocked out in grey.

Independent trials (probability) matrix

	fpoordxbLT	dxblT	dxBT	mL	mIBr	mLT	mLTacc	mT	mTacc	ps	Tpel	xbLT	xbT	xbTacc
fpoordxbLT		0.097	0.016	0.032	0.048	0.145	0.097	0.048	0.194	0.145	0.065	0.016	0.097	0.081
dxblT	0.051		0.017	0.034	0.051	0.153	0.102	0.051	0.203	0.153	0.068	0.017	0.102	0.085
dxBT	0.047	0.094		0.031	0.047	0.141	0.094	0.047	0.188	0.141	0.063	0.016	0.094	0.078
mL	0.048	0.095	0.016		0.048	0.143	0.095	0.048	0.190	0.143	0.063	0.016	0.095	0.079
mIBr	0.048	0.097	0.016	0.032		0.145	0.097	0.048	0.194	0.145	0.065	0.016	0.097	0.081
mLT	0.054	0.107	0.018	0.036	0.054		0.107	0.054	0.214	0.161	0.071	0.018	0.107	0.089
mLTacc	0.051	0.102	0.017	0.034	0.051	0.153		0.051	0.203	0.153	0.068	0.017	0.102	0.085
mT	0.048	0.097	0.016	0.032	0.048	0.145	0.097		0.194	0.145	0.065	0.016	0.097	0.081
mTacc	0.057	0.113	0.019	0.038	0.057	0.170	0.113	0.057		0.170	0.075	0.019	0.113	0.094
ps	0.054	0.107	0.018	0.036	0.054	0.161	0.107	0.054	0.214		0.071	0.018	0.107	0.089
Tpel	0.049	0.098	0.016	0.033	0.049	0.148	0.098	0.049	0.197	0.148		0.016	0.098	0.082
xbLT	0.047	0.094	0.016	0.031	0.047	0.141	0.094	0.047	0.188	0.141	0.063		0.094	0.078
xbT	0.051	0.102	0.017	0.034	0.051	0.153	0.102	0.051	0.203	0.153	0.068	0.017		0.085
xbTacc	0.050	0.100	0.017	0.033	0.050	0.150	0.100	0.050	0.200	0.150	0.067	0.017	0.100	

Transition probability matrix

	fpoordxbLT	dxblT	dxbt	mL	mIBr	mLT	mLTacc	mT	mTacc	ps	Tpel	xbLT	xbT	xbTacc
fpoordxbLT		0.667	0.000	0.000	0.000	0.000	0.000	0.000	0.333	0.000	0.000	0.000	0.000	0.000
dxblT	0.000		0.000	0.000	0.000	0.500	0.333	0.000	0.000	0.000	0.000	0.000	0.167	0.000
dxbt	0.000	0.000		0.000	0.000	0.000	0.000	1.000	0.000	0.000	0.000	0.000	0.000	0.000
mL	0.000	0.000	0.000		0.000	0.500	0.000	0.000	0.000	0.000	0.000	0.000	0.500	0.000
mIBr	0.000	0.000	0.000	0.000		0.667	0.000	0.000	0.333	0.000	0.000	0.000	0.000	0.000
mLT	0.000	0.300	0.000	0.000	0.100		0.000	0.000	0.200	0.300	0.000	0.000	0.000	0.100
mLTacc	0.143	0.143	0.000	0.000	0.143	0.000		0.143	0.286	0.000	0.143	0.000	0.000	0.000
mT	0.000	0.000	0.000	0.333	0.000	0.000	0.000		0.333	0.000	0.333	0.000	0.000	0.000
mTacc	0.000	0.000	0.000	0.000	0.000	0.083	0.250	0.000		0.500	0.167	0.000	0.000	0.000
ps	0.167	0.000	0.167	0.000	0.167	0.167	0.167	0.167	0.000		0.000	0.000	0.000	0.000
Tpel	0.000	0.000	0.000	0.000	0.000	0.000	0.000	0.000	1.000	0.000		0.000	0.000	0.000
xbLT	0.000	0.000	0.000	0.000	0.000	0.000	0.000	0.000	0.000	0.000	0.000		0.000	1.000
xbT	0.167	0.000	0.000	0.167	0.000	0.000	0.000	0.000	0.000	0.000	0.000	0.167		0.500
xbTacc	0.000	0.000	0.000	0.000	0.000	0.200	0.000	0.000	0.000	0.000	0.000	0.000	0.800	

Difference matrix

	fpoordxbLT	dxblT	dxBT	mL	mIBr	mLT	mLTacc	mT	mTacc	ps	Tpel	xbLT	xbT	xbTacc
fpoordxbLT		0.570	-0.016	-0.032	-0.048	-0.145	-0.097	-0.048	0.140	-0.145	-0.065	-0.016	-0.097	-0.081
dxblT	-0.051		-0.017	-0.034	-0.051	0.347	0.232	-0.051	-0.203	-0.153	-0.068	-0.017	0.065	-0.085
dxBT	-0.047	-0.094		-0.031	-0.047	-0.141	-0.094	0.953	-0.188	-0.141	-0.063	-0.016	-0.094	-0.078
mL	-0.048	-0.095	-0.016		-0.048	0.357	-0.095	-0.048	-0.190	-0.143	-0.063	-0.016	0.405	-0.079
mIBr	-0.048	-0.097	-0.016	-0.032		0.522	-0.097	-0.048	0.140	-0.145	-0.065	-0.016	-0.097	-0.081
mLT	-0.054	0.193	-0.018	-0.036	0.046		-0.107	-0.054	-0.014	0.139	-0.071	-0.018	-0.107	0.011
mLTacc	0.092	0.041	-0.017	-0.034	0.092	-0.153		0.092	0.082	-0.153	0.075	-0.017	-0.102	-0.085
mT	-0.048	-0.097	-0.016	0.301	-0.048	-0.145	-0.097		0.140	-0.145	0.269	-0.016	-0.097	-0.081
mTacc	-0.057	-0.113	-0.019	-0.038	-0.057	-0.086	0.137	-0.057		0.330	0.091	-0.019	-0.113	-0.094
ps	0.113	-0.107	0.149	-0.036	0.113	0.006	0.060	0.113	-0.214		-0.071	-0.018	-0.107	-0.089
Tpel	-0.049	-0.098	-0.016	-0.033	-0.049	-0.148	-0.098	-0.049	0.803	-0.148		-0.016	-0.098	-0.082
xbLT	-0.047	-0.094	-0.016	-0.031	-0.047	-0.141	-0.094	-0.047	-0.188	-0.141	-0.063		-0.094	0.922
xbT	0.116	-0.102	-0.017	0.133	-0.051	-0.153	-0.102	-0.051	-0.203	-0.153	-0.068	0.150		0.415
xbTacc	-0.050	-0.100	-0.017	-0.033	-0.050	0.050	-0.100	-0.050	-0.200	-0.150	-0.067	-0.017	0.700	

254

All positive differences are highlighted in beige in the table. These represent facies transitions that occur more frequently than would be expected in a random system.

Binomial probability matrix

	fpoordxbLT	dxblT	dxblT	mL	mIBr	mLT	mLTacc	mT	mTacc	ps	Tpel	xbLT	xbT	xbTacc
fpoordxbLT		0.03							0.48					
dxblT						0.05	0.12						0.47	
dxblT								0.05						
mL						0.27							0.18	
mIBr						0.06			0.48					
mLT		0.08			0.42					0.21				
mLTacc	0.31	0.53			0.31			0.31	0.43		0.39			
mT				0.09					0.48		0.18			
mTacc							0.15			0.01	0.23			
ps	0.28		0.10		0.28	0.65	0.49	0.28						
Tpel									0.00					
xbLT														0.08
xbT	0.27			0.19								0.10		0.01
xbTacc							0.56						0.00	

All significant facies transitions (i.e. those ≤ 0.10) are written in bold.

Chi square matrix

	fpoordxbLT	dxblT	dxbt	mL	mIBr	mLT	mLTacc	mT	mTacc	ps	Tpel	xbLT	xbT	xbTacc	TOTAL
fpoordxbLT		10.068	0.048	0.097	0.145	0.435	0.290	0.145	0.303	0.435	0.194	0.048	0.290	0.242	12.742
dxblT	0.305		0.102	0.203	0.305	4.749	3.166	0.305	1.220	0.915	0.407	0.102	0.249	0.508	12.536
dxbt	0.047	0.094		0.031	0.047	0.141	0.094	19.380	0.188	0.141	0.063	0.016	0.094	0.078	20.411
mL	0.095	0.190	0.032		0.095	1.786	0.190	0.095	0.381	0.286	0.127	0.032	3.440	0.159	6.909
mIBr	0.145	0.290	0.048	0.097		5.621	0.290	0.145	0.303	0.435	0.194	0.048	0.290	0.242	8.149
mLT	0.536	3.471	0.179	0.357	0.402		1.071	0.536	0.010	1.207	0.714	0.179	1.071	0.013	9.746
mLTacc	1.165	0.117	0.119	0.237	1.165	1.068		1.165	0.233	1.068	0.582	0.119	0.712	0.593	8.343
mT	0.145	0.290	0.048	8.430	0.145	0.435	0.290		0.303	0.435	3.360	0.048	0.290	0.242	14.464
mTacc	0.679	1.358	0.226	0.453	0.679	0.528	1.983	0.679		7.704	1.322	0.226	1.358	1.132	18.331
ps	1.433	0.643	7.440	0.214	1.433	0.001	0.198	1.433	1.286		0.429	0.107	0.643	0.536	15.795
Tpel	0.246	0.492	0.082	0.164	0.246	0.738	0.492	0.246	16.400	0.738		0.082	0.492	0.410	20.827
xbLT	0.047	0.094	0.016	0.031	0.047	0.141	0.094	0.047	0.188	0.141	0.063		0.094	10.878	11.878
xbT	1.583	0.610	0.102	3.120	0.305	0.915	0.610	0.305	1.220	0.915	0.407	7.935		12.208	30.236
xbTacc	0.250	0.500	0.083	0.167	0.250	0.083	0.500	0.250	1.000	0.750	0.333	0.083	24.500		28.750
TOTAL	6.676	18.218	8.525	13.602	5.265	16.641	9.270	24.732	23.034	15.171	8.193	9.025	33.524	27.241	190.368

Appendix D: Geochemistry data

Table D1 – Major elements, LOIs and totals, all in wt.%.

Sample	Unit	SiO ₂	TiO ₂	Al ₂ O ₃	Fe ₂ O ₃	MnO	MgO	CaO	Na ₂ O	K ₂ O	P ₂ O ₅	LOI	Total
T59	Buco	57.51	0.92	15.89	9.84	0.18	3.22	7.26	3.67	1.79	0.24	0.57	101.13
T66	Buco	59.04	0.95	15.78	9.50	0.18	2.76	6.18	3.67	1.97	0.27	0.65	100.96
T69 - DARK	Buco	62.22	0.89	15.31	7.96	0.18	1.75	4.50	4.44	2.54	0.30	0.65	100.78
T69 - LIGHT	Buco	61.98	0.88	15.08	7.82	0.18	1.74	4.42	4.29	2.53	0.29	1.38	100.63
T2.40	Buco	57.53	0.93	15.73	9.78	0.18	3.14	6.10	3.17	1.92	0.27	2.43	101.21
T2.42	Buco	58.30	0.93	15.83	9.83	0.18	2.94	6.61	3.88	1.81	0.25	-0.49	100.11
T2.43	Buco	57.88	0.92	15.72	9.77	0.18	2.96	6.60	3.83	1.85	0.24	-0.48	99.55
T2.46	Buco	57.36	0.93	15.78	9.73	0.18	3.03	6.36	3.23	1.76	0.24	2.15	100.78
T2.47	Buco	57.61	0.93	15.88	9.82	0.18	3.00	6.26	3.20	1.78	0.23	2.21	101.16
T2.50A	Buco	57.84	0.92	15.72	9.75	0.18	2.95	6.58	3.88	1.88	0.24	-0.46	99.56
T2.50A-R	Buco	57.69	0.92	15.67	9.74	0.18	2.95	6.55	3.91	1.94	0.24	-0.46	99.43
T2.50B	Buco	57.98	0.92	15.67	9.70	0.18	2.87	6.44	3.96	1.95	0.25	-0.36	99.61
T2.52	Buco	57.86	0.93	15.77	9.69	0.18	3.01	6.08	3.21	1.95	0.25	2.10	101.05
T2.53	Buco	57.79	0.93	15.53	9.48	0.19	2.72	6.24	3.63	1.98	0.27	0.62	99.42
T2.54	Buco	57.64	0.93	15.69	9.52	0.19	2.88	6.47	3.67	1.94	0.27	-0.02	99.21
T2.56	Buco	57.91	0.93	15.64	9.66	0.19	2.87	6.49	3.79	1.88	0.26	0.15	99.77
T2.61	Buco	57.68	0.92	15.72	9.89	0.18	3.01	6.69	3.72	1.82	0.24	-0.34	99.61
T2.78	Buco	61.32	0.87	14.79	7.71	0.18	1.52	4.22	4.21	2.56	0.30	1.80	99.51
T2.81	Buco	61.07	0.83	15.31	8.10	0.18	2.15	5.27	4.12	2.05	0.22	0.63	99.96
T2.82	Buco	56.21	0.87	16.96	9.15	0.16	2.73	7.45	2.90	1.37	0.22	1.29	99.31
T2.101	Buco	56.91	0.94	16.10	9.86	0.17	2.80	6.47	3.10	1.79	0.26	1.11	99.51
T3.4	Buco	58.15	0.92	16.33	9.78	0.18	3.10	6.51	3.54	1.78	0.24	0.14	100.72
T3.10	Buco	58.01	0.92	16.36	9.87	0.18	3.18	6.68	3.76	1.81	0.24	-0.32	100.77

Sample	Unit	SiO ₂	TiO ₂	Al ₂ O ₃	Fe ₂ O ₃	MnO	MgO	CaO	Na ₂ O	K ₂ O	P ₂ O ₅	LOI	Total
T3.11A	Buco	57.99	0.94	16.43	10.01	0.18	3.28	6.79	3.52	1.74	0.24	0.00	101.14
T3.11B	Buco	58.02	0.93	16.39	10.01	0.18	3.29	6.87	3.77	1.76	0.24	-0.39	101.12
T24	Tagaytay	63.04	0.65	14.50	6.56	0.170	0.74	2.52	3.76	2.34	0.188	4.24	98.72
T25	Tagaytay	59.68	0.97	15.64	9.69	0.20	2.49	5.49	3.88	1.96	0.28	0.58	100.90
T42	Tagaytay	64.17	0.73	14.78	5.85	0.18	0.98	3.03	3.95	2.49	0.22	4.51	100.90
T49	Tagaytay	59.26	0.78	15.99	8.90	0.19	2.14	5.46	3.62	1.50	0.226	1.13	99.22
T51A	Tagaytay	60.95	0.74	15.56	7.43	0.20	1.52	4.40	4.00	1.79	0.273	1.97	98.85
T2.68	Tagaytay	60.13	0.99	15.95	9.14	0.18	2.50	5.79	3.66	2.25	0.31	0.59	101.50
T2.69	Tagaytay	60.34	0.85	15.73	8.37	0.20	2.18	5.08	3.85	1.82	0.25	1.70	100.38
T2.70	Tagaytay	56.24	0.72	17.14	8.88	0.18	4.16	8.40	3.22	1.25	0.16	1.12	101.48
T2.74	Tagaytay	63.22	0.76	15.19	6.57	0.16	1.34	3.66	3.74	2.45	0.23	3.61	100.94
T2.83	Tagaytay	58.93	1.02	14.71	10.13	0.19	2.15	5.46	3.90	2.34	0.37	0.32	99.56
T2.89	Tagaytay	62.68	0.69	14.70	6.06	0.19	1.27	3.60	4.04	2.35	0.30	3.62	99.52
T2.76A	Balagbag	56.74	1.05	15.49	10.59	0.18	3.22	6.98	3.51	1.91	0.30	-0.16	99.89
T2.76B	Balagbag	57.76	0.98	15.44	9.81	0.18	2.94	5.90	2.97	1.98	0.43	2.54	100.99
T2.77	Balagbag	58.02	1.01	15.50	10.15	0.18	3.11	6.16	2.96	2.01	0.30	1.58	101.00
T2.99	Balagbag	57.83	1.01	15.19	10.09	0.17	2.80	6.31	3.16	2.08	0.35	0.40	99.42
T2.100	Balagbag	56.70	1.02	15.30	10.47	0.17	3.20	6.87	3.25	1.94	0.29	0.20	99.48
T2.75	Burol	57.57	0.95	15.41	10.31	0.18	3.00	6.75	3.45	1.89	0.27	-0.26	99.60
T2.92	Burol	56.70	1.03	15.31	10.82	0.19	3.00	6.90	3.40	1.81	0.27	0.31	99.78
T2.96	Burol	61.95	0.83	14.68	7.64	0.17	1.73	4.44	4.17	2.09	0.24	1.51	99.49
T2.97	Burol	55.92	0.95	17.16	9.05	0.14	2.48	6.72	3.15	1.78	0.42	1.41	99.22
T2.98	Burol	57.66	0.95	15.37	10.33	0.18	3.03	6.77	3.53	1.90	0.28	-0.35	99.72
T13	Pasong	57.32	0.83	15.97	9.72	0.179	2.74	6.50	3.63	1.62	0.242	-0.07	98.73
T15	Pasong	58.28	0.82	15.85	9.26	0.177	2.46	5.94	3.60	1.76	0.260	0.60	99.03
T62	Pasong	55.63	0.88	16.03	10.39	0.18	3.17	7.39	3.40	1.37	0.248	0.12	98.82

Sample	Unit	SiO ₂	TiO ₂	Al ₂ O ₃	Fe ₂ O ₃	MnO	MgO	CaO	Na ₂ O	K ₂ O	P ₂ O ₅	LOI	Total
T63	Pasong	55.56	0.86	15.89	10.17	0.18	3.17	7.23	3.13	1.37	0.250	0.78	98.61
T79	Pasong	57.94	0.83	16.06	9.59	0.18	2.62	6.35	3.72	1.66	0.241	-0.14	99.11
T2.21	Pasong	58.75	0.93	16.41	9.75	0.18	3.10	6.52	3.96	1.90	0.25	-0.41	101.42
T2.66	Pasong	57.61	0.99	16.73	9.70	0.17	3.07	6.76	3.20	1.68	0.22	1.19	101.36
T2.67	Pasong	58.65	0.93	16.18	9.81	0.18	3.17	6.67	3.85	1.87	0.24	-0.31	101.29
T2.86	Pasong	58.66	0.93	15.99	9.78	0.18	3.05	6.44	3.51	1.85	0.24	0.25	100.94
T3.1	Pasong	58.06	0.94	16.52	9.89	0.18	3.22	6.70	3.82	1.84	0.24	-0.22	101.22
T3.2A	Pasong	57.98	0.94	16.44	9.87	0.18	3.11	6.49	3.36	1.78	0.24	0.47	100.90
T3.12	Pasong	58.12	0.93	16.44	9.69	0.18	3.12	6.55	3.75	1.88	0.25	-0.23	100.73
T3.13	Pasong	57.50	0.94	16.10	9.64	0.18	3.03	6.45	3.74	1.87	0.25	-0.30	99.44
T3.16	Pasong	57.36	0.93	16.15	9.88	0.18	3.21	6.73	3.78	1.79	0.24	-0.26	100.06
T3.20	Pasong	59.23	0.97	15.93	8.72	0.17	2.56	5.62	3.92	2.37	0.30	0.11	99.96
T3.21	Pasong	56.29	0.96	16.21	10.38	0.18	3.73	7.79	3.32	1.45	0.25	0.40	100.99
T27	Indang	59.21	0.78	16.24	8.24	0.159	2.02	5.44	3.45	1.58	0.321	1.49	98.99
T28	Indang	61.88	0.72	15.46	6.68	0.192	1.43	4.08	3.82	1.97	0.297	2.62	99.16
T31	Indang	59.14	0.81	16.07	8.35	0.19	2.34	5.75	3.90	1.57	0.518	0.31	99.04
T2.33	Indang	59.38	0.95	16.17	8.74	0.19	2.40	5.71	3.48	2.01	0.28	1.09	100.46
T2.35	Indang	61.09	0.95	15.58	8.59	0.21	2.34	5.56	3.50	1.96	0.31	1.04	101.24
T2.64	Indang	62.07	0.93	15.73	8.01	0.17	2.12	4.94	4.31	2.67	0.33	-0.20	101.11
T2.65	Indang	59.35	0.93	15.80	8.81	0.16	2.45	5.28	3.15	2.09	0.27	1.86	100.16
T2.88	Indang	60.75	0.90	15.45	8.13	0.18	1.92	4.94	3.98	2.33	0.27	0.51	99.43
T2.88-R	Indang	60.70	0.91	15.45	8.13	0.18	1.95	4.95	4.00	2.35	0.27	0.54	99.49
T4-WB	Tadlac Cave	61.02	0.67	15.25	6.72	0.171	1.57	4.35	4.08	1.89	0.319	2.79	98.86
T4-WT	Tadlac Cave	59.10	0.72	15.90	7.87	0.180	2.17	5.55	4.03	1.56	0.313	1.86	99.27
T4-BB	Tadlac Cave	61.84	0.69	15.54	6.95	0.174	1.65	4.57	4.35	1.85	0.380	1.08	99.11
T4-BT	Tadlac Cave	60.52	0.71	15.75	7.44	0.177	1.87	4.99	4.19	1.70	0.364	1.16	98.90

Sample	Unit	SiO ₂	TiO ₂	Al ₂ O ₃	Fe ₂ O ₃	MnO	MgO	CaO	Na ₂ O	K ₂ O	P ₂ O ₅	LOI	Total
T2.3	Tadlac Cave	60.74	0.76	15.47	7.48	0.18	2.29	5.45	4.31	1.92	0.36	0.60	99.60
T2.4	Tadlac Cave	60.37	0.73	14.98	7.01	0.18	2.12	5.04	4.27	2.02	0.35	2.39	99.53
T2.5	Tadlac Cave	68.21	0.62	14.99	5.01	0.15	0.94	2.83	4.93	2.79	0.19	0.60	101.27
T2.6	Tadlac Cave	61.98	0.73	15.92	6.79	0.17	2.01	4.69	3.82	2.15	0.29	2.82	101.38
T2.7	Tadlac Cave	66.27	0.68	14.77	5.41	0.16	1.11	3.04	4.64	3.04	0.23	1.29	100.64
T2.8	Tadlac Cave	61.39	0.74	15.38	7.11	0.18	2.05	5.07	4.39	2.04	0.36	0.99	99.75
T2.9	Tadlac Cave	60.90	0.74	15.02	7.08	0.17	2.05	4.93	4.19	2.05	0.35	2.26	99.77
T35	Alitagtag	64.29	0.58	14.75	5.39	0.16	0.92	2.68	4.26	2.29	0.220	2.74	98.27
T36	Alitagtag	64.78	0.58	14.82	5.37	0.16	0.96	2.73	4.53	2.27	0.234	1.98	98.42
T2.11	Alitagtag	64.62	0.64	14.54	5.54	0.16	1.09	3.23	4.46	2.71	0.24	2.15	99.41
T2.12	Alitagtag	64.32	0.69	15.68	6.12	0.17	1.27	3.45	4.06	2.53	0.23	2.69	101.22
T2.13	Alitagtag	64.80	0.63	14.58	5.49	0.16	1.08	3.24	4.65	2.64	0.25	1.95	99.49
T3.17	Alitagtag	64.29	0.65	15.01	5.59	0.16	1.17	3.23	4.16	2.61	0.25	3.78	100.91
T3.19A	Alitagtag	63.76	0.67	14.78	5.09	0.15	1.31	4.30	4.38	2.72	0.20	3.72	101.07
T3.19B	Alitagtag	57.62	0.81	15.41	7.66	0.17	3.33	7.01	3.89	1.86	0.39	3.05	101.26
T3.22	Alitagtag	60.18	0.88	16.20	8.29	0.18	2.66	5.82	4.12	1.83	0.47	0.54	101.24
T3.23	Alitagtag	61.90	0.79	15.71	6.97	0.17	2.02	4.78	4.25	2.27	0.32	1.78	101.00
T9	Unknown	58.04	0.83	15.80	9.45	0.177	2.62	6.27	3.82	1.70	0.243	-0.01	98.94
T10	Unknown	64.94	0.57	14.70	4.85	0.141	0.62	2.13	4.04	2.78	0.153	3.73	98.65
T21	Unknown	63.11	0.80	14.91	7.54	0.16	1.45	3.92	4.25	2.83	0.34	1.14	100.46
T21	Unknown	63.41	0.80	14.99	7.58	0.16	1.46	3.98	4.25	2.80	0.34	1.14	100.95
T47	Unknown	54.75	0.93	18.61	9.62	0.14	2.95	7.20	2.22	0.99	0.15	3.58	101.16
T48	Unknown	59.28	0.84	15.79	8.62	0.16	2.62	5.90	3.61	2.15	0.24	1.04	100.28
T54	Unknown	60.72	0.98	15.05	8.92	0.17	1.94	4.75	3.82	2.67	0.36	1.28	100.70
T58	Unknown	56.93	0.95	16.31	10.68	0.17	3.23	6.88	3.04	1.59	0.24	0.96	101.00
T70	Unknown	56.72	0.98	15.91	10.82	0.18	3.68	7.45	3.42	1.65	0.24	-0.07	101.01

Sample	Unit	SiO ₂	TiO ₂	Al ₂ O ₃	Fe ₂ O ₃	MnO	MgO	CaO	Na ₂ O	K ₂ O	P ₂ O ₅	LOI	Total
T71	Unknown	56.76	0.79	18.21	8.31	0.14	2.12	7.12	3.42	1.40	0.210	0.78	99.29
T75	Unknown	62.82	0.64	14.76	5.58	0.16	1.14	2.94	3.82	2.23	0.190	4.04	98.32
T2.1	Unknown	64.90	0.61	14.22	4.95	0.15	0.92	2.47	3.22	3.03	0.18	5.42	100.09
T2.10	Unknown	61.63	0.79	16.66	7.15	0.14	1.37	4.17	3.40	2.03	0.20	3.31	100.85
T2.14	Unknown	64.88	0.59	13.97	4.86	0.15	0.84	2.68	4.00	2.87	0.19	4.34	99.37
T2.15	Unknown	59.35	0.99	15.57	8.65	0.17	2.20	5.32	3.85	2.45	0.34	0.83	99.75
T2.16	Unknown	60.40	0.98	15.09	8.67	0.18	1.93	4.98	3.95	2.57	0.35	0.61	99.76
T2.17	Unknown	57.78	1.00	15.71	9.75	0.17	2.93	6.55	3.52	1.92	0.28	0.25	99.90
T2.18	Unknown	60.87	0.93	15.42	8.06	0.17	2.02	4.93	4.18	2.65	0.33	-0.17	99.44
T2.19	Unknown	60.98	0.88	14.95	8.04	0.18	1.73	4.62	4.25	2.47	0.30	0.97	99.41
T2.20	Unknown	56.09	0.99	15.74	10.87	0.18	3.46	7.48	3.54	1.59	0.24	-0.27	99.92
T2.24	Unknown	56.25	1.00	17.24	10.40	0.19	2.66	5.57	2.75	1.35	0.20	3.25	100.89
T2.25(12)	Unknown	56.33	1.02	17.61	10.57	0.20	2.11	4.42	2.06	1.23	0.16	5.43	101.16
T2.25(19)	Unknown	56.17	1.02	17.67	10.67	0.20	2.17	4.50	2.09	1.22	0.17	5.29	101.18
T2.26	Unknown	58.21	0.93	15.96	9.38	0.18	2.44	5.35	2.98	1.78	0.24	3.07	100.57
T2.26-R	Unknown	58.76	0.92	16.11	9.44	0.18	2.47	5.40	2.97	1.78	0.24	3.08	101.41
T2.27	Unknown	60.52	0.92	15.87	8.81	0.21	2.05	4.88	3.71	2.13	0.28	1.83	101.22
T2.29	Unknown	58.78	0.96	15.53	9.61	0.13	1.74	3.92	2.52	2.00	0.30	4.87	100.40
T2.30	Unknown	60.02	0.95	16.39	9.29	0.29	1.64	3.10	1.70	1.16	0.13	6.26	100.95
T2.31	Unknown	56.48	0.91	18.63	9.34	0.46	2.37	4.21	2.45	1.32	0.19	4.53	100.88
T2.32	Unknown	57.74	0.94	19.96	8.86	0.17	0.97	2.38	1.62	0.91	0.12	7.29	100.96
T2.37	Unknown	55.43	1.12	16.05	11.15	0.15	2.92	7.09	3.69	1.68	0.26	1.03	100.63
T2.38A	Unknown	59.76	0.96	15.13	8.92	0.19	2.17	5.17	4.25	2.26	0.40	0.40	99.62
T2.38B	Unknown	59.76	0.96	15.09	8.87	0.19	2.10	5.13	4.24	2.33	0.42	0.34	99.44
T2.45	Unknown	56.31	0.95	15.27	10.28	0.17	3.09	6.25	2.94	1.75	0.24	2.49	99.77
T2.48	Unknown	60.41	0.97	15.07	9.04	0.19	2.02	5.03	4.19	2.35	0.37	0.04	99.69

Sample	Unit	SiO ₂	TiO ₂	Al ₂ O ₃	Fe ₂ O ₃	MnO	MgO	CaO	Na ₂ O	K ₂ O	P ₂ O ₅	LOI	Total
T2.49	Unknown	58.23	0.92	15.83	9.26	0.17	2.24	6.23	3.91	2.10	0.29	0.42	99.62
T2.57	Unknown	57.33	0.91	15.92	9.46	0.19	3.17	6.41	2.76	1.74	0.23	2.53	100.67
T2.57-R	Unknown	57.81	0.92	16.05	9.54	0.19	3.20	6.45	2.76	1.71	0.23	2.57	101.45
T2.58	Unknown	55.11	1.02	17.14	10.49	0.20	2.95	5.80	2.59	1.80	0.36	3.46	100.97
T2.62	Unknown	59.69	0.93	15.89	9.18	0.24	2.25	5.20	3.61	2.20	0.29	1.78	101.29
T2.71	Unknown	59.08	0.90	16.17	9.02	0.19	2.99	6.36	3.92	1.73	0.39	0.11	100.96
T2.72	Unknown	59.97	0.86	16.13	8.53	0.18	2.83	6.13	3.64	1.80	0.31	0.55	100.97
T2.73	Unknown	59.37	0.87	15.97	8.64	0.19	2.82	6.01	3.88	1.81	0.37	0.80	100.82
T2.79A	Unknown	56.25	0.99	15.71	10.82	0.18	3.45	7.47	3.59	1.67	0.24	-0.27	100.09
T2.79B	Unknown	58.91	0.99	15.88	9.21	0.19	2.64	6.11	4.05	1.96	0.30	-0.20	100.06
T2.80	Unknown	56.10	0.98	15.53	10.72	0.18	3.39	7.38	3.55	1.69	0.23	-0.18	99.61
T2.84	Unknown	56.65	0.93	15.79	10.18	0.18	3.18	7.05	3.75	1.73	0.23	-0.19	99.50
T2.85	Unknown	56.44	1.07	15.77	11.37	0.20	3.09	6.44	3.24	1.63	0.25	0.93	100.44
T2.87	Unknown	58.72	0.93	16.07	9.73	0.18	3.05	6.47	3.78	1.90	0.25	0.01	101.13
T2.90	Unknown	58.61	0.89	15.66	8.97	0.17	2.48	6.00	3.14	1.70	0.24	1.68	99.55
T2.93	Unknown	60.10	1.00	14.79	9.25	0.16	2.00	5.28	3.45	2.06	0.31	1.20	99.65
T2.94	Unknown	56.80	1.02	15.22	10.72	0.19	3.05	6.86	3.39	1.82	0.27	0.37	99.75
T2.95	Unknown	60.10	0.97	14.22	9.72	0.19	2.29	5.22	3.78	2.00	0.29	0.43	99.28
T2.104A	Unknown	61.47	0.82	15.43	7.90	0.18	2.02	5.06	4.24	2.10	0.21	0.19	99.66
T2.104B	Unknown	61.12	0.83	15.31	8.13	0.18	2.16	5.24	4.23	2.06	0.22	-0.12	99.38
T2.105	Unknown	60.98	0.78	15.60	7.49	0.17	1.78	4.58	4.15	2.14	0.20	1.55	99.45
T3.3A	Unknown	60.56	0.89	16.39	8.06	0.19	2.60	5.55	4.24	1.82	0.56	0.34	101.25
T3.3B	Unknown	67.09	0.66	15.14	4.68	0.15	0.88	2.68	4.47	3.04	0.16	2.54	101.49
T3.8B	Unknown	60.99	0.93	16.21	8.33	0.18	2.30	5.26	3.78	2.19	0.29	0.66	101.17
T3.9B	Unknown	57.35	0.95	16.54	10.09	0.17	3.12	6.52	3.13	1.57	0.22	0.94	100.63
T3.14A	Unknown	57.23	1.05	16.11	10.95	0.19	3.04	6.39	3.28	1.71	0.25	1.01	101.23

Sample	Unit	SiO ₂	TiO ₂	Al ₂ O ₃	Fe ₂ O ₃	MnO	MgO	CaO	Na ₂ O	K ₂ O	P ₂ O ₅	LOI	Total
T3.14A-R	Unknown	57.01	1.06	16.09	10.88	0.19	3.01	6.37	3.28	1.73	0.25	1.00	100.91
T3.14B	Unknown	66.18	0.65	15.12	5.10	0.14	0.85	2.75	4.43	3.23	0.17	2.62	101.23
T3.24A	Unknown	61.84	0.79	15.66	7.58	0.18	2.00	4.84	4.11	2.21	0.21	1.71	101.16
T3.24B	Unknown	59.41	0.89	15.67	8.50	0.18	2.48	5.55	3.98	1.94	0.22	-0.20	98.67
2020 ASH	Unknown	55.72	1.01	16.01	10.22	0.17	2.83	6.77	3.35	1.88	0.29	1.05	100.82

Table D2 – Half of trace element data in ppm

Sample	Unit	As	Ba	Ce	Co	Cr	Cs	Cu	Ga	La	Mo	Nb	Nd	Ni	Pb
T59	Buco	2.4	454.7	37.2	24.2	8.2	<1.9	134.9	17.6	18.8	2.3	6.5	20.7	<0.8	13.1
T66	Buco	2.9	505.6	44.1	22.8	2.7	<1.8	102.3	18.6	20.9	2.0	6.8	22.6	<0.8	16.6
T69 - DARK	Buco	3.8	625.7	55.2	11.1	0.0	7.6	48.5	17.7	28.0	2.5	8.3	25.1	<0.7	20.8
T69 - LIGHT	Buco	4.2	620.7	59.0	15.6	0.0	3.0	45.9	18.6	27.5	2.2	8.0	28.7	<0.7	19.3
T2.40	Buco	3.5	557.0	40.6	22.9	8.3	<1.8	123.7	17.5	20.0	1.8	6.4	19.3	<0.8	14.4
T2.42	Buco	1.0	454.2	42.0	27.9	14.9	<1.80	121.6	18.0	19.6	2.5	6.5	19.4	<0.76	13.9
T2.43	Buco	2.4	447.8	45.7	25.9	13.9	1.8	127.6	18.3	17.7	2.3	6.2	19.7	<0.76	14.2
T2.46	Buco	4.3	478.7	37.1	24.2	7.0	3.3	130.0	17.9	19.5	2.0	6.4	17.6	<0.8	12.7
T2.47	Buco	4.4	447.8	37.0	26.6	12.4	2.9	128.2	17.2	23.4	2.1	6.6	16.0	<0.8	13.7
T2.50A	Buco	2.3	461.7	36.8	28.6	10.2	<1.80	127.0	18.0	19.5	2.3	6.5	17.9	<0.76	12.5
T2.50A-R	Buco	2.2	451.4	39.2	27.0	7.6	<1.82	125.9	17.7	18.0	2.4	6.5	18.8	<0.77	13.6
T2.50B	Buco	2.6	460.8	37.7	27.0	2.7	<1.82	124.5	19.0	22.2	2.4	6.7	19.3	<0.76	13.7
T2.52	Buco	4.4	462.9	39.8	26.7	5.7	<1.8	121.3	17.9	20.8	2.2	6.4	17.3	<0.8	14.0
T2.53	Buco	2.3	482.7	43.4	25.8	5.2	<1.81	95.0	18.0	22.6	2.3	6.7	21.9	<0.76	13.5
T2.54	Buco	2.2	466.0	43.5	25.4	7.0	<1.81	90.9	17.4	21.9	2.3	6.4	18.8	<0.76	13.1
T2.56	Buco	3.2	469.7	49.1	26.1	4.8	4.9	109.6	19.0	21.8	2.5	6.6	21.2	<0.76	13.3
T2.61	Buco	1.5	451.2	42.7	26.5	3.3	<1.82	131.9	17.9	20.6	2.2	6.5	21.3	<0.77	11.8

Sample	Unit	As	Ba	Ce	Co	Cr	Cs	Cu	Ga	La	Mo	Nb	Nd	Ni	Pb
T2.78	Buco	4.2	627.4	54.4	14.6	0.0	4.8	40.0	16.9	30.4	2.9	8.5	26.9	<0.68	20.6
T2.81	Buco	2.7	514.5	42.4	19.2	0.0	2.1	44.2	18.5	22.8	2.3	7.5	21.8	<0.70	17.6
T2.82	Buco	1.7	368.0	26.7	24.3	3.4	<1.81	84.0	18.4	13.5	1.9	5.7	15.9	<0.74	12.3
T2.101	Buco	4.7	449.0	39.3	24.9	6.0	2.6	125.2	18.0	18.5	2.3	6.7	16.6	<0.76	13.4
T3.4	Buco	2.2	432.3	39.4	24.3	2.1	<1.8	130.5	17.8	20.7	1.9	6.3	19.1	<0.8	12.2
T3.10	Buco	1.5	456.2	37.2	26.5	7.2	3.9	140.4	19.1	20.5	2.2	6.5	20.8	<0.8	13.0
T3.11A	Buco	1.1	439.5	43.9	25.0	6.3	1.4	139.8	18.0	21.8	2.0	6.4	17.6	<0.8	12.4
T3.11B	Buco	2.0	443.4	39.2	27.0	13.5	2.1	143.4	17.2	21.5	2.2	6.4	23.3	<0.8	11.8
T24	Tagaytay	4.0	622.8	53.4	9.8	<0.7	<1.8	28.3	15.6	26.7	2.5	8.9	24.6	<0.6	22.0
T25	Tagaytay	3.6	500.0	48.2	22.1	<0.7	2.5	123.9	18.9	24.5	2.1	7.1	26.7	<0.8	17.0
T42	Tagaytay	3.4	588.7	49.1	8.9	<0.7	1.7	13.3	17.0	27.0	2.2	8.1	26.7	<0.6	20.4
T49	Tagaytay	0.9	411.6	39.5	20.7	1.3	<1.9	88.7	19.3	19.1	2.4	6.4	21.6	<0.7	15.3
T51A	Tagaytay	2.3	483.8	45.0	15.4	<0.7	<1.8	23.2	17.7	19.8	2.4	7.1	22.5	<0.7	16.9
T2.68	Tagaytay	3.7	530.1	49.3	20.2	1.3	3.8	120.7	17.8	25.8	2.7	8.5	24.7	<0.7	18.2
T2.69	Tagaytay	2.8	443.4	36.9	18.3	<0.7	<1.8	59.9	17.8	19.9	1.9	6.5	21.3	<0.7	14.8
T2.70	Tagaytay	2.6	319.4	25.5	25.1	8.4	<1.8	76.9	17.3	12.0	1.2	5.0	13.9	1.4	10.7
T2.74	Tagaytay	4.9	604.3	50.4	10.8	<0.7	4.3	21.0	16.4	26.2	2.4	8.7	24.7	<0.8	20.1
T2.83	Tagaytay	3.5	548.5	54.2	25.3	<0.71	2.9	120.4	18.4	26.4	2.6	7.8	25.5	<0.77	18.1
T2.89	Tagaytay	3.2	573.7	47.7	9.9	<0.65	<1.70	17.3	17.4	25.9	2.5	7.9	24.4	1.1	19.7
T2.76A	Balagbag	3.3	485.8	42.5	29.5	9.2	<1.85	187.2	17.9	22.0	2.3	7.4	22.4	3.2	16.7
T2.76B	Balagbag	4.6	516.4	48.4	24.9	2.6	4.0	151.7	16.9	23.2	1.9	7.0	21.6	1.8	17.0
T2.77	Balagbag	4.8	493.8	48.9	26.3	7.2	2.7	162.0	17.6	23.4	2.3	7.6	22.7	2.5	16.5
T2.99	Balagbag	4.1	520.2	54.9	27.8	9.4	3.0	142.2	16.9	24.5	2.5	7.8	25.9	2.2	18.3
T2.100	Balagbag	2.5	483.4	43.7	29.8	17.2	<1.83	190.1	18.4	22.9	2.6	7.4	20.1	5.2	15.7
T2.75	Burol	3.0	459.0	47.4	28.6	6.0	2.1	110.8	17.7	23.7	2.3	7.0	22.7	<0.77	16.7
T2.92	Burol	2.9	441.1	42.2	29.0	6.1	<1.76	141.6	18.0	18.2	2.4	7.2	18.9	<0.79	14.3

Sample	Unit	As	Ba	Ce	Co	Cr	Cs	Cu	Ga	La	Mo	Nb	Nd	Ni	Pb
T2.96	Burol	3.1	516.9	42.2	17.2	0.0	1.8	27.4	16.3	22.0	1.9	6.9	20.6	<0.67	15.9
T2.97	Burol	4.7	448.8	45.3	24.9	6.8	<1.80	112.4	17.3	19.4	2.4	6.9	22.2	<0.73	16.0
T2.98	Burol	4.3	480.8	45.8	27.5	5.6	<1.84	113.4	16.5	23.1	2.7	7.1	20.0	<0.78	17.3
T13	Pasong	1.8	450.0	38.8	26.9	10.8	2.5	130.1	18.5	21.5	2.1	6.4	19.2	<0.8	13.6
T15	Pasong	2.3	487.1	40.6	24.7	3.9	2.9	96.6	17.8	22.7	2.4	7.0	21.0	<0.8	14.7
T62	Pasong	2.1	401.9	35.8	27.6	15.5	2.2	148.1	17.2	16.5	2.3	5.9	18.6	<0.8	12.8
T63	Pasong	2.2	409.6	33.8	27.1	10.6	<1.9	130.7	18.2	17.6	2.2	6.3	17.3	2.1	12.5
T79	Pasong	1.7	460.1	38.6	24.9	7.8	<1.9	123.9	19.5	19.4	2.5	6.9	18.5	<0.8	46.5
T2.21	Pasong	2.1	469.3	41.0	25.7	10.8	<1.8	117.6	18.3	24.5	2.1	6.5	18.7	<0.8	14.0
T2.66	Pasong	4.3	425.0	35.9	24.5	11.8	<1.8	108.5	19.1	18.6	2.0	6.2	19.3	<0.8	13.5
T2.67	Pasong	1.4	461.6	42.4	25.0	4.8	2.9	136.1	18.6	18.9	2.2	6.4	20.1	<0.8	13.6
T2.86	Pasong	1.9	458.4	41.6	25.2	4.2	<1.8	121.5	17.9	20.6	2.0	6.3	20.1	<0.8	13.3
T3.1	Pasong	1.9	454.9	34.8	25.0	1.4	<1.9	136.3	16.7	20.8	1.9	6.4	15.8	<0.8	12.9
T3.2A	Pasong	2.4	452.4	41.0	23.6	4.6	<1.9	130.8	19.5	21.0	2.2	6.6	21.2	<0.8	12.1
T3.12	Pasong	1.6	461.7	39.5	25.5	5.5	<1.8	123.9	17.6	16.8	2.3	6.5	21.5	<0.8	12.9
T3.13	Pasong	1.6	465.6	41.6	25.6	5.3	<1.8	127.3	17.3	20.0	2.3	6.6	21.3	<0.8	13.7
T3.16	Pasong	2.2	450.2	40.4	25.5	4.9	<1.8	136.8	16.5	18.9	2.0	6.6	19.0	<0.8	12.0
T3.20	Pasong	3.5	535.8	48.7	20.4	1.1	3.5	97.5	17.4	22.8	2.6	8.3	24.0	<0.7	19.2
T3.21	Pasong	2.2	392.0	27.7	27.5	14.3	<1.9	158.7	16.2	16.0	2.0	5.5	13.3	<0.8	11.8
T27	Indang	2.6	436.8	39.7	19.6	0.0	<1.9	44.3	18.4	21.4	2.0	6.9	22.8	<0.7	15.3
T28	Indang	4.2	541.6	42.9	13.1	0.0	<1.8	15.6	17.6	24.2	2.5	7.8	25.4	<0.7	17.6
T31	Indang	2.4	430.2	38.7	18.6	0.0	3.3	45.7	17.7	19.0	2.3	6.8	22.6	<0.7	14.0
T2.33	Indang	4.4	473.6	45.0	19.1	0.0	3.4	28.7	18.7	21.7	1.8	7.3	18.6	<0.7	15.3
T2.35	Indang	5.4	666.1	32.9	18.9	2.9	<1.8	26.1	16.2	18.5	2.3	7.5	20.9	<0.7	15.4
T2.64	Indang	4.1	587.8	53.1	16.6	0.0	2.5	62.6	17.2	28.3	3.0	9.3	29.1	<0.7	21.6
T2.65	Indang	8.9	585.6	41.2	20.4	13.2	<1.8	100.7	16.5	23.6	2.0	7.7	23.3	3.9	15.9

Sample	Unit	As	Ba	Ce	Co	Cr	Cs	Cu	Ga	La	Mo	Nb	Nd	Ni	Pb
T2.88	Indang	4.6	511.5	42.8	17.1	0.0	1.9	24.2	17.0	22.0	2.5	8.5	19.9	<0.70	18.4
T2.88-R	Indang	3.9	513.1	43.4	16.2	0.0	2.8	24.3	16.7	20.7	2.4	8.4	18.6	<0.71	18.2
T4-WB	Tadlac Cave	3.5	538.8	45.6	13.6	0.0	<1.8	28.7	16.5	25.7	2.5	7.7	22.6	<0.7	18.1
T4-WT	Tadlac Cave	3.2	465.9	41.6	18.8	0.0	3.3	25.5	17.1	20.5	2.2	6.6	20.4	<0.7	14.8
T4-BB	Tadlac Cave	3.3	529.1	44.2	14.8	0.0	3.1	38.1	17.8	23.6	2.2	7.7	20.3	<0.7	18.2
T4-BT	Tadlac Cave	3.8	500.2	38.7	16.4	0.0	<1.8	33.3	19.1	21.7	2.2	7.2	20.6	<0.7	17.1
T2.3	Tadlac Cave	2.9	534.3	42.4	15.8	0.0	<1.72	43.8	16.7	20.7	2.3	6.9	24.4	<0.68	53.8
T2.4	Tadlac Cave	2.4	552.7	44.6	14.3	0.0	2.9	43.4	16.8	21.7	2.3	7.2	22.6	<0.66	66.9
T2.5	Tadlac Cave	3.9	672.3	54.2	8.6	0.0	<1.7	19.3	16.0	26.2	2.5	9.3	26.3	<0.6	23.9
T2.6	Tadlac Cave	6.2	536.8	43.8	14.2	0.0	2.7	39.3	16.5	19.7	2.0	7.2	25.2	<0.7	15.7
T2.7	Tadlac Cave	3.9	642.4	52.7	8.6	0.0	3.7	12.9	15.5	30.1	2.6	8.9	27.2	<0.6	22.2
T2.8	Tadlac Cave	1.6	514.6	42.6	16.3	0.0	<1.72	34.8	17.6	22.9	2.1	7.3	23.4	<0.67	17.5
T2.9	Tadlac Cave	2.7	517.2	45.0	15.8	0.0	2.2	31.2	16.6	21.1	2.4	7.4	24.5	<0.66	17.4
T35	Alitagtag	3.9	579.5	48.8	8.0	0.0	1.8	14.8	15.3	26.3	2.4	8.1	26.7	<0.6	20.3
T36	Alitagtag	3.7	583.9	49.4	7.9	0.0	<1.7	12.8	16.7	25.6	2.7	8.1	24.3	<0.6	20.9
T2.11	Alitagtag	2.9	595.6	44.5	8.7	0.0	3.5	18.7	16.4	27.5	2.4	8.2	26.3	<0.61	19.5
T2.12	Alitagtag	3.7	589.5	50.3	12.3	0.0	2.4	33.7	17.4	25.5	2.1	7.9	26.9	<0.6	19.2
T2.13	Alitagtag	3.0	632.2	53.7	7.4	0.0	2.9	23.9	17.3	24.8	2.5	8.0	25.3	<0.60	77.6
T3.17	Alitagtag	3.6	595.2	49.5	7.9	0.0	<1.7	24.2	15.8	28.5	2.2	7.9	25.2	<0.6	19.9
T3.19A	Alitagtag	4.1	611.4	48.8	8.5	0.0	2.5	12.8	15.1	25.7	2.4	8.6	25.6	<0.6	19.8
T3.19B	Alitagtag	2.3	456.5	39.6	17.7	0.0	<1.8	38.2	15.0	21.6	1.9	6.7	22.5	<0.7	14.0
T3.22	Alitagtag	2.6	458.2	40.0	17.6	0.0	2.5	27.7	17.1	20.4	1.9	6.7	22.5	<0.7	13.3
T3.23	Alitagtag	2.8	528.9	48.2	14.5	0.0	<1.8	16.9	16.8	22.5	2.1	7.9	21.7	<0.7	16.6
T9	Unknown	2.1	466.4	41.0	26.0	8.2	<1.9	119.9	17.0	20.1	2.3	6.7	19.6	<0.8	14.4
T10	Unknown	4.7	657.6	52.0	6.4	<0.6	2.0	10.5	16.0	31.5	3.1	10.3	28.5	<0.6	22.3
T21	Unknown	4.3	664.5	58.4	14.5	<0.7	2.4	63.7	16.3	31.2	2.7	8.7	26.4	<0.7	19.9

Sample	Unit	As	Ba	Ce	Co	Cr	Cs	Cu	Ga	La	Mo	Nb	Nd	Ni	Pb
T21	Unknown	3.7	674.1	57.3	17.3	<0.7	4.1	64.4	17.1	29.0	2.8	8.6	28.0	<0.7	19.0
T47	Unknown	2.1	306.2	24.7	21.7	12.3	<1.8	75.3	18.3	11.2	1.6	5.6	15.6	4.1	11.0
T48	Unknown	3.6	477.7	41.6	20.3	0.9	2.5	85.8	18.5	20.2	2.3	7.6	20.8	<0.7	16.5
T54	Unknown	4.7	656.1	56.1	18.2	<0.7	4.6	100.3	18.0	29.5	2.6	9.6	26.6	1.1	22.6
T58	Unknown	3.3	438.8	44.5	26.7	11.6	<1.8	145.1	18.4	21.0	2.1	6.9	20.0	<0.8	14.8
T70	Unknown	3.1	425.5	36.1	29.1	20.1	<1.9	159.0	18.7	21.9	2.1	6.4	16.0	0.9	13.6
T71	Unknown	12.7	392.8	31.3	17.7	5.1	<1.9	41.7	19.3	14.9	1.9	6.9	16.8	<0.7	31.5
T75	Unknown	3.8	579.2	47.9	10.1	<0.6	<1.8	21.9	16.3	24.6	2.7	8.6	23.9	<0.6	19.1
T2.1	Unknown	2.9	644.5	51.0	9.8	<0.63	5.8	26.4	15.4	28.0	2.5	9.1	25.3	<0.57	49.1
T2.10	Unknown	4.1	533.7	48.2	14.4	<0.7	4.4	50.7	17.8	27.2	2.0	7.5	23.5	<0.7	18.5
T2.14	Unknown	3.7	618.0	50.1	6.6	<0.63	3.6	20.7	14.2	28.6	2.6	8.2	25.0	<0.58	22.3
T2.15	Unknown	3.8	545.7	55.7	18.1	<0.7	<1.8	58.6	17.7	25.1	2.7	8.8	25.8	<0.7	17.8
T2.16	Unknown	3.6	563.3	51.5	18.2	<0.71	3.1	63.0	17.0	29.6	3.2	9.4	24.5	<0.73	19.7
T2.17	Unknown	3.6	462.9	38.8	26.8	7.1	<1.84	128.5	17.7	21.4	2.5	7.6	20.0	<0.77	16.4
T2.18	Unknown	5.1	581.1	51.7	15.1	<0.70	2.3	63.0	18.0	28.3	3.0	9.5	26.2	<0.71	22.0
T2.19	Unknown	3.5	605.9	54.2	16.1	<0.68	2.8	46.2	17.8	28.0	2.6	8.2	26.8	<0.69	20.1
T2.20	Unknown	2.3	427.7	41.0	30.5	12.8	1.9	159.8	18.6	18.5	2.4	6.4	17.8	1.7	16.4
T2.24	Unknown	4.0	626.3	46.2	26.8	4.4	2.4	128.7	19.3	15.7	1.9	6.4	20.9	<0.7	14.1
T2.25(12)	Unknown	5.2	753.8	47.7	26.2	<0.7	<1.8	135.0	18.6	24.8	1.5	6.4	21.7	<0.7	17.4
T2.25(19)	Unknown	4.5	718.6	46.1	26.4	<0.7	<1.8	133.8	19.5	22.3	1.5	6.6	24.6	1.0	16.7
T2.26	Unknown	3.9	518.1	44.1	22.6	<0.7	2.8	120.1	18.5	24.2	1.8	6.7	21.9	<0.7	15.7
T2.26-R	Unknown	4.3	524.3	39.9	24.9	0.8	4.2	119.6	18.6	23.4	1.9	6.7	18.5	<0.7	16.0
T2.27	Unknown	4.8	592.8	46.2	21.4	<0.7	2.8	76.2	18.1	26.1	2.7	7.8	23.2	<0.7	19.1
T2.29	Unknown	7.3	730.5	60.7	20.0	<0.7	4.9	92.9	17.4	30.3	1.9	8.4	25.0	0.7	18.9
T2.30	Unknown	4.9	655.4	48.2	26.3	2.6	<1.7	91.0	17.2	30.8	1.4	7.2	27.1	0.9	16.1
T2.31	Unknown	7.0	800.2	40.2	29.1	11.1	<1.7	49.2	19.6	22.6	1.7	6.9	25.0	6.0	15.4

Sample	Unit	As	Ba	Ce	Co	Cr	Cs	Cu	Ga	La	Mo	Nb	Nd	Ni	Pb
T2.32	Unknown	5.2	388.3	55.6	15.0	<0.7	3.1	45.5	20.8	34.3	1.4	8.5	28.5	<0.7	21.8
T2.37	Unknown	28.8	427.9	31.3	23.3	17.8	6.3	190.0	19.6	15.2	2.8	6.5	16.9	<0.8	14.3
T2.38A	Unknown	3.8	551.2	54.1	21.8	<0.70	<1.79	44.4	18.4	28.5	2.7	7.6	24.9	<0.73	15.6
T2.38B	Unknown	2.9	550.4	49.1	20.8	<0.70	4.4	44.6	17.3	26.1	2.9	7.8	21.8	<0.73	15.4
T2.45	Unknown	5.0	445.1	41.6	26.3	7.4	2.7	144.1	18.1	19.1	2.4	6.4	21.3	<0.77	13.9
T2.48	Unknown	2.9	569.8	54.1	19.1	<0.71	4.0	44.8	17.2	27.3	2.4	7.5	25.0	<0.73	16.6
T2.49	Unknown	2.9	518.8	47.1	24.0	0.7	<1.82	147.7	18.5	24.7	2.6	7.3	20.8	<0.75	14.8
T2.57	Unknown	5.5	509.0	37.4	27.5	10.9	3.6	105.1	18.3	22.2	1.9	6.8	17.8	<0.8	14.8
T2.57-R	Unknown	5.0	501.9	40.2	24.8	14.0	<1.8	104.3	18.5	23.5	2.0	6.9	18.2	1.3	14.9
T2.58	Unknown	5.2	474.8	45.3	26.6	8.1	4.3	119.6	19.6	21.7	1.8	7.1	21.1	<0.8	16.1
T2.62	Unknown	4.1	538.4	46.5	22.4	<0.7	3.1	50.9	18.0	24.1	2.4	8.6	19.9	<0.7	16.7
T2.71	Unknown	1.6	425.5	41.1	20.0	8.1	2.9	52.7	17.7	18.8	2.0	6.5	20.2	<0.7	14.6
T2.72	Unknown	2.9	454.7	40.2	22.0	<0.7	2.2	55.9	18.4	18.3	2.0	6.9	21.7	<0.7	14.6
T2.73	Unknown	2.5	445.6	40.2	20.7	<0.7	<1.8	34.8	17.9	20.1	2.2	6.8	19.9	<0.7	13.7
T2.79A	Unknown	0.7	426.6	36.9	30.7	16.3	<1.82	150.3	18.5	18.3	2.0	6.3	16.9	<0.80	8.3
T2.79B	Unknown	4.7	426.8	40.9	21.7	6.6	<1.72	29.9	18.5	19.8	2.4	7.5	18.6	<0.75	15.6
T2.80	Unknown	1.5	425.9	37.9	31.6	14.3	<1.84	156.4	18.2	19.5	2.5	6.2	16.5	2.2	12.0
T2.84	Unknown	1.8	424.4	35.6	27.4	11.5	<1.76	154.9	17.9	15.3	2.8	6.2	14.4	<0.78	16.3
T2.85	Unknown	2.9	432.9	38.0	24.2	3.2	2.9	174.7	19.6	21.3	2.0	6.6	18.4	<0.8	14.2
T2.87	Unknown	2.6	472.3	39.9	26.3	8.8	<1.8	125.5	18.4	22.0	2.4	6.5	20.0	<0.8	14.3
T2.90	Unknown	2.9	441.5	36.8	22.8	1.5	<1.79	73.3	17.6	16.4	1.7	6.5	17.9	<0.72	14.7
T2.93	Unknown	4.1	514.5	41.6	21.3	1.7	4.9	102.0	17.6	21.2	2.5	7.4	18.5	<0.74	15.7
T2.94	Unknown	3.7	456.3	41.9	32.0	5.9	3.8	140.4	18.7	20.7	2.6	7.3	18.6	<0.79	14.8
T2.95	Unknown	6.7	510.1	44.3	24.3	<0.71	<1.79	109.7	18.1	21.2	2.3	7.2	21.6	<0.76	20.0
T2.104A	Unknown	2.7	519.6	43.0	18.0	<0.69	2.1	47.0	17.4	21.0	2.5	7.4	20.3	<0.69	18.8
T2.104B	Unknown	2.8	504.9	40.0	17.4	<0.68	<1.73	60.0	17.1	21.1	2.4	7.4	18.7	<0.71	18.2

Sample	Unit	As	Ba	Ce	Co	Cr	Cs	Cu	Ga	La	Mo	Nb	Nd	Ni	Pb
T2.105	Unknown	2.9	513.9	42.3	18.6	<0.67	3.8	31.1	17.0	20.7	2.7	7.7	20.6	<0.68	17.7
T3.3A	Unknown	2.2	466.1	45.6	16.0	<0.7	<1.8	14.6	16.8	24.4	2.1	6.8	22.8	<0.7	14.8
T3.3B	Unknown	3.3	664.4	54.5	6.7	<0.7	5.5	8.2	16.0	27.6	2.9	9.4	27.5	<0.6	21.0
T3.8B	Unknown	3.9	504.5	43.9	15.7	<0.7	<1.8	21.2	17.8	22.5	2.2	8.1	22.4	<0.7	16.7
T3.9B	Unknown	1.6	437.3	35.1	25.3	6.1	<1.9	129.4	17.8	20.1	1.8	6.2	19.6	<0.8	12.6
T3.14A	Unknown	3.9	448.9	44.1	26.0	4.2	4.5	135.4	16.8	19.6	2.2	7.7	26.2	<0.8	15.0
T3.14A-R	Unknown	3.9	449.0	47.7	27.9	4.6	1.5	135.3	16.5	27.5	2.2	7.7	20.6	<0.8	15.3
T3.14B	Unknown	3.9	667.5	56.1	7.9	<0.7	4.0	11.4	16.3	30.4	2.8	9.8	26.5	<0.6	21.2
T3.24A	Unknown	2.8	546.8	49.6	15.3	<0.7	2.0	54.3	17.5	23.0	2.4	7.8	23.6	<0.7	17.9
T3.24B	Unknown	2.4	480.1	45.4	18.8	<0.7	<1.8	75.7	18.2	19.8	1.9	7.3	20.8	<0.7	17.0
2020 ASH	Unknown	6.4	458.5	47.3	21.4	13.3	<1.9	137.8	17.8	23.7	2.3	6.9	24.6	3.3	14.2

Table D3 – Second half of trace element data in ppm

Sample	Unit	Rb	Sb	Sc	Se	Sn	Sr	Th	U	V	W	Y	Zn	Zr
T59	Buco	49.5	<1.1	26.2	<0.7	<1.0	318.5	8.1	2.1	271.7	<1.3	26.9	89.4	123.1
T66	Buco	53.7	<1.1	24.4	<0.7	<1.0	313.5	9.1	2.3	221.4	1.5	30.4	90.5	137.6
T69 - DARK	Buco	69.6	<1.0	18.7	<0.6	<1.0	276.7	11.0	2.6	85.6	2.4	35.4	93.6	176.0
T69 - LIGHT	Buco	68.2	<1.0	18.4	<0.6	<1.0	270.1	10.2	2.7	88.1	<1.1	34.7	94.5	172.1
T2.40	Buco	50.2	<1.1	25.6	<0.7	<1.0	309.9	8.2	1.8	250.3	<1.2	28.5	90.7	128.0
T2.42	Buco	52.5	<1.11	24.1	<0.71	<1.03	321.2	7.6	2.2	248.0	1.4	27.5	91.3	130.6
T2.43	Buco	52.3	<1.11	25.6	<0.72	<1.03	321.1	7.5	2.1	253.4	<1.24	27.0	90.0	129.6
T2.46	Buco	50.4	<1.1	26.9	<0.7	<1.0	335.2	8.1	1.6	249.1	<1.3	30.0	88.9	126.2
T2.47	Buco	50.6	<1.1	26.9	<0.7	<1.0	320.3	7.6	2.1	249.0	<1.2	27.1	87.7	125.3
T2.50A	Buco	52.7	<1.11	27.2	<0.71	<1.02	321.1	7.0	1.6	258.5	<1.24	27.6	90.6	129.7
T2.50A-R	Buco	52.1	<1.09	25.4	<0.71	<1.03	322.2	8.5	2.2	253.2	<1.24	27.6	89.2	130.1

Sample	Unit	Rb	Sb	Sc	Se	Sn	Sr	Th	U	V	W	Y	Zn	Zr
T2.50B	Buco	53.3	<1.11	25.1	<0.72	<1.03	319.6	8.3	2.5	245.3	<1.25	27.6	91.1	132.9
T2.52	Buco	54.1	<1.1	25.8	<0.7	<1.0	304.2	7.8	2.7	249.6	1.4	28.3	89.6	125.5
T2.53	Buco	53.5	<1.10	24.0	<0.70	<1.01	317.9	8.4	2.8	223.3	<1.22	28.5	94.6	135.0
T2.54	Buco	52.9	<1.10	23.5	<0.71	<1.02	322.7	8.6	2.5	224.8	<1.23	28.1	91.0	132.2
T2.56	Buco	53.0	<1.10	24.7	<0.71	<1.02	321.1	7.7	2.8	236.0	<1.23	28.0	90.9	131.7
T2.61	Buco	51.4	<1.11	26.6	<0.71	<1.03	322.7	6.7	2.1	265.5	<1.24	26.5	90.7	127.6
T2.78	Buco	70.0	<1.03	17.5	<0.66	2.0	267.5	11.2	3.2	75.3	1.4	35.5	93.5	181.6
T2.81	Buco	54.9	1.2	23.1	<0.67	<0.98	282.3	8.3	2.7	158.9	<1.15	33.4	90.3	155.3
T2.82	Buco	36.2	<1.08	30.2	<0.70	<1.01	337.0	5.2	1.0	216.6	<1.22	25.0	80.7	105.2
T2.101	Buco	53.1	<1.09	31.8	<0.72	<1.02	298.4	8.1	2.2	252.3	<1.24	27.9	88.8	135.2
T3.4	Buco	50.5	<1.1	24.6	<0.7	<1.0	322.8	7.2	2.2	257.5	<1.3	27.4	89.0	125.7
T3.10	Buco	50.5	<1.1	26.5	<0.7	<1.0	326.6	7.6	1.9	274.5	<1.3	27.9	90.1	126.1
T3.11A	Buco	48.4	<1.1	24.4	<0.7	<1.0	327.9	7.7	2.3	289.9	<1.3	27.8	91.1	123.3
T3.11B	Buco	49.7	<1.1	27.5	<0.7	1.2	328.1	7.3	2.1	290.0	<1.3	27.9	90.3	124.2
T24	Tagaytay	74.6	<1.0	16.6	<0.6	<0.9	218.0	12.4	3.3	22.1	2.2	40.0	90.0	201.1
T25	Tagaytay	55.1	<1.1	27.5	<0.7	<1.0	306.9	8.9	1.7	204.0	<1.2	36.3	97.5	150.4
T42	Tagaytay	68.2	<0.9	17.2	<0.6	1.0	233.7	9.4	3.2	19.8	<1.0	37.9	89.7	175.9
T49	Tagaytay	47.9	<1.1	27.9	<0.7	<1.0	301.1	7.5	2.5	192.3	1.6	31.7	94.0	129.2
T51A	Tagaytay	56.5	<1.0	19.7	<0.6	<1.0	293.3	8.1	2.3	75.5	2.1	33.2	94.5	149.0
T2.68	Tagaytay	67.5	<1.1	23.9	<0.7	<1.0	298.6	9.8	2.6	194.5	1.6	34.5	93.5	174.6
T2.69	Tagaytay	50.0	<1.0	25.1	-0.3	<1.0	293.6	7.2	1.6	135.5	1.8	30.9	92.8	135.2
T2.70	Tagaytay	33.8	<1.1	31.4	<0.7	<1.0	351.2	4.9	1.9	204.9	<1.2	23.0	80.0	88.2
T2.74	Tagaytay	67.4	<1.0	17.9	<0.6	<0.9	237.1	10.0	2.9	62.4	1.4	37.9	85.2	189.9
T2.83	Tagaytay	66.6	<1.09	23.1	<0.72	<1.03	274.3	10.5	2.9	178.7	1.5	36.2	102.5	171.5
T2.89	Tagaytay	65.0	<0.96	16.6	<0.60	1.2	255.4	9.6	2.8	36.4	<1.03	37.2	88.5	177.1
T2.76A	Balagbag	54.6	<1.14	28.2	<0.74	<1.05	295.5	8.6	2.2	294.6	1.3	30.9	95.0	145.7

Sample	Unit	Rb	Sb	Sc	Se	Sn	Sr	Th	U	V	W	Y	Zn	Zr
T2.76B	Balagbag	60.2	<1.1	24.9	<0.7	<1.0	291.6	9.1	2.7	230.5	<1.3	31.3	91.8	144.7
T2.77	Balagbag	60.2	<1.1	27.8	<0.7	<1.0	282.3	8.8	2.1	255.9	1.9	32.1	92.9	151.9
T2.99	Balagbag	61.1	<1.11	26.0	0.9	1.1	275.4	9.7	2.7	246.8	3.3	39.1	94.4	162.1
T2.100	Balagbag	55.6	<1.12	27.2	<0.73	<1.05	289.2	9.1	2.5	282.0	<1.28	31.5	94.0	148.4
T2.75	Burol	54.8	<1.13	27.4	<0.73	<1.04	290.7	9.0	3.0	260.1	<1.27	33.4	91.7	146.2
T2.92	Burol	51.5	<1.11	28.4	<0.73	<1.05	305.5	8.6	2.5	281.0	<1.27	30.2	95.8	140.7
T2.96	Burol	56.6	<1.02	16.9	<0.65	1.4	280.3	9.2	2.5	135.7	<1.11	30.6	87.7	150.9
T2.97	Burol	51.1	<1.08	27.2	<0.70	<1.01	292.4	7.9	2.4	270.3	<1.21	31.9	81.8	134.1
T2.98	Burol	55.1	<1.11	27.9	<0.73	1.7	290.7	9.3	3.4	264.8	3.0	32.1	93.9	147.1
T13	Pasong	50.9	<1.1	24.8	<0.7	<1.0	321.5	7.4	2.2	261.1	2.2	27.2	91.3	126.4
T15	Pasong	55.9	<1.1	24.5	<0.7	<1.0	312.2	8.1	2.5	219.0	2.7	28.6	90.2	140.5
T62	Pasong	43.2	<1.1	29.5	<0.7	<1.1	341.7	6.4	1.9	304.1	<1.3	26.3	90.7	111.6
T63	Pasong	42.8	<1.1	29.8	<0.7	<1.1	335.2	6.6	1.7	295.5	<1.3	25.9	90.5	112.4
T79	Pasong	52.7	<1.1	26.4	<0.7	<1.0	323.0	8.4	2.4	249.1	<1.3	27.9	89.9	131.9
T2.21	Pasong	53.1	<1.1	26.0	<0.7	<1.0	326.4	9.0	2.6	250.9	<1.3	28.7	91.7	132.4
T2.66	Pasong	54.0	<1.1	28.0	<0.7	<1.0	329.4	6.8	2.6	284.4	<1.3	27.7	89.2	119.2
T2.67	Pasong	51.9	<1.1	27.1	<0.7	<1.0	324.3	7.7	2.2	268.9	<1.3	27.9	90.5	128.4
T2.86	Pasong	51.8	<1.1	26.7	<0.7	<1.0	323.0	8.0	2.2	257.9	<1.3	27.8	90.4	129.7
T3.1	Pasong	50.5	<1.1	25.3	<0.7	<1.0	325.0	7.9	2.4	272.1	<1.3	27.4	91.7	125.3
T3.2A	Pasong	49.8	1.1	25.3	<0.7	<1.0	321.4	7.6	1.7	269.7	<1.3	28.5	91.8	127.9
T3.12	Pasong	51.2	<1.1	25.0	<0.7	<1.0	322.2	8.7	2.5	261.6	<1.3	28.1	89.5	129.0
T3.13	Pasong	52.4	<1.1	23.8	<0.7	<1.0	322.8	8.5	2.6	254.7	<1.3	28.4	90.9	130.9
T3.16	Pasong	49.4	1.2	26.7	<0.7	<1.0	323.9	7.3	2.4	281.5	<1.3	27.4	90.1	124.5
T3.20	Pasong	69.8	<1.1	23.0	<0.7	<1.0	311.8	9.1	2.8	203.5	<1.2	31.8	92.8	170.3
T3.21	Pasong	39.2	<1.1	27.3	<0.7	<1.0	338.9	6.1	2.2	329.1	<1.3	25.9	89.2	103.3
T27	Indang	49.1	<1.0	23.6	<0.7	1.0	314.6	7.4	2.7	169.5	<1.2	38.7	87.3	135.6

Sample	Unit	Rb	Sb	Sc	Se	Sn	Sr	Th	U	V	W	Y	Zn	Zr
T28	Indang	59.5	<1.0	21.6	<0.6	<0.9	273.5	8.4	2.5	97.5	1.7	36.8	85.2	162.7
T31	Indang	47.6	<1.1	22.5	<0.7	5.6	357.9	7.1	2.5	142.3	<1.2	32.0	93.6	128.9
T2.33	Indang	55.8	<1.1	23.3	<0.7	<1.0	339.3	7.5	2.3	170.8	<1.2	31.0	90.3	150.2
T2.35	Indang	54.8	<1.1	25.7	<0.7	<1.0	334.4	7.8	2.4	178.2	2.1	30.4	89.7	146.0
T2.64	Indang	79.0	<1.1	20.4	<0.6	1.8	290.3	10.9	3.6	128.6	<1.2	34.2	93.0	192.8
T2.65	Indang	82.4	<1.0	24.9	<0.6	<1.0	308.3	8.4	2.4	211.8	<1.2	31.3	84.9	152.6
T2.88	Indang	66.0	<1.05	22.5	0.9	<0.98	318.1	8.5	2.6	132.3	<1.16	34.1	91.9	175.8
T2.88-R	Indang	66.0	<1.04	22.2	<0.67	<0.98	317.1	8.8	2.9	131.1	<1.16	33.7	91.2	174.4
T4-WB	Tadlac Cave	57.3	<1.0	16.4	<0.6	<1.0	260.7	8.4	2.5	101.3	2.6	34.0	88.0	157.9
T4-WT	Tadlac Cave	47.2	<1.0	21.8	<0.7	<1.0	308.6	6.8	2.2	152.4	2.5	30.4	87.7	128.6
T4-BB	Tadlac Cave	56.9	<1.0	17.8	<0.6	<1.0	276.9	8.5	2.9	102.9	<1.1	34.7	90.3	155.4
T4-BT	Tadlac Cave	52.7	<1.0	19.0	<0.7	<1.0	295.2	8.3	2.4	124.4	<1.2	33.1	90.2	143.5
T2.3	Tadlac Cave	52.7	<1.04	19.0	<0.66	<0.96	295.6	7.6	2.7	111.9	1.8	33.4	91.4	143.2
T2.4	Tadlac Cave	54.7	<1.03	19.3	<0.66	<0.95	277.2	9.1	3.4	103.1	1.2	33.3	94.6	147.4
T2.5	Tadlac Cave	77.5	<1.0	13.0	<0.6	1.3	192.1	11.3	3.6	31.1	<1.1	40.3	78.9	208.8
T2.6	Tadlac Cave	57.3	<1.0	17.8	<0.6	<0.9	274.8	7.3	1.8	98.1	2.2	33.6	82.7	151.3
T2.7	Tadlac Cave	74.8	<1.0	14.0	<0.6	1.0	211.5	10.9	2.7	32.0	2.1	40.9	83.0	201.3
T2.8	Tadlac Cave	54.9	<1.03	18.0	<0.65	<0.95	281.3	8.0	2.9	105.3	<1.11	34.0	87.2	149.0
T2.9	Tadlac Cave	54.9	<1.02	19.1	<0.64	1.2	271.0	8.3	2.6	108.9	<1.09	33.7	84.4	148.9
T35	Alitagtag	70.6	<1.0	15.4	<0.6	0.9	217.0	9.8	2.7	36.5	1.4	36.6	80.6	179.7
T36	Alitagtag	70.9	<1.0	13.4	<0.6	<0.9	220.7	9.3	2.5	33.3	1.9	36.7	81.7	181.2
T2.11	Alitagtag	71.6	<0.97	15.4	<0.61	<0.90	218.6	9.0	2.3	33.8	1.1	37.5	81.6	180.9
T2.12	Alitagtag	68.2	<1.0	16.8	<0.6	<0.9	229.6	9.6	2.8	54.2	2.1	39.8	81.9	174.4
T2.13	Alitagtag	71.1	1.1	14.1	<0.61	1.3	220.0	10.6	3.3	32.7	1.4	37.0	86.9	180.1
T3.17	Alitagtag	69.1	<1.0	15.5	<0.6	1.6	214.7	9.8	2.5	44.1	1.9	37.0	81.3	174.7
T3.19A	Alitagtag	70.9	<1.0	14.2	<0.6	2.8	230.4	9.8	3.4	36.6	1.7	37.0	76.1	190.3

Sample	Unit	Rb	Sb	Sc	Se	Sn	Sr	Th	U	V	W	Y	Zn	Zr
T3.19B	Alitagtag	49.9	<1.0	21.7	<0.6	<1.0	344.6	7.8	2.5	151.6	1.3	32.0	83.8	134.0
T3.22	Alitagtag	50.0	<1.1	21.1	<0.6	<1.0	340.7	7.1	2.2	157.4	<1.2	33.0	90.8	134.5
T3.23	Alitagtag	59.8	<1.0	21.3	1.0	1.1	287.1	8.4	2.8	117.1	1.7	34.5	84.5	160.3
T9	Unknown	52.7	<1.1	25.7	<0.7	<1.0	317.3	7.7	1.9	241.3	<1.3	28.0	87.7	133.0
T10	Unknown	85.5	<0.9	16.1	<0.6	1.1	195.1	11.9	3.4	9.9	3.3	41.6	75.0	232.6
T21	Unknown	78.5	<1.0	17.8	<0.6	<1.0	257.8	12.5	3.2	68.3	1.9	34.9	90.2	191.7
T21	Unknown	79.2	<1.0	17.1	<0.6	<1.0	258.8	11.7	3.1	69.0	<1.2	35.1	90.4	191.7
T47	Unknown	32.7	<1.0	32.3	<0.7	<1.0	330.7	5.7	1.6	237.2	<1.2	26.3	70.1	109.6
T48	Unknown	61.5	<1.0	23.1	0.8	<1.0	315.5	7.6	1.9	210.0	1.2	29.9	84.8	153.8
T54	Unknown	77.2	<1.0	19.9	<0.7	4.7	246.1	12.1	3.1	114.1	2.7	40.5	99.3	204.4
T58	Unknown	46.0	<1.1	29.9	<0.7	<1.0	287.4	7.7	2.4	275.4	<1.3	28.9	88.2	133.7
T70	Unknown	47.2	<1.1	29.8	<0.7	<1.1	313.8	7.5	2.5	330.0	<1.3	27.4	91.6	121.0
T71	Unknown	52.6	<1.1	25.6	<0.7	1.5	362.7	6.3	1.6	238.2	<1.2	25.8	66.2	129.9
T75	Unknown	70.0	<0.9	16.2	<0.6	<0.9	239.6	9.9	2.7	66.8	2.3	34.9	77.8	184.1
T2.1	Unknown	76.6	<0.94	14.1	<0.58	1.1	180.7	11.1	3.3	28.0	1.4	35.6	82.6	203.4
T2.10	Unknown	64.0	<1.0	20.8	<0.6	1.0	283.8	9.1	2.8	101.9	2.3	31.8	79.7	160.2
T2.14	Unknown	77.7	<0.94	13.2	<0.58	0.9	185.4	10.4	2.9	22.0	2.9	43.6	78.0	191.1
T2.15	Unknown	72.1	1.2	24.1	<0.7	2.0	286.4	9.3	2.3	146.5	1.9	37.1	98.0	188.1
T2.16	Unknown	76.3	<1.08	21.6	<0.69	2.3	274.0	10.4	2.5	126.1	2.1	37.0	96.2	200.8
T2.17	Unknown	58.7	<1.11	24.8	<0.72	2.7	331.9	8.8	2.8	280.4	2.2	28.1	90.6	146.8
T2.18	Unknown	78.8	<1.07	21.8	<0.68	2.8	292.3	11.3	3.4	131.0	<1.18	34.0	92.9	193.3
T2.19	Unknown	68.6	<1.05	19.6	<0.67	1.6	279.7	10.8	3.3	101.2	3.3	34.9	93.1	175.3
T2.20	Unknown	47.4	<1.14	29.6	<0.74	<1.06	318.6	7.8	2.5	332.5	<1.30	27.5	93.7	122.9
T2.24	Unknown	40.7	<1.1	28.9	<0.7	<1.0	344.8	8.6	2.2	226.5	<1.2	29.6	88.1	128.7
T2.25(12)	Unknown	54.2	<1.1	27.0	<0.6	<1.0	317.0	8.4	1.7	176.0	1.6	28.6	83.8	134.3
T2.25(19)	Unknown	54.8	<1.1	28.3	<0.7	<1.0	319.4	9.3	2.7	177.2	<1.2	29.6	82.9	137.7

Sample	Unit	Rb	Sb	Sc	Se	Sn	Sr	Th	U	V	W	Y	Zn	Zr
T2.26	Unknown	51.6	<1.1	24.1	<0.7	<1.0	358.1	8.1	1.3	203.2	<1.2	31.1	90.9	140.2
T2.26-R	Unknown	51.6	<1.1	25.0	<0.7	<1.0	357.3	8.4	2.0	203.6	<1.2	30.7	90.3	140.3
T2.27	Unknown	61.8	<1.1	22.0	<0.7	1.9	283.0	10.2	2.1	163.1	1.8	33.4	96.6	162.5
T2.29	Unknown	65.1	<1.1	24.0	<0.6	<1.0	279.2	11.0	2.5	127.2	<1.2	34.5	96.5	180.8
T2.30	Unknown	50.0	<1.0	27.4	<0.6	<0.9	216.2	8.0	2.1	170.3	1.3	39.8	87.9	141.7
T2.31	Unknown	63.0	<1.0	28.4	<0.6	<1.0	228.4	7.7	1.7	197.2	1.8	42.1	88.3	140.0
T2.32	Unknown	37.3	<1.0	26.2	<0.6	<0.9	169.3	10.8	2.2	139.1	2.0	38.9	85.2	185.0
T2.37	Unknown	46.8	<1.1	27.7	<0.7	<1.1	338.7	7.7	2.5	493.2	<1.3	26.0	89.1	124.7
T2.38A	Unknown	63.9	<1.09	19.5	<0.70	2.0	302.3	9.7	2.9	123.9	1.6	32.7	96.7	158.7
T2.38B	Unknown	64.0	<1.06	20.3	<0.69	<1.00	301.2	9.9	2.2	118.1	<1.19	33.4	97.2	159.0
T2.45	Unknown	66.0	<1.11	27.2	<0.72	<1.02	347.1	7.2	2.3	286.7	<1.24	27.3	90.5	125.8
T2.48	Unknown	66.6	<1.08	22.4	<0.70	<1.00	290.2	10.8	3.7	130.8	<1.20	33.1	98.7	164.7
T2.49	Unknown	59.8	<1.10	23.9	<0.70	<1.01	315.1	9.0	2.2	199.6	<1.22	30.0	91.1	147.4
T2.57	Unknown	51.4	<1.1	28.8	<0.7	<1.0	306.7	8.1	2.7	224.2	<1.2	27.8	87.9	130.9
T2.57-R	Unknown	51.3	1.2	28.9	<0.7	<1.0	306.9	7.0	1.6	222.6	1.6	28.0	85.8	130.4
T2.58	Unknown	51.4	<1.1	31.8	<0.7	<1.0	248.9	8.7	2.4	195.0	<1.3	33.4	97.3	144.9
T2.62	Unknown	61.2	<1.1	25.9	<0.7	<1.0	309.5	8.0	1.9	149.9	<1.2	33.7	97.4	165.6
T2.71	Unknown	46.1	<1.1	24.9	1.0	<1.0	346.5	7.0	2.6	202.1	1.8	30.6	87.5	124.0
T2.72	Unknown	49.8	<1.0	25.0	<0.6	<1.0	325.3	6.9	1.9	194.5	1.3	30.9	85.1	133.1
T2.73	Unknown	48.2	<1.0	25.0	0.8	<1.0	330.4	6.3	1.6	190.1	1.8	32.0	87.1	131.2
T2.79A	Unknown	47.8	<1.13	27.8	<0.74	<1.06	320.1	7.5	2.4	323.3	<1.29	28.0	89.8	124.2
T2.79B	Unknown	55.2	<1.08	24.9	<0.70	<1.01	352.7	7.1	2.2	185.1	<1.21	31.1	90.7	147.4
T2.80	Unknown	46.6	<1.12	30.1	<0.74	<1.05	316.2	6.5	1.9	322.7	<1.29	27.5	89.6	121.6
T2.84	Unknown	47.7	<1.11	27.4	<0.72	<1.04	333.6	7.7	1.7	283.2	1.5	26.2	88.5	119.8
T2.85	Unknown	50.3	<1.1	33.8	<0.7	<1.1	308.7	7.9	2.5	313.3	1.8	30.6	98.7	128.7
T2.87	Unknown	52.9	<1.1	26.5	<0.7	<1.0	319.9	8.2	2.3	252.7	1.6	28.1	93.8	131.1

Sample	Unit	Rb	Sb	Sc	Se	Sn	Sr	Th	U	V	W	Y	Zn	Zr
T2.90	Unknown	47.8	1.2	28.2	<0.69	1.2	305.1	7.0	2.3	198.3	<1.19	31.7	89.5	129.3
T2.93	Unknown	60.2	<1.07	23.0	<0.69	3.9	302.5	9.4	2.4	221.9	<1.20	29.7	89.6	158.4
T2.94	Unknown	52.4	<1.11	27.6	<0.73	<1.05	307.3	7.9	1.5	285.1	1.4	30.5	97.4	141.9
T2.95	Unknown	54.4	<1.08	25.4	<0.70	2.1	298.3	9.0	2.2	221.2	<1.22	32.2	95.9	152.1
T2.104A	Unknown	57.5	1.8	23.8	<0.66	2.4	276.7	8.8	3.3	150.6	<1.14	33.9	90.9	159.6
T2.104B	Unknown	55.9	<1.05	23.8	<0.67	<0.98	284.7	8.3	1.9	158.8	1.2	33.5	91.7	157.6
T2.105	Unknown	57.2	<1.02	22.2	<0.65	1.2	262.8	8.2	2.5	129.6	<1.12	33.2	87.2	161.9
T3.3A	Unknown	49.2	1.7	22.6	<0.6	1.4	350.2	7.2	2.3	119.0	<1.2	33.7	92.9	133.7
T3.3B	Unknown	77.1	<0.9	14.0	<0.6	1.2	208.8	11.1	3.4	18.8	<1.0	38.7	76.4	205.8
T3.8B	Unknown	62.4	<1.1	22.7	0.9	<1.0	327.9	7.8	2.4	150.7	1.3	34.3	92.3	167.0
T3.9B	Unknown	47.6	<1.1	28.2	<0.7	<1.0	323.2	8.0	2.1	275.7	<1.3	27.3	89.5	123.1
T3.14A	Unknown	50.1	<1.1	29.3	<0.7	1.2	296.5	8.3	2.0	297.7	<1.3	32.9	95.9	145.0
T3.14A-R	Unknown	49.8	<1.1	30.4	<0.7	<1.0	296.2	8.1	2.1	284.9	<1.3	33.2	95.7	145.3
T3.14B	Unknown	83.3	1.1	14.3	<0.6	<0.9	206.1	10.7	2.9	16.0	1.7	40.5	76.7	223.9
T3.24A	Unknown	59.2	1.8	22.9	<0.6	<1.0	264.7	7.8	2.5	142.0	2.0	34.9	91.6	162.2
T3.24B	Unknown	53.1	<1.1	23.6	<0.6	<1.0	295.5	7.6	2.3	187.8	<1.2	33.6	93.2	146.7
2020 ASH	Unknown	55.2	<1.1	26.0	1.9	<1.0	300.3	7.6	2.7	267.1	<1.3	31.0	96.8	142.4

Appendix E: Precision and accuracy calculations

Table E1 – Bardon Hill Microgranodiorite data in wt.%

	SiO ₂	TiO ₂	Al ₂ O ₃	Fe ₂ O ₃	MnO	MgO	CaO	Na ₂ O	K ₂ O	P ₂ O ₅
Consensus	68.07	0.43	14.35	5.81	0.14	2.50	3.63	3.94	0.87	0.07
06/12/2018 00:47	68.24	0.38	14.30	5.76	0.14	2.43	3.10	3.78	0.75	0.08
21/11/2018 18:50	68.55	0.39	14.19	5.81	0.14	2.50	3.60	3.68	0.77	0.08
01/11/2018 19:31	68.67	0.39	14.32	5.80	0.14	2.50	3.58	3.67	0.76	0.08
12/12/2018 01:46	68.50	0.38	14.14	5.76	0.14	2.46	3.01	3.31	0.74	0.08
12/12/2018 01:46	68.50	0.38	14.14	5.76	0.14	2.46	3.01	3.31	0.74	0.08
21/02/2019 01:01	68.46	0.41	14.27	5.82	0.14	2.51	3.55	3.66	0.85	0.08
27/06/2019 02:37	68.26	0.41	14.35	5.82	0.14	2.67	3.61	3.67	0.85	0.08
09/05/2018 14:15	68.54	0.41	14.53	5.83	0.14	2.66	3.59	3.63	0.84	0.07
28/05/2019 18:50	68.15	0.42	14.48	5.81	0.14	2.66	3.57	3.68	0.84	0.08
19/06/2019 02:32	68.41	0.41	14.42	5.82	0.14	2.65	3.59	3.68	0.85	0.08
02/07/2019 23:32	68.41	0.41	14.42	5.82	0.14	2.67	3.58	3.68	0.85	0.08
02/07/2019 23:32	68.41	0.41	14.42	5.82	0.14	2.67	3.58	3.68	0.85	0.08
10/09/2020 01:26	68.52	0.42	14.40	5.80	0.14	2.78	3.58	3.77	0.84	0.09
16/07/2020 16:45	68.60	0.41	14.49	5.86	0.14	2.65	3.59	3.87	0.84	0.09
25/08/2020 22:12	68.53	0.41	14.41	5.74	0.14	2.62	3.58	3.79	0.84	0.09

	SiO ₂	TiO ₂	Al ₂ O ₃	Fe ₂ O ₃	MnO	MgO	CaO	Na ₂ O	K ₂ O	P ₂ O ₅
02/09/2020 23:19	68.54	0.41	14.41	5.81	0.14	2.61	3.58	3.76	0.85	0.09
14/10/2020 00:23	68.44	0.39	14.32	5.80	0.14	2.52	3.55	3.72	0.80	0.09
12/11/2020 18:12	68.54	0.41	14.41	5.80	0.14	2.60	3.53	3.92	0.85	0.09
12/11/2020 18:12	68.54	0.41	14.41	5.80	0.14	2.60	3.53	3.92	0.85	0.09
Mean	68.5	0.4	14.4	5.8	0.1	2.6	3.5	3.7	0.8	0.1
Std. Dev.	0.1	0.0	0.1	0.0	0.0	0.1	0.2	0.2	0.0	0.0
% Std. Dev.	0.2	3.6	0.8	0.5	0.5	3.7	5.8	4.3	5.1	6.5
% Uncertainty	0.6	-6.3	0.1	-0.1	-0.9	3.6	-1.1	-6.2	-5.9	18.1

Table E2 – Half of CRB – basalt data in ppm

	As	Ba	Ce	Co	Cr	Cu	Ga	La	Mo	Nb	Nd	Pb
Consensus	0.6	708	53.9	53.5	13.5	19.6	22.2	25.5	1.5	12.7	28.7	13.4
01/12/2018 06:45	1.0	720.4	53.6	39.2	36.5	44.2	22.5	25.9	2.0	13.6	29.9	14.0
10/11/2018 05:30	1.0	728.2	56.3	37.6	36.5	42.9	22.1	28.5	2.3	13.7	30.0	9.7
16/11/2018 18:21	1.4	713.3	53.9	40.5	34.3	42.9	23.9	26.8	1.92	13.50	31.6	10.24
06/11/2018 13:20	0.6	719.3	53.8	40.1	34.3	43.0	22.7	24.8	1.8	13.3	27.7	13.9
14/12/2018 03:38	0.8	722.2	57.2	38.1	35.2	42.9	22.5	25.6	2.0	13.6	31.2	14.3
17/03/2017 23:54	0.4	724.5	54.0	36.5	19.2	42.7	22.6	25.7	2.2	12.2	31.9	14.6
16/02/2019 07:48	0.1	718.3	56.3	38.8	34.7	42.8	22.0	24.9	2.0	13.6	26.9	14.5
28/06/2019 06:54	1.3	722.5	58.1	40.4	35.8	42.5	22.7	25.6	2.1	13.4	29.4	13.1
12/04/2019 00:06	1.3	718.6	56.9	38.8	35.3	42.7	22.0	29.0	2.3	13.6	28.4	14.7
04/06/2019 22:53	1.2	721.5	56.0	37.7	36.3	43.1	21.8	29.4	2.2	13.7	29.0	13.2

	As	Ba	Ce	Co	Cr	Cu	Ga	La	Mo	Nb	Nd	Pb
08/06/2019 01:44	0.4	723.4	56.3	40.0	35.3	43.1	22.4	27.3	2.4	14.0	28.3	14.1
13/07/2019 05:12	0.9	725.6	55.3	40.4	34.8	43.0	22.6	26.2	2.0	13.4	31.7	14.1
17/07/2019 01:30	1.3	727.6	60.0	37.5	34.6	42.4	22.7	26.0	2.1	13.7	26.9	12.5
28/06/2019 06:54	1.3	722.5	58.1	40.4	35.8	42.5	22.7	25.6	2.1	13.4	29.4	13.1
26/09/2020 00:53	0.8	725.3	54.4	37.8	34.5	44.3	22.8	25.5	1.9	13.5	27.9	14.7
27/08/2020 22:20	0.7	731.1	55.6	35.8	34.8	43.9	22.2	29.9	1.9	13.9	31.2	14.2
12/09/2020 04:11	1.3	724.5	53.7	36.8	36.4	45.1	22.9	29.8	1.8	13.6	29.7	13.4
18/09/2020 07:54	0.2	732.8	60.3	33.1	35.5	44.8	23.9	30.0	1.9	13.5	29.8	13.7
16/10/2020 03:17	1.1	711.1	55.4	37.9	35.4	44.0	21.8	27.3	1.6	13.1	28.4	13.9
06/11/2020 00:19	1.6	715.3	54.6	34.6	33.6	44.5	22.2	28.9	1.8	13.3	29.5	11.5
10/12/2020 21:35	1.9	720.3	57.2	37.5	35.5	44.0	23.3	26.1	2.1	13.4	28.0	13.5
Mean	1.0	722.3	56.1	38.1	34.5	43.4	22.6	27.1	2.0	13.5	29.4	13.4
Std. Dev.	0.5	5.4	2.0	2.0	3.6	0.8	0.6	1.8	0.2	0.4	1.5	1.4
% Std. Dev.	47.5	0.7	3.5	5.2	10.4	1.9	2.6	6.6	9.8	2.6	5.2	10.3
% Uncertainty	63.3	2.0	3.9	-28.8	155.5	121.4	1.7	6.4	33.6	5.9	2.4	-0.5

Table E3 – Second half of CRB – basalt data in ppm

	Rb	Sc	Sr	Th	U	V	Y	Zn	Zr
Consensus	46.6	32.4	334.9	5.8	1.7	404.4	36.9	128.5	190.3
01/12/2018 06:45	49.2	30.2	334.2	5.9	1.8	395.6	36.8	124.4	198.8
10/11/2018 05:30	48.8	29.1	333.8	6.1	1.0	398.2	37.2	123.2	198.3
16/11/2018 18:21	49.0	30.1	334.8	6.4	2.1	397.0	37.6	123.8	198.8
06/11/2018 13:20	49.0	29.1	333.8	6.8	1.9	398.2	37.4	124.3	198.7
14/12/2018 03:38	48.8	30.0	333.7	6.4	2.2	393.3	37.3	125.7	198.2
17/03/2017 23:54	49.0	28.7	332.3	5.5	2.2	395.5	38.7	124.3	198.1

	Rb	Sc	Sr	Th	U	V	Y	Zn	Zr
16/02/2019 07:48	49.1	29.8	334.3	6.8	2.0	400.5	37.7	125.6	199.1
28/06/2019 06:54	48.5	29.2	333.8	5.6	1.5	396.1	37.6	124.7	198.5
12/04/2019 00:06	49.4	30.8	333.7	6.1	2.1	398.3	37.7	126.3	199.2
04/06/2019 22:53	48.8	29.8	332.9	6.6	2.0	396.9	37.1	125.6	198.2
08/06/2019 01:44	49.0	30.5	333.7	6.5	1.9	396.3	37.4	125.4	199.0
13/07/2019 05:12	48.9	28.8	334.0	6.0	1.7	397.3	37.5	123.8	198.3
17/07/2019 01:30	48.6	28.5	333.8	5.5	1.3	398.0	37.6	123.7	198.5
28/06/2019 06:54	48.5	29.2	333.8	5.6	1.5	396.1	37.6	124.7	198.5
26/09/2020 00:53	48.7	30.3	333.3	6.8	2.3	397.8	38.3	126.0	197.5
27/08/2020 22:20	49.0	30.0	333.9	6.2	1.9	396.3	38.5	126.2	198.0
12/09/2020 04:11	49.2	29.2	334.5	6.2	2.0	397.1	38.4	125.2	197.8
18/09/2020 07:54	49.0	29.5	334.1	6.0	1.2	395.5	38.5	126.5	198.3
16/10/2020 03:17	49.0	28.3	333.5	6.7	1.8	396.3	38.5	124.3	198.7
06/11/2020 00:19	48.9	29.2	333.8	6.2	2.3	397.7	37.6	125.6	196.5
10/12/2020 21:35	49.0	29.7	335.0	5.7	1.9	398.9	37.8	128.0	197.7
Mean	48.9	29.5	333.8	6.2	1.8	397.0	37.8	125.1	198.3
Std. Dev.	0.2	0.7	0.6	0.4	0.4	1.5	0.5	1.1	0.6
% Std. Dev.	0.5	2.3	0.2	7.0	19.2	0.4	1.4	0.9	0.3
% Uncertainty	5.0	-8.9	-0.3	6.5	10.4	-1.8	2.3	-2.6	4.2

Appendix F: JMP Tukey Kramer and canonical structure data

Tables of the Tukey Kramer p-values of elements that show significant differences between different formations.

Table F1 – Tukey Kramer significant p-values of major immobile and potentially mobile elements

		SiO ₂	TiO ₂	Al ₂ O ₃	Fe ₂ O ₃	MnO	Na ₂ O	K ₂ O
Alitagtag	Tadlac Cave		0.0001					
	Indang		0.0001	0.0484	0.0001	0.0022	0.0085	
	Pasong	0.0001	0.0001	0.0001	0.0001	0.0038	0.0001	0.0001
	Burol	0.0001	0.0001		0.0001		0.0017	
	Balagbag	0.0001	0.0001		0.0001		0.0001	0.0027
	Buco	0.0001	0.0001	0.0035	0.0001	0.0003	0.0001	
Tadlac Cave	Indang				0.0025		0.0048	
	Pasong	0.0001	0.0001	0.0002	0.0001		0.0001	
	Burol	0.0013	0.0001		0.0001		0.001	
	Balagbag	0.0002	0.0001		0.0001		0.0001	
	Buco	0.0001	0.0001		0.0001		0.0001	
Indang	Pasong	0.0086			0.0001			
	Burol				0.0186			
	Balagbag		0.001		0.0002		0.041	

		SiO ₂	TiO ₂	Al ₂ O ₃	Fe ₂ O ₃	MnO	Na ₂ O	K ₂ O
	Buco				0.0013			
Pasong	Burol							
	Balagbag		0.0177	0.0139				
	Buco							
Burol	Balagbag							
	Buco							
Balagbag	Buco		0.0151				0.0296	
TOTAL		9	13	5	14	3	12	2

		Ba	Ce	Cu	La	Mo	Nb	Nd	Rb	Sc	Sr	Th	V	Y	Zn	Zr
	Buco															
Balagbag	Buco			0.0002										0.0262		
TOTAL		5	2	15	2	0	6	4	3	10	6	1	13	9	7	6

Table F3 – Total canonical structure data for the two most significant canons (i.e. canon1 and canon2) on JMP using only immobile and mobile elements

	Canon1	Canon2
SiO₂	0.684368	0.166944
TiO₂	-0.79243	0.066888
Al₂O₃	-0.22459	-0.269331
Fe₂O₃	-0.8008	-0.14347
MnO	-0.23084	-0.02967
Na₂O	0.65381	-0.1464
K₂O	0.352883	0.217864
Ba	0.435436	0.288596
Ce	0.07898	0.262795
Cu	-0.8457	-0.18091
La	0.241629	0.252385
Mo	0.012277	0.157921
Nb	0.395033	0.51606
Nd	0.354601	0.332845
Rb	0.348461	0.383972
Sc	-0.69013	-0.083
Sr	-0.32318	-0.16399
Th	0.073725	0.242015
V	-0.75062	-0.22152
Y	0.476162	0.517595
Zn	-0.56154	0.073376
Zr	0.410473	0.424076

References

- Allen, J., 1982. *Sedimentary Structures: Their Character and Physical Basis*. Elsevier, Amsterdam.
- Allen, S.R., 2001. Reconstruction of a major caldera-forming eruption from pyroclastic deposit characteristics: Kos Plateau Tuff, eastern Aegean Sea. *Journal of Volcanology and Geothermal Research*, 105: 141-162.
- Allen, S.R., 2005. Complex spatter- and pumice-rich pyroclastic deposits from an andesitic caldera-forming eruption: the Siwi pyroclastic sequence, Tanna, Vanuatu. *Bulletin of Volcanology*, 67: 27-41.
- Allen, S.R. and Cas, R.A.F., 1998. Rhyolitic fallout and pyroclastic density current deposits from a phreatoplinian eruption in the eastern Aegean Sea, Greece. *Journal of Volcanology and Geothermal Research*, 86: 219-251.
- Allen, S.R. and Cas, R.A.F., 2001. Transport of pyroclastic flows across the sea during the explosive, rhyolitic eruption of the Kos Plateau Tuff, Greece. *Bulletin of Volcanology*, 62: 441-456.
- Allen, S.R. and McPhie, J., 2000. Water-settling and resedimentation of submarine phreatomagmatic and dome-derived rhyolitic pumice at Yali, eastern Aegean, Greece. *Journal of Volcanology and Geothermal Research*, 95: 285-307.
- Armada, L.T., Yumul, G.P., Ku, C.Y., Doo, W.B., Wu, W.N., Dimalanta, C. and Yumul, G.P., 2012. Possible northward extension of the Philippine Fault Zone offshore Luzon Island (Philippines). *Marine Geophysical Research*, 33: 369-377.
- Arpa, M.C.B., Patino, L.C. and Vogel, T.A., 2008. The basaltic to trachydacitic upper Diliman Tuff in Manila: Petrogenesis and comparison with deposits from Taal and Laguna Calderas. *Journal of Volcanology and Geothermal Research*, 177(4): 1020-1034.
- Asan, K., 2020. Whole-Rock Elemental and Sr-Nd Isotope Geochemistry and Petrogenesis of the Miocene Elmadağ Volcanic Complex, Central Anatolia (Ankara, Turkey). *Geosciences*, 10: 348.

- Aslan, A., 2013. Fluvial Environments - Sediments. In: S.A. Elias and C.J. Mock (Editors), *Encyclopedia of Quaternary Science*. Elsevier, pp. 672-685.
- Aurelio, M., 2000. Tectonics of the Philippines revisited. *Journal of the Geological Society of the Philippines*, 55: 119-183.
- Austin-Erickson, A., Büttner, R., Dellino, P., Ort, M.H. and Zimanowski, B., 2008. Phreatomagmatic explosions of rhyolitic magma: Experimental and field evidence. *Journal of Geophysical Research*, 113(B11): 1-12.
- Bachmann, O. and Bergantz, G., 2008. The Magma Reservoirs That Feed Supereruptions. *Elements*, 4: 17-21.
- Bachmann, O., Deering, C.D., Ruprecht, J.S., Huber, C., Skopelitis, A. and Schnyder, C., 2012. Evolution of silicic magmas in the Kos-Nisyros volcanic center, Greece: A petrological cycle associated with caldera collapse. *Contributions to Mineralogy and Petrology*, 163: 151-166.
- Bachmann, O. and Huber, C., 2016. Silicic magma reservoirs in the Earth's crust. *American Mineralogist*, 101: 2377-2404.
- Bacon, C.R., 1983. Eruptive history of Mount Mazama and Crater Lake Caldera, Cascade Range, U.S.A. *Journal of Volcanology and Geothermal Research*, 18: 59-115.
- Bacon, C.R., 1986. Magmatic inclusions in silicic and intermediate volcanic rocks. *Journal of Geophysical Research*, 91(B6): 6091-6112.
- Bacon, C.R. and Druitt, T.H., 1988. Compositional evolution of the zoned calcalkaline magma chamber of Mount Mazama, Crater Lake, Oregon. *Contributions to Mineralogy and Petrology*, 98: 224-256.
- Bacon, C.R. and Lanphere, M.A., 2006. Eruptive history and geochronology of Mount Mazama and the Crater Lake region, Oregon. *GSA Bulletin*, 118(11/12): 1331-1359.
- Báez, W., Bustos, E., Chiodi, A., Reckziegel, F., Arnosio, M., de Silva, S., Giordano, G., Viramonte, J.G., Sampietro-Vattuone, M.M. and Peña-Monné, J.L., 2020. Eruptive style and flow dynamics of the pyroclastic density currents related to the Holocene Cerro Blanco eruption (Southern Puna plateau, Argentina). *Journal of South American Earth Sciences*, 98: 1-19.
- Baines, P.G., 1995. *Topographic Effects in Stratified Flows*. Cambridge University Press, Cambridge.

- Barberi, F., Navarro, J.M., Rosi, M., Santacroce, R. and Sbrana, A., 1988. Explosive interaction of magma with ground water: insights from xenoliths and geothermal drillings. *Rendiconti della Societa Italiana di Mineralogia e Petrologia*, 43(4): 901-926.
- Barker, S.J., Wilson, C.J.N., Illsley-Kemp, F., Leonard, G.S., Metsel, E.R.H., Mauriohoho, K. and Charlier, B.L.A., 2020. Taupō: an overview of New Zealand's youngest supervolcano. *New Zealand Journal of Geology and Geophysics*, 64(2-3): 320-346.
- Barker, S.J., Wilson, C.J.N., Smith, E.G.C., Charlier, B.L.A., Wooden, J.L., Hiess, J. and Ireland, T.R., 2014. Post-supereruption magmatic reconstruction of Taupo Volcano (New Zealand), as reflected in zircon ages and trace elements. *Journal of Petrology*, 55: 1511-1533.
- Barrier, E., Huchon, P. and Aurelio, M., 1991. Philippine fault: A key for Philippine kinematics. *Geology*, 19: 32-35.
- Bau, M. and Knittel, U., 1993. Significance of slab-derived partial melts and aqueous fluids for the genesis of tholeiitic and calc-alkaline island-arc basalts: evidence from Mt. Arayat, Philippines. *Chemical Geology*, 105: 233-251.
- Baumgartner, L.P. and Olsen, S.N., 1995. A least-squares approach to mass transport calculations using the isocon method. *Economic Geology*, 90: 1261-1270.
- Bautista, B.C., Bautista, M.L.P., Oike, K., Wu, F.T. and Punongbayan, R.S., 2001. A new insight on the geometry of subducting slabs in northern Luzon, Philippines. *Tectonophysics*, 339: 279-310.
- Bear, A.N., Cas, R.A.F. and Giordano, G., 2009. The implications of spatter, pumice and lithic clast rich proximal co-ignimbrite lag breccias on the dynamics of caldera forming eruptions: The 151 ka Sutri eruption, Vico Volcano, Central Italy. *Journal of Volcanology and Geothermal Research*, 181: 1-24.
- Begét, J., Mason, O. and Anderson, P., 1992. Age, extent and climatic significance of the c. 3400 BP Aniakchak tephra, western Alaska, USA. *The Holocene*, 2: 51-56.
- Belousov, A. and Belousova, M., 2001. Eruptive process, effects and deposits of the 1996 and ancient basaltic phreatomagmatic eruptions in

- Karymskoye lake, Kamchatka, Russia. *Sedimentology*, 68(4): 1698-1727.
- Benage, M.C., Dufek, J., Degruyter, W., Geist, D., Harpp, K. and Rader, E., 2014. Tying textures of breadcrust bombs to their transport regime and cooling history. *Journal of Volcanology and Geothermal Research*, 274: 92-107.
- Bernard, A., Knittel, U., Weber, B.C., Weis, D., Albrecht, A., Hattori, K., Klein, J. and Oles, D., 1996. Petrology and geochemistry of the 1991 eruption products of Mount Pinatubo. In: C.G. Newhall and R.S. Punongbayan (Editors), *Fire and mud: eruptions and lahars of Mount Pinatubo, Philippines*. PHIVOLCS and University of Washington Press, pp. 767-797.
- Biró, T., Hencz, M., Németh, K., Karátson, D., Márton, E., Szakács, A., Bradák, B., Szalai, Z., Pécskay, Z. and Kovács, I.J., 2020. A Miocene Phreatoplinian eruption in the North-Eastern Pannonian Basin, Hungary: The Jató Member. *Journal of Volcanology and Geothermal Research*, 401: 1-21.
- Blackford, J.J., Payne, R.J., Heggen, M.P., de la Riva Caballero, A. and van der Plicht, J., 2014. Age and impacts of the caldera-forming Aniakchak II eruption in western Alaska. *Quaternary Research*, 82: 85-95.
- Blum-Oeste, M. and Wörner, G., 2016. Central Andean magmatism can be constrained by three ubiquitous end-members. *Terra Nova*, 28: 434-440.
- Bond, A. and Sparks, R.S.J., 1976. The Minoan eruption of Santorini, Greece. *Journal of the Geological Society, London*, 132: 1-16.
- Borchardt, G.A., Aruscavage, P.J. and Millard Jr, H.T., 1972. Correlation of the Bishop Ash, a Pleistocene Marker Bed, Using Instrumental Neutron Activation Analysis. *Journal of Sedimentary Petrology*, 42(2): 301-306.
- Brand, B.D. and Clarke, A.B., 2012. An unusually energetic basaltic phreatomagmatic eruption: using deposit characteristics to constrain dilute pyroclastic density current dynamics. *Journal of Volcanology and Geothermal Research*, 243: 81-90.
- Branney, M.J., 1991. Eruption and depositional facies of the Whorneyside Tuff Formation, English Lake District: an exceptionally large-magnitude

- phreatoplinian eruption. *Geological Society of America Bulletin*, 103: 886-897.
- Branney, M.J. and Kokelaar, B.P., 1992. A reappraisal of ignimbrite emplacement: progressive aggradation and changes from particulate to non-particulate flow during emplacement of high-grade ignimbrite. *Bulletin of Volcanology*, 54: 504-520.
- Branney, M.J. and Kokelaar, B.P., 1994. A reappraisal of ignimbrite emplacement: progressive aggradation and changes from particulate to non-particulate flow during emplacement of high-grade ignimbrites - Reply. *Bulletin of Volcanology*, 56: 138-143.
- Branney, M.J. and Kokelaar, B.P., 1997. Giant bed from a sustained catastrophic density current flowing over topography: Acatlàn ignimbrite, Mexico. *Geology*, 25: 115-118.
- Branney, M.J. and Kokelaar, P., 2002. *Pyroclastic Density Currents and the Sedimentation of Ignimbrites*. The Geological Society, London.
- Brenna, M., Cronin, S.J., Smith, I.E.M., Sohn, Y.K. and Maas, R., 2012. Spatio-temporal evolution of a dispersed magmatic system and its implications for volcano growth, Jeju Island Volcanic Field, Korea. *Lithos*, 148: 337-352.
- Brown, R.J. and Andrews, G.D.M., 2015. Deposits of Pyroclastic Density Currents. In: H. Sigurdsson (Editor), *The Encyclopedia of Volcanoes* (2nd ed.). Elsevier, pp. 631-648.
- Brown, R.J., Barry, T.L., Branney, M.J., Pringle, M.S. and Bryan, S.E., 2003. The Quaternary pyroclastic succession of southeast Tenerife, Canary Islands: explosive eruptions, related caldera subsidence, and sector collapse. *Geological Magazine*, 140(3): 265-288.
- Brown, R.J., Bonadonna, C. and Durant, A.J., 2012. A review of volcanic ash aggregation. *Physics and Chemistry of the Earth*, 45-46: 65-78.
- Brown, R.J. and Branney, M.J., 2004. Event-stratigraphy of a caldera-forming ignimbrite eruption on Tenerife: the 273 ka Poris Formation. *Bulletin of Volcanology*, 66: 392-416.
- Brown, R.J. and Branney, M.J., 2013. Internal flow variations and diachronous sedimentation within extensive, sustained, density-stratified pyroclastic density currents flowing down gentle slopes, as revealed by the internal

- architectures of ignimbrites on Tenerife. *Bulletin of Volcanology*, 75(727): 1-24.
- Brown, R.J., Branney, M.J., Maher, C. and Dávila-Harris, P., 2010. Origin of accretionary lapilli within ground-hugging density currents: Evidence from pyroclastic couplets on Tenerife. *Geological Society of America Bulletin*, 122: 305-320.
- Bunsen, R., 1851. Ueber die prozesse der vulkanischen Gesteinsbildungen Islands. *Annalen der Physics*, 83: 197-272.
- Büttner, R., Dellino, P., La Volpe, L., Lorenz, V. and Zimanowski, B., 2002. Thermohydraulic explosions in phreatomagmatic eruptions as evidenced by the comparison between pyroclasts and products from Molten Fuel Coolant Interaction experiments. *Journal of Geophysical Research*, 107(B11): ECV 5-1-ECV 5-14.
- Büttner, R., Dellino, P. and Zimanowski, B., 1999. Identifying magma-water interaction from the surface features of ash particles. *Nature*, 401: 688-690.
- Calibo, M., Honrado, M., Paguican, E.M. and Listanco, E., 2010. Monogenetic fields in the Macolod Corridor, NIGS Research Symposium 2010: Dangerous Grounds: A Geological Perspective on Philippine Disasters, Quezon City.
- Carey, R.J., Houghton, B.F. and Thordarson, T., 2009. Abrupt shifts between wet and dry phases of the 1875 eruption of Askja Volcano: Microscopic evidence for macroscopic dynamics. *Journal of Volcanology and Geothermal Research*, 184: 256-270.
- Carey, R.J., Houghton, B.F. and Thordarson, T., 2010. Tephra dispersal and eruption dynamics of wet and dry phases of the 1875 eruption of Askja Volcano, Iceland. *Bulletin of Volcanology*, 72: 259-278.
- Carey, S., Sigurdsson, H., Mandeville, C. and Bronto, S., 1996. Pyroclastic flows and surges over water: an example from the 1883 Krakatau eruption. *Bulletin of Volcanology*, 57: 493-511.
- Carrasco-Núñez, G. and Branney, M.J., 2005. Progressive assembly of a massive layer of ignimbrite with a normal-to-reverse compositional zoning: the Zaragoza ignimbrite of central Mexico. *Bulletin of Volcanology*, 68: 3-20.

- Cas, R.A.F., Wright, H.M.N., Folkes, C.B., Lesti, C., Porreca, M., Giordano, G. and Viramonte, J.G., 2011. The flow dynamics of an extremely large volume pyroclastic flow, the 2.08-Ma Cerro Galán Ignimbrite, NW Argentina, and comparison with other flow types. *Bulletin of Volcanology*, 73: 1583-1609.
- Cas, R.A.F. and Wright, J.V., 1987. *Volcanic Successions: Modern and Ancient*. Allen and Unwin, London.
- Cashman, K.V. and Scheu, B., 2015. Magmatic Fragmentation. In: H. Sigurdsson (Editor), *The Encyclopedia of Volcanoes* (2nd ed.). Elsevier, pp. 459-471.
- Castillo, P.R. and Newhall, C.G., 2004. Geochemical Constraints on Possible Subduction Components in Lavas of Mayon and Taal Volcanoes, Southern Luzon, Philippines. *Journal of Petrology*, 45(6): 1089-1108.
- Castillo, P.R. and Punongbayan, R.S., 1996. Petrology and Sr, Nd, and Pb isotopic geochemistry of Mount Pinatubo volcanic rocks. In: C.G. Newhall and R.S. Punongbayan (Editors), *Fire and mud: eruptions and lahars of Mount Pinatubo, Philippines*. PHIVOLCS and University of Washington Press, pp. 799-806.
- Caulfield, J.T., Cronin, S.J., Turner, S.P. and Cooper, L.B., 2011. Mafic Plinian volcanism and ignimbrite emplacement at Tofua volcano, Tonga. *Bulletin of Volcanology*, 73: 1259-1277.
- Cavazos-Álvarez, J.A. and Carrasco-Núñez, G., 2020. Anatomy of the Xáltipan ignimbrite at Los Humeros Volcanic Complex; the largest eruption of the Trans-Mexican Volcanic Belt. *Journal of Volcanology and Geothermal Research*, 392: 1-18.
- Chesner, C.A., 2012. The Toba Caldera Complex. *Quaternary International*, 258: 5-18.
- Cioni, R., Pistolesi, M. and Rosi, M., 2015. Plinian and Subplinian Eruptions. In: H. Sigurdsson (Editor), *The Encyclopedia of Volcanoes* (2nd ed.). Elsevier, pp. 519-535.
- Cioni, R., Sbrana, A. and Vecchi, R., 1992. Morphological features of juvenile pyroclasts from magmatic and phreatomagmatic deposits of Vesuvius. *Journal of Volcanology and Geothermal Research*, 51: 61-78.

- Cioni, R., Tadini, A., Gurioli, L., Bertagnini, A., Mulas, M., Bevilacqua, A. and Neri, A., 2020. Estimating eruptive parameters and related uncertainties for pyroclastic density currents deposits: worked examples from Somma-Vesuvius (Italy). *Bulletin of Volcanology*, 82(65): 1-20.
- Cole, P., 1991. Migration direction of sand-wave structures in pyroclastic-surge deposits: implications for depositional processes. *Geology*, 19: 1108-1111.
- Cole, P.D., Guest, J.E., Duncan, A.M. and Pacheco, J.-M., 2001. Capelinhos 1957 - 1958, Faial, Azores: deposits formed by an emergent surtseyan eruption. *Bulletin of Volcanology*, 63: 204-220.
- Cole, P.D. and Scarpati, C., 1993. A facies interpretation of the eruption and emplacement mechanisms of the upper part of the Neapolitan Yellow Tuff, Campi Flegrei, southern Italy. *Bulletin of Volcanology*, 55: 311-326.
- Colgate, S.A. and Sigurgeirsson, T., 1973. Dynamic mixing of water and lava. *Nature*, 244: 552-555.
- Corradini, M.L., 1982. Analysis and Modeling of Large-Scale Steam Explosion Experiments. *Nuclear Science and Engineering*, 82(4): 429-447.
- Crandell, D.R., 1989. Gigantic debris avalanche of Pleistocene age from ancestral Mount Shasta volcano, California, and debris-avalanche hazard zonation. Report, USGS Numbered Series.
- Crowe, B.M. and Fisher, R.V., 1973. Sedimentary Structures in Base-Surge Deposits with Special Reference to Cross-Bedding, Ubehebe Craters, Death Valley, California. *Geological Society of America Bulletin*, 84: 663-682.
- Dahlgren, R.A., Macías, F., Camps Arbestain, M., Chesworth, W., Robarge W.P., Bache, B.W., Emerson, W.W., Hartmann, R., Kostic, N., Spaargaren, O., Arnalds, O., 2008. Andosols. In: W. Chesworth (Editor), *Encyclopaedia of soil science*. Springer, Dordrecht, The Netherlands, pp. 39-46.
- Dahlgren, R.A., Saigusa, M. and Ugolini, F.C., 2004. The nature, properties, and management of volcanic soils. *Advances in Agronomy*, 82: 113-182.
- Daly, R.A., 1925. The geology of Ascension Island. *Proceedings of the American Academy of Arts and Sciences*, 60(1): 3-80.

- Daly, R.A., 1933. *Igneous Rocks and Depths of the Earth*. McGraw Hill, New York.
- Darteville, S., Ernst, G.G.J., Stix, J. and Bernard, A., 2002. Origin of the Mount Pinatubo climactic eruption cloud: Implications for volcanic hazards and atmospheric impacts. *Geology*, 30(7): 663-666.
- Davidson, J., Turner, S.P., Handley, H., Macpherson, C. and Dosseto, A., 2007. Amphibole "sponge" in arc crust? *The Geological Society of America*, 35(9): 787-790.
- Dávila-Harris, P., Ellis, B.S., Branney, M.J. and Carrasco-Núñez, G., 2013. Lithostratigraphic analysis and geochemistry of a vitric spatter-bearing ignimbrite: the Quaternary Adeje Formation, Cañadas volcano, Tenerife. *Bulletin of Volcanology*, 75.
- de Maisonneuve, C.B. and Bergal-Kuvikas, O., 2020. Timing, magnitude and geochemistry of major Southeast Asian volcanic eruptions: identifying tephrochronologic markers. *Journal of Quaternary Science*, 35(1-2): 272-287.
- De Rita, D., Giordano, G., Esposito, A., Fabbri, M. and Rodani, S., 2002. Large volume phreatomagmatic ignimbrites from the Colli Albani volcano (Middle Pleistocene, Italy). *Journal of Volcanology and Geothermal Research*: 77-98.
- De Silva, S.L. and Francis, P.W., 1989. Correlation of Large Ignimbrites - Two Case Studies from the Central Andes of Northern Chile. *Journal of Volcanology and Geothermal Research*, 37: 133-149.
- Defant, M.J., De Boer, J.Z. and Oles, D., 1988. The western Central Luzon volcanic arc, the Philippines: two arcs divided by rifting? *Tectonophysics*, 145: 305-317.
- Defant, M.J., Jacques, D., Maury, R.C., De Boer, J. and Joron, J.-L., 1989. Geochemistry and tectonic setting of the Luzon arc, Philippines. *Geological Society of America Bulletin*, 101: 663-672.
- Defant, M.J., Maury, R.C., Ripley, E.M., Feigenson, M.D. and Jacques, D., 1991. An Example of Island-Arc Petrogenesis: Geochemistry and Petrology of the Southern Luzon Arc, Philippines. *Journal of Petrology*, 32: 455-500.

- Defant, M.J. and Ragland, P.C., 1988. Recognition of contrasting magmatic processes using SB-systematics. An example from the Central Luzon arc, the Philippines. *Chemical Geology*.
- de'Gennaro, M., Cappelletti, P., Langella, A., Perrotta, A. and Scarpati, C., 2000. Genesis of zeolites in the Neapolitan Yellow Tuff: geological, volcanological and mineralogical evidence. *Contributions to Mineralogy and Petrology*, 139: 17-35.
- Dellino, P., Frazzetta, G. and La Volpe, L., 1990. Wet surge deposits at La Fossa di Vulcano: depositional and eruptive mechanisms. *Journal of Volcanology and Geothermal Research*, 43: 215-233.
- Dellino, P., Isaia, R., La Volpe, L. and Orsi, G., 2004. Interaction between particles transported by fallout and surge in the deposits of the Agnano-Monte Spina eruption (Campi Flegrei, Southern Italy). *Journal of Volcanology and Geothermal Research*, 133: 193-210.
- Delmelle, P., Kusakabe, M., Bernard, A., Fischer, T., De Brouwer, S. and Del Mundo, E., 1998. Geochemical and isotopic evidence of seawater contamination of the hydrothermal system of Taal Volcano, Luzon, the Philippines. *Bulletin of Volcanology*, 59: 562-576.
- Delmelle, P., Opfergelt, S., Cornelis, J.-T. and Ping, C.-L., 2015. Volcanic Soils. In: H. Sigurdsson (Editor), *The Encyclopedia of Volcanoes* (2nd ed.). Elsevier, pp. 1253-1264.
- Delos Reyes, P.J., Bornas, M.A.V., Dominey-Howes, D., Pidlaoan, A.C., Magill, C.R. and Solidum, R.U., 2018. A synthesis and review of historical eruptions at Taal Volcano, Southern Luzon, Philippines. *Earth-Science Reviews*, 177: 565-588.
- Di Vito, M.A., Isaia, R., Orsi, G., Southon, J., de Vita, S., Antonio, M.D., Pappalardo, L. and Piochi, M., 1999. Volcanism and deformation since 12,000 years at the Campi Flegrei caldera (Italy). *Journal of Volcanology and Geothermal Research*, 91: 221-246.
- Dobran, F., Neri, A. and Macedonio, G., 1993. Numerical simulation of collapsing volcanic columns. *Journal of Geophysical Research*, B98: 4231-4259.
- Douillet, G.A., 2021. The supercritical question for pyroclastic dune bedforms: an overview. *Sedimentology*, 68(4): 1698-1727.

- Douillet, G.A., Pacheco, D.A., Kueppers, U., Letort, J., Tsang-Hin-Sun, É., Bustillos, J., Hall, M., Ramón, P. and Dingwell, D.B., 2013. Dune bedforms produced by dilute pyroclastic density currents from the August 2006 eruption of Tungurahua volcano, Ecuador. *Bulletin of Volcanology*, 75(762), 1-20.
- Druitt, T.H., 1992. Emplacement of the 18 May 1980 lateral blast deposit ENE of Mount St. Helens, Washington. *Bulletin of Volcanology*, 54(7): 554-572.
- Druitt, T.H. and Bacon, C.R., 1986. Lithic Breccia and Ignimbrite Erupted During the Collapse of Crater Lake Caldera, Oregon. *Journal of Volcanology and Geothermal Research*, 29: 1-32.
- Druitt, T.H., Mellors, R.A., Pyle, D.M. and Sparks, R.S.J., 1989. Explosive volcanism on Santorini, Greece. *Geological Magazine*, 126: 95-213.
- Druitt, T.H. and Sparks, R.S.J., 1984. On the formation of calderas during ignimbrite eruptions. *Nature*, 310: 679-681.
- Dufek, J., Manga, M. and Staedter, M., 2007. Littoral blasts: Pumice-water heat transfer and the conditions for steam explosions when pyroclastic flows enter the ocean. *Journal of Geophysical Research*, 112(B11201): 1-16.
- DuFrane, S.A., Asmerom, Y., Mukasa, S.B., Morris, J.D. and Dreyer, B.M., 2006. Subduction and melting processes inferred from U-Series, Sr–Nd–Pb isotope, and trace element data, Bicol and Bataan arcs, Philippines. *Geochimica et Cosmochimica Acta*, 70: 3401-3420.
- Edgar, C.J., Cas, R.A.F., Olin, P.H., Wolff, J.A., Martí, J. and Simmons, J.M., 2017. Causes of complexity in a fallout dominated plinian eruption sequence: 312 ka Fasnía Member, Diego Hernández Formation, Tenerife, Spain. *Journal of Volcanology and Geothermal Research*, 345: 21-45.
- Eichelberger, J.C., 1975. Origin of andesite and dacite: evidence of mixing at Glass Mountain in California and at other circum-Pacific volcanoes. *Geological Society of America Bulletin*, 86: 1381-1391.
- Elburg, M.A., 2010. Sources and Processes in Arc Magmatism: the Crucial Role of Water. *Geologica Belgica*, 13(3): 119-134.
- Ellis, B.S., Schmitz, M.D. and Hill, M., 2019. Reconstructing a Snake River Plain 'super-eruption' via compositional fingerprinting and high-precision U/Pb

- zircon geochronology. *Contributions to Mineralogy and Petrology*, 174(101): 1-16.
- Ellis, B.S., Wolff, J.A., Boroughs, S., Mark, D.F., Starkel, W.A. and Bonnicksen, B., 2013. Rhyolitic volcanism of the central Snake River Plain: a review. *Bulletin of Volcanology*, 75(745): 1-19.
- Evans, L.J., 1982. Dating Methods of Pleistocene Deposits and Their Problems: VII. Paleosols. *Geoscience Canada*, 9(3): 155-160.
- Ewart, A., 1982. The mineralogy and petrology of Tertiary-Recent orogenic volcanic rocks: with special reference to the andesitic-basaltic compositional range. *Andesites: Orogenic Andesites and Related Rocks*, 7: 25-98.
- Ewart, A. and Griffin, W.L., 1994. Application of proton-microprobe data to trace-element partitioning in volcanic rocks. *Chemical Geology*, 117(1-4): 251-284.
- Fan, J., Zhao, D., Dong, D. and Zhang, G., 2017. P-wave tomography of subduction zones around the central Philippines and its geodynamic implications. *Journal of Asian Earth Sciences*, 146: 76-89.
- Fedele, L., Scarpati, C., Sparice, D., Perrotta, A. and Laiena, F., 2016. A chemostratigraphic study of the Campanian Ignimbrite eruption (Campi Flegrei, Italy): Insights on magma chamber withdrawal and deposit accumulation as revealed by compositionally zoned stratigraphic and facies framework. *Journal of Volcanology and Geothermal Research*, 324: 105-117.
- Fernandez-Turiel, J.L., Rejas, M., Pérez Torrado, F.J., Saavedra Alonso, J. and Rodriguez-Gonzalez, A., 2018. Dataset of glass and mineral geochemical data of Holocene volcanic ashes of NW Argentina. DIGITAL.CSIC.
- Fielding, C.R., 2006. Upper flow regime sheets, lenses and scour fills: extending the range of architectural elements for fluvial sediment bodies. *Sedimentary Geology*, 190: 227-240.
- Firth, C.W., Cronin, S.J., Turner, S.P., Handley, H.K., Gaidry, C. and Smith, I., 2015. Dynamics and pre-eruptive conditions of catastrophic, ignimbrite-producing eruptions from the Yenkahe Caldera, Vanuatu. *Journal of Volcanology and Geothermal Research*, 308: 39-60.

- Fisher, R.V., Orsi, G., Ort, M. and Heiken, G., 1993. Mobility of a large-volume pyroclastic flow - emplacement of the Campanian ignimbrite, Italy. *Journal of Volcanology and Geothermal Research*, 56: 205-220.
- Fisher, R.V. and Schmincke, H.-U., 1984. *Pyroclastic Rocks*. Springer-Verlag, Berlin, 472 pp.
- Forni, F., Degruyter, W., Bachmann, O., De Astis, G. and Mollo, S., 2018. Long-term magmatic evolution reveals the beginning of a new caldera cycle at Campi Flegrei. *Science Advances*, 4: 1-11.
- Förster, H., Oles, D., Knittel, U., Defant, M.J. and Torres, R.C., 1990. The Macolod Corridor: A rift crossing the Philippine island arc. *Tectonophysics*, 183: 265-271.
- Francis, P. and Oppenheimer, C., 2003. *Volcanoes*. Oxford University Press, New York.
- Galgana, G., Hamburger, M., McCaffrey, R., Corpuz, E. and Chen, Q., 2007. Analysis of crustal deformation in Luzon, Philippines using geodetic observations and earthquake focal mechanisms. *Tectonophysics*, 432: 63-87.
- Gelman, S.E., Deering, C.D., Gutierrez, F.J. and Bachmann, O., 2013. Evolution of the Taupo Volcanic Center, New Zealand: Petrological and thermal constraints from the Omega dacite. *Contributions to Mineralogy and Petrology*, 166: 1355-1374.
- Geronimo, S., 1988. Characteristics, depositional facies and emplacement mechanisms of the Buco base surge sequence, Batangas province, University of the Philippines, 81 pp.
- Gervasio, F.C., 1968. The geology structures and landscape development of Manila and suburbs. *Philippine Geologist*, 22: 178-192.
- Geshi, N., Yamada, I., Matsumoto, K., Nishihara, A. and Miyagi, I., 2020. Accumulation of rhyolite magma and triggers for a caldera-forming eruption of the Aira Caldera, Japan. *Bulletin of Volcanology*, 82(44): 1-18.
- Geyer, A. and Martí, J., 2014. A short review of our current understanding of the development of ring faults during collapse caldera formation. *Frontiers in Earth Science*, 2(22): 1-13.

- Gingerich, P.D., 1969. Markov analysis of cyclic alluvial sediments. *Journal of Sedimentary Petrology*, 39: 331-332.
- Giordano, G., De Rita, D., Cas, R. and Rodani, S., 2002. Valley pond and ignimbrite veneer deposits in the small-volume phreatomagmatic 'Peperino Albano' basic ignimbrite, Lago Albano maar, Colli Albani volcano, Italy: influence of topography. *Journal of Volcanology and Geothermal Research*, 118: 131-144.
- Gonnermann, H.M., 2015. Magma Fragmentation. *Annual Review of Earth and Planetary Sciences*, 43: 431-458.
- Graettinger, A.H., Skilling, I., McGarvie, D. and Hoskuldsson, A., 2013. Subaqueous basaltic magmatic explosions trigger phreatomagmatism: a case study from Askja, Iceland. *Journal of Volcanology and Geothermal Research*, 264: 17-35.
- Grant, J.A., 1986. The isocon diagram—a simple solution to Gresens' equation for metasomatic alteration. *Economic Geology*, 81: 1976-1982.
- Grant, J.A., 2005. Isocon analysis: A brief review of the method and applications. *Physics and Chemistry of the Earth*, 30: 997-1004.
- Guilbaud, M.N., Alcalá-Reygosa, J., Schimmelpfennig, I., Arce, J.L., and ASTER Team, 2022. Testing less-conventional methods to date a late-pleistocene to Holocene eruption: Radiocarbon dating of paleosols and ³⁶Cl exposure ages at Pelado volcano, Sierra Chichinautzin, Central Mexico. *Quaternary Geology*, 68(101252): 1-12.
- Gurioli, L., Colo, L., Bollasina, A.J., Harris, A.J.L., Whittington, A. and Ripepe, M., 2014. Dynamics of Strombolian explosions: Inferences from field and laboratory studies of erupted bombs from Stomboli volcano. *Journal of Geophysical Research: Solid Earth*, 119: 319-345.
- GVP, 2021A. Niijima. Smithsonian Institution. Last accessed: 12/11/2021. <https://volcano.si.edu/volcano.cfm?vn=284020>.
- GVP, 2021B. Taal. Smithsonian Institution. Last accessed: 05/12/2021. <https://volcano.si.edu/volcano.cfm?vn=273070>.
- Hahn, G.A., Rose, W.I.J. and Meyers, T., 1979. Geochemical correlation of genetically related rhyolitic ash-flow and air-fall ashes, central and western Guatemala and the equatorial Pacific. In: C. Chapin and W. Elston (Editors), *Ash-Flow Tuffs*. Geological Society of America, Denver.

- Hall, M.L. and Mothes, P.A., 2008. Quiltoa volcano - Ecuador: An overview of young dacitic volcanism in a lake-filled caldera. *Journal of Volcanology and Geothermal Research*, 176: 44-55.
- Hargrove, T.R., 1991. *The Mysteries of Taal - A Philippine volcano and lake, her sea life and lost towns*. Bookmark Publishing, Manila.
- Harper, C.W.J., 1984. Improved method of facies analysis. In: R.G. Walker (Editor), *Facies models*. Geoscience Canada, pp. 11-13.
- Heiken, G. and Wohletz, K., 1985. *Volcanic Ash*. University of California Press, 246 pp.
- Heiken, G.H., 1971. Tuff rings: examples from the Fort Rock - Christmas Lake Valley Basin, south-central Oregon. *Journal of Geophysical Research*, 76: 5615-5626.
- Heiken, G.H., 1972. Morphology and petrography of volcanic ashes. *Geological Society of America Bulletin*, 83: 1961-1988.
- Hooper, D.M., McGinnis, R.N. and Necsoiu, M., 2012. Volcaniclastic aeolian deposits at Sunset Crater, Arizona: Terrestrial analogs for Martian dune forms. *Earth Surface Processes and Landforms*, 37: 1090-1105.
- Hosner, P.A., Sánchez-González, L.A., Peterson, A.T. and Moyle, R.G., 2014. Climate-Driven Diversification and Pleistocene Refugia in Philippine Birds: Evidence from Phylogeographic Structure and Paleoenvironmental Niche Modeling. *Evolution*, 68(9): 2658-2674.
- Houghton, B., White, J.D.L. and Van Eaton, A.R., 2015. Phreatomagmatic and Related Eruption Styles. In: H. Sigurdsson (Editor), *The Encyclopedia of Volcanoes* (2nd ed.). Elsevier, pp. 538-552.
- Houghton, B.F., Hobden, B.J., Cashman, K.V., Wilson, C.J.N. and Smith, R.T., 2003. Large-Scale Interaction of Lake Water and Rhyolitic Magma During the 1.8 ka Taupo Eruption, New Zealand. In: J.D.L. White, J.L. Smellie and D.A. Clague (Editors), *Explosive Subaqueous Volcanism*. Geophysical Monograph Series. AGU, Washington D.C., pp. 97-109.
- Houghton, B.F. and Wilson, C.J.N., 1989. A vesicularity index for pyroclastic deposits. *Bulletin of Volcanology*, 51: 451-462.
- Hsu, Y.-J., Yu, S.-B., Loveless, J.P., Bacolcol, T., Solidum, R., Luis Jr, A., Pelicano, A. and Woessner, J., 2016. Interseismic deformation and

- moment deficit along the Manila subduction zone and the Philippine Fault system. *Journal of Geophysical Research: Solid Earth*, 121: 7639-7665.
- Huff, W.D., 1983. Correlation of Middle Ordovician K-bentonites based on chemical fingerprinting. *Journal of Geology*, 91: 657-669.
- Hughes, G.R. and Mahood, G.A., 2011. Silicic calderas in arc settings: characteristics, distribution, and tectonic controls. *Geological Society of America Bulletin*, 123: 1577-1595.
- Humphreys, M.C.S., Cooper, G.F., Zhang, J., Loewen, M., Kent, A.J.R., Macpherson, C.G. and Davidson, J.P., 2019. Unravelling the complexity of magma plumbing at Mount St. Helens: a new trace element partitioning scheme for amphibole. *Contributions to Mineralogy and Petrology*, 174(9): 1-15.
- James, M.R., Gilbert, J.S. and Lane, S.J., 2002. Experimental investigation of volcanic particle aggregation in the absence of a liquid phase. *Journal of Geophysical Research*, 107(B9): ECV 4-1-ECV 4-13.
- Janda, R.J., Daag, A.S., Delos Reyes, P.J., Newhall, C.G., Pierson, T.C., Punongbayan, R.S., Rodolfo, K.S., Solidum, R.U. and Umbal, J.V., 1996. Assessment and response to lahar hazard around Mount Pinatubo, 1991 to 1993. In: C.G. Newhall and R.S. Punongbayan (Editors), *Fire and Mud: Eruptions and Lahars of Mount Pinatubo, Philippines*. PHIVOLCS and University of Washington Press, pp. 61-106.
- Jenner, F.E., O'Neill, H.S.C., Arculus, R.J. and Mavrogenes, J.A., 2010. The Magnetite Crisis in the Evolution of Arc-related Magmas and the Initial Concentration of Au, Ag and Cu. *Journal of Petrology*, 51(12): 2445-2464.
- Jochum, K.P., Weis, U., Schwager, B., Stoll, B., Wilson, S.A., Haug, G.H., Andreae, M.O. and Enzweiler, J., 2015. Reference Values Following ISO Guidelines for Frequently Requested Rock Reference Materials. *Geostandards and Geoanalytical Research*, 40(3): 333-350.
- Karátson, D., Telbisz, T., Gertisser, R., Strasser, T., Nomikou, P., Druitt, T., Vereb, V., Quidelleur, X. and Kósik, S., 2020. Constraining the landscape of Late Bronze Age Santorini prior to the Minoan eruption: Insights from volcanological, geomorphological and archaeological findings. *Journal of Volcanology and Geothermal Research*, 401.

- Kent, A.J., 2014. Preferential eruption of andesitic magmas: implications for volcanic magma fluxes at convergent margins. *Geological Society of London Special Publication*, 385: 257-280.
- Klappa, C.F., 1980. Rhizoliths in terrestrial carbonates - classification, recognition, genesis and significance. *Sedimentology*, 27: 613-629.
- Klaver, M., Blundy, J.D. and Vroon, P.Z., 2018. Generation of arc rhyodacites through cumulate-melt reactions in a deep crustal hot zone: Evidence from Nisyros volcano. *Earth and Planetary Science Letters*, 497: 169-180.
- Knittel, I. and Oles, D., 1994. Basaltic Volcanism Associated with Extensional Tectonics in the Taiwan-Luzon Island-Arc: Evidence for Non-Depleted Sources and Subduction Zone Enrichment. *Special Publications of the Geological Society of London*: 77-93.
- Knittel, U. and Defant, M.J., 1988. Sr isotopic and trace element variations in Oligocene to Recent igneous rocks from the Philippine island arc: evidence for Recent enrichment in the sub-Philippine mantle. *Earth and Planetary Science Letters*, 87: 87-99.
- Knittel, U., Hegner, E., Bau, M. and Satir, M., 1997. Enrichment Processes in the Sub-Arc Mantle: A Sr-Nd-Pb Isotopic and REE Study of Primitive Arc Basalts from the Philippines. *Canadian Mineralogy*, 35: 327-346.
- Knott, T.R., Branney, M.J., Reichow, M.K., Finn, D.R., Tapster, S. and Coe, R.S., 2020. Discovery of two new super-eruptions from the Yellowstone hotspot track (USA): Is the Yellowstone hotspot waning? . *Geology*, 48.
- Kobayashi, T., Mirabueno, M.H.T., Bornas, M.A.V., Torii, M., Laguerta, E.P., Daag, A.S., Bariso, E.B., Nakamura, T. and Okuno, M., 2014. Eruptive Sequence and Characteristics of the Irosin Ignimbrite, Southern Luzon, Philippines. *Journal of Geography (Chigaku Zasshi)*, 123(1): 123-132.
- Kokelaar, P., 1986. Magma-water interactions in subaqueous and emergent basaltic volcanism. *Bulletin of Volcanology*, 48: 275-289.
- Kokelaar, P. and Branney, M.J., 1996. On pyroclastic flow emplacement - Comment. *Journal of Geophysical Research*, B101: 5653-5655.
- Kokelaar, P., Raine, P. and Branney, M.J., 2007. Incursion of a large-volume, spatter-bearing pyroclastic density current into a caldera lake: Pavey Ark ignimbrite, Scafell caldera, England. *Bulletin of Volcanology*, 70: 23-54.

- Koyaguchi, T. and Woods, A.W., 1996. On the formation of eruption columns following explosive mixing of magma and surface-water. *Journal of Geophysical Research*, 101(B3): 5561-5574.
- Kramer, W., Weatherall, G. and Offler, R., 2001. Origin and correlation of tuffs in the Permian Newcastle and Wollombi Coal Measures, NSW, Australia, using chemical fingerprinting. *International Journal of Coal Geology*, 47: 115-135.
- Ku, Y.-P., Chen, C.-H., Song, S.-R., Iizuka, Y. and Shen, J.J.-S., 2009. A 2 Ma record of explosive volcanism in southwestern Luzon: Implications for the timing of subducted slab steepening. *Geochemistry, Geophysics, Geosystems*, 10(6): 1-20.
- Lajoie, J., Lanzafame, G., Rossi, P.L. and Tranne, C.A., 1992. Lateral facies variations in hydromagmatic pyroclastic deposits at Linosa, Italy. *Journal of Volcanology and Geothermal Research*, 54: 135-143.
- Lanzo, G., Basile, S., Brai, M. and Rizzo, S., 2010. Volcanic products of Lipari (Aeolian islands, Italy): Multivariate analysis of petrographic and radiometric data. *Radiation Measurements*, 45: 816-822.
- Lavigne, F., Degaei, J.-P., Komorowski, J.-C., Guillet, S., Robert, V., Lahitte, P., Oppenheimer, C., Stoffel, M., Vidal, C.M., Surono, Pratomo, I., Wassmer, P., Hajdas, I., Hadmoko, D.S. and de Belizal, E., 2013. Source of the great A.D. 1257 mystery eruption unveiled, Samalas volcano, Rinjani Volcanic Complex, Indonesia. *The Proceedings of the National Academy of Sciences (PNAS)*, 110(42): 16742-16747.
- Lebti, P.P., Thouret, J.-C., Wörner, G. and Fornari, M., 2006. Neogene and Quaternary ignimbrites in the area of Arequipa, Southern Peru: Stratigraphical and petrological correlations. *Journal of Volcanology and Geothermal Research*, 154: 251-275.
- Lian, O.B. and Shane, P.A., 2000. Optical dating of paleosols bracketing the widespread Rotoehu tephra, North Island, New Zealand. *Quaternary Science Reviews*, 19(16): 1649-1662.
- Lim, J.B., 1983. Correlating the orientation of tectonic stress with the flank eruptions of Taal Volcano. *The Philippine Journal of Volcanology*, 1: 41-65.

- Listanco, E., 1994. Space-Time patterns in evolution of calderas. A Case study at Taal volcano, Philippines. University of Tokyo, Tokyo.
- Liu, E.J., Cashman, K.V. and Rust, A.C., 2015. Optimising shape analysis to quantify volcanic ash morphology. *GeoResJ*, 8: 14-30.
- Lorenz, V., 1974. Vesiculated tuff and associated features. *Sedimentology*, 21: 273-291.
- Loughlin, S.C., Vye-Brown, C., Sparks, R.S.J., Brown, S.K., Barclay, J., Calder, E.S., Cottrell, E., Jolly, G., Komorowski, J.-C., Mandeville, C., Newhall, C., Palma, J., Potter, S. and Valentine, G., 2015. An introduction to global volcanic hazard and risk. In: S.C. Loughlin, S. Sparks, S.K. Brown, S.F. Jenkins and C. Vye-Brown (Editors), *Global Volcanic Hazards and Risk*. Cambridge University Press, Cambridge.
- Lowe, D.J., 2016. Introduction to tephra-derived soils, North Island, New Zealand Joint conference of the New Zealand Society of Soil Science and Soil Science Australia, Hamilton, New Zealand
- Lowe, D.J. and Tonkin, P.J., 2010. Unravelling upbuilding pedogenesis in tephra and loess sequences in New Zealand using tephrochronology, 19th World Congress of Soil Science, Soil Solutions for a Changing World Brisbane, Australia.
- Lowenstern, J.B. and Hurwitz, S., 2008. Monitoring a Supervolcano in Repose: Heat and Volatile Flux at the Yellowstone Caldera. *Elements*, 4: 35-40.
- Luhr, J.F. and Carmichael, I.S.E., 1980. The Colima Volcanic complex, Mexico. I. Post-caldera andesites from Volcán Colima. *Contributions to Mineralogy and Petrology*, 71: 343-372.
- Luhr, J.F. and Melson, W.G., 1996. Mineral and glass compositions in June 15, 1991, pumices: evidence for dynamic equilibrium in the dacite of Mount Pinatubo. In: C.G. Newhall and R.S. Punongbayan (Editors), *Fire and mud: eruptions and lahars of Mount Pinatubo, Philippines*. PHIVOLCS and University of Washington Press, pp. 733-750.
- Machida, H., Blong, R.J., Specht, J., Moriwaki, H., Torrence, R., Hayakawa, Y., Talai, B., Lolok, D. and Pain, C.F., 1996. Holocene Explosive Eruptions of Witori and Dakataua Caldera Volcanoes in West New Britain, Papua New Guinea. *Quaternary International*, 34-36: 65-78.

- Madden-Nadeau, A.L., Cassidy, M., Pyle, D.M., Mather, T.A., Watt, S.F.L., Engwell, S.L., Abdurrachman, M., Nurshal, M.E.M., Tappin, D.R. and Ismail, T., 2021. The magmatic and eruptive evolution of the 1883 caldera-forming eruption of Krakatau: integrating field- to crystal-scale observations. *Journal of Volcanology and Geothermal Research*, 411: 1-21.
- Maeno, F. and Taniguchi, H., 2007. Spatiotemporal evolution of a marine caldera-forming eruption, generating a low-aspect ratio pyroclastic flow, 7.3 ka, Kikai caldera, Japan: Implication from near-vent eruptive deposits. *Journal of Volcanology and Geothermal Research*, 167: 212-238.
- Mancarella, D. and Simeone, V., 2012. Capillary barrier effects in unsaturated layered soils, with special reference to the pyroclastic veneer of the Pizzo d'Alvano, Campania, Italy. *Bulletin of Engineering Geology and the Environment*, 71: 791-801
- Manville, V., Newton, E.H. and White, J.D.L., 2005. Fluvial responses to volcanism: re-sedimentation of the 1800a Taupo ignimbrite eruption in the Rangitaiki River catchment, North Island, New Zealand. *Geomorphology*, 65: 49-70.
- Manville, V. and Wilson, C.J.N., 2004. The 26.5 ka Oruanui eruption, New Zealand: A review of the roles of volcanism and climate in the post-eruptive sedimentary response. *New Zealand Journal of Geology and Geophysics*, 47(3): 525-547.
- Martinez, M.M.L. and Williams, S.N., 1999. Basaltic andesite to andesite scoria pyroclastic flow deposits from Taal Caldera, Philippines. *Journal of the Geological Society of the Philippines*, 54(1&2): 1-18.
- Mason, B.G., Pyle, D.M. and Oppenheimer, C., 2004. The size and frequency of the largest explosive eruptions on Earth. *Bulletin of Volcanology*, 66: 735-748.
- Mastrolorenzo, G., Brachi, L. and Canzanella, A., 2001. Vesicularity of various types of pyroclastic deposits of Campi Flegrei volcanic field: evidence of analogies in magma rise and vesiculation mechanisms. *Journal of Volcanology and Geothermal Research*, 109: 41-53.

- McClelland, E., Wilson, C.J.N. and Bardot, L., 2004. Palaeotemperature determinations for the 1.8-ka Taupo ignimbrite, New Zealand, and implications for the emplacement history of a high-velocity pyroclastic flow. *Bulletin of Volcanology*, 66: 492-513.
- McDaniel, P.A., Lowe, D.J., Arnalds, O. and Ping, C.-L., 2012. Andisols. In: P.M. Huang, Y. Li and M.E. Sumner (Editors), *Handbook of Soil Sciences*. CRC Press (Taylor & Francis), Boca Raton, Florida, pp. 33.29-33.48.
- McDonald, J.H., 2014. *Handbook of Biological Statistics*. Sparky House Publishing, Baltimore.
- McKee, C.O., 2015. Tavui Volcano: neighbour of Rabaul and likely source of the Middle Holocene penultimate major eruption in the Rabaul area. *Bulletin of Volcanology*, 77(80): 1-21.
- Mellors, R.A. and Sparks, R.S.J., 1991. Spatter-rich pyroclastic flow deposits on Santorini, Greece. *Bulletin of Volcanology*, 53: 327-342.
- Merriam, R. and Bischoff, J.L., 1975. Bishop Ash: A Widespread Volcanic Ash Extended to Southern California. *Journal of Sedimentary Petrology*, 45(1): 207-211.
- Miall, A.D., 1996. *The Geology of Fluvial Deposits*. Springer.
- Middleton, G.V., 1965. Antidune cross-bedding in a large flume. *Journal of Sedimentary Research*, 35(4): 922-927.
- Miklius, A., Flower, M.F.J., Huijsmans, J.P.P., Mukasa, S.B. and Castillo, P., 1991. Geochemistry of Lavas from Taal Volcano, Southwestern Luzon, Philippines: Evidence for Multiple Magma Supply Systems and Mantle Source Heterogeneity. *Journal of Petrology*, 32: 593-627.
- Miller, C.F. and Wark, D.A., 2008. Supervolcanoes and their Explosive Supereruptions. *Elements*, 4: 11-16.
- Miller, J., 1989. *Statistics for Advanced Level*. Cambridge University Press, Cambridge, 442 pp.
- Miyabuchi, Y., 2009. A 90,000-year tephrostratigraphic framework of Aso Volcano, Japan. *Sedimentary Geology*, 220: 169-189.
- Monzier, M., Robin, C. and Eissen, J.-P., 1994. Kuwae (~1425 A.D.): the forgotten caldera. *Journal of Volcanology and Geothermal Research*, 59: 207-218.

- Moore, J.G., 1966. Base surge at 1965 eruption of Taal Volcano, Philippines. *Transactions American Geophysical Union*, 47(1): 194.
- Moore, J.G., 1967. Base Surge in Recent Volcanic Eruptions. *Bulletin Volcanologique*, 30: 337-363.
- Moore, J.G., Nakamura, K. and Alcaraz, A., 1966. The 1965 eruption of Taal volcano. *Science*, 151(3713): 955-960.
- Moorhouse, B.L. and White, J.D.L., 2016. Interpreting ambiguous bedforms to distinguish subaerial base surge from subaqueous density current deposits. *The Depositional Record*, 2: 173-195.
- Morgan, L.A., Doherty, D.J. and Leeman, W.P., 1984. Ignimbrites of the Eastern Snake River Plain: Evidence for Major Caldera-Forming Eruptions. *Journal of Geophysical Research*, 89(110): 8665-8678.
- Mueller, S.B., Kueppers, U., Ayriss, P.M., Jacob, M. and Dingwell, D.B., 2016. Experimental volcanic ash aggregation: Internal structuring of accretionary lapilli and the role of liquid bonding. *Earth and Planetary Science Letters*, 433: 232-240.
- Mueller, S.B., Kueppers, U., Huber, M.S., Hess, K.-U., Poesges, G., Ruthensteiner, B. and Dingwell, D.B., 2018. Aggregation in particle rich environments: a textural study of examples from volcanic eruptions, meteorite impacts, and fluidized bed processing. *Bulletin of Volcanology*, 80(32): 1-17.
- Mukasa, S.B., Flower, M.F.J. and Miklius, A., 1994. The Nd-, Sr- and Pb-isotopic character of lavas from Taal, Laguna de Bay and Arayat volcanoes, southwestern Luzon, Philippines: implications for arc magma petrogenesis. *Tectonophysics*, 235: 205-221.
- Mukasa, S.B., McCabe, R. and Gill, J.B., 1987. Pb-isotopic composition of volcanic rocks in the West and East Philippines Island Arcs: presence of the dupal isotopic anomaly. *Earth and Planetary Science Letters*, 84: 153-164.
- Mulder, T., Razin, P. and Faugeres, J.-C., 2009. Hummocky cross-stratification-like structures in deep-sea turbidites: Upper Cretaceous Basque basins (Western Pyrenees, France). *Sedimentology*, 56: 997-1015.
- Myers, M.L., Druitt, T.H., Schiavi, F., Gurioli, L. and Flaherty, T., 2021. Evolution of magma decompression and discharge during a Plinian event (Late

- Bronze-Age eruption, Santorini) from multiple eruption-intensity proxies. *Bulletin of Volcanology*, 83(18): 1-17.
- Nairn, I.A., McKee, C.O., Talai, B. and Wood, C.P., 1995. Geology and eruptive history of the Rabaul Caldera area, Papua New Guinea. *Journal of Volcanology and Geothermal Research*, 69: 255-284.
- Navarrete, I.A., Tsutsuki, K., Kondo, R. and Asio, V.B., 2008. Genesis of soils across a late Quaternary volcanic landscape in the humid tropical island of Leyte, Philippines. *Australian Journal of Soil Research* 46(5): 1-12.
- Neall, V.E., 2006. Volcanic soils. In: W. Verheye (Editor), *Land use and land cover, Encyclopaedia of life support systems (EOLSS)*. EOLSS Publishers with UNESCO, Oxford, UK, pp. 23.
- Németh, K. and Cronin, S.J., 2009. Phreatomagmatic volcanic hazards where rift-systems meet the sea, a study from Ambae Island, Vanuatu. *Journal of Volcanology and Geothermal Research*, 180: 246-258.
- Németh, K. and Kósik, S., 2020. Review of Explosive Hydrovolcanism. *Geosciences*, 10(44): 1-27.
- Neri, A., Bevilacqua, A., Esposito Ongaro, T., Isaia, R., Aspinall, W.P., Bisson, M., Flandoli, F., Baxter, P.J., Bertagnini, A. and Iannuzzi, E., 2015. Quantifying volcanic hazard at Campi Flegrei caldera (Italy) with uncertainty assessment: II. Pyroclastic density current invasion maps. *Journal of Geophysical Research: Solid Earth*, 120: 2330-2349.
- Neri, A., Esposito Ongaro, T., Voight, B. and Widiwijayanti, C., 2014. Pyroclastic density current hazards and risk. In: J.F. Shroder and P. Papale (Editor), *Volcanic Hazards, Risk, and Disasters*: 109-140.
- Newhall, C., Hendley, J.W. and Stauffer, P.H., 1998. The Cataclysmic 1991 Eruption of Mount Pinatubo, Philippines. *USGS Factsheet* 113-97.
- Newhall, C., Self, S. and Robock, A., 2018. Anticipating future Volcanic Explosivity Index (VEI) 7 eruptions and their chilling impacts. *Geosphere*, 14(2): 572-603.
- Newhall, C.G. and Self, S., 1982. The Volcanic Explosivity Index (VEI): An Estimate of Explosive Magnitude for Historical Volcanism. *Journal of Geophysical Research*, 87(C2): 1231-1238.
- Nielsen, R.L., Ustunisik, G., Weinstein, A.B., Tepley III, F.J., Johnston, A.D. and Kent, A.J.R., 2017. Trace element partitioning between plagioclase

- and melt: An investigation of the impact of experimental and analytical procedures. *Geochemistry, Geophysics, Geosystems*, 18: 3359-3384.
- OCHA, 2020. Philippines. UN Office for the Coordination of Humanitarian Affairs. Last accessed: 13/10/2021. <https://www.unocha.org/philippines>.
- Oles, D., 1991. Geology of the Macolod corridor intersecting the Bataan-Mindoro island arc, the Philippines, German Research Society Project and German Agency for Technical Cooperation Project.
- Onyekuru, S.O., Iwuagwu, C.J., Okenyi, J., Opara, K.D. and Nwigbo, U.N., 2019. Characterization of the Upper Cretaceous Sediments in the Ikpankwu-Ihube Axis, Okigwe, Southeastern Nigeria. *International Journal of Geosciences*, 10: 724-744.
- Paguican, E.M., Grosse, P., Fabbro, G.N. and Kervyn, M., 2021. Morphometric classification and spatial distribution of Philippine volcanoes. *Journal of Volcanology and Geothermal Research*, 418.
- Palladino, D.M., Gaeta, M., Giaccio, B. and Sottili, G., 2014. On the anatomy of magma chamber and caldera collapse: The example of trachy-phonolitic explosive eruptions of the Roman Province (central Italy). *Journal of Volcanology and Geothermal Research*, 281: 12-26.
- Palladino, D.M. and Simeì, S., 2005. Eruptive dynamics and caldera collapse during the Onano eruption, Vulcini, Italy. *Bulletin of Volcanology*, 67: 423-440.
- Palladino, D.M., Valentine, G.A., Sottili, G. and Taddeucci, J., 2015. Maars to calderas: End-members on a spectrum of explosive volcanic depressions. *Frontiers in Earth Science*, 3.
- Pallister, J.S., Hoblitt, R.P., Meeker, G.P., Knight, R.J. and Siems, D.F., 1996. Magma mixing at Mount Pinatubo: petrographic and chemical evidence from the 1991 deposits. In: C.G. Newhall and R.S. Punongbayan (Editors), *Fire and mud: eruptions and lahars of Mount Pinatubo, Philippines*. PHIVOLCS and University of Washington Press, pp. 687-731.
- Pan, B., de Silva, S.L., Xu, J., Liu, S. and Xu, D., 2020. Late Pleistocene to present day eruptive history of the Changbaishan-Tianchi Volcano, China/DPRK: New field, geochronological and chemical constraints. *Journal of Volcanology and Geothermal Research*, 399: 1-18.

- Papike, J.J., Keith, T.E.C., Spilde, M.N., Galbreath, K.C., Shearer, C.K. and Laul, J.C., 1991. Geochemistry and mineralogy of fumarolic deposits, Valley of Ten Thousand Smokes, Alaska: Bulk chemical and mineralogical evolution of dacite-rich protolith. *American Mineralogist*, 76: 1662-1673.
- Pardo, N., Macias, J.L., Giordano, G., Cianfarra, P., Avellán, D.R. and Bellatreccia, F., 2009. The ~1245 yr BP Asososca maar eruption: The youngest event along the Nejapa–Miraflores volcanic fault, Western Managua, Nicaragua. *Journal of Volcanology and Geothermal Research*, 184: 292-312.
- Parfitt, R.L., 2009. Allophane and imogolite: role in soil biogeochemical processes. *Clay Minerals*, 44: 135-155.
- Patel, A., Manga, M., Carey, R.J. and Degruyter, W., 2013. Effects of thermal quenching on mechanical properties of pyroclasts. *Journal of Volcanology and Geothermal Research*, 258: 24-30.
- Pearce, J.A., 1982. Trace element characteristics of lavas from destructive plate boundaries. In: R.S. Thorpe (Editor), *Andesites*. John Wiley & Sons, pp. 525-548.
- Pedrazzi, D., Sunye-Puchol, I., Aguirre-Díaz, G., Costa, A., Smith, V.C., Poret, M., Dávila-Harris, P., Miggins, D.P., Hernández, W. and Gutiérrez, E., 2019. The Ilopango Tierra Blanca Joven (TBJ) eruption, El Salvador: Volcano-stratigraphy and physical characterization of the major Holocene event of Central America. *Journal of Volcanology and Geothermal Research*, 377: 81-102.
- Pérez, W., Freundt, A. and Kutterolf, S., 2020. The basaltic plinian eruption of the ~6 ka San Antonio Tephra and formation of the Masaya caldera, Nicaragua. *Journal of Volcanology and Geothermal Research*, 401: 1-17.
- Perugini, D. and Poli, G., 2012. The mixing of magmas in plutonic and volcanic environments: Analogies and differences. *Lithos*, 153: 261-277.
- PHIVOLCS, 2018. Volcanoes of the Philippines. Last accessed: 11/09/2021. <https://wovodat.phivolcs.dost.gov.ph/volcano/ph-volcanoes>.
- PHIVOLCS, 2020. Taal Volcano Hazard Maps and Summary of Prone Barangays. Last accessed: 11/09/2021.

<https://www.phivolcs.dost.gov.ph/index.php/volcano-hazard/gisweb-volcano-hazard-maps>.

PHIVOLCS, 2022. Taal Volcano Bulletins. Last accessed: 28/03/2022.

<https://www.phivolcs.dost.gov.ph/index.php/volcano-hazard/volcano-bulletin2/taal-volcano>.

Ponomareva, V.V., Kyle, P.R., Melekestsev, I.V., Rinkleff, P.G., Dirksen, O.V., Sulerzhitsky, L.D., Zaretskaia, N.E. and Rourke, R., 2004. The 7600 (¹⁴C) year BP Kurile Lake caldera-forming eruption, Kamchatka, Russia: stratigraphy and field relationships. *Journal of Volcanology and Geothermal Research*, 136: 199-222.

Powers, D.W. and Easterling, P.G., 1982. Improved methodology for using embedded Markov chains to describe cyclical sediments. *Journal of Sedimentary Petrology*, 52: 913-924.

Prave, A. and Duke, W., 1990. Small-scale hummocky cross-stratification in turbidites: a form of antidune stratification? *Sedimentology*, 37: 531-539.

Preece, K., Mark, D.F., Barclay, J., Cohen, B.E., Chamberlain, K.J., Jowitt, C., Vye-Brown, C., Brown, R.J. and Hamilton, S., 2018. Bridging the gap: ⁴⁰Ar/³⁹Ar dating of volcanic eruptions from the 'Age of Discovery'. *Geology*, 46(12): 1035-1038.

Punongbayan, R.S., Self, S., Torres, R.C., Listanco, E.L. and Corpuz, E.G., 1995. Taal Decade Volcano International Workshop, Tagaytay City, Philippines.

Pyle, D.M., 2015. Sizes of Volcanic Eruptions. In: H. Sigurdsson (Editor), *The Encyclopedia of Volcanoes* (2nd ed.). Elsevier, pp. 257-264.

Ramos, E.G., 1986. Lakeshore landslides: unrecognised hazards around Taal Volcano. *Philippine Journal of Volcanology*, 3: 28-53.

Rausch, J., Grobéty, B. and Vonlanthen, P., 2015. Eifel maars: Quantitative shape characterization of juvenile ash particles (Eifel Volcanic Field, Germany). *Journal of Volcanology and Geothermal Research*, 291: 86-100.

Reeves, C.C., 1968. Lacustrine Sediments: Clastic. In: C.C. Reeves (Editor), *Developments in Sedimentology*. Elsevier.

- Reubi, O. and Blundy, J., 2009. A dearth of intermediate melts at subduction zone volcanoes and the petrogenesis of arc andesites. *Nature*, 461: 1269-1273.
- Reyes-Dávila, G.A., Arámbula-Mendoza, R., Espinasa-Pereña, R., Pankhurst, M.J., Navarro-Ochoa, C., Savov, I., Vargas-Bracamontes, D.M., Cortés-Cortés, A., Gutiérrez-Martínez, C., Valdés-González, C., Domínguez-Reyes, T., González-Amezcuca, M., Martínez-Fierros, A., Ramírez-Vázquez, C.A., Cárdenas-González, L., Castañeda-Bastida, E., Vázquez Espinoza de los Monteros, D.M., Nieto-Torres, A., Campion, R., Courtois, L. and Lee, P.D., 2016. Volcán de Colima dome collapse of July, 2015 and associated pyroclastic density currents. *Journal of Volcanology and Geothermal Research*, 320: 100-106.
- Riehle, J., Meyer, C., Ager, T., Kaufman, D. and Ackerman, R., 1987. The Aniakchak tephra deposit, a late Holocene marker horizon in western Alaska. *US Geological Survey Circular* 998: 19-22.
- Robin, C., Eissen, J.-P. and Monzier, M., 1993. Giant tuff cone and 12-km-wide associated caldera at Ambrym Volcano (Vanuatu, New Hebrides Arc). *Journal of Volcanology and Geothermal Research*, 55: 225-238.
- Robin, C., Monzier, M. and Eissen, J.-P., 1994. Formation of the mid-fifteenth century Kuwae caldera (Vanuatu) by an initial hydroclastic and subsequent ignimbritic eruption. *Bulletin of Volcanology*, 56: 170-183.
- Robock, A., 2000. Volcanic Eruptions and Climate. *Review of Geophysics*, 38(2): 191-219.
- Roche, O., Druitt, T.H. and Merle, O., 2000. Experimental study of caldera formation. *Journal of Geophysical Research*, 105B: 395-416.
- Rodríguez, A. and van Bergen, M.J., 2017. Superficial alteration mineralogy in active volcanic systems: An example of Poás volcano, Costa Rica. *Journal of Volcanology and Geothermal Research*, 346: 54-80.
- Rolandi, G., Munno, R. and Postiglione, I., 2004. The A.D. 472 eruption of the Somma volcano. *Journal of Volcanology and Geothermal Research*, 129: 291-319.
- Rollinson, H., 1993. *Using Geochemical Data: Evaluation, Presentation, Interpretation*. Pearson Education Limited, Essex.

- Rooyackers, S.M., Stix, J., Berlo, K. and Barker, S.J., 2020. Emplacement of unusual rhyolitic to basaltic ignimbrites during collapse of a basalt-dominated caldera: The Halarauður eruption, Krafla (Iceland). *The GSA Bulletin*, 132(9/10): 1881-1902.
- Rose, W.I., Newhall, C.G., Bornhorst, T.J. and Self, S., 1987. Quaternary Silicic Pyroclastic Deposits of Atitlán Caldera, Guatemala. *Journal of Volcanology and Geothermal Research*, 33: 57-80.
- Rosi, M., 1992. A model for the formation of vesiculated tuff by the coalescence of accretionary lapilli. *Bulletin of Volcanology*, 54: 429-434.
- Rosi, M., Vezzoli, L., Aleotti, P. and De Censi, M., 1996. Interaction between caldera collapse and eruptive dynamics during the Campanian Ignimbrite eruption, Phlegraean Fields, Italy. *Bulletin of Volcanology*, 57: 541-554.
- Rust, B.R. and Gibling, M.R., 1990. Three-dimensional antidunes as HCS mimics in a fluvial sandstone: the Pennsylvanian South Bar Formation near Sydney, Nova Scotia. *Journal of Sedimentary Petrology*, 60: 540-548.
- Rymer, H., Sparks, S., Self, S., Grattan, J., Oppenheimer, C. and Pyle, D., 2005. *Super-eruptions: Global effects and future threats*. Geological Society of London.
- Salisbury, M.J., Jicha, B.R., de Silva, S.L., Singer, B.S., Jiménez, N.C. and Ort, M.H., 2011. $^{40}\text{Ar}/^{39}\text{Ar}$ chronostratigraphy of Altiplano-Puna volcanic complex ignimbrites reveals the development of a major magmatic province. *Geological Society of America Bulletin*, 123(5/6): 821-840.
- Scarpati, C., Cole, P. and Perrotta, A., 1993. The Neapolitan Yellow Tuff - A large volume multiphase eruption from Campi Flegrei, Southern Italy. *Bulletin of Volcanology*, 55: 343-356.
- Scarpati, C. and Perrotta, A., 2012. Erosional characteristics and behavior of large pyroclastic density currents. *Geology*, 40(11): 1035-1038.
- Scarpati, C., Sparice, D. and Perrotta, A., 2020. Dynamics of large pyroclastic currents inferred by the internal architecture of the Campanian Ignimbrite. *Nature Scientific Reports*, 10(22230): 1-13.
- Schmincke, H.-U., Fisher, R.V. and Waters, A.C., 1973. Antidune and chute and pool structures in the base surge deposits of the Laacher See area, Germany. *Sedimentology*, 20: 553-574.

- Schumacher, R. and Schmincke, H.-U., 1991. Internal structure and occurrence of accretionary lapilli - a case study at Laacher See Volcano. *Bulletin of Volcanology*, 53: 612-634.
- Schwarzacher, W., 1975. *Markov Chains, Developments in Sedimentology*. Elsevier, Amsterdam.
- Scott, W.E., Hoblitt, R.P., Torres, R.C., Self, S., Martinez, M.M.L. and Nillos, T.J., 1996. Pyroclastic Flows of the June 15, 1991, Climactic Eruption of Mount Pinatubo. In: C.G. Newhall and R.S. Punongbayan (Editors), *Fire and Mud: Eruptions and Lahars of Mount Pinatubo, Philippines*. PHIVOLS and University of Washington Press.
- Self, S., 1983. Large-scale phreatomagmatic silicic volcanism: a case study from New Zealand. *Journal of Volcanology and Geothermal Research*, 17: 433-469.
- Self, S., 2006. The effects and consequences of very large explosive volcanic eruptions. *Philosophical Transactions of the Royal Society A*, 364(1845): 2073-2097.
- Self, S. and Blake, S., 2008. Consequences of Explosive Supereruptions. *Elements*, 4: 41-46.
- Self, S. and Sparks, R.S.J., 1978. Characteristics of widespread pyroclastic deposits formed by the interaction of silicic magma and water. *Bulletin of Volcanology*, 41(3).
- Selles, A., Deffontaines, B., Hendrayana, H. and Violette, S., 2015. The eastern flank of the Merapi volcano (Central Java, Indonesia): Architecture and implications of volcanoclastic deposits. *Journal of Asian Earth Sciences*, 108: 33-47.
- Selley, R.C., 1970. Studies of sequence in sediments using a simple mathematical device. *Quarterly Journal of the Geological Society of London*, 125: 557-581.
- Shane, P., Smith, V. and Nairn, I., 2005. High temperature rhyodacites of the 36 ka Hauparu pyroclastic eruption, Okataina Volcanic Centre, New Zealand: Change in a silicic magmatic system following caldera collapse. *Journal of Volcanology and Geothermal Research*, 147: 357-376.

- Sheridan, M.F. and Updike, R.G., 1975. Sugarloaf Mountain Tephra - a Pleistocene rhyolitic deposit of base-surge origin in northern Arizona. *Geological Society of America Bulletin*, 86(4): 571-581.
- Sheridan, M.F. and Wohletz, K.H., 1983A. Hydrovolcanism: Basic Considerations and Review. *Journal of Volcanology and Geothermal Research*, 17: 1-29.
- Sheridan, M.F. and Wohletz, K.H., 1983B. Origin of accretionary lapilli from the Pompeii and Avelino deposits of Vesuvius In: R. Gooley (Editor), *Microbeam analysis*. San Francisco Press, San Francisco, pp. 35-38.
- Shoji, S., Dahlgren, R. and Nanzyo, M., 1993. Genesis of Volcanic Ash Soils. In: M.N. S. Shoji, R. Dahlgren (Editor), *Developments in Soil Science* Elsevier, pp. 37-71.
- Siddall, M., Rohling, E., Almogi-Labin, A., Hemleben, C., Meischner, D., Schmelzer, I. and Smeed, D., 2003. Sea-level fluctuations during the last glacial cycle. *Nature*, 423: 853-858.
- Sigurdsson, H. and Carey, S., 1989. Plinian and co-ignimbrite tephra fall from the 1815 eruption of Tambora volcano. *Bulletin of Volcanology*, 51: 243-270.
- Sisson, T.W., 1982. Sedimentary characteristics of the airfall deposit produced by the major pyroclastic surge of May 18, 1980 at Mount St. Helens, Washington, University of California.
- Skipper, K., 1971. Antidune cross-stratification in a turbidite sequence, cloridorme formation, Gaspé, Quebec. *Sedimentology*, 17: 51-68.
- Smith, G., Rowley, P., Williams, R., Giordano, G., Trolese, M., Silleni, A., Parsons, D.R. and Capon, S., 2020. A bedform phase diagram for dense granular currents. *Nature Communications*, 11(2873): 1-11.
- Smith, V.C., Isaia, R. and Pearce, N.J.G., 2011A. Tephrostratigraphy and glass compositions of post-15 kyr Campi Flegrei eruptions: implications for eruption history and chronostratigraphic markers. *Quaternary Science Reviews*, 30: 3638-3660.
- Smith, V.C., Pearce, N.J.G., Matthews, N.E., Westgate, J.A., Petraglia, M.D., Haslam, M., Lane, C.S., Korisettar, R. and Pal, J.N., 2011B. Geochemical fingerprinting of the widespread Toba tephra using biotite compositions. *Quaternary International*, 246: 97-104.

- Smith, V.C., Shane, P. and Nairn, I.A., 2005. Trends in rhyolite geochemistry, mineralogy, and magma storage during the last 50 kyr at Okataina and Taupo volcanic centres, Taupo Volcanic Zone, New Zealand. *Journal of Volcanology and Geothermal Research*, 148: 372-406.
- Sohn, C. and Sohn, Y.K., 2019. Distinguishing between primary and secondary volcanoclastic deposits. *Nature Scientific Reports*, 9(12425).
- Sohn, Y.K. and Chough, S.K., 1989. Depositional processes of the Suwolbong tuff ring, Cheju Island (Korea). *Sedimentology*, 36: 837-855.
- Sohn, Y.K. and Park, K.H., 2005. Composite tuff ring/cone complexes in Jeju Island, Korea: possible consequences of substrate collapse and vent migration. *Journal of Volcanology and Geothermal Research*, 141: 157-175.
- Sorem, R.K., 1982. Volcanic ash clusters: tephra rafts and scavengers. *Journal of Volcanology and Geothermal Research*, 13: 63-71.
- Sparks, R.S.J., 1976. Grain size variations in ignimbrites and implications for the transport of pyroclastic flows. *Sedimentology*, 23: 147-188.
- Sparks, R.S.J., Bursik, M.I., Carey, S.M., Gilbert, J.S., Glaze, L.S., Sigurdsson, H. and Woods, A.W., 1997. *Volcanic Plumes*. Wiley, Chichester.
- Sparks, R.S.J., Self, S. and Walker, G.P.L., 1973. Products of ignimbrite eruptions. *Geology*, 1: 115-118.
- Sparks, R.S.J., Wilson, L. and Sigurdsson, H., 1981. The Pyroclastic Deposits of the 1875 Eruption of Askja, Iceland. *Philosophical Transactions of the Royal Society of London*, 299(1447): 241-273.
- Srivastava, A.K., Bansod, M.N., Singh, A. and Sharma, N., 2019. Geochemistry of paleosols and calcretes from Quaternary sediments of Purna alluvial basin, central India: An emphasis on paleoclimate. *Rhizosphere*, 11(100162): 1-12.
- Soil Survey Staff, 2014. *Keys to Soil Taxonomy*.
- Stelling, P., Gardner, J.E. and Begét, J., 2005. Eruptive history of Fisher Caldera, Alaska, USA. *Journal of Volcanology and Geothermal Research*, 139: 163-183.
- Stovall, W.K., Houghton, B.F., Hammer, J.E., Fagents, S.A. and Swanson, D.A., 2012. Vesiculation of high fountaining Hawaiian eruptions: episodes 15 and 16 of 1959 Kīlauea Iki. *Bulletin of Volcanology*, 74: 441-455.

- Suñe-Puchol, I., Aguirre-Díaz, G.J., Dávila-Harris, P., Miggins, D.P., Pedrazzi, D., Costa, A., Ortega-Obregón, C., Lacan, P., Hernández, W. and Gutiérrez, E., 2019. The Ilopando caldera complex, El Salvador: origin and early ignimbrite-forming eruptions of a graben/pull-apart caldera structure. *Journal of Volcanology and Geothermal Research*, 371: 1-19.
- Tabor, N.J., Myers, T.S. and Michel, L.A., 2017. Sedimentologist's Guide for Recognition, Description, and Classification of Paleosols. In: K.E. Zeigler and W. Parker (Editor), *Terrestrial Depositional Systems*. Elsevier, pp. 165-208.
- Taddeucci, J., Alatorre-Ibargüengoitia, M.A., Cruz-Vázquez, O., Del Bello, E., Scarlato, P. and Ricci, T., 2017. In-flight dynamics of volcanic ballistic projectiles. *Review of Geophysics*, 55: 675-718.
- Talbot, J.P., Self, S. and Wilson, C.J.N., 1994. Dilute gravity current and rain-flushed ash deposits in the 1.8 ka Hatepe Plinian deposit, Taupo, New Zealand. *Bulletin of Volcanology*, 56: 538-551.
- Tatsumi, Y., Hamilton, D.L. and Nesbitt, R.W., 1986. Chemical characteristics of fluid phase released from a subducted lithosphere and origin of arc magmas: Evidence from high-pressure experiments and natural rocks. *Journal of Volcanology and Geothermal Research*, 29(1-4): 293-309.
- Tewari, R.C. and Khan, Z.A., 2017. Structures and sequences in early Permian fluvial Barakar rocks of peninsular India Gondwana basins using binomial and Markov chain analysis. *Arabian Journal of Geosciences*, 10(13): 1-15.
- Textor, C., Graf, H.-F., Herzog, M., Oberhuber, J.M., Rose, W.I. and Ernst, G.G.J., 2006. Volcanic particle aggregation in explosive eruption columns. Part I: Parameterization of the microphysics of hydrometeors and ash. *Journal of Volcanology and Geothermal Research*, 150: 359-377.
- Tomita, K., Kanai, T., Kobayashi, T. and Oba, N., 1985. Accretionary lapilli formed by the eruption of Sakurajima volcano. *Journal of the Japanese Association of Mineralogists Petrologists and Economic Geologists*, 80: 49-54.
- Torres, R.C., Self, S. and Punongbayan, R.S., 1995. Attention Focuses on Taal: Decade Volcano of the Philippines. *EOS Transactions*, 76(24): 241-248.

- Townsend, M., Huber, C., Degruyter, W. and Bachmann, O., 2019. Magma Chamber Growth During Intercaldera Periods: Insights From Thermo-Mechanical Modeling With Applications to Laguna del Maule, Campi Flegrei, Santorini, and Aso. *Geochemistry, Geophysics, Geosystems*, 20: 1574-1591.
- Trolese, M., Giordano, G., Cifelli, F., Winkler, A. and Mattei, M., 2017. Forced transport of thermal energy in magmatic and phreatomagmatic large volume ignimbrites: Paleomagnetic evidence from the Colli Albani volcano, Italy. *Earth and Planetary Science Letters*, 478: 179-191.
- Türk, G., 1979. Transition analysis of structural sequences: discussion. *Bulletin of the Geological Society of America* 90: 989-991.
- Uehara, G., 2005. Volcanic Soils. In: D. Hillel (Editor), *Encyclopedia of Soils in the Environment*. Elsevier, 225-232.
- Ugolini, F.C. and Dahlgren, R.A., 2002. Soil Development in Volcanic Ash. *Global Environmental Research* 6: 69-82.
- Valentine, G.A., Perry, F.V. and WoldeGabriel, G., 2000. Field characteristics of deposits from spatter-rich pyroclastic density currents at Summer Coon volcano, Colorado. *Journal of Volcanology and Geothermal Research*, 104: 187-199.
- Vallance, J.W. and Iverson, R.M., 2015. Lahars and Their Deposits. In: H. Sigurdsson (Editor), *The Encyclopedia of Volcanoes* (2nd ed.). Elsevier, pp. 650-664.
- Van Eaton, A.R., Herzog, M., Wilson, C.J.N. and McGregor, J., 2012. Ascent dynamics of large phreatomagmatic eruption clouds: the role of microphysics. *Journal of Geophysical Research*, 117(B03203).
- Van Eaton, A.R. and Wilson, C.J.N., 2013. The nature, origins and distribution of ash aggregates in a large-scale wet eruption deposit: Oruanui, New Zealand. *Journal of Volcanology and Geothermal Research*, 250: 129-154.
- van Wyk de Vries, B. and Davies, T., 2015. Landslides, Debris Avalanches, and Volcanic Gravitational Deformation In: H. Sigurdsson (Editor), *The Encyclopedia of Volcanoes* (2nd ed.). Elsevier, pp. 665-685.
- Veitch, G. and Woods, A.W., 2001. Particle aggregation in volcanic eruption columns. *Journal of Geophysical Research*, 106(26): 5596-5614.

- Vepraskas, M.J., 1992. Redoximorphic Features for Identifying Aquic Conditions, NC State University, Raleigh.
- Vespa, M., Keller, J. and Gertisser, R., 2006. Interplinian explosive activity of Santorini volcano (Greece) during the past 150,000 years. *Journal of Volcanology and Geothermal Research*, 153: 262-286.
- Vidal, C.M., Komorowski, J.-C., Métrich, N., Pratomo, I., Kartadinata, N., Prambada, O., Michel, A., Carazzo, G., Lavigne, F., Rodysill, J., Fontijn, K. and Surono, 2015. Dynamics of the major plinian eruption of Samalas in 1257 A.D. (Lombok, Indonesia). *Bulletin of Volcanology*, 77(73): 1-24.
- Vinkler, A.P., Cashman, K., Giordano, G. and GropPELLI, G., 2012. Evolution of the mafic Villa Senni caldera-forming eruption at Colli Albani volcano, Italy, indicated by textural analysis of juvenile fragments. *Journal of Volcanology and Geothermal Research*, 235-236: 37-54.
- Vistelius, A.B., 1949. On the question of the mechanism of the formation of strata. *Doklady Akademii Nauk SSSR*, 164: 191-194.
- Vogel, T.A., Flood, T.P., Patino, L.C., Wilmot, M.S., Maximo, R.P.R., Arpa, C.B., Arcilla, C.A. and Stimac, J.A., 2006. Geochemistry of silicic magmas in the Macolod Corridor, SW Luzon, Philippines: evidence of distinct, mantle-derived, crustal sources for silicic magmas. *Contributions to Mineralogy and Petrology*, 151: 267-281.
- Walker, G.P.L., 1981. Characteristics of two phreatoplinian ashes, and their water-flushed origin. *Journal of Volcanology and Geothermal Research*, 9: 395-407.
- Walker, G.P.L., 1984. Characteristics of dune-bedded pyroclastic surge bedsets. *Journal of Volcanology and Geothermal Research*, 20: 281-296.
- Walker, G.P.L., 1993. Basaltic-volcano systems. In: H.M. Prichard, T. Alabaster, N.B.W. Harris and C.R. Neary (Editors), *Magmatic Processes and Plate Tectonics*. Geological Society Special Publication. Geological Society, pp. 3-38.
- Walker, G.P.L. and Croasdale, R., 1971. Two plinian-type eruptions in the Azores. *Journal of the Geological Society of London*, 127: 17-55.
- Walker, R.G., 1967. Upper flow regime bed forms in turbidites of the Hatch Formation, Devonian of New York State. *Journal of Sedimentary Research*, 37(4): 1052-1058.

- Waltham, D., 1994. Mathematics: A simple tool for geologists. Chapman and Hall, London, 189 pp.
- Waters, A.C. and Fisher, R.V., 1971. Base Surges and Their Deposits: Capelinhos and Taal Volcanoes. *Journal of Geophysical Research*, 76(20): 5596-5614.
- White, J.D.L., 1996. Pre-emergent construction of a lacustrine basaltic volcano, Pahvant Butte, Utah (USA). *Bulletin of Volcanology*, 58: 249-262.
- White, J.D.L. and Valentine, G.A., 2016. Magmatic versus phreatomagmatic fragmentation: Absence of evidence is not evidence of absence. *Geosphere*, 12: 1478-1488.
- Wilson, C.J.N., 1985. The Taupo Eruption, New Zealand II. The Taupo Ignimbrite. *Philosophical Transactions of the Royal Society A*, 314: 229-310.
- Wilson, C.J.N., 2001. The 26.5 ka Oruanui eruption, New Zealand: an introduction and overview. *Journal of Volcanology and Geothermal Research*, 112: 133-174.
- Wilson, C.J.N., Blake, S., Charlier, B.L.A. and Sutton, A.N., 2006. The 26.5 ka Oruanui eruption, Taupo Volcano, New Zealand: development, characteristics and evacuation of a large rhyolitic magma body. *Journal of Petrology*, 47(1): 35-69.
- Wilson, C.J.N. and Hildreth, W., 1997. The Bishop Tuff: New Insights from Eruptive Stratigraphy. *The Journal of Geology*, 105(4): 407-440.
- Wilson, C.J.N. and Walker, G.P.L., 1985. The Taupo Eruption, New Zealand I. General aspects. *Philosophical Transactions of the Royal Society A*, 314: 199-228.
- Witte, L.C., Cox, J.E. and Bouvier, J.E., 1970. The vapor explosion. *Journal of Metals*, 22(2): 39-44.
- Wohletz, K., Orsi, G. and De Vita, S., 1995. Eruptive mechanisms of the Neapolitan Yellow Tuff interpreted from stratigraphic, chemical, and granulometric data. *Journal of Volcanology and Geothermal Research*, 67: 263-290.
- Wohletz, K.H., 1983. Mechanisms of Hydrovolcanic Pyroclast Formation: Grain-Size, Scanning Electron Microscopy, and Experimental Studies. *Journal of Volcanology and Geothermal Research*, 17: 31-63.

- Wohletz, K.H. and McQueen, R.G., 1984. Experimental studies of hydromagmatic volcanism. In: N.R. Council (Editor), *Explosive Volcanism: Inception, Evolution, and Hazards*. National Academy Press, Washington D.C.
- Wohletz, K.H. and Sheridan, M.F., 1979. A model of pyroclastic surge. In: C.E. Chapin and W.E. Elston (Editor), *Ash-flow Tuffs*. The Geological Society of America, Boulder, Colorado, pp. 177-194.
- Wolfe, J.A., Manuzon, M.S. and Divis, A.F., 1978. The Taysan Porphyry Copper Deposit, Southern Luzon Island, Philippines. *Economic Geology*, 73: 608-617.
- Wolfe, J.A. and Self, S., 1983. Structural Lineaments and Neogene Volcanism in Southwestern Luzon. In: D.E. Hayes (Editor), *The Tectonic and Geologic Evolution of the Southeast Asian Seas and Islands: Part 2*. American Geophysical Union, Washington D.C.
- Woods, A.W., Bursik, M.I. and Kurbatov, A.V., 1998. The interaction of ash flows with ridges. *Bulletin of Volcanology*, 60: 38-51.
- Wotzlaw, J.-F., Schaltegger, U., Frick, D.A., Dungan, M.A., Gerdes, A. and Günther, D., 2013. Tracking the evolution of large-volume silicic magma reservoirs from assembly to supereruption. *Geology*, 41(8): 867-870.
- Wulf, S., Kraml, M. and Keller, J., 2008. Towards a detailed distal tephrostratigraphy in the Central Mediterranean: The last 20,000 yrs record of Lago Grande di Monticchio. *Journal of Volcanology and Geothermal Research*, 177: 118-132.
- Xu, H. and Maccarthy, I.A.J., 1998. Markov chain analysis of vertical facies sequences using a computer software package (SAVFS): Courtmacsherry Formation (Tournaisian), Southern Ireland. *Computers & Geosciences*, 24: 131-139.
- Yokoyama, I., Alcaraz, A. and Pena, O., 1975. Gravimetric Studies of Taal Volcano, Philippines. *Bulletin of Volcanology*, 39: 479-489.
- Yokoyama, S. and Tokunaga, T., 1978. Base-surge deposits of Mukaiyama volcano, Nii-jima, Izu Islands. *Bulletin of the Volcanological Society of Japan*, 23: 249-262.

- Yumul Jr, G.P., Dimalanta, C.B., Tamayo Jr, R.A. and Maury, R.C., 2003. Collision, subduction and accretion events in the Philippines: A synthesis. *The Island Arc*, 12: 77-91.
- Zimanowski, B., Büttner, R., Dellino, P., White, J.D.L. and Wohletz, K.H., 2015. Magma-Water Interaction and Phreatomagmatic Fragmentation. In: H. Sigurdsson (Editor), *The Encyclopedia of Volcanoes* (2nd ed.). Elsevier, pp. 473-484.
- Zimanowski, B., Büttner, R., Lorenz, V. and Häfele, H.-G., 1997. Fragmentation of basaltic melt in the course of explosive volcanism. *Journal of Geophysical Research: Solid Earth*, 102: 803-814.
- Zlotnicki, J., Sasai, Y., Johnston, M., Vargemezis, G., Villacorte, E., Reniva, P., Alanis, P. and Gordon Jr, J.M., 2017. Taal volcano in Philippines: What is the future?, IAVCEI, Portland.